Mechanical Rock Property Characterisation and Assessment of Sandstone Reservoirs in the Southern Taranaki Basin

---

A thesis

submitted in partial fulfilment of the requirements for the degree

of

Doctor of Philosophy in Engineering Geology

at the

University of Canterbury

by

Sophie Hill

UNIVERSITY OF CANTERBURY

2019

Frontispiece

Braided river succession through the Paleocene aged Farewell Formation reservoir outcropping at the southernmost edge of the Taranaki Basin – Cape Farewell

Abstract

The application of geomechanics to petroleum development involves predicting and minimising rock deformation by providing an enhanced understanding of the in-situ stress distribution across an interval using geomechanical models. During drilling, local stress perturbations occur in response to the redistribution of the in-situ stress field around the wellbore excavation; if the application of stresses acting upon the reservoir exceeds the rock strength, irreversible deformation will occur through shearing or compaction. Thus, accurate determination of the strength parameters e.g. uniaxial compressive strength (UCS), used as input parameters, is crucial for reliable geomechanical modelling. A constrained geomechanical model enables optimization of wellbore stability and production, reducing the potential for common geomechanical problems such as borehole breakouts and/or sand production.

The southern Taranaki Basin represents a region of extensive petroleum development in New Zealand with many exploratory boreholes. Despite this, the offshore region is poorly represented in terms of geomechanical assessment, despite more complex and deeper petroleum prospects than onshore. Geomechanical studies previously undertaken in the Taranaki region by industry highlight the need for increased laboratory testing to better constrain the rock strength across the basin. In cases where the availability of rock strength laboratory measurements is limited, rock strength is often approximated using empirical relationships utilizing physical properties, but these are uncalibrated and often result in under/overestimation of strength predictions. In addition, empirical rock strength relations rarely consider petrographical properties such as grain size as input parameters, despite grain size providing a dominant control on rock strength.

The characterisation undertaken in this research project was done using a proposed workflow from qualitative analysis of reservoirs using facies descriptions, petrographical analysis for mineralogical and textural properties, and acquisition of data to develop a rock property database. Evaluation of laboratory data through statistical analysis was used to develop locally calibrated physical property-rock strength relations

for improved strength predictions. These were used to develop strength profiles along well trajectories, alongside failure criteria parameters, for downhole stability analysis at any depth. Data acquisition of physical property measurements such as density, porosity, sonic wave velocities, uniaxial compressive rock strength were used in conjunction with wireline data for core log calibration. Key findings of this research have highlighted the textural properties of siliclastic rocks, noticeably grain size and grain sorting, should provide the principal basis for mechanical rock property characterisation of reservoirs. The results of this study are presented as discussions of three main research questions.

The first, identifies the dominant microscale controls on physical rock properties, and shows that sedimentary facies can be used to allocate quantifiable data to a reservoir unit. Grain size and grain sorting provide the dominant control on physical rock properties at the microscale. The dominant pore type e.g. intergranular pores and micropores is a result of grain sorting; pore throat diameter and porosity fraction exhibit a proportional relationship. Grain size demonstrates a control on permeability with smaller grain sizes attributed to lower flow rates; under a constant grain size there is a proportional relationship between pore throat diameter and permeability. Sedimentary facies are associated with changes in grain size and sorting as a result of the depositional environment, and thus can provide the basis for quantifiable units of physical rock properties and mechanical strength parameters.

The second, identifies the dominant controls on the mechanical rock properties, and how these can be incorporated to accurately predict rock strength. Results demonstrate the statistically strongest relationships for sandstones are with porosity and grain size. In general, the use of porosity fraction is most suited for strength prediction of sandstone strength. The use of a grain size variable within porosity-strength prediction can act to further constrain strength measurements between clean and shaly sands. For the purpose of this empirical rock strength relationship, grain size is considered independent of porosity fraction. This research shows that the proposed empirical strength relationship can be extrapolated across a wide spatial and age distribution to other reservoir intervals to provide a first estimate of strength.

The third, shows how the assessment of formation stability is improved by determination of mechanical strength and failure parameters using locally calibrated empirical relationships. The main implications of the research findings suggest that without local calibration of predictive relations, there is an increased likelihood of under/overestimation of rock strength. In the example of the strike-slip regime proposed for the Maui-Maari region, over-prediction of UCS from uncalibrated logs can lead to underestimation of the rock surrounding the wellbore subjected to a partial normal stress regime.

Acknowledgements

First and foremost, a special thank you to my fiancé Ben Wallace for proofreading, and for his endless love, support, and encouragement at every stage of this journey. Thank you to my primary supervisor Marlene Villeneuve, and the rest of my supervisory team David McNamara, Kari Bassett and Hannu Seebeck for their ongoing support and reviews throughout the duration of my thesis. Thank you to the staff at GNS, Karsten Kroeger, Angela Griffin and Mark Lawrence for feedback and advice. Thank you to the Geological Sciences staff at the University of Canterbury, particularly to Cathy Higgins, Sarah Pope, Rob Spiers and Chris Grimshaw for their continual technical support and advice. A special thanks to my family in the UK, and my closest friend Jess McCormack for their love and support. Lastly, thank you to the postgraduate cohort at UC for their invaluable support and keeping me sane over the past three years, particularly Kate, Romy, Laura, Clare, and Jess.

This project was funded by the Ministry of Business, Innovation and Employment through the GNS PSF research project – Understanding petroleum source rocks, fluids, and plumbing systems in New Zealand Basins.

Table of Contents

List of Figures

List of Tables

List of Quantitative Data

Measurement	**Symbol**	**Unit**
Length	L or h	mm or cm
Diameter	D	mm or cm
Bulk Volume	V	cm^3
Grain Volume	Vs	cm^3
Pore Volume	Vv	cm^3
Mass	M	g
Bulk Density	ρ	g/cm^3 or kg/m^3
Grain Size	D	μm
Pore Throat Diameter/Radius	D	μm
Porosity	n	% or unitless
Permeability	K	mD or m^2
Ultrasonic Wave velocities	Vp or Vs	m/s
Compressional Slowness	DTC	μs/ft
Youngs Modulus	E	GPa
Poisson's Ration	v	Unitless
Axial Stress and Confining Pressure	σ_1 or σ_3	MPa
Cohesion	C	MPa
Friction Angle	ϕ	^{o}
Hoek Brown Material Constant	m_i	Unitless
Unconfined Compressive Strength	UCS (or σ_{ci})	MPa
Axial and Lateral Strain	ε_1 or ε_2	Unitless

Chapter One – Introduction

1.1. Context of Study

Over the past hundred years there have been notable developments in the adoption of geomechanics in the oil and gas industry, from underpinning theoretical studies (Kirsch, 1898; Anderson, 1905; Terzaghi, 1925; Biot, 1941) to the computational 3D modelling of producing fields (Frischbutter and Henk, 2010; Fischer and Henk 2013). The development of science and practice of geomechanics has been driven by industry need (Ali et al., 2003). Geomechanical modelling is used to paradigm the evolution of stresses acting within a petroleum system at every stage of reservoir development, from prediction of far field in-situ regional stresses across a basin, to the localised stress concentration around a borehole (Addis, 2017). The impact of stress field evolution during production can be significant to formation stability, and consequential to coupled fluid flow processes (Settari and Mourits, 1998; Settari and Walters, 2001; Longuemare et al., 2002). During production, excavation of rock by drilling results in localised changes in the stress field; if the application of stresses acting upon the reservoir exceed the rock strength, irreversible deformation will occur through shearing or compaction (Fjaer et al., 2008). The use of geomechanical modelling for petroleum development has increased in global popularity over the past half century and led to significant improvements in field production and recovery (Moos 2014; Addis 2017); however, this practice has not yet been established for New Zealand basins. A constrained model enables optimization of wellbore stability and production, reducing the potential for common geomechanical problems such as borehole breakouts and/or sand production (Last et al., 1995). Existing geomechanical reports for the Taranaki Basin are concerned with understanding the in-situ stresses for pore pressure evaluation (New Zealand Oil and Gas, 2010), wellbore stability (Swift Energy, 2007a; Swift Energy, 2007b; Shell Todd Oil Services Limited, 2001) and fault stability analysis (Todd Energy, 2010; Massiot et al., 2019). Geomechanical studies previously undertaken in the Taranaki region by industry highlight the need for increased laboratory testing to better constrain the rock strength across the basin (Shell Todd Oil Services Limited, 2001; Shell Todd Oil Services

Limited, 2002; New Zealand Overseas Petroleum Limited, 2005; OMV New Zealand Limited, 1998-2006; Swift Energy, 2007a; Swift Energy, 2007b; Todd Energy, 2010).

The mechanical parameters used to characterise the deformational behaviour of a rock can be obtained through direct measurements from laboratory testing. Uniaxial compressive tests provide a measure of the unconfined compressive strength (UCS) of the rock. Triaxial compression tests provide a measure of rock strength under reservoir confinement conditions; the strength is a measure of the differential stress under which the rock fails (Wong et al., 1997; Baud et al., 2000). The quantitative geomechanical data from uniaxial and triaxial compression tests can define a failure criterion envelope for a reservoir interval to predict reservoir failure; delineating the boundary between intact and failed rock plotted in stress space. For the purpose of this study, Mohr-Coulomb and Generalised Hoek Brown Criterion are considered; material strength parameters are determined from these criterions (Hoek and Brown, 1997; Labuz and Zang 2012).

In cases where the availability of laboratory measurements is limited, strength is often approximated using empirical relationships utilizing other physical properties. Physical reservoir properties e.g. density, porosity and interval transit time, usually derived from wireline logs, are utilized as input variables for rock strength prediction (Coates and Denoo 1981; McNally 1987; Fjaer et al., 1992; Moos et al., 1999; Chang et al 2006; Khahsar et al, 2009). These empirical relations provide a preliminary strength prediction; however, without calibration to the local reservoirs, strength predictions are often poorly constrained and can be unreliable. For optimum results strength profiles should be calibrated with laboratory strength data. Proposed relationships are often constrained to a single lithotype e.g. sandstones; however, this assumes a clean formation. In reality, sandstone reservoirs consist of a combination of lithotypes: in the Taranaki Basin, most reservoir intervals are considered to be shaly sandstones (Massiot et al., 2019). Several studies have investigated the control of physical properties on the mechanical behaviour of sandstones, but few consider petrographical properties such as grain size as input parameters into empirical rock strength relations (Ulusay et al., 1994; Amanpour, 2018).

1.2. Aims

The principal aim of this thesis is to provide a mechanical rock property characterisation for sandstone reservoirs in the southern Taranaki Basin. The rock property characterisation for the southern Taranaki Basin is presented as a new proposed workflow for preliminary geomechanical model development (Figure 1.1). From qualitative analysis and data acquisition, to statistical analysis and application, the assessment of formation stability in the southern Taranaki Basin is achieved through accurate determination and prediction of mechanical strength parameters.

1.3. Research Methodology

1.3.1. Research Questions

1) What are the dominant microscale controls on physical rock properties, and can sedimentary facies be used to allocate quantifiable data to a reservoir unit?

2) Which are the dominant controls on the rock mechanical properties, and how can these be incorporated to accurately predict strength?

3) How is the assessment of formation stability improved from determination of rock strength parameters using locally calibrated relationships?

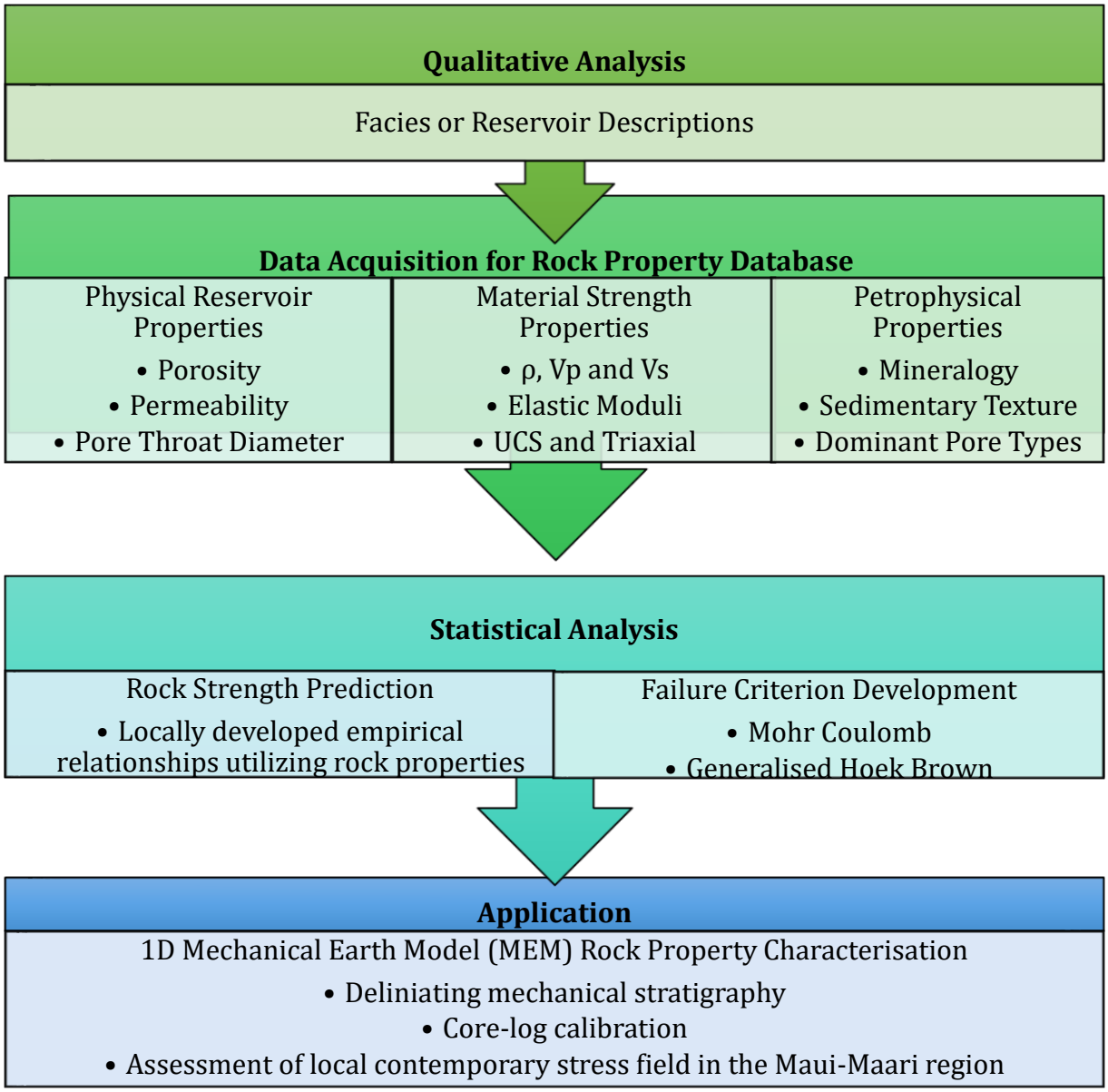

Figure 1-1 Proposed workflow for mechanical rock property characterisation for the Southern Taranaki Basin

1.3.2. **Thesis Structure**

Chapter 2 introduces the background understanding of the topic with a comprehensive literature review, used to establish the scientific context and emphasise the gap in information which is augmented by this research. The overlap of sedimentology, rock mechanics and petroleum engineering requires a foundational understanding of all three fields to set the context of this work. Chapter 3 presents an extensive methodological section, incorporating field studies, laboratory testing to industry standards, and data analysis.

Chapter 4 presents the preliminary research topic focused on microscale heterogeneities within sandstones e.g. sedimentary texture and pore characteristics, and their impact on physical reservoir properties e.g. porosity and permeability. Porosity and permeability data are a key component of reservoir simulation models. For models to be representative at a reservoir scale, measurements must be quantified in a systematic manner which incorporates as much fine detail as possible. The use of depositional facies to characterise porosity and permeability is a common and acknowledged method combined with outcrop lithofacies descriptions to aid wireline interpretations and delineate the spatial distributions.

Chapter 5 evaluates the quantitative physical and mechanical properties acquired from laboratory testing of core plugs from offshore Taranaki basin reservoirs. The quantitative data are used to develop and refine empirical models for rock strength prediction in the Taranaki Basin. Statistical analysis was used for quantitative assessment of derived empirical relations to provide a level of confidence for extrapolation. Failure envelopes were derived from uniaxial and triaxial data for both the Mohr-Coulomb and Generalised Hoek-Brown Criteria, used to determine rock strength parameters and assess reservoir stability.

Chapter 6 presents the rock mechanical property component of a 1D MEM for the Maui-Maari region of the southern Taranaki Basin, attributed across two stratigraphic intervals from the Whio-1 well trajectory. A typical workflow for the rock property

component of a 1D MEM utilizes well data from physical properties, density and sonic velocities, which provide the basis for prediction of the elastic and mechanical strength parameters. The strength parameter logs allow for failure criterion development at any depth without the need for laboratory testing and when used in conjunction with local stress measurements this allows for reservoir stability assessment. This chapter further discusses the impact of strength prediction on the assessment of the contemporary stress field.

The thesis format is structured with the main research presented in three core chapters (4, 5 and 6). The individual research questions of each core chapter are addressed at the end of each section, with a concise description of results and detailed discussion, with overarching conclusions drawn in Chapter 7.

1.3.3. **Research Objectives and Scientific Contributions**

The scientific contributions are presented in Table 1.1 and outline the main research objectives and associated chapters.

Table 1-1 Summary of scientific contributions, research objectives and relevant chapters

Scientific contribution	Research Objectives	Relevant Chapter(s)
Develop a rock property database with physical and mechanical strength parameters attributed to reservoir rocks from the southern Taranaki Basin	Best practice for data acquisition from outcrop and core studies	Chapters 3, 4 and 5
	Determine the textural controls on the physical and mechanical strength properties	Chapters 4 and 5
Determine appropriate empirical relationships for strength prediction within the Southern Taranaki Basin	Develop locally calibrated strength prediction relationships using statistical analysis of rock property data.	Chapter 5
	Construct appropriate rock failure criteria from strength data e.g. Mohr Coulomb and Hoek-Brown	
	Assess rock strength prediction for sands, shales and shaly sandstones	Chapters 5 and 6
Construct a 1D MEM rock property characterisation	Development of mechanical stratigraphy from GR logs, characterised by strength and failure criterion parameter logs	Chapter 6
	Assessment of local contemporary stress field in the Maui-Maari region	Chapter 6

Chapter Two – Literature Review

2.1. Petroleum Exploration in the Taranaki Basin

The Taranaki Basin, covering an area of approximately 330,000 km^2, has a rich history of petroleum exploration with over 400 onshore and offshore appraisal and production wellbores drilled to date (Greer et al., 2013; King and Thrasher, 1996). The Taranaki Basin has seen continuous production since the early 1900s, with an increase of petroleum exploration in the region from the 1950s. This was consequential of the discovery of large gas-condensate fields, including the onshore Kapuni and Mangahewa Fields, in 1959 and 1961 respectively, and offshore Maui Field in 1969; at that time, the Maui Field represented one of the largest gas fields in the world (New Zealand Petroleum Basins, 2014/15). The discovery of petroleum fields both onshore and offshore have been made at a steady rate since then. The Maari-Manaia Field, New Zealand's largest offshore oilfield was discovered in 1983, with subsequent oil-condensate accumulations found in the eastern adjacent offshore Kupe Field in 1986. Into the 21st century, continued exploration has led to the discovery of other smaller fields including the offshore Tui, Amokura and Pateke Fields. However, the significant gas-condensate discovery of the onshore Pohokura Field in 2000 provided renewed confidence in the petroleum potential of the Taranaki Basin. The Pohokura field is currently New Zealand's largest gas-condensate field, since the steady decline in gas reserves attributed to the Maui Field since production began. Current production is focused onshore or on the shallow shelf edge surrounding the Taranaki Peninsula (Figure 2.1). Of the petroleum fields mentioned above, hydrocarbon reserves are constrained to the Eocene-Paleocene Kapuni Group strata (Mangahewa, Kaimiro and Farewell Formations); the only exception is the Maari Field with oil reserves found predominantly in the Miocene reservoirs, although smaller accumulations occur in the Lower Mangahewa Formation. Though current production is exclusive to the Paleocene-Pliocene sedimentary succession, older and deeper deposits are recognised as potential reservoir prospects; the Late Cretaceous North Cape Formation is seen as a key

hydrocarbon target in the deep-water exploration blocks of the western side of the Taranaki Basin (Higgs et al., 2010; Stagpoole et al., 2001).

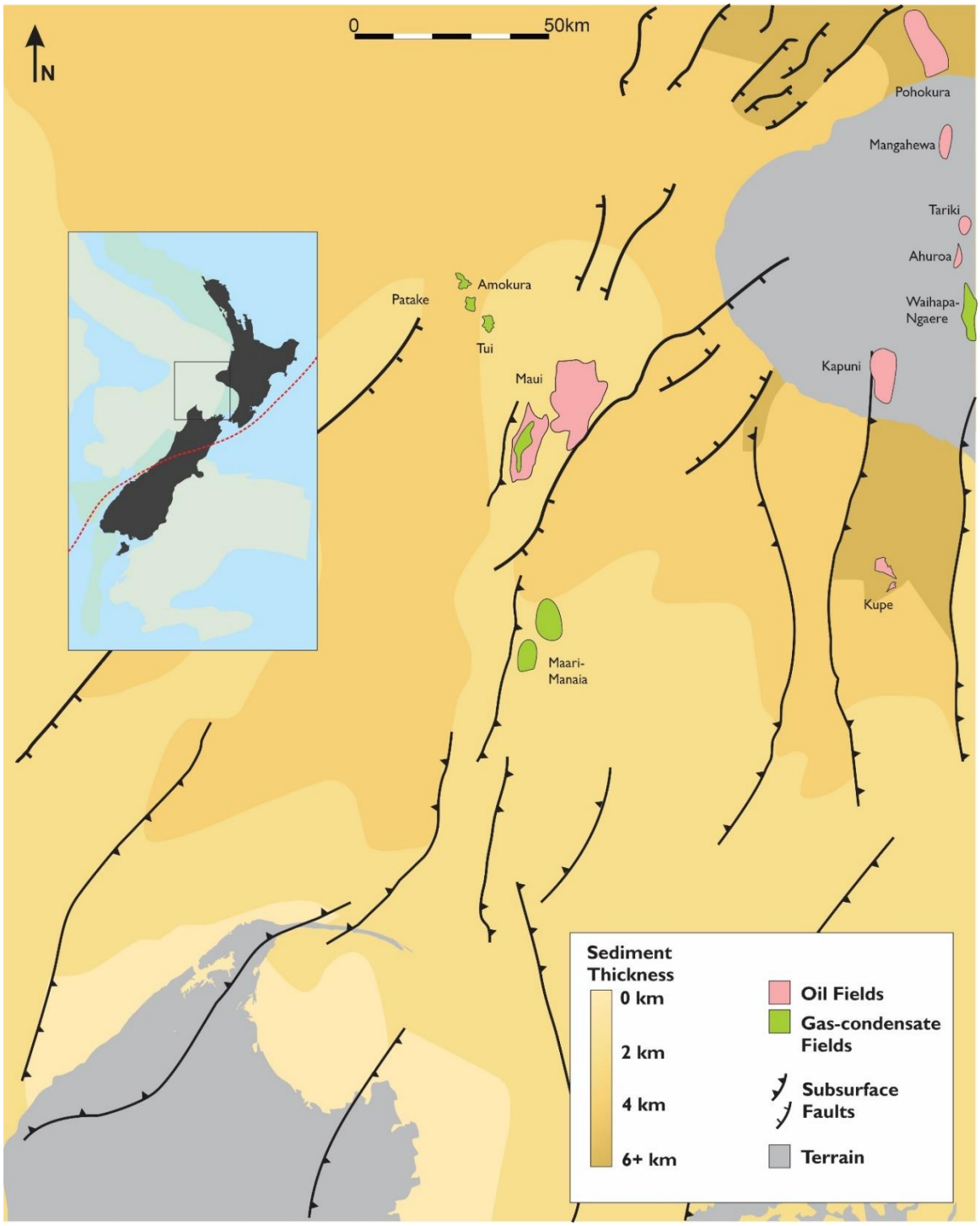

Figure 2-1 Regional map of the Taranaki Basin with reference to both onshore and offshore petroleum fields (Adapted from GNS PBE).

2.2. Geomechanics in the Oil and Gas Industry

Geomechanical issues can impact every stage of a reservoir's productive life cycle, from preliminary appraisal to field abandonment (Addis, 2017). During drilling, local stress perturbations occur in response to the redistribution of the in-situ stress field around the wellbore excavation, or during production removal of pore fluids can reduce the effective stresses acting on the rock, instigating reservoir compaction. The application of geomechanics to petroleum development involves predicting and minimising this rock deformation by providing an enhanced understanding of the in-situ stress distribution across an interval; this leads to significant improvements in the economic performance of a field from drilling, production and recovery.

Unplanned geomechanical issues cost the petroleum industry billions of dollars a year due to non-productive time (NPT). The major cause of non-productive time (NPT) is wellbore instability, causing borehole collapse, lost circulation, stuck pipe, lost hole and sand production during the producing life of the well (Moazzeni et al., 2010). Such issues are noted to occur in the Goss & Trapper wellbores within the TAWN (Tariki, Ahuroa, Waihapa and Ngaere) fields of the Taranaki Basin; a subsequent 1-D geomechanical model was developed for this region following these issues (Swift Energy, 2007a). Irrespective of this, there is a deficient use of geomechanics in the Taranaki Basin, although there has been an increase of geomechanical reports generated since 2001. Individual geomechanical studies were undertaken to ensure a minimal risk of formation damage and wellbore instability during drilling, or to provide sand failure, pore pressure and fracture gradient predictions (Shell Todd Oil Services Limited, 2002; New Zealand Oil and Gas, 2010; Todd Energy, 2014). The geomechanical studies attributed to the offshore region of the Taranaki Basin is generally unrepresentative. To date, petroleum reports detailing comprehensive 1D MEMs for the Taranaki Basin are all in proximity of the onshore Taranaki Peninsula e.g. Pohokura Field, Mangahewa Field, TAWN fields, Kauri field and the Te Kiri Prospect (Shell Todd Oil Services Limited, 2001; Swift Energy, 2007a; Swift Energy, 2007b; Todd Energy, 2010; Todd Energy, 2015). The offshore region of the Taranaki Basin is poorly represented, despite more complex and deeper petroleum prospects; the only offshore reports are attributed to the Amokura

Field, and Kaupokonui Prospect in the Southern Taranaki Basin (New Zealand Overseas Petroleum Limited, 2005; New Zealand Oil and Gas, 2010). In turn, no comprehensive 3D geomechanical model has ever been developed within the Taranaki region.

2.3. Building a Geomechanical Model

A geomechanical model comprises three types of input data: the in-situ stress field and pore pressures, material rock properties and the reservoir geometry (Guerra et al., 2019). Geomechanical models can be 1D (along the wellbore), 3D (full field appraisal) and 4D (Real time production). Advances in computational capabilities have allowed for the development of 3D modelling software, such as the finite element method, to gain quantitative insights into the stress distribution of reservoirs (Fischer and Henk, 2013; Herwanger et al., 2014). A proposed workflow for the construction of a 3D geomechanical model is outlined in Figure 2.2 (Guerra et al., 2019; Fischer and Henk, 2013).

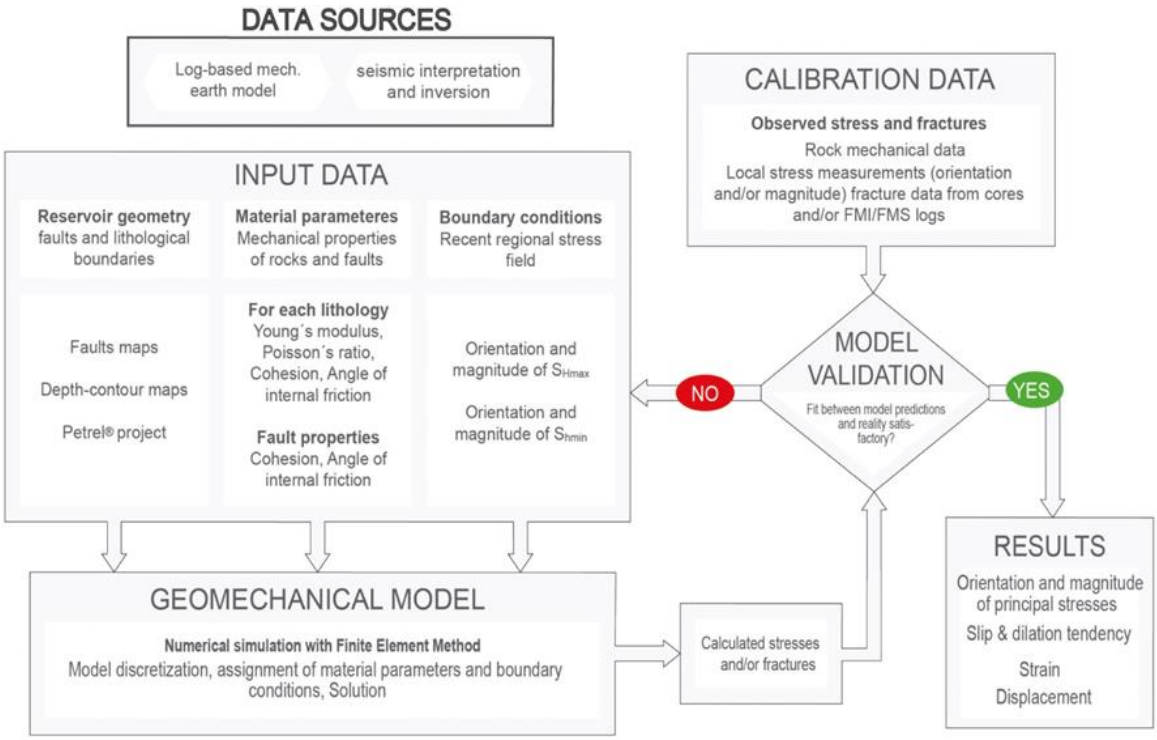

Figure 2-2 Proposed workflow for the construction of a 3D geomechanical model (Guerra et al., 2019; Fischer and Henk, 2013).

The disadvantage of computational 3D and 4D geomechanical simulations is the large quantity of input data required to constrain and calibrate the model; this data is often absent in the early appraisal stage of field development (Guerra et al., 2019). To overcome this, one-dimensional mechanical earth models (1-D MEM) can be constructed using a wireline log-based approach for mechanical characterisation of the formation in proximity to the wellbore surroundings. Log data, including sonic velocities, density, porosity and gamma ray, are used to represent mechanical rock properties and the state of stress near the borehole (Ali et al., 2003), Figure 2.3.

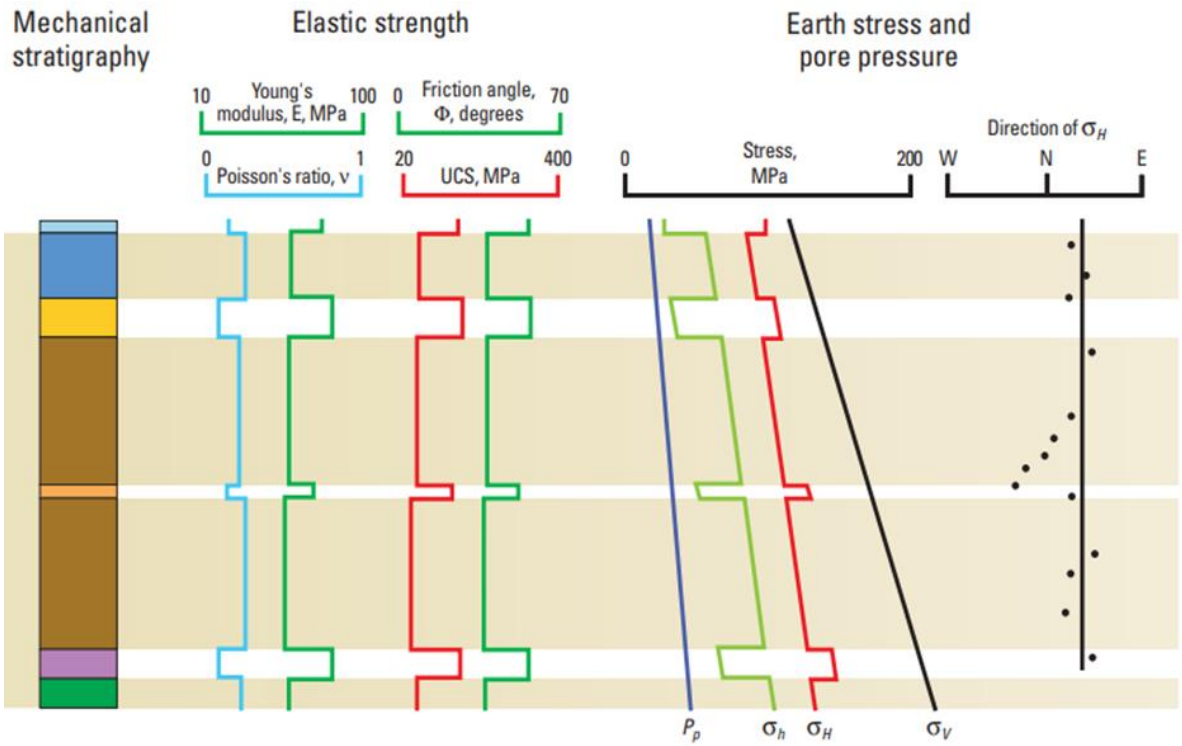

Figure 2-3 Example of a 1D log based mechanical earth model providing continuous profiles of in-situ stresses, mechanical rock properties and stratigraphy (Ali et al., 2003).

This preliminary geomechanical assessment of an individual wellbore allows for effective operation of petroleum fields during early production, used to predict optimal mud weight window, stability of future wells by pore pressure and fracture gradient prediction, and design of optimal well trajectories. Building a 1D MEM during the well planning phase and updating in real time has proven to be extremely valuable in delivering complex wells safely whilst minimising the non-productive time during drilling due to wellbore instability (Plumb et al., 2000; Goodman, 2005). For

geomechanical characterisation across a 3D spatial distribution, the individual 1D geomechanical models can provide input parameters used in conjunction with seismic inversion data to build a 3D geomechanical model (Wendt et al., 2013).

2.3.1. **Boundary Conditions**

2.3.1.1. In-situ Stress Vector

The in-situ stress tensor describes the current state of stress acting within a basin in a three-dimensional space; defined by three orthogonal principal stresses, S_1, S_2 and S_3, each with a magnitude and orientation (Zoback, 2007). Assuming one of the principal stresses is acting vertical, S_v, the other two principal stresses can be represented by maximum horizontal stress (S_{Hmax}) and minimum horizontal stress (S_{hmin}). The orientation of these three principal stresses will control the type of stress regime within a basin (Figure 2.4), based upon the classification scheme for relative stress magnitudes and faulting style (Anderson, 1905).

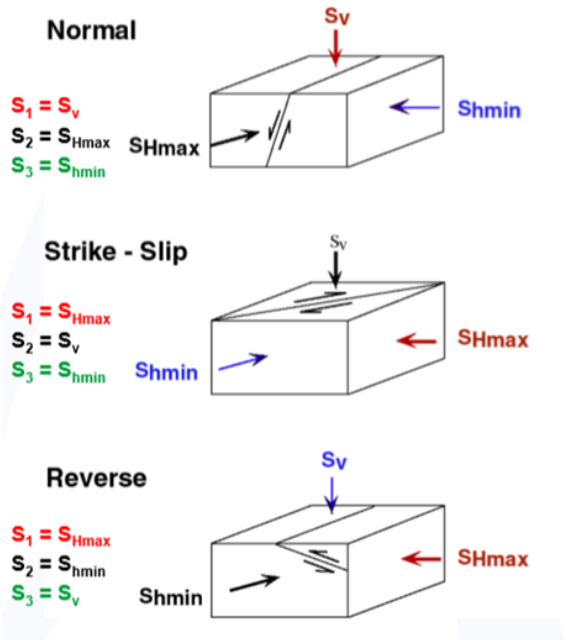

Figure 2-4 Anderson's classification scheme for stress regime based upon relative stress magnitudes (Anderson, 1905).

At a first order scale, geological indicators can be used to determine the orientation of the contemporary horizontal stresses such as earthquake focal plane mechanisms, fault slip data and intrusive features, and regional stress patterns - data compilation found in the World Stress Map (Heidbach et al., 2008; Zoback, 1992)

2.3.1.2. Evaluation from Wellbore Data

Determination of the state of stress at depth in an oil and gas fields is a tractable problem that can be addressed with data routinely obtained during wellbore drilling.
Assuming a vertical wellbore, the vertical principal stress is in alignment with the wellbore axis, where S_v is a measure of overburden weight, see Equation 2.1 (Wiprut and Zoback, 2000, Zoback et al., 2003).

$$S_v = \rho_w g z_w + \int_0^z \rho(z - z_w) g \, dz \tag{2.1}$$

Where,
Sv = overburden (MPa)
z = depth below sea level (m)
ρ = formation density from density log (kg/m3)
zw = water depth (m)
ρw = density of water (1029kg/m3)

The orientation of S_{hmin} and S_{Hmax} are often reflected in geological structures formed during drilling (Figure 2.5). During the excavation of material from drilling, the far field stresses can no longer be supported and are redistributed around the wellbore circumference. The location of borehole breakouts implies the direction of minimum principal stress, due to a stress concentration in the orientation of S_{hmin} azimuth ($\sigma_{\theta\theta}^{min}$), see Equation 2.2.

$$\sigma_{\theta\theta}^{max} = 3S_{Hmax} - S_{hmin} - 2P_0 \quad (2.2)$$

Where,

S_{Hmax} = Maximum horizontal stress (MPa)

S_{hmin} = Minimum horizontal stress (MPa)

$\sigma_{\theta\theta}$= Minimum circumferential hoop stress (MPa)

The location of drilling induced fractures implies the direction maximum principal stress, due to a stress reduction in the orientation of S_{Hmax} azimuth($\sigma_{\theta\theta}^{min}$), see Equation 2.3.

$$\sigma_{\theta\theta}^{min} = 3S_{hmin} - S_{Hmax} - 2P_0 \quad (2.3)$$

The variation of circumferential stress around a borehole amplifies the far field in-situ stresses concentration by a factor of 4 (Equation 2.4).

$$\sigma_{\theta\theta}^{max} - \sigma_{\theta\theta}^{min} = 4(S_{Hmax} - S_{hmin}) \quad (2.4)$$

By considering the failure around a borehole in terms of the three principal stresses, failure will occur once the rock strength is exceeded (Zoback, 2007).

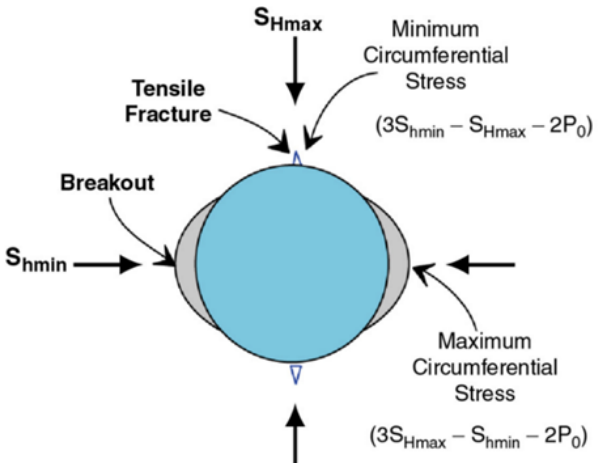

Figure 2-5 Distribution of circumferential hoop stresses and in-situ stresses, with reference to borehole breakouts and stress induced tensile fractures (From Smith et al., 2006).

The magnitude of S_{hmin} can be calculated from formation integrity tests (FIT) and leak-off tests (LOT). S_{Hmax} is the most difficult stress vector to quantify due to the lack of technique for direct measurement; the S_{Hmax} can be derived using Equation 2.5 (Barton et al., 1988, Zoback et al., 2003).

$$S_{Hmax} = \frac{\sigma_c + 2P_p + \Delta P + \sigma^{\Delta T} - S_{hmin}(1 + 2\cos(2\theta))}{1 - 2\cos(2\theta)} \quad (2.5)$$

Where,

σ_c = Uniaxial compressive strength (MPa)

Pp = Pore Pressure (MPa)

ΔP = Pressure difference between formation and borehole

$\sigma^{\Delta T}$ = Thermal stress effect

$2\Theta = \pi - \emptyset$, $\emptyset$ is the angle of borehole breakout (width) in radians

2.3.1.3. In-situ stresses of the Southern Taranaki Basin

Today, the region denotes the western limit of tectonic deformation associated with the active Hikurangi subduction zone (Reilly et al., 2015). In a seismically active region, such as the Taranaki Basin, constraining the current state of stress is essential for an effective

petroleum producing region. The assumption of one vertical principal stress is consistent with earthquake focal mechanisms and stress inversions from the region (Sherburn and White, 2006; Townend et al., 2012). The most recently published literature proposed by Rajabi et al. (2016) and Massiot et al. (2019) utilized borehole data to assess the contemporary stress field across the Taranaki Basin; Massiot et al. (2019) determined a favourable orientation of S_{Hmax} as ENE-WSW with localised rotations from subsurface structures. This is in agreement with Rajabi et al. (2016) and is broadly consistent with regional structures such as the Cape Egmont Fault Zone. This is in contrast to the proposed E-W S_{Hmax} orientation of Sherburn and White (2006) from earthquake focal mechanism data.

According to single focal mechanism (FMS) data, a strike slip tectonic stress regime exists across the Taranaki region, with suggestions of localised normal faulting regimes (Rajabi et al., 2016). Assessment of individual petroleum reports highlights the Pohokura, Moana, Kauri, TAWN fields and the Te Kiri Prospect are positioned within a strike-slip regime (Shell Todd Oil Services Limited, 2001; OMV NZ, 2006; Swift Energy, 2007a; Swift Energy, 2007b; Todd Energy, 2010). Massiot et al. (2019) delineated the in-situ stress field across the southern Taranaki Basin in the Tui, Maui and Maari-Manaia regions, also suggesting a strike-slip to normal stress regime, with similar magnitudes for S_{Hmax} and S_v ($S_{Hmax}/S_v \sim 1$); similar to the Mangatoa and Mangahewa fields (Mildren, 2009; Todd Energy, 2015). The localisation of the normal stress regimes suggests this may be resultant from the deviation of S_{Hmax} from its regional trend, due to the presence of geological structures e.g. faults (Rajabi et al., 2016). A major drawback of the S_{Hmax} calculations, as proposed in Equation 2.5, is the reliance on uncalibrated predictive tools for determination of mechanical rock parameters (Massiot et al., 2019). This is emphasised when evaluating a region within a transitioning stress regime, where inaccurate assessment of present-day stresses can lead to expensive instability or collapse of boreholes (Zoback, 2007).

2.3.2. **Mechanical Rock Properties**

The compressive rock strength of an interval is a key component for understanding the geomechanical characterisation of a region; the uniaxial compressive strength (UCS) is utilized as an input parameter for in-situ stress field calculations and the variation of compressive rock strength with confining pressure is used to delineate failure envelopes used for wellbore stability analysis.

The deformational behaviour of a rock under an application of stress can be described by the mechanical rock properties (Fjaer et al., 1992). Under stable stress conditions, the deformation at depth can be described by the elastic rock properties, Young's Modulus and Poisson's Ratio. Under critically stress conditions where the application of stress acting on the rock exceeds the rock strength, subsequent failure results in irreversible deformation such as compaction and shearing. The term rock strength is a measure of the peak stress at the point of rock failure; referring to the maximum principal stress at which a sample loses the ability support the applied stress (Zoback, 2007). The measure of the compressional strength will increase as a function of confining pressure (Jaeger and Cook, 1979), with the lowest compressional strength represented by the unconfined compressive strength, UCS. At low confining pressures rock fails as a combination of tensile and shear failure (Diederichs, 2003), whereas as confining pressures increase rock fails through shear failure and compaction (Siratovich et al., 2016).

The mechanical rock properties can be derived through laboratory testing, with the results from triaxial experiments plotted in principal stress space represented by peak stress (σ_1) and confining pressure (σ_3). The variance of peak stress with different confining pressures at the point of rock failure can be used to delineate a strength envelope, referred to as a failure criterion. A failure criterion is a method to graphically represent the failure of rock under different confining pressures. These criteria, defined by two material failure parameters, can be used to constrain the rock strength at depth.

2.3.2.1. Failure Criterion

2.3.2.1.1. Mohr Coulomb Failure Criteria

The Mohr-Coulomb failure criterion is the most commonly used due to the easy application as a linearized function (Labuz and Zang, 2012), Figure 2.6. The basic concepts for the Mohr-Coulomb strength criterion represents the two components of the shear strength by material parameters - cohesion constant, and a mobilised friction which varies with normal stress (Zhao, 2000), expressed in Equation 2.6:

$$\tau = C + \sigma_n \tan\phi \tag{2.6}$$

Where,

τ = shear stress (MPa)

σ_n = normal stress (MPa)

c = cohesion (MPa)

ϕ = angle of internal friction

The angle of internal friction is a measure of the dependence of rock strength on confining pressure such that a higher value of ϕ indicates a higher sensitivity of strength to confining pressure (Chang et al., 2006).

By applying the following stress transformations, the failure criterion can be expressed in terms of principal stresses:

$$\sigma_n = \frac{1}{2}(\sigma_1 + \sigma_3) + \frac{1}{2}(\sigma_1 - \sigma_3)\cos 2\beta$$

$$\tau = \frac{1}{2}(\sigma_1 - \sigma_3)\sin 2\beta$$

$$\beta = \frac{\pi}{4} + \frac{\phi}{2}$$

β = Orientation of the critical plane of failure

Expressed as a function of principal stresses, see Equation 2.7.

$$\sigma_1 = \frac{2C\cos\phi}{1-\sin\phi} + \frac{1+\sin\phi}{1-\sin\phi}\sigma_3 \tag{2.7}$$

Where,

σ_1 = Maximum principal stress (Peak)

σ_3 = Minimum principal stress (Confining pressure)

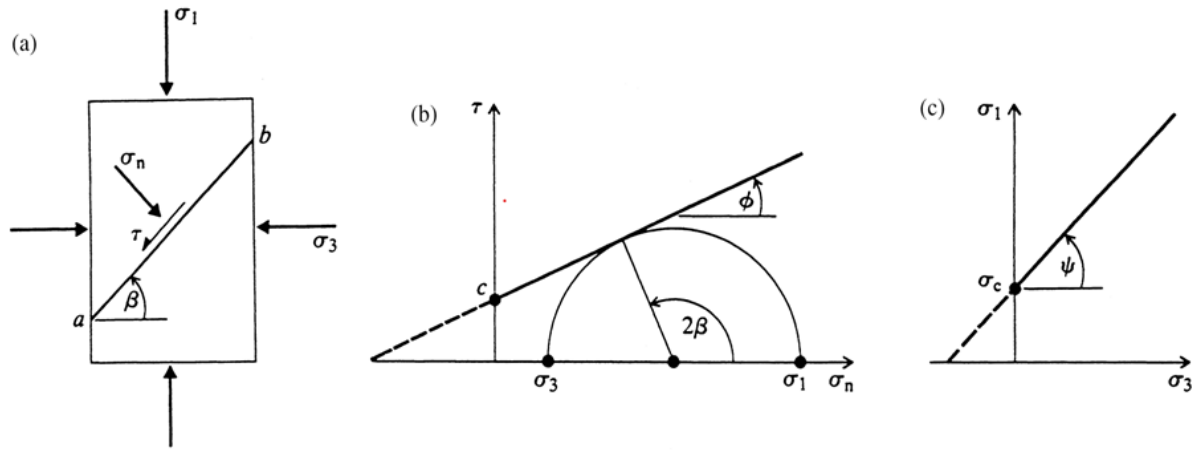

Figure 2-6 The Mohr–Coulomb strength criterion: [a] shear failure on plane a-b, [b] strength envelope of shear and normal stresses, and [c] strength envelope of principal stresses (from Zhao, 2000).

The uniaxial compressive strength (σ_c) is related to material parameters (c and ϕ) by Equation 2.8.

$$\sigma_c = \frac{2c\cos\phi}{1-\sin\phi} \tag{2.8}$$

2.3.2.1.2. Generalised Hoek-Brown Criterion

The Generalised Hoek-Brown criterion uses a non-linear relationship and is defined by the major and minor principal stresses based upon the unconfined compressive strength of intact rock (σ_{ci}) and material constants (m) and (s) (Hoek and Brown, 1980), Equation 2.9:

$$\sigma_1 = \sigma_3 + \sigma_{ci}\left(m_i \frac{\sigma_3}{\sigma_{ci}} + S\right)^{0.5} \quad (2.9)$$

Where,

σ_{ci}= Unconfined compressive strength (MPa) - empirical fitting to test data

m_i and s = material parameters.

In terms of equivalence between the material parameters, 'm' is analogous to the frictional strength of the rock. The m_i value was found to depend on mineralogy, composition and grain size (Hoek et al., 1992). The 's' parameter is a measure of rock mass characteristics, with 1.0 representing intact rock. The Hoek Brown criterion is an empirical strength criterion developed primarily from extensive analysis of laboratory test data covering a wide range of intact rock types (Zoback, 2007).

2.3.2.1.3. Comparison of Failure Criteria

The main disadvantage of the Mohr-Coulomb criterion is that it ignores the non-linearity of rock strength behaviour. In many instances, studies have found that the non-linear form of the Hoek–Brown criterion gave a better fit to their experimental data than the linear Mohr–Coulomb criterion (Ghazvinian et al., 2008; Benz et al., 2008; Zhao, 2000). An advantageous factor is the ability to incorporate rock mass properties into the failure criterion (Hoek and Brown, 2019) with material constants that vary by lithotype for rock mass characterisation of reservoirs (e.g. Villeneuve et al., 2018; Heap et al., 2019).

In practical terms. most researchers have an intuitive feel for the physical meanings of cohesion and friction, which is not the case for the Hoek-Brown parameters; there is a

lack of published literature correlating Hoek-Brown parameters to commonly measured wireline properties. In turn, some geotechnical software is still written in terms of the Mohr-Coulomb failure criterion and it may be necessary to determine equivalent angles of friction and cohesive strengths for each rock mass and stress range when the Hoek-Brown criterion is applied (Eberhardt, 2012). The quantitative conversion of Hoek–Brown to Mohr–Coulomb parameters is done by fitting an average linear relationship to the non-linear Hoek–Brown envelope for a range of minor principal stress values (Hoek et al. 2002). The disadvantage of both the Mohr Coulomb and Generalised Hoek-Brown criterions is the disregard of the influence of the intermediate principal stress (σ_2) on rock strength, by assuming ($\sigma_2=\sigma_3$). The assumption of no significant impact of the intermediate principal stress on the Mohr-Coulomb and Hoek-Brown criteria is developed in agreement with Walsh and Brace (1964). However, subsequent investigations suggest the intermediate principal stress has a substantial influence on rock strength (Takahashi et al., 1989; Colmenares and Zoback, 2002). This led to the development and assessment of 3D failure criteria using poly-axial data to independently assess the influence of the intermediate principal stress (Drucker and Prager, 1952; Mogi, 1971; Al-Ajmi and Zimmerman, 2005). This included a revised 3D Hoek-Brown criterion, which also inherits the advantages of the original Hoek–Brown strength criterion (Pan and Hudson, 1988; Zhang and Zhu, 2007; Zhang, 2008).

In drilling assessment, a linear poro-elasticity stress model in conjunction with a failure criterion is used to assess the strength of the rock and determine the optimum mud pressure to stabilise a wellbore (Zhang et al., 2010; Gholami et al., 2013). Therefore, the selection of the appropriate failure criterion is fundamental to avoid the occurrence of wellbore instabilities such as breakouts and drilling induced fractures. The redistribution of stress around a borehole (section 2.3.1.1) can result in an intermediate principal stress substantially larger than the minor principal stress; a failure criterion assuming σ2=σ3 would under predict the rock strength (Eberhardt, 2012). In general, it is suggested that the Mohr–Coulomb criterion under-predicts the polyaxial rock strength and estimates the highest minimum mud pressure required for wellbore stability (Zhang et al., 2010; Gholami et al., 2013).

2.3.2.2. Rock Strength Prediction

The determination of mechanical rock properties is reliant on laboratory testing data. However, in most cases core samples are unavailable for laboratory testing to derive these parameters; furthermore, sampled core intervals are usually <1% of a stratigraphic interval, which most often neglects the overburden formations. The most common technique used to determine the UCS is to use an empirical physical property-rock strength relation as a prediction tool; the basis for these relations is the fact that many of the same factors that affect rock strength also affect the elastic properties and other parameters, such as porosity (Zoback, 2007). Table 2.1 summarises the most well-established physical property-rock strength relationships. The most utilized physical property parameters utilized in rock strength prediction relationships are from the compressional sonic velocities (Freyburg, 1972; McNally, 1987; Fjaer et al., 1992; Moos et al., 1999). Most empirical rock strength relationships are defined for individual rock types e.g. sandstones and shales, as summarised by Chang et al. (2006). However, many of these proposed relationships come with recommended constraints which limit their application e.g. McNally (1987) a well-used relation, was only developed for use in fine grained sandstones; this is impractical as most sedimentary rocks will vary in grain size within a narrow interval. In turn, the use of more than one independent variable for UCS prediction is uncommon (Fjaer et al., 1992; Moos et al., 1999; Chang et al., 2006). The proposed relationships developed from different regions, often produce under-estimation or over-estimation of UCS, In such a case where core samples are available, the laboratory measurements can be used to calibrate the rock strength tools to the local region in order to refine strength predictions (Oyler et al., 2010; Todd Energy, 2015; Kazianis, 2018)

Table 2-1 Physical property- strength relationships proposed for UCS prediction of sandstone.

$0.035V_p - 31.5$	Freyburg (1972)
$1200e^{-0.036\Delta t}$	McNally (1987)
$1.745 \times 10^{-9}\rho V_p^2 - 21$	Moos et al. (1999)
$2.28 + 4.1089\text{E}$	Bradford et al. (1998)
$1200e^{0.0267E}$	Chang et al. (2006).
$254(1 - 2.7\phi)^2$	Vernik et al. (1993)
$277e^{-10\phi}$	Chang et al. (2006)

If the material parameters defining the failure criteria can be estimated, in a similar technique to UCS, it is possible to fully define the rock strength profile at depth without triaxial testing. In principle, an accurate estimation of ϕ is as important as that of UCS to correctly predict rock strength at depth, especially for weak rocks (Chang et al., 2006). Attempts have been made to find relationships between the angle of internal friction (ϕ) and geophysical log measurements (Weingarten and Perkins, 1995; Chang et al, 2006). A practical disadvantage of the Hoek-Brown criterion is the absence of published literature relating the material parameter, m_i, to commonly measured physical properties from geophysical logs (Zoback, 2007).

2.3.2.3. Rock strength data for the Taranaki Basin

Every geomechanical report generated for the Taranaki Basin has stated a requirement for increased mechanical laboratory data to better constrain and calibrate rock strength and friction equations. Irrespective of this, all strength data for sandstones and shales available for the region are summarised in Appendix A.

Different physical property-rock strength relationships have been used to predict rock strength parameters for input into stress field calculations for borehole stability assessment in the Taranaki region (Shell Todd Oil Services Limited, 2001; Swift Energy,

2007b; Todd Energy, 2010; Todd Energy, 2015; Massiot et al., 2019). McNally (1987) represents the most commonly applied equation for rock strength prediction, utilized in the Kauri and Mangahewa fields, Te Kiri Prospect and the Tui-Maui-Maari region; other relations including Fjaer et al. (1992) and Moos et al. (1999) have been applied to reservoir intervals from the Pohokura field and Te Kiri Prospect correspondingly. Access to mechanical laboratory data allows for refinement of the property-rock strength relationships utilized in the region. In a similar technique applied by Oyler et al. (2010), Kazianis (2018) adopted the McNally equation for rock strength prediction of tertiary shales using mechanical laboratory data of local reservoirs from the region to refine the correlation coefficients of the equation, thereby improving the rock strength prediction. Similarly, mechanical rock data attributed to the Mangahewa field was used to develop a correlation equation between the dynamic Youngs Modulus and UCS (Todd Energy, 2015), producing a modified version of the Chang et al. (2006) relationship.

Chapter Three – Methodology

3.1. Sample Selection

3.1.1. Reservoir Outcrop

Reservoir analogues are onshore exposures of rock that reflect similar attributes to that of an offshore reservoir. Reservoir analogues can be used for detailed characterization of sedimentary facies, drawing comparison to modern depositional environments (Alexander 1993); this can provide an indication of facies scale heterogeneities that might be present at depth (see chapter 4). The study area where analogue samples were obtained represents onshore exposure of the Late Cretaceous North Cape Formation and Paleocene, Farewell Formation (Figure 3.1). Samples of these outcrops will provide quantitative data on porosity and permeability across different depositional facies within a restricted marine-fluvial depositional environment. Quantification of physical properties based on sedimentary facies requires a strong sample representation; the use of outcrop analogues allowed for an unrestricted amount of sample material for testing.

Figure 3-1 Reservoir analogues of the Paleocene Farewell Formation (left) and Late Cretaceous North Cape Formation (right).

3.1.2. **Drill Core**

Drill core of sampled reservoir intervals can be used to obtain direct indispensable information on rock properties. The expensive cost to retrieve drill core often results in limited availability of sample material, particularly for destructive strength testing for geomechanical data. Due to the absence of geomechanical data attributed to the Taranaki Basin, sample selection was approached in a systematic manner and incorporates a wide spatial distribution over four reservoir horizons, Mangahewa 'C' sands, Kaimiro 'D' sands, Farewell 'F' sands, and the North Cape formation. Sample representation across a wide scale, as opposed to an in-depth focus in a single locality, allows for quantitative data to be better utilized for further studies. Permission was granted from New Zealand Petroleum and Minerals (NZP&M) to sub-sample core plugs from five petroleum wells (Figure 3.2): Moki-1, Maui-A1(G), MBW(2), MBR(2) and Tane-1, see chapter 5.

Figure 3-2 Example of reservoir intervals from petroleum boreholes Moki-1, Maui-A1(G), and MBR(2) used to subsample core plugs for non-destructive and destructive laboratory testing.

3.1.3. **Side Wall Core Plugs**

Wireline tools are used for the acquisition of side wall core plugs at regularly spaced intervals, along the borehole axis, which encompasses many formations within the borehole section. Permission was granted from NZP&M to analyse side wall cores from Whio (1) in the Maari-Manaia Field between depths 1444m-2815m (Figure 3.3). Core plugs can be used for strength testing. Rock property data can be used to calibrate wireline logs along the length of the borehole. The recovery rate of sample retrieval will determine the suitability of side wall core samples for destructive strength testing, which require a 2:1, length to width ratio (see section 3.3.5). For samples with a short length, physical rock property measurements can be acquired, rock strength needs to be predicted.

Figure 3-3 : Example of Whio-1 side wall core plugs used for non-destructive testing.

3.2. Sample Preparation

3.2.1. **Drilling**

Eighty drill core plugs were successfully sub-sampled from drill core at the NZP&M Featherston Core Store, New Zealand. A diamond encrusted drill bit was used to core block samples with a sufficient flow of water to cool and flush cuttings. A similar approach was used to drill blocks of reservoir analogue obtained in the field, however weakly consolidated and/or coarser grained sandstones posed difficult to obtain, thus a process of trial and error was required in order to acquire suitable samples for laboratory testing (Figure 3.4). An increased weathering and clay presence in analogue outcrops resulted in frequent disintegration of samples that was unavoidable. Due to the large quantity of samples required for repetitive testing, the frequent loss of material during sample preparation suggested this method of sampling was not effective for weak unconsolidated rock.

Figure 3-4 Process of trial and error for acquisition of weak unconsolidated sandstones from outcrop blocks; ineffective and unpredictable method due to the frequent loss of material during sample preparation.

To account for anisotropic control on rock properties (such as bedding and internal structure), core plugs were sampled in two orthogonal directions. Reservoir analogue samples were taken both parallel and Perpendicular from the outcrop, where a three-dimensional exposure was available; some instances only allowed for bedding parallel

samples to be collected. Drill core samples were taken both parallel and perpendicular to the borehole axis which often aligned with bedding (Figure 3.5). The condition of the core specimens when tested will impact the data collected, and thus testing should be completed as soon as possible following sample collection. In order to retain sample conditions prior to further sample preparation, core specimens were wrapped in plastic film to maintain moisture levels, and aluminium foil for physical support.

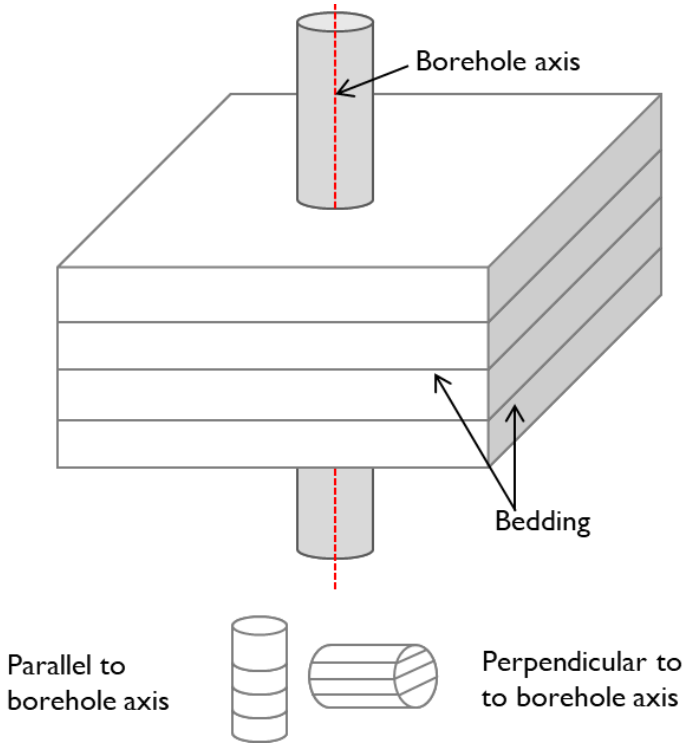

Figure 3-5 Drill core samples orientated (parallel and perpendicular) in relation to the borehole axis. Perpendicular sample orientation often aligns with bedding.

3.2.2. **Shape Conformance and Dimensional properties**

Cylindrical test specimens were further prepared for laboratory testing in accordance with the ASTM standard practice D4543-19 (2019) in the University of Canterbury Rock Mechanics Laboratory. A requirement of sample preparation is for end surfaces to be as flat and parallel as possible. Once cut to size, core plugs underwent a surface grinder; this is beneficial for both dimensional measurements and application of an even load in subsequent testing. Direct measurements of diameter and length were recorded using

callipers, to an accuracy of two decimal places (0.01mm); for each measurement, three readings were acquired and averaged. The cylindrical core sample diameters were 20mm or 25mm, with an approximate 2:1 length to width ratio required for strength testing.

3.3. Methods of Quantification

Laboratory data acquisition is comprised of petrographical analysis, non-destructive core analysis and destructive strength testing. The methods applied to each test material are summarized in Table 3.1.

Table 3-1 Summary of techniques utilized for data acquisition at each stage of the project from different sourced sample materials

Technique	Reservoir analogue	Drill core	Sidewall core
Optical Microscopy	✓	✓	✓
Scanning Electron Microscopy	✓	×	×
X-Ray Diffraction	✓	×	×
Bulk Density	✓	✓	✓
Water Saturation	×	✓	✓
Nitrogen Pycnometry	✓	✓	✓
Mercury Porosimetry	✓	×	×
Permeability	✓	✓	✓
Dry Vp/Vs	✓	✓	✓
Saturated Vp/Vs	×	✓	✓
Uniaxial compressive Test	✓	✓	×
Triaxial Compression Test	×	✓	×

Petrographical analysis characterizes the sedimentary framework of the samples so we can later explore its control on physical and mechanical rock properties. Non-destructive core analysis allows for repetitive use of a sample for numerous tests including density, porosity, permeability and sonic wave velocities. Finally, destructive strength testing, including UCS and triaxial tests are performed on samples. The destructive nature of strength tests limits further testing on the samples; thus, is the final method used on a sample. All quantifiable data from techniques listed in table 3.1 can be found in appendices A-H.

3.3.1. **Petrographical Evaluation**

Optical microscopy was used to characterize any mineralogical or textural properties which may influence the physical and geomechanical rock properties. Textural characterization focused on grain sorting and mean grain size (D). Grain size analysis was achieved from a thin section petrographic study and collation with existing data from petroleum reports. For each thin section, average grain size determination was achieved using a consistent method of 100-120 grains measured at the long axis; data is presented as a mean grain size (D). Thin sections, stained with a blue dye, are used to identify the presence and nature of pore spaces in approximately 100 samples. For composition, a Pelcon Point Counter was used to define the mineral percentages of samples; this was done from a raster of 200 points over the thin sections with a step length of 1mm. XRD analysis was undertaken on 15 samples, by SpectraChem Ltd Lower Hutt, with the purpose to identify and quantify clay mineral types to assess for any diagenetic controls. A Pelcon Point Counter was used to define the mineral percentage contribution for each sample; this was done from 200 points over the raster scan with a step length of 1mm.

X-ray diffraction (XRD) analysis was undertaken in order to acquire bulk rock chemistry data, used for comparison with point count data. XRD analysis was undertaken by SpectraChem Ltd, Lower Hutt, using the Bruker D8 Advance diffractometer. Mineral

phase identification and quantification was carried out using an EVA SIROQUANT search/match programme.

Scanning Electron Microscopy (SEM) using the JEOL JSM IT-300 variable pressure SEM microscope was undertaken at the Electron Microscopy Centre, University of Canterbury, New Zealand (Figure 3.6). Features utilized include the Oxford Aztec SDD energy dispersive x-ray analysis system used for elemental and chemical analysis of a sample. In turn, Backscatter Electron (BSE) images provided sandstone textures at a greater magnification down to 10 μm, a greater clarity for microscale processes effecting grains and clay mineral structure. The JEOL JSM 7000F field emission, high resolution scanning electron microscope was utilized for closer investigation on pore space geometries (<10 μm).

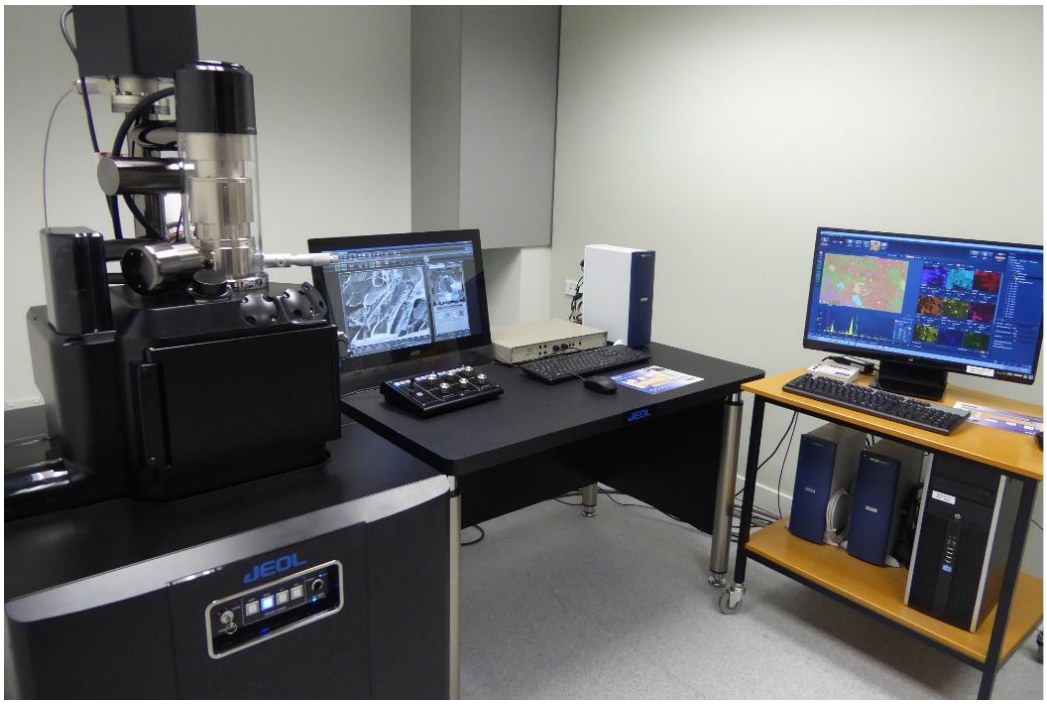

Figure 3-6 JEOL JSM IT-300 variable pressure SEM microscope for BSE Imagery and energy dispersive x-ray analysis

3.3.2. **Density**

To determine the porosity and density, input parameters (dimensions and mass) are required and are calculated using the formulae defined in Ulusay and Hudson (2007). Bulk volume was determined using the caliper method, with several readings recorded and averaged for each dimension. For cylindrical samples, bulk volume is expressed as:

$$V = \pi r^2 h$$

Where,

V = bulk volume (cm^3)

r = radius (cm)

h= length (cm)

For samples with irregular shapes, bulk volume can be determined using the buoyancy method. The buoyancy method relies on the Archimedes Principle, where bulk volume is measured from the difference between, saturated and submerged masses, subject to water density. A specimen is saturated by water immersion in a vacuum for a minimum of 12 hours until all air bubbles are removed. Firstly, the sample is transferred to a hanging basket suspended within the immersion bath, and the saturated-submerged mass is recorded (scale was zeroed prior to sample placement in basket). Subsequently, the sample is removed from the immersion bath to be surface dried, the saturated-surface dry mass is recorded.

$$V = \frac{M_{sat} - M_{sub}}{\rho_w}$$

Where,

M_{sat} = saturated-submerged (g)

M_{sub} = saturated-surface dry mass (g)

ρ_w = density of water ($1g/cm^3$)

Samples are oven dried at 60˚C for at least 48 hours before mass measurement. Dry masses (M_s) are recorded to an accuracy of 0.01g. Dry bulk density (ρ) is a measure of weight per unit volume, and is expressed as:

$$\rho = \frac{M_s}{V}$$

3.3.3. **Porosity**

Porosity can be expressed as a percentage or a porosity fraction. Total porosity is a measure of the interconnected and isolated pores, contributing towards pore volume, regardless of the flow capability. Effective porosity is a measure of interconnected pores excluding isolated pore and represents the pores which contribute towards an effective flow, thus is an important measurement for reservoir quality assessment and typically used by industry. For the purpose of this study, porosity refers to effective porosity. Multiple techniques can be used to provide a measure porosity, including gas pycnometry and mercury porosimetry.

Pore volume is a measure of void space within a rock sample, used in conjunction with bulk volume this can be expressed as a porosity fraction value:

$$n = \frac{V_v}{V}$$

Where,

V_v = Pore Volume

n = Porosity Fraction

3.3.3.1. Porosity determination using water saturation

The core specimen bulk volume was calculated from average caliper readings from each dimension, see above. The oven dry sample is initially weighed to determine the dry mass (M_s). The sample is subsequently saturated by water immersion in a vacuum for 12 hours and the saturated-surface dry mass determined. The pore volume is a calculated as:

$$V_v = \frac{M_{sat} - M_s}{\rho_w}$$

3.3.3.2. Nitrogen Pycnometry

This technique utilizes the Micrometrics AccuPycII1340 gas Pycnometer, using a high purity nitrogen gas (99.5%) as a displacement medium to accurately measure grain volume (Figure 3.7). The oven dry core is positioned and sealed into a calibrated sample chamber of known volume (V_{sample}). The nitrogen gas is introduced to the sample chamber to a fixed pressure (p_1), filling available void space through the interconnected pores of the sample. Valve A is opened allowing for the nitrogen gas to expand into a reference chamber, also of known volume ($V_{reference}$), the stabilized pressure (P_2) is then recorded. The pressure is then vented off to atmosphere. P_1 and P_2 are both measured on the pressure transducer; this technique is cycled 10 times to increase measurement accuracy. The difference in gas compressibility between the sample chamber and reference chamber is due to the solid volume of the incompressible sample. Thus, the pressure observed upon filling the sample chamber, and the stabilized pressure following the discharge of gas into the reference chamber, represent a ratio which can be used to compute the sample solid phase, grain volume V_s where:

$$V_s = v_{sample} + \frac{V_{reference}}{1 - \left(\frac{P_1}{P_2}\right)}$$

In terms of pore volume, this is expressed as:

$$V_v = V - V_s$$

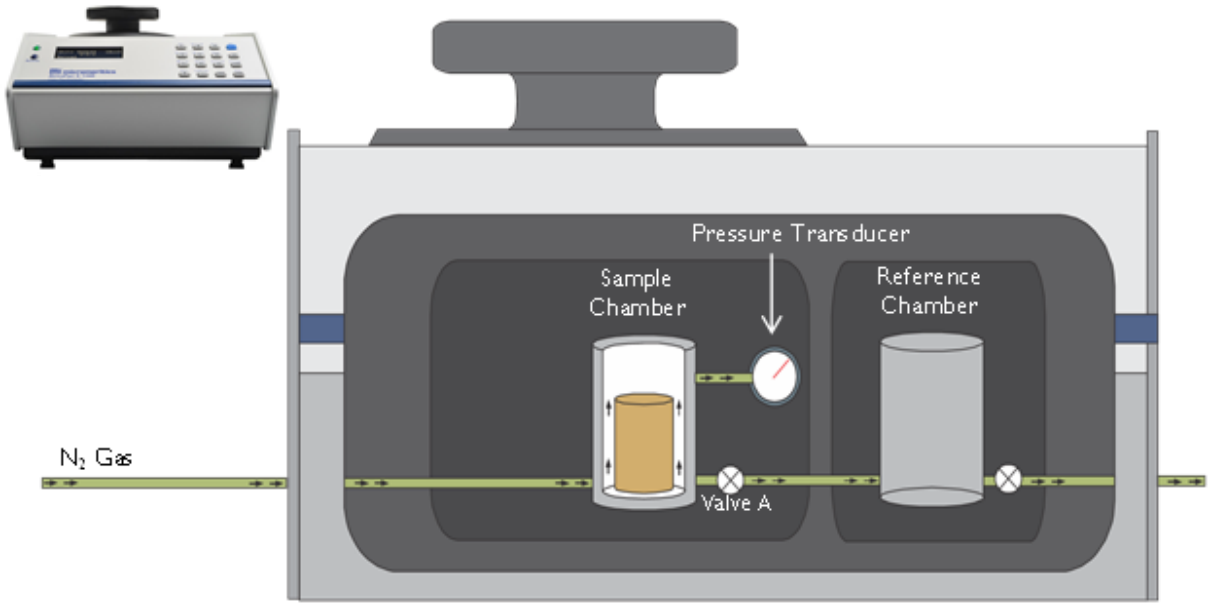

Figure 3-7 Schematic diagram of Micrometrics AccuPycII1340 gas Pycnometer, using high purity nitrogen gas to measure grain volume for porosity determination

3.3.3.3. Mercury Intrusion Porosimetry

Mercury Intrusion Porosimetry (MIP) tests were carried out by the Materials and Engineering Research Institute (MERI), Sheffield Hallam University using a PASCAL 140/240 porosimeter, following ASTM standard D4404-18, for quantitative pore structure characterization. The MIP technique can be used for evaluation of porosity, pore volume distribution, and average pore diameters (Webb 2001).

Mercury will only enter the pore when the external pressure exceeds that of the capillary pressure at the pore entrance. A porosimeter uses a pressurized chamber to incrementally intrude non-wetting liquid mercury into pore spaces, with large pores filling first. This relationship is expressed mathematically in Washburn's Equation (1921):

$$D = \frac{-4\gamma \cos\theta}{P_c}$$

Where,

P_c = capillary pressure (MPa/m^2)

γ = surface tension of Hg (0.48 N/m)

θ = contact angle of mercury in air (140^o)

D = diameter of pore throat for a cylindrical pore (m).

It is capable of measuring pore throat diameters in the range of 0.0074 μm to 116 μm. Pore volume (Vv) is the simplest form of measurement using this method and is equivalent to the total volume of mercury intruded during the experiment.

3.3.4. **Permeability**

Gas (nitrogen) permeability was measured using either the steady state method or transient method, dependent upon the permeability of the sample. High permeability samples (0.1mD m2 – 1000mD) were tested using a steady state permeameter (Fig. 3). Low permeability test specimens (<0.1mD) were tested using the transient method in a pulse decay permeameter. Apparent permeability (K_{gas}) is expressed as (Scheidegger, 1974):

$$K_{gas} = Q\left(\frac{2\eta L}{A}\right)\left(\frac{P_{down}}{P_{up}^2 - P_{down}^2}\right)$$

Where,

P= Pore Pressure (MPa)

Q=flow rate (m^3/s)

A = specimen cross sectional area (m^2)

L = length (m). Pore fluid viscosity

η, was set at 1.78×10^{-5} Pa.s as nitrogen gas at room temperature

The steady state permeameter setup used for measuring flow rates in high permeability samples is exhibited in Figure 3.8. The specimen was placed in a rubber sleeve within a hoek cell pressure vessel. A small amount of axial load was applied to hold the pressure

vessel in place, followed by a manually applied confining pressure via a hand pump. The sample and confining pressure fluid are separated via a rubber sleeve. The sample was allowed to rest for 50 minutes for the stress to equilibrate, after which nitrogen gas is introduced at an applied pressure at the upstream end inlet (P_{up}), flowing through and saturating the sample, before exiting at atmospheric pressure at the downstream end outlet (P_{down}). This produces a pore pressure gradient (P_{up}-P_{down}) where the differential pressure was a measure of pressure change in the system. For an individual test specimen, steady-state volumetric flow rates (Q), up to 500ml/min, were measured under several pressure gradients, recorded on the downstream side of the hoek cell (Heap et al., 2018).

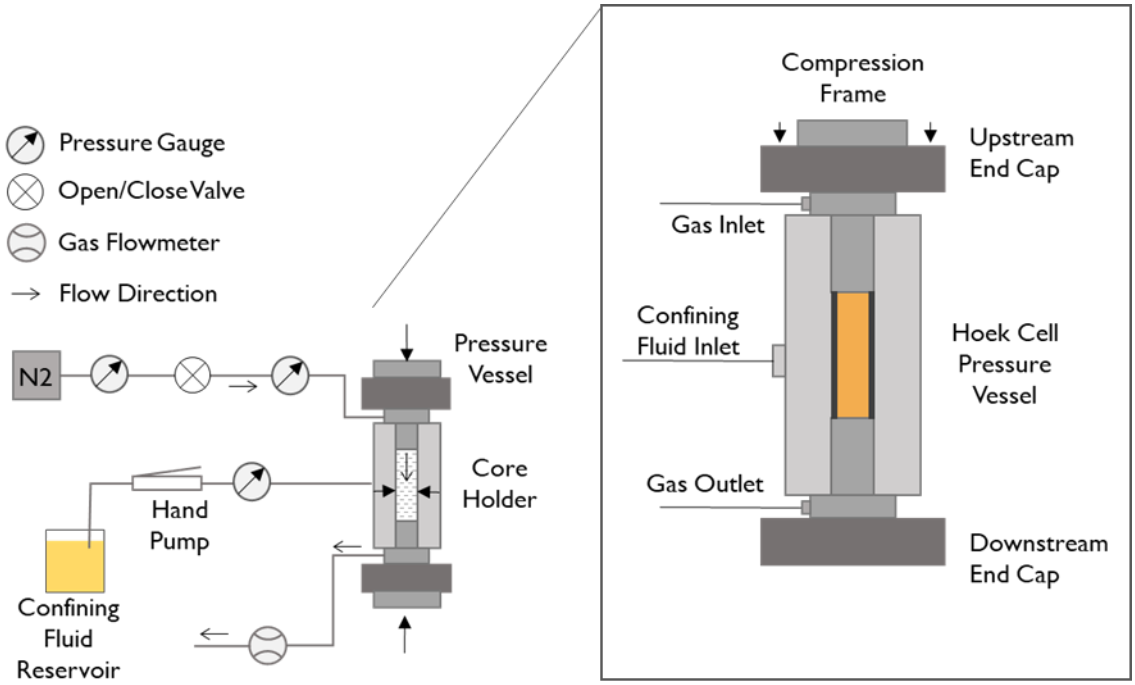

Figure 3-8 Schematic diagram of steady state permeameter setup for determining volumetric flow rates across different pressure gradients over high permeability samples.

The transient (pulse decay) method used for low permeability measurements was conducted using the Corelab PDP-200 (Figure 3.9). The sample was placed inside the core holder and a hydrostatic confining pressure is manually applied with a hydraulic pump. The system uses nitrogen gas to saturate the test specimen to a set pore pressure between 10-30MPa, for higher expected permeabilities lower pore pressures are used. The downstream gas valve is opened, allowing for a pressure differential to develop

across the sample. They system measures the pressure differential decay across a specimen at regularly timed intervals. Overall, the upstream pore pressure decreases, and the downstream pressure increases, however the gas differential across the sample decays in a logarithmic trend. The PDP software converts the differential pressure to apparent gas permeability. For full description of pulse decay methods refer to Cant et al. (2018).

[a]

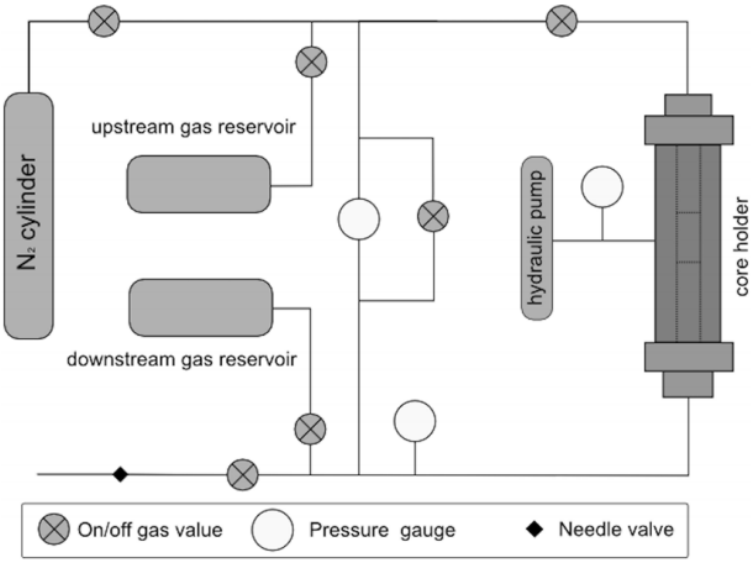

[b]

Figure 3-9 [a] Schematic diagram of pulse decay permeameter of Corelab PDP-200 from Cant et al. (2018) used for determination on low permeability samples. [b] Equipment setup at the University of Canterbury's Rock Mechanics Laboratory.

To determine the true permeability Klinkenberg corrections were used where required in both steady state and transient methods. The Klinkenberg correction accounted for any gas slippage within the pores (Klinkenberg, 1941); this phenomenon states gas flow rates are faster than water at grain boundaries. To perform a Klinkenberg correction an individual permeability test must be performed at several pore pressures. The intercept of the linear regression between apparent gas permeability versus the inverse of mean pore pressure can be measured as true permeability. This can be expressed as:

$$K_{true} = K_{gas}\left(1 + \frac{b}{P_{mean}}\right)$$

Where,

K_{true} = true permeability

K_{gas} = gas permeability at a particular pore pressure

b = Klinkenberg slip factor

P_{mean} = mean pore pressure.

3.3.5. **Sonic Wave Velocities**

The compressional (Vp) and shear wave (Vs) sonic velocities were measured along the axis of core specimens, using a GCTS (Geotechnical Consulting and Testing Systems) Computer-Aided Ultrasonic Velocity Testing System (CATS ULT-100) device (Figure 3.10). Two platens are positioned at the top and bottom of the sample length. Piezoelectric transducers are used to measure the sonic velocities. A CMT 100kN load frame was used to apply a small amount of axial load (2kN) to ensure full contact between sample end surfaces and piezoelectric platens; this strengthens the velocity signal producing coherent waveforms. The two transducers act as an emitter and a receiver which produce a waveform, the first deflection from horizontal on the wave form indicates the arrival time of the P and S waves; 100 waveforms were collected for each velocity measurement, in an attempt to omit background noise.

Both dry and saturated P waves were acquired; for saturated compressional wave, test specimens were saturated by water immersion for at least 12 hours. The wave velocities were used to determine the dynamic elastic moduli (GPa) of the rock including Dynamic

Youngs Modulus (E) and the Dynamic Poisson's Ratio (v). The calculations for these parameters are defined below in terms of sonic wave velocities V_p and V_s. and dry bulk density (kg/m^3).

$$E = \frac{\rho V_s^2 (3V_p^2 - 4V_s^2)}{(V_p^2 - V_s^2)}$$

$$v = \frac{V_p^2 - 2V_s^2}{2(V_p^2 - V_s^2)}$$

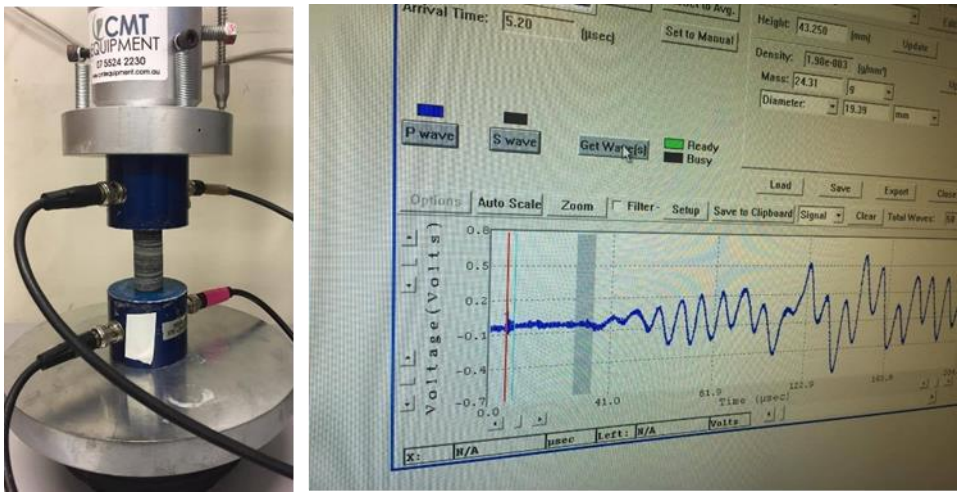

Figure 3-10 Laboratory setup for wave velocity measurements with piezoelectric transducers positioned either side of test specimen under a low axial load application; example of ideal compressional waveform using CATS ULT-100.

3.3.6. **Destructive Strength Testing**

Sample preparation in accordance with ASTM standard D4543-19 is important for strength experiments, as parallel end surfaces allow for the correct application of evenly distributed axial load on to the sample. The strength testing procedures followed guidelines from the ASTM standard D7012-14; this standard incorporates guidelines for, unconfined compressive tests, undrained triaxial compressive strength tests, and associated elastic moduli calculation from the two tests. For all test specimens, a length to width ratio 2:1 is desirable, for strength data acquired with a smaller ratio a considered approach with proper judgement is required before application.

3.3.6.1. Uniaxial Compressive Tests (UCS)

UCS tests were carried out using a 100kN load frame (S178 Multi-Tester) commissioned by CMT Equipment, Australia. Experiments were run under a continuously applied axial load until rock failure, with a fixed axial strain rate of 1x10-5m/s. Real time data was collected through LabVIEW software of axial load, and in some examples, axial/radial displacement. Displacement measurements were recorded via an axial extensometer and axial/radial strain gauges. When utilized, two axial and two radial strain gauges were attached to a sample, orientated horizontally and vertically orthogonal to each other.

All test specimens considered non-conformable fell under the suggested minimum sample diameter of 50mm for UCS testing. Due to the non-conformance of sample diameter to industry standard, a correction is applied to all UCS laboratory data, using the formulae proposed by Hoek and Brown (1980):

$$\sigma_{cd} = \sigma_{c50}\left(\frac{50}{d}\right)^{0.18}$$

Where,

σ_{cd} = raw UCS value (MPa)

d = sample diameter (mm)

σ_{c50} = corrected UCS value for a 50mm diameter sample.

3.3.6.2. Conventional Triaxial Compressive Tests

Deformation experiments under conventional triaxial conditions ($\sigma_1 > \sigma_2 = \sigma_3$) followed the testing procedure guidelines from the ASTM D7012-14. The triaxial experiment setup used for determining rock strength under different confining pressures exhibits a similar arrangement to the steady state permeameter. The specimen was placed in a rubber sleeve within a hoek cell pressure vessel, with top and bottom platens in contact with the specimen edge surfaces. A small amount of axial load was applied with the S178 multitester to hold the platens in place, followed by a manually applied confining

pressure via a hydraulic pump to secure the pressure vessel in place. For triaxial tests each specimen was hydrostatically loaded up to a fixed confining pressure ($\sigma_2 = \sigma_3$) between 5 and 30MPa; the axial load was subsequently applied at a continuous fixed rate of 1x10-5m/s until the sample failed. Real time data was collected through LabVIEW software of axial load (σ_1), and axial displacement using an extensometer. Triaxial compressive strength is a measure of the differential pressure at the point of failure, between axial and confining pressure, expressed as σ_1-σ_3.

3.3.6.3. Static Elastic Moduli Calculations

Strain measurements can be directly obtained dependent on the type of apparatus used. However, for strain gauges and extensometers a calculation was required utilizing the deformation readings. Axial strain, ε_1, is calculated as:

$$\varepsilon_1 = \frac{\Delta L}{L}$$

Where,

L = original undeformed length

ΔL = change in axial measured axial length

For strain gauges and the extensometer, ΔL is provided as a direct measurement from deformation readings. However, the original undeformed length L represents the length of the gauge for strain gauges, and length of the sample for extensometer measurements.

Radial strain gauges were only used on few UCS samples, with lateral strain ε_1, calculated as:

$$\varepsilon_2 = \frac{\Delta D}{D}$$

Where,

D = original sample diameter

ΔD = change in diameter width

ΔD is provided as a direct measurement from deformation readings. The axial and lateral strain can be used to determine the Poisson's Ratio, v, expressed below:

$$v = -\frac{\varepsilon_2}{\varepsilon_1}$$

The graphical representation of strength experiments utilizing stress and strain data, UCS (σ_1 versus ε_1) and triaxial (σ_1 - σ_3 versus ε_1), display the complete deformation behavior of a sample. The Young's Modulus was calculated based upon the linear proportion of the stress-strain graph attributed to each test, this is expressed as:

$$E = \frac{\sigma}{\varepsilon_1}$$

3.4. Methods of Statistical Analysis

Early investigation was centralized on more qualitative research, this focused on in-field geological observations of sedimentary facies and wellbore core descriptions. Qualitative descriptions at the outset were the only basis of evidence, thus facilitated in establishing separate classifications on which to group the quantitative data. Any parameter can be a source of uncertainty due to the unavoidable inherent natural variability which exist in geology; this can question the most preliminary observations on which research is based. Regardless, in order to conceptualize and produce predictive models, quantification of geological properties was a requirement. This early qualitative research provided a fundamental understanding of the geology of the study area and assisted in determining sample collection points from the field and selected boreholes. For the most part, quantitative research was undertaken for this study and used to assess the physical and geomechanical properties of key reservoirs in the southern Taranaki Basin, expressed in terms of equations and graph-plots.

3.4.1. **Regression Analysis**

The goal of regression analysis is to delineate a line for a data series that best describes the variation of dependent variable, Y, in response to a change in independent variable, X. Regression analysis can be utilized in several ways; to assess the statistical strength of predictor variables and determine values of fitting parameters 'a' and 'b'.

A linear regression function is presented as follows:

$$Y = a + bX$$

Where y is the dependent variable, x is the independent variable, a is regression line intercept on the y axis and b is the regression coefficient (slope of the regression line). For this type of regression to be applied, a linear relationship must exist between the dependent variable and each independent variable. Any function can be modified to a linear trend, by transformation of the appropriate axes.

Multiple linear regression utilizes two or more independent variables to predict the dependent variable. The multiple linear regression is expressed as function:

$$Y = a + b_1X_1 + b_2X_2 + \ldots + b_nX_n$$

Where y is the dependent variable, $x_{1,2,3}$ are the independent variables, n is the amount of independent variables, a is the y axis intercept and $b_{1,2,3}$ are regression coefficients.

The most common function describing the regression is a straight line but can be modelled by both power and exponential laws. The power law function expressed as function:

$$Y = aX^b$$

Where y is the dependent variable, x is the independent variable, a is regression line intercept on the y axis and b is the regression coefficient (slope of the regression line).

Regression analysis was undertaken utilizing software programs Microsoft Excel-Data Analysis, RocScience and SPSS.

3.5. Application

3.5.1. Empirical Strength Prediction

Each physical property was plotted against the rock strength parameters to determine empirical strength relationships. Statistical analysis was undertaken on the empirical strength relationship to determine the ability for each physical parameter to act as a predictor for strength. A simple linear regression using the least square method allowed for calculation of 'P' for each data series; a probability factor that quantitatively assesses for the statistical significance of a correlation between the dependent and independent variables.

A null hypothesis states there is no relationship between the independent variable (x) and the dependent variable (y); the null hypothesis infers that the linear regression slope is equal to zero. The alternative hypothesis states that if there is a significant linear relationship between the independent variable and the dependent variable the linear regression slope is not equal to zero. A small 'P' value (<0.05 – attributed to 95% certainty) suggests a statistically significant correlation and that the null hypothesis should be rejected, in support for an alternative hypothesis. In an effort to further refine the prediction tool, multiple linear regression in SPSS was used to determine regression coefficients to develop a physical property-rock strength empirical relationship based as a function of two independent variables, porosity fraction and mean grain size; see chapter 5.

3.5.2. Development of Failure Criteria

RocData (RocScience 2019) was used to employ a regression analysis of the triaxial data to derive the Hoek-Brown and Mohr-Coulomb failure criterion parameters. The Generalized Hoek-Brown criterion is defined by the major and minor principal stresses based upon the unconfined compressive strength of intact rock (σ_{ci}) and material constants (m_i) (Hoek and Brown, 2019), and is expressed as:

$$\sigma_1 = \sigma_3 + \sigma_{ci}\left(m_i \frac{\sigma_3}{\sigma_{ci}} + 1\right)^{0.5}$$

For Hoek-Brown, the following equations are used to manually determine the strength parameters (Hoek and Brown, 1997):

$$\boldsymbol{\sigma_{ci}} = \sqrt{\frac{\sum \boldsymbol{y}}{\boldsymbol{n}} - \left[\frac{\sum \boldsymbol{xy} - \left(\frac{\sum \boldsymbol{x} \sum \boldsymbol{y}}{\boldsymbol{n}}\right)}{\sum \boldsymbol{x^2} - \left(\frac{(\sum \boldsymbol{x})^2}{\boldsymbol{n}}\right)}\right] \frac{\sum \boldsymbol{x}}{\boldsymbol{n}}}$$

$$m_i = \frac{1}{\sigma_{ci}} - \left[\frac{\sum xy - \left(\frac{\sum x \sum y}{n}\right)}{\sum x^2 - \left(\frac{(\sum x)^2}{n}\right)}\right]$$

Where $x = \sigma_3$, $y = (\sigma_1 - \sigma_3)^2$, and n is the number of triaxial tests.

The Mohr Coulomb failure criterion imposes a linear relationship and is defined by the major and minor principal stresses with an angle of internal friction (Ø) and cohesion (C), expressed as:

$$\sigma_1 = \frac{2C\cos\phi}{1-\sin\phi} + \frac{1+\sin\phi}{1-\sin\phi}\sigma_3$$

To determine by the Mohr-Coulomb parameters the triaxial data were plotted in radius space (Labuz and Zang, 2012). Such that a linear regression through the data points will give two fitting parameters, 'a' and 'b' such that:

$$\tau_m = \sigma_m a + b$$

Where,

X is representative of mean normal stress (σ_m) = $(\sigma_1 + \sigma_3)/2$

Y is the maximum shear stress (τ_m) = $(\sigma_1 - \sigma_3)/2$

This can also be expressed as:

$$\tau_m = \sigma_m \sin\phi + C\cos$$

Where the failure parameters, angle of internal friction (ϕ) and Cohesion (C) are solved for as follows:

$$\boldsymbol{\phi = \sin^{-1} a}$$

$$C = \frac{b}{\cos\phi}$$

The development of mechanical rock property logs calibrated from laboratory data are used to constrain the geomechanical properties with depth. As of then, the empirical rock strength and rock failure predictions developed for reservoirs in the Taranaki Basin are considered for their implications of geomechanical stability in the Southern Taranaki Basin, see chapter 6.

3.6. Evaluation and Justification of Applied Methods

3.6.1. **Sample Selection**

For reservoir analogues, sample collection was systematically selected to be representative of the local stratigraphy from the Farewell and North Cape formations. The localities selected for outcrop sampling was based upon places where significant lithofacies analysis had been previously completed, providing the basis for sample selection (Higgs et al., 2010, Joyce, 2018, Smithies, 2018). The amount of samples acquired at each outcrop location was based upon the diversity of facies associations e.g. 136 samples were acquired from Oyster Point characterized by four facies associations, in comparison to approximately 20 samples acquired from Wairoa River and Peck's Point, both characterized by a single facies association. The amount of samples taken for each facies is unevenly distributed, heavily weighted towards cross-bedded sandstones and massive sandstones. This is due to the presence of these facies being commonly

represented the different facies associations. Limitations in sampling arose from the inability to drill clay rich weathered sandstones e.g. Wairoa River and Peck's Point, and coarse lithic rich sandstones e.g. Whahariki Beach, thus there is an unavoidable bias towards the very fine-medium grained sandstones.

For drill core, sample selection was centralized around the Maui-Manaia Region from four wells, Maui A1 (G), MBR-1, MBW-2 and Moki-1, which incorporated numerous Paleogene sandstone reservoirs e.g. Mangahewa, Kaimiro and Farewell Formation. The absence of mechanical rock property data attributed to this region meant a systematic approach was adopted to incorporate numerous intervals across depth and a spatial distribution. In turn, the use of drill core from offshore reservoirs, Farewell and North Cape formations allowed for comparison between the onshore and offshore reservoirs. However, limited drill core availability recognized for the North Cape Formation due to the substantial depth, resulted in the incorporation of drill core data from a more northern well, Tane-1. Limitations in sampling arose from core availability for destructive testing. The condition of the core (age, moisture content and discontinuities) limited the areas which could be sampled, and most likely will affect the measured laboratory physical and strength properties.

3.6.2. **Sample Preparation**

A process of trial and error was required to assess the technique used to prepare core plugs for weak rocks (Figure 3.4); this included variation of drill bit size, corer edge thickness, drill rotation speed, flatness of drilling surface, application of water and sharpness of diamond retipped drill bit. The following outlines the most successful method for drilling into highly weather outcrop blocks. A freshly tipped diamond drill corer with a razor thin corer edge provided the best setup for core plug sampling. The drill bit size did not affect the sample recovery rate but expect to lose significant diameter during coring; if a certain sample size is required, aim to use a drill bit 2-3mm larger in diameter. The maximum rotation speed should be employed, with the application of water should be kept as low as possible. importantly, the drill corer

should be exposed to a flat surface of the outcrop block for drilling and lowered at a slow constant pace; do not retract the drill once plug is being cored. This process is useful if only a small quantity of samples, however for copious amounts of sampling this method is impractical due to the extensive loss of material.

For our study, following an unsuccessful trial and error process of sampling core plugs from outcrop blocks, it was deemed that in-field drilling posed the only viable option left in order to acquire the desired material (Figure 3.11). Whilst conducting fieldwork, in order to avoid indiscriminate coring in the field a code of conduct should be applied to benefit the wider scientific community and general population. Following approval from local organizations and landowners, aim to core in unpopulated localities on less exposed outcrop faces, and be considerate of other geological features which may be of interest to others; outcrop coring should only be undertaken if necessary.

If possible, samples were cored in two orthogonal directions, parallel and perpendicular to bedding. For outcrop samples, in many instances it was difficult to acquire counterpart vertical samples due to the absence of a flat horizontal surface. For downhole samples, it was difficult to acquire horizontal samples of the appropriate length due to the minimum available thickness or the drill core.

Figure 3-11 [a] Process of in-field rock coring; [b] Hand drill with water for lubrication and cooling used to efficiently sample core plugs from outcrop; [c] Infilling of drill holes post sample collection

3.6.3. **Laboratory Techniques**

A statistical approach to data analysis provides a level of confidence in the reported results and interpretations, this is important when developing predictive tools for further extrapolation. The integrated use of both qualitative and quantitative data provides the most comprehensive overview to a study. Independent of research focus, analysis followed a typical order from qualitative descriptions, to summation of quantitative data and data validation. Descriptive statistics were used to resolve and summarize the vast amount of data gathered during the laboratory testing phase of the research; this can be expressed in terms of central tendency (average value) or the dispersion of a data set. For an accurate measure of a variable, both a mean value, range and standard deviation are expected; this assumption is applied at the earliest stage of data acquisition. Descriptive statistics were used to provide a quantitative summation of petrographical rock properties, point count analysis of mineral composition percentages and calculation of mean grain size. Physical property and rock strength measurements acquired during laboratory testing including porosity, permeability, V_p and V_s, and unconfined compressive strength were compared with expected values from published tables; this helped in identifying any outlier data points.

The most important parameter considered in this study, excluding rock strength, is porosity. Thus, the measure of pore volume attributed to each sample requires a level of certainty. Porosity fraction measurements were determined utilizing three methods, water saturation, nitrogen pycnometry, and mercury porosimetry. Gas displacement pycnometry is recognized as one the most reliable techniques used for obtaining measurements of apparent volume and density, more accurate and reproducible than Archimedes water method. Gas pycnometry maintains the product integrity, allowing for repeatability of testing and a fast analysis. Mercury porosimetry and water saturation are both fluid based methods, as opposed to gas pycnometry; fluid-based mercury porosimetry and water saturation porosity methods can result in alteration of the integrity of the rock, seen as a destructive.

Due to the small molecular size nitrogen gas can infiltrate into smaller micropore spaces, beyond the lower limit of measurable pore throat diameter of 0.0074 μm through mercury injection. This infers that when using gas pycnometry for pore volume estimates, a standard industry practice, a substantial amount of detectable pore volume could be attributed to micropores which may not contribute to effective flow in fluid reservoirs. This has serious implications for decisions regarding reservoir economic viability. Regarding mercury porosimetry, whilst this technique can provide data on pore volume distribution across pore throat diameter intervals, it cannot provide any information regarding the frequency or population of pores without an understanding of the real pore shapes; the formula used for predicting pore throat measurements assume a cylindrical pore shape. Due to the influence of water on clay rich rocks e.g. swelling or slaking of rocks, any sample undergoing strength testing was not saturated for porosity determination or ultrasonic wave velocity measurements; in order to prevent potential alteration of sedimentary framework of the rock.

Though our research has focused on rock strength prediction, utilizing porosity and grains size, the acquisition of data on drill core provided a full characterization of physical rock properties and strength parameters for each test specimen through laboratory testing. This enables the user to handle the data set dependent upon the area of interest. In reality, the properties of rock cores measured in the laboratory usually do not accurately reflect large-scale in situ properties because of strong influence from large scale heterogeneities including joints, faults, weakness planes, and other factors; these features were avoided during sample selection. Therefore, laboratory values for intact specimens must be employed with proper judgment in engineering and rock mechanics applications (ASTM D7012-14).

The procedures outlined in ASTM standards used to specify data collection and record are regarded as industry standard; this generates reliable results which can be used in comparison with other data following the same recognized methodology.

Chapter Four – Assessment of Micro-Scale Reservoir Heterogeneities and their control on Physical Properties of Sandstones in the Pakawau Sub-basin

4.1. Introduction

Porosity and permeability are integral to reservoir simulation models used for the assessment of flow capabilities across a reservoir; these physical properties provide the basis for all other assumptions and calculations. In order to reduce the inaccuracy of reservoir models, these physical properties need to be quantified in a systematic way which incorporates as much fine detail as possible. Reservoir simulation models use mappable flow units to define a specific volume of the reservoir with similar pore characteristics to which to attribute flow properties. The use of sedimentary facies to characterise porosity and permeability is a common and acknowledged method, with outcrop lithofacies descriptions used to aid wireline interpretations and delineate the spatial distributions (Chantellier and Hitchings, 1987, Sech et al., 2009, White et al., 2004).

Extensive work has been undertaken on facies characterisation of the Pakawau Sub-basin (Thrasher, 1992, Bal and Lewis, 1994, Higgs et al., 2010, Joyce, 2018, Smithies, 2018); however limited work exists on quantification of the physical properties of these onshore reservoir outcrops. The key objective of this study is to quantify the physical properties of different facies types of sandstones using outcrops of Late Cretaceous-Paleocene reservoir units in the Pakawau Sub-basin. We will assess the elements of microscale rock heterogeneity, which may be detrimental or advantageous to the reservoirs' flow capabilities. Rock heterogeneities include, but are not limited to, pore

structure and type, sedimentary texture (grain size and sorting), mineralogy, alteration of framework grains, and clay distribution. With this understanding, we will show how facies characterisation conducted by geologists, utilizing reservoir outcrops and drill core from offshore wells, can be used to make first-order assessments of petrographical properties exhibited within a facies.

The second objective is to compare the quantifiable property measurements of the sandstone facies from the Late Cretaceous-Paleocene reservoirs within the Pakawau Sub-basin from this study, with similar facies types found within the offshore reservoirs of the Maui-Maari Field. This will enable us to determine if any consistency exists across like facies in the two different regions.

4.2. Geological Setting

4.2.1. Tectonic History

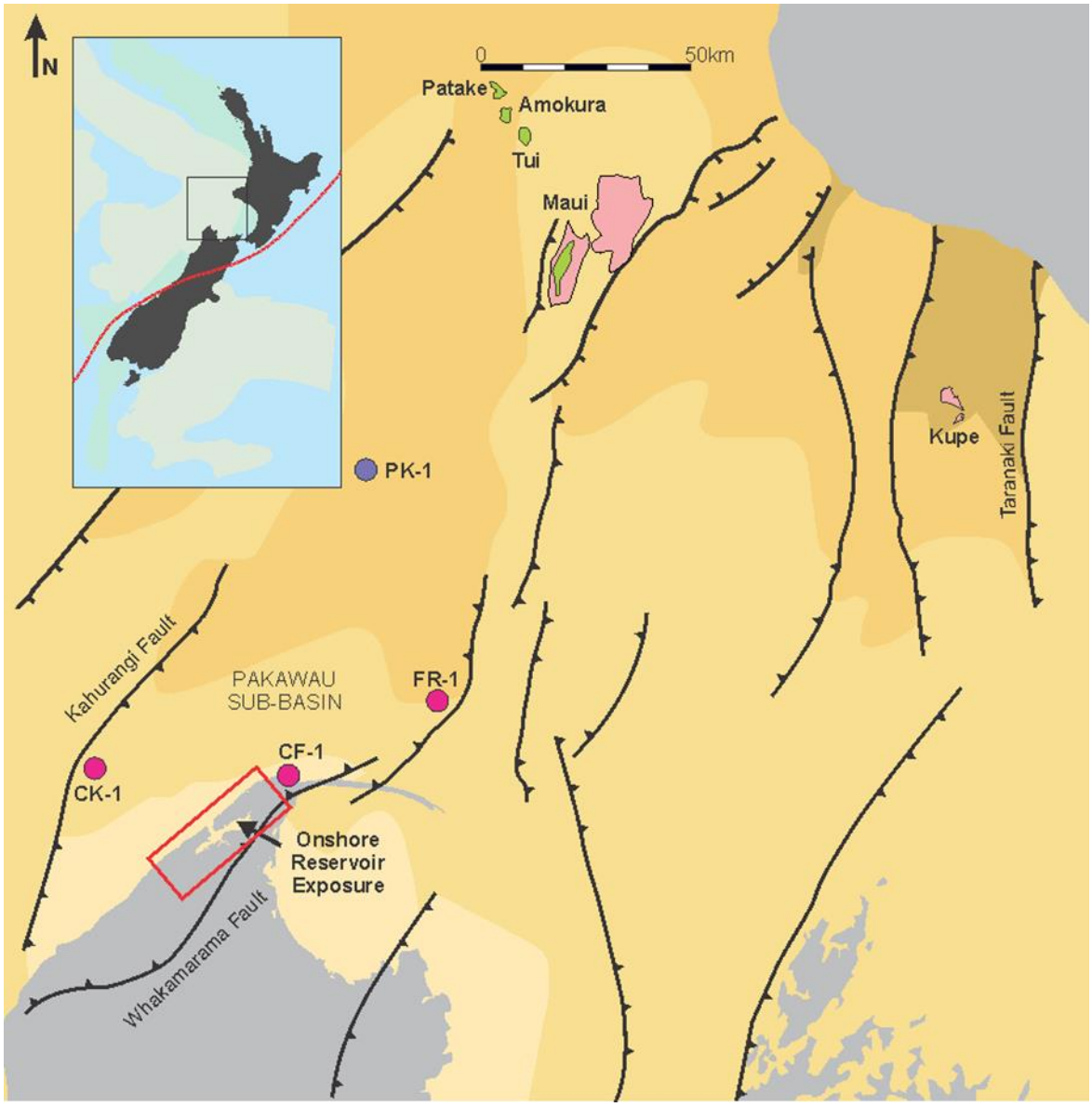

Figure 4-1 Location map of the Taranaki Basin, a Cretaceous-Cenozoic sedimentary rift basin, located on the western coast of New Zealand. The Pakawau Sub-basin formed during the 'West Coast-Taranaki rift' phase and contains the sole onshore exposure of the Farewell and North Cape Formation reservoirs.

The Taranaki Basin, the only petroleum producing province in new Zealand, is located on the west coast of New Zealand, spanning an area of 100,000 km (2014) (Figure 4.1). A Cretaceous-Cenozoic rift basin, the subsurface structure of the basin reflects multiple

phases of extensional and compressional deformation (King and Thrasher, 1996). An early rift-phase in the mid Cretaceous reflects the widespread stretching of Zealandia, preceding the Gondwana breakup; this formed a series of half-grabens with strikes trending NW/NNW (Strogen et al., 2017). A second phase of rifting ensued from the Late Cretaceous and into the Paleocene, aptly named the West Coast-Taranaki rift. This second rifting phase is thought to be associated with the spreading of the Tasman Sea and resulted in a series of NE orientated half grabens, including the Pakawau Sub-basin. The onset of the West Coast- Taranaki rift phase in proximal (landward) parts of the Taranaki Basin resulted in a restricted marine environment, controlled by basin-bounding normal faults (Strogen et al., 2017). This is reflected in the stratigraphy with a transition from shoreface sandstones in the north, to coastal plain successions in the south (Joyce, 2018). During the Early Paleocene, transgression and thermal rift subsidence across the basin is interpreted from a wide marine-influenced shoreline belt across the central Taranaki Basin, trending northeast to southwest (King and Thrasher, 1996), transitioning into coastal plain and fluvial successions in the south (Figure 4.2). The Pakawau Sub-basin is the southernmost sub-basin in the southern Taranaki Basin, bound in the northwest by the Kahurangi Fault and in the east by the Whakamarama Fault (Bal and Lewis, 1994; Stark, 1996; Thrasher, 1992). Inversion of the Whakamarama Fault in the Late Miocene resulted in the onshore exposure of the previously deeply buried Late Cretaceous – Palaeocene strata, accounting for 10% of the Pakawau sub-basin (Knox, 1982). The onshore exposure of the North Cape and Farewell formations is limited to north-western South Island, where they lie unconformably over Palaeozoic metasedimentary basement (Rattenbury et al., 1998; Rattenbury and Isaac, 2012). Pakawau Sub-basin deposits are confirmed in the lithostratigraphic sequence from offshore wellbores including Cook-1 (CK-1), Cape Farewell 1 (CF-1), and Fresne 1 (FR-1). Though the Pakawau Sub-basin deposits are much shallow than their counterpart offshore reservoirs in the Maui region, and might exhibit different burial and diagenetic histories.

4.2.2. **Stratigraphy**

In the central southern Taranaki Basin, the North Cape Formation, represented by shallow marine sandstones, encompasses both generating source rocks and potential reservoir rocks (Browne et al., 2008; King and Thrasher, 1996), with weak/moderate oil shows in several wells including Pukeko-1 (PK-1). The Farewell Formation, also characterised by shallow marine sandstones, is a producing Paleocene reservoir in the Maui-B, Kupe, Patake, Amokura and Tui Fields (Higgs, 2012) (Figure 4.1).

This study is focused on the onshore exposure of the North Cape and Farewell formations in the Pakawau Sub-basin which record the transition from a restricted marginal marine to a coastal plain succession (Figure 4.2). In the Pakawau Sub-basin, North Cape deposits, reaching up to 1.5 km in thickness, conformably overlie the older terrestrial Rakopi Formation. The North Cape Formation contains marine-influenced sedimentation, with evidence from dinoflagellates documented in previous studies (Bal and Lewis, 1994; Stark, 1996; Thrasher, 1992; Wizevich et al., 1992) and tidally influenced sedimentary structures e.g. bidirectional cross ripple laminations with mud drapes (Wizevich, 1992; Joyce, 2018). However, the absence of marine macrofossils and abundant carbonaceous material implies a restricted marine environment (Wizevich et al., 1992). The North Cape Formation is interpreted as an ancient estuarine marine embayment fed by fan deltas prograding off the Whakamarama Fault scarp (Higgs et al., 2010; Joyce, 2018). The restricted estuarine setting (Bal and Lewis, 1994; Higgs et al., 2010; Joyce, 2018; Smithies, 2018) is characterised by channelized sandstones, thinly interbedded sandstones/siltstones and localised coal deposits (Browne et al., 2008; Stark, 1996; Thrasher, 1992; Joyce, 2018). An upwards transition from high energy tidal channels of a delta front to terrestrial fluvial delta plain suggests progradation of fan deltas away from the Whakamarama Fault; this is in agreement with paleoflow data (Smithies, 2018).

In the Pakawau Sub-basin, Farewell Formation is composed of complex stacked channel sandstones capped by thin finer organic rich beds characteristic of braided river and flood plain deposits, recorded up to 800 m thick. This strata is interpreted as a fluvial

river system, with increased conglomeratic content up section (Bridge and Lunt, 2006; Lunt et al., 2004). The formation unconformably overlies the older North Cape Formation (Bal and Lewis, 1994). This unconformable basal contact is suggested to denote the K/T boundary and correlates with the top Cretaceous seismic reflection horizon observed in offshore seismic profiles (Thrasher, 1992). A marine regression within the Farewell Formation is marked by the onset of fluvial terrestrial deposits (Bal, 1992); the cause of the regression is not understood but may reflect a slowing of subsidence rates or increased sediment supply (Smithies, 2018).

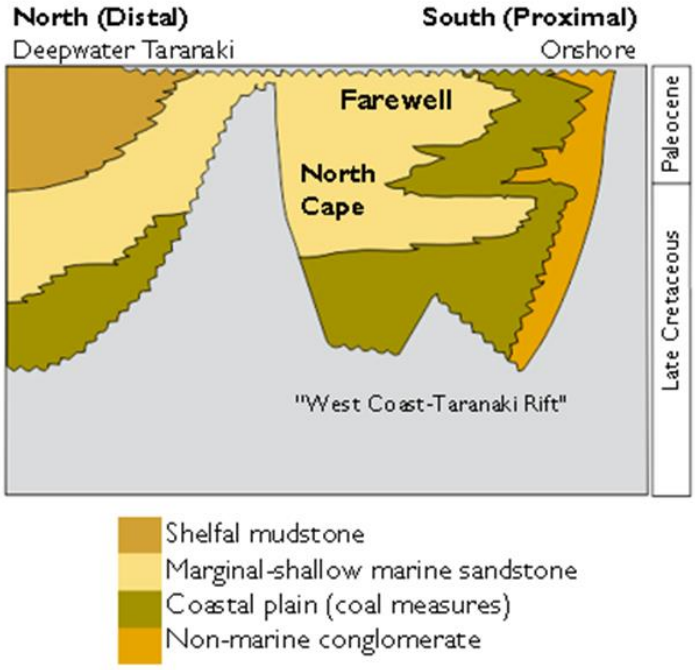

Figure 4-2 Late Cretaceous-Paleocene chronostratigraphy of the Taranaki Basin. A transition from shoreface sands in the north, to coastal plain successions in the south associated with the Pakawau Sub-basin - Adapted from King and Thrasher (1996).

4.3. Methods and Materials

4.3.1. Outcrop Sampling

Onshore reservoirs of the North Cape and Farewell formations located near the Whanganui Inlet (40°34'59.7"S 172°35'25.1"E) provided sample material for laboratory testing (Figure 4.2). Four sedimentary facies associations are recognised within the fluvial-restricted marine environment interpreted from outcrop: Delta Front [DF], Supratidal Flats [SF], Delta Plain [DP] and Braided River [BR]. The Delta Front, Supratidal Flats and Delta Plain facies associations are exclusively ascribed to the North Cape Formation, with the Braided River facies association attributed to the Farewell Formation. The four principal sedimentary facies associations identified for this study were observed at (Figure 4.3): Wairoa River [1], Pecks Point [2], Oyster Point [3], and Whareriki Beach [4].

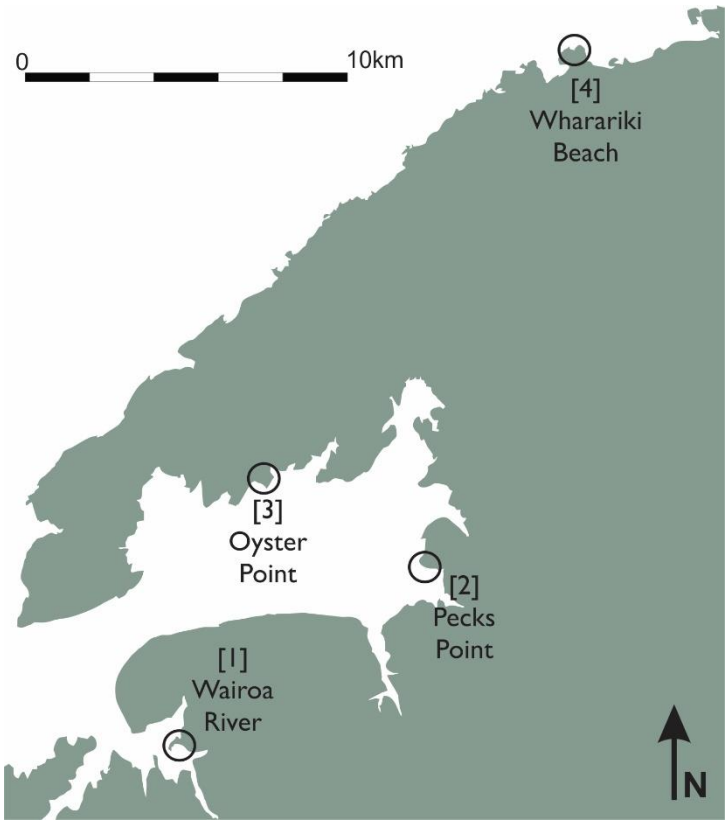

Figure 4-3 Regional map of the onshore exposure of the North Cape and Farewell Formation reservoir analogues in the Pakawau Sub-basin surrounding the Whanganui Inlet. Localities [1-4] represent study sites with well documented facies analysis by Higgs (2010), Joyce (2018) and Smithies (2018) which provided the basis for sample selection

A facies association is representative of a sub-environment consisting of an arrangement of individual facies which formed from different sedimentary processes e.g. a braided river setting is comprised of channel sandstones, gravel bar and flood plain deposits, each characterised as individual facies (Reading, 2009).

The Delta Front facies association [DF] is characterised by thickly bedded (≤2 m), fine- to coarse-grained sandstones often displaying bidirectional cross bedding with mud drapes and tidal bundles (Bal and Lewis, 1994; Higgs et al., 2010; Joyce, 2018; Titheridge, 1977). The facies is represented by high energy, marginal marine, tide dominated channels flowing away from fan deltas off the Whakamarama Fault. A fan delta interpretation is supported by coarse conglomeratic deposits observed near Pecks Point and paleocurrent data (Smithies, 2018). The DF deposits account for 10-15% of exposed North Cape Formation and are observed at locations [2] and [3].

The Supratidal Flats [SF] facies association is characterised by thinly bedded (≤0.5 m), organic rich, very fine- to medium-grained sandstones with rhythmic interbedding of carbonaceous siltstones, mudstones, and thin coal seams (Bal and Lewis, 1994; Higgs et al., 2010; Joyce, 2018). Asymmetric ripple and planar laminations, localised burrow structures, and organic stringers are also observed. The facies is representative of salt marshes, mudflats and localised tidal channels within a low-lying estuarine zone with fluctuating energy conditions (Bal and Lewis, 1994; Joyce, 2018; Ongley and Macpherson, 1923). Progradation of the shoreline is highlighted by the progression from interbedded sandstone and siltstone to mudstone and coal at the top of the succession (Smithies, 2018), where coal is restricted or only thinly developed due to the influence of saline water. The SF deposits account for 35-40% of exposed North Cape Formation and are observed at locations [1] and [3].

The Delta Plain [DP] facies association is characterised by thinly bedded (≥1 m), fine-grained sandstone, interbedded with mudstone, rare conglomerates, and sparse thick coal seams (Bal and Lewis, 1994; Higgs et al., 2010; Joyce, 2018). Thick sandstone beds display wispy laminations and localised trough cross bedding. The facies is interpreted

as being deposited in a low energy delta plain to delta front setting with meandering channels, crevasse splays and interdistributary bays (Bal and Lewis, 1994); Higgs et al. (2010) and Joyce (2018) confirmed the non-marine deposition. The DP deposits account for 40-45% of North Cape Formation outcrops and is observed at location [3].

The Braided River [BR] facies association is characterised by thickly bedded (≥ 5m), trough cross bedded, fine to coarse grained sandstones, with gravel lags, siltstone lenses and intermittent thin organic rich planar beds (Bal and Lewis, 1994; Higgs et al., 2010; Joyce, 2018; smithies, 2018). The facies is interpreted as high energy, migrating fluvial channels and gravel bars with intermittent low energy flood plain/loam beds in a braided river environment. Up section the unit becomes more conglomeratic (Titheridge, 1977), indicative of more proximal alluvial deposits and/or an increase in energy within the depositional environment. The extensive BR setting of the Farewell Formation is observed at locations [3] and [4].

The four facies associations described above do not include all of the depositional environments of the Pakawau Sub-basin strata but are a major representative of the stratigraphy from the onshore region. The descriptions of the four facies associations provide an overview of the variability of individual facies found within a single sub-environment. Oyster Point provides a type section where all four facies associations used in this research were observed (Figure 4.4).

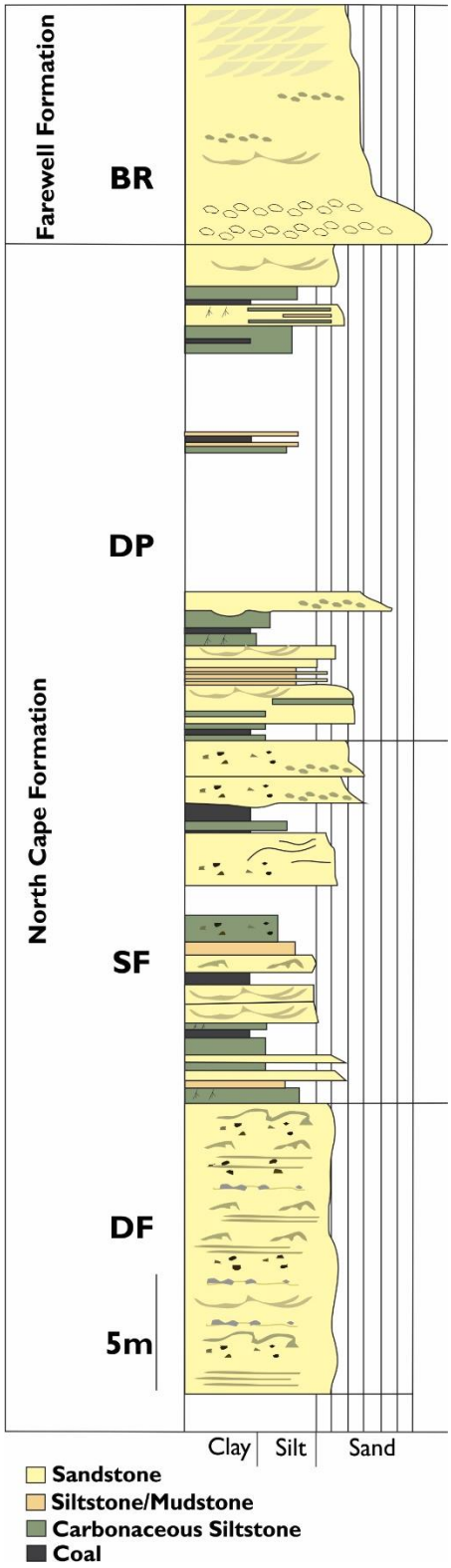

Figure 4-4 Facies type section within the North Cape and Farewell formations at Oyster Point comprising of Delta Front (DF), Supratidal Flats (SF), Delta Plain (DP) and Braided River (BR) facies associations.

Table 4-1 Individual sandstone facies exhibited within the different facies associations and corresponding sample count for this study.

Sandstone Facies	Facies	Facies Associations	Number of samples
Massive to wavy bedded	Sw	DF, DP and BR	103
Cross bedded sandstones	Sx	DF, SF, DP and BR	69
Carbonaceous sandstone	CS	SF, DP and BR	47
Heterolithic interbedded	Hl	DF and SF	11
Planar laminated sandstones	Sp	DF, SF, DP and BR	0

The dominant sandstone facies types observed within the stratigraphy can be constrained to cross bedded sandstones (Sx), massive to wavy bedded sandstones (Sw), carbonaceous sandstones (CS), planar laminated sandstones (Sp), and heterolithic interbedded sandstones (Hl), in accordance with Joyce (2018). Each of these facies types is not restricted to a single association, often with overlapping facies observed in the different facies associations (DF, SF, DP and BR). Table 4.1 provides a summary of sandstone facies types sampled in this study from the different facies associations. The DF facies association is dominated by cross bedded, wavy bedded, planar laminated, and heterolithic sandstone facies. The SF facies association encompasses wavy bedded, planar laminated and heterolithic sandstones facies. Both the DP and BR facies associations are dominated by cross bedded, wavy bedded, planar laminated and carbonaceous sandstone facies. The sample distribution of the individual facies from each location is presented in Appendix B. Given the abundance of sandstone within the stratigraphy, and inability to sample very coarse grained, poorly consolidated sandstones and clay rich mudstones in the region, an unavoidable sampling bias exists in this study towards sandstone facies types, constrained by coarse grained silt to medium grained sandstone. In addition, no planar laminated sandstone facies were sampled. Cross bedded and wavy bedded sandstones are the most represented facies within the stratigraphy, and thus are more weighted in the sample acquisition.

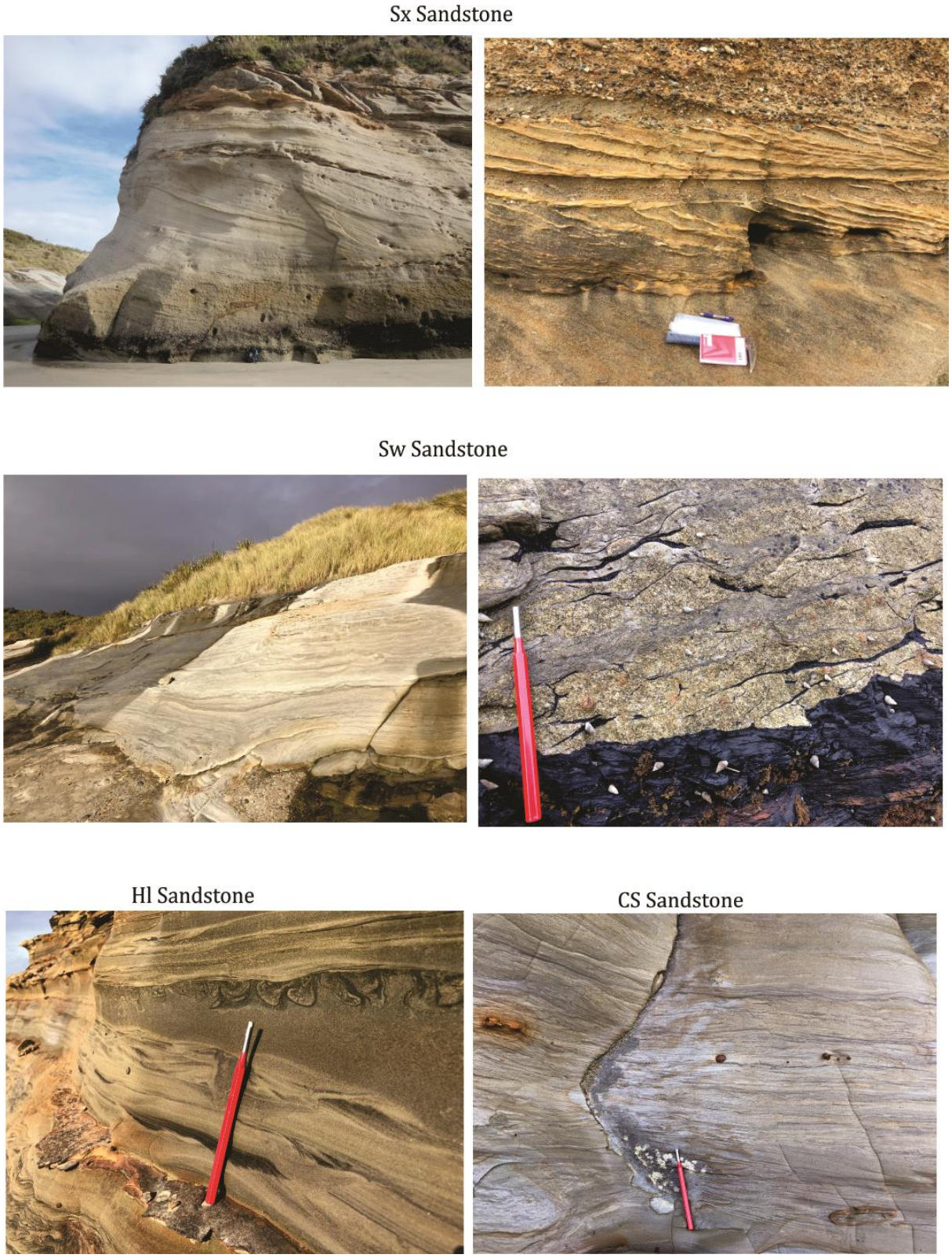

Figure 4-5 Examples of sandstone facies types observed in the field: Cross bedded sandstone (Sx), Wavy bedded sandstone (Sw), Heterolithic sandstone (Hl) and Carbonaceous sandstone (CS).

4.3.2. **Non-Destructive Testing**

250 drill core specimens collected from outcrop were prepared for laboratory testing in accordance with ASTM Practice D4543–08 (2008) in the University of Canterbury Rock Mechanics Lab. The cylindrical cores, 20 mm in diameter, were drilled both parallel and Perpendicular where possible to account for any anisotropy. Sample dimensions and recorded masses were used to determine bulk density measurements (Ulusay and Hudson, 2007). Prior to testing samples were oven-dried for at least 48 hours at 60°C. Sample dimensions and recorded masses were used to determine bulk density measurements (Ulusay and Hudson, 2007). Grain volume (Vs) measurements were undertaken using the AccuPyc II 134 nitrogen pycnometer (Micromeritics Instrument Corporation), used to calculate pore volume (V-Vs), then to calculate the porosity as the ratio of the pore volume to the bulk volume. Gas (nitrogen) permeability was measured using either the steady state method or transient method, depending on the permeability of the sample. Low permeability test specimens (<0.1 mD) were tested using the transient method in a Core Laboratories PDP-200 Permeameter (Cant et al., 2018). Higher permeability samples (0.1 mD – 1000 mD) were tested using a steady state permeameter (Figure 3.8). Apparent permeability (K_{gas}) is expressed in Equation 4.1 as (Scheidegger, 1974):

$$K_{gas} = Q\left(\frac{2\eta L}{A}\right)\left(\frac{P_{down}}{P_{up}^2 - P_{down}^2}\right) \quad (4.1)$$

Where,

P= Pore Pressure (MPa)

Q=flow rate (m^3/s)

A = specimen cross sectional area (m^2)

L = length (m). Pore fluid viscosity

η, was set at 1.78×10^{-5} Pa.s as nitrogen gas at room temperature

To determine the true permeability Klinkenberg corrections were used where required in both steady state and transient methods. This can be expressed in Equation .2:

$$K_{true} = K_{gas}\left(1 + \frac{b}{P_{mean}}\right) \quad (4.2)$$

Where,

K_{true} = true permeability (mD)

K_{gas} = gas permeability at a particular pore pressure (mD)

b = Klinkenberg slip factor

P_{mean} = mean pore pressure (MPa)

Optical microscopy was undertaken on 17 thin sections, across each sampled facies, used to identify the textural properties which could affect the physical rock properties e.g. porosity and permeability; thin sections were stained with a blue dye used to identify the presence and nature of pore spaces. In turn, a brief overview of the mineralogical properties was provided through point count analysis on thin sections using a Pelcon Point Counter. XRD analysis was undertaken on the 17 sandstones, by Spectrachem Ltd, Lower Hutt, in order to corroborate point count data, and quantify clay mineral types.

Four cross bedded sandstone samples were selected for quantitative analysis of their pore structure characteristics. Mercury Intrusion Porosimetry (MIP) tests were carried out by the Materials and Engineering Research Institute (MERI) at Sheffield Hallam University using a PASCAL 140/240 porosimeter for quantitative pore structure characterisation of the four sandstones. It is capable of measuring pore throat diameters in the range of 0.0074 μm to 116 μm and particle diameters in the range of 0.015 μm to 330 μm. Pore throat diameters are classified as nano, micro, meso, macro and megapore throat types (Doveton, 2014).

Scanning Electron Microscopy (SEM) was undertaken on a carbon coated thin sections from each of the four sandstones and was used to investigate sandstone texture at a greater magnification (down to 10 μm). Backscatter Electron (BSE) images provide a greater clarity for microscale processes effecting grains and clay mineral structure (100-

10 μm), and pore space geometries (<10 μm). All quantifiable data attributed to this chapter can be found in Appendices C, D and E.

4.4. Quantification of physical reservoir properties (porosity and permeability)

4.4.1. Results

4.4.1.1. Textural Properties

The Late Cretaceous-Palaeocene sandstones range from very fine to coarse grained (Figure 4.6): cross bedded sandstones (100-300 μm), wavy bedded sandstones (120-235 μm), heterolithic laminated sandstones (85 μm), and carbonaceous sandstones (40-100 μm). In general, heterolithic laminated (Hl) and carbonaceous (CS) sandstones are very fine-fine grained, whereas cross bedded (Sx) and wavy bedded (Sw) sandstones are fine-medium grained. Poor to moderate grain sorting is exhibited in the cross bedded, wavy bedded and carbonaceous sandstones, compared with moderate to good sorting displayed within the heterolithic laminated sandstones; a larger grain size range is associated with more poorly sorted sandstones. The roundness of the detrital grains are subangular to sub-rounded, with more angular grains exhibited within cross bedded and wavy bedded sandstones. Sub-parallel alignment of elongate grains e.g. micas, is observed in some finer grained sandstone.

The main pore types are recognised within the sandstones can be categorised as primary pores, intergranular (IG) and micropores (M), and secondary pores (S). The moderate-well sorted heterolithic sandstones predominantly exhibit an intergranular pore type. The poor-moderately sorted cross bedded sandstones, carbonaceous sandstones and wavy bedded sandstones also predominantly display an intergranular pore type, but often larger intergranular pores have been are infilled with matrix increasing the contribution from micropores. Finer grained sandstones e.g. Hl and CS

exhibit smaller intergranular pores, in comparison to coarser grained sandstones e.g. Sx and Sw sandstones which exhibit larger intergranular pores. Secondary pores are exhibited within the sandstones mainly as localised dissolution pores. Wavy bedded sandstones display an increased secondary pore presence from grain dissolution, with regular clay infiltrate (Table 4. 2). Intragranular pores are exhibited along cleavages of buckled mica grains and within microfracture quartz grain in coarser grained sandstones.

Table 4-2 Overview of individual sampled facies from each location with associated textural properties. Grain sorting: Well sorted (W), moderately sorted (M) and poorly sorted (P). Grain shape: Angular (A), subangular (SA) and subrounded (SR). Pore types: Intergranular (IG), micropore (M) and secondary pore (S).

Sample Code	Facies Association	Sandstone Facies	Grain Sorting	Grain Shape	Average Grain Size (μm)	Grain Size Range (μm)	Dominant Pore Type
OYPA1	DF	Hl	W	SA-SR	85	50-125	IG
PP	DF	Sx	M	A-SA	220	160-280	IG
OYPBRS	BR	Sx	P	SA-SR	300	200-400	IG, M and S
OYPBRrS	BR	Sx	P-M	SA-SR	100	<150	IG and M
CFBR	BR	Sx	P	A-SA	225	150-300	IG
WKFGS	BR	Sx	M	A-SA	300	200-400	IG and S
WRNA2S	SF	Sx	M	A-SA	162.5	75-250	IG and S
OYPA2C	SF	CS	M	SA-SR	100	<120	IG and S
OYPA3C	DP	CS	M	SA-SR	50	25-150	IG
WRNA2C	SF	CS	M	SA-SR	40	<50	IG
WKBRC	BR	CS	M	SA-SR	50	<100	IG
OYPLOS	SF	Sw	P-M	A-SR	200	150-300	M and S
OYPUSS	SF	Sw	P-M	SA-SR	150	100-200	M and S
OYPNC L	DP	Sw	P-M	A-SR	185	120-250	IG and S
OYPNC U	DP	Sw	P-M	A-SR	200	150-320	IG and S
OYPBROL	BR	Sw	M	SA-SR	120	<150	IG and S
WKBRS	BR	Sw	P-M	SA-SR	175	100-350	M and S

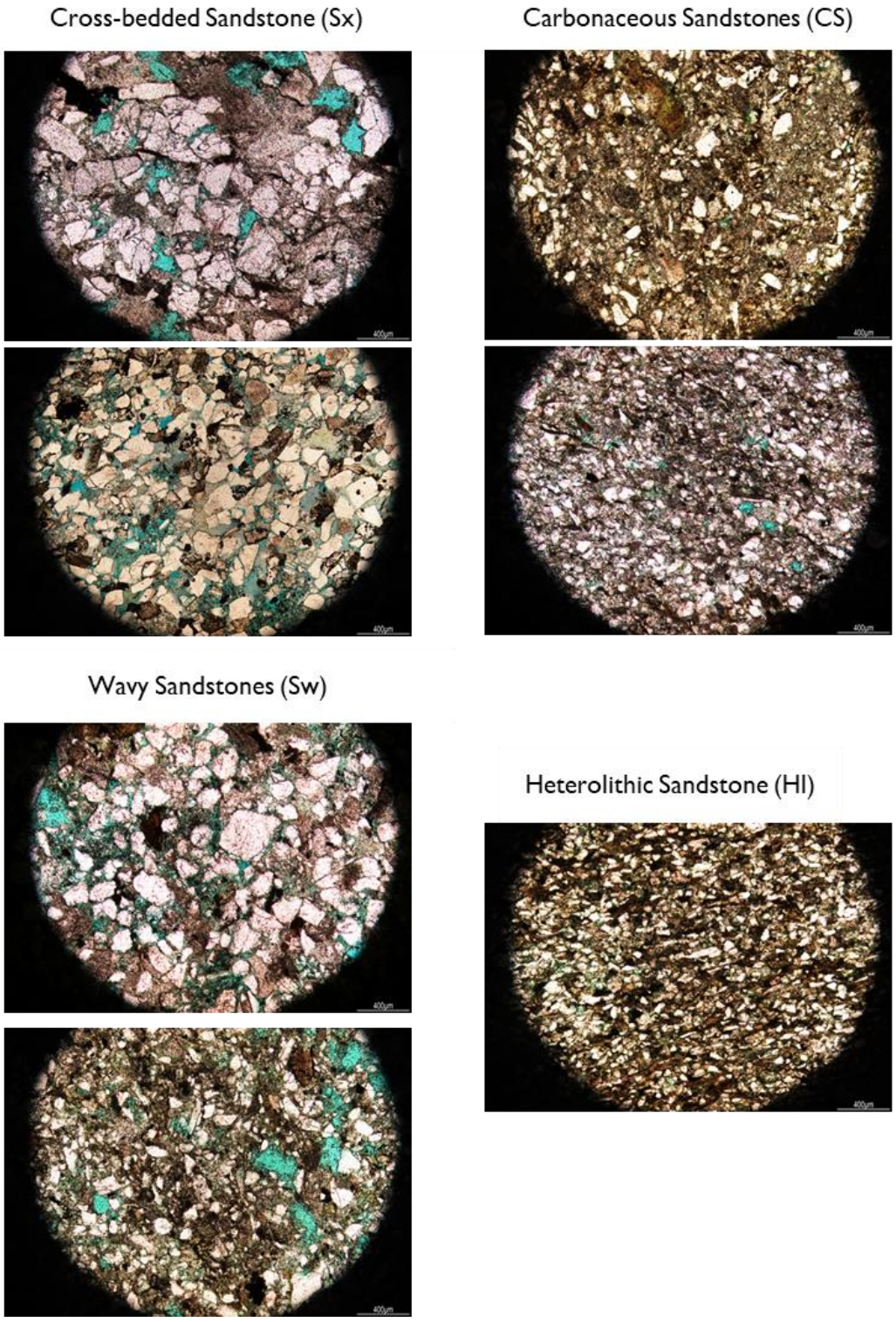

Figure 4-6 Textural properties of Sx, Sw, Hl, and CS sandstone facies

4.4.1.2. Brief Overview of Mineral Properties

The mineral compositions of the sandstones are mostly classified as Arkose-Lithic Arkose (Folk, 1968). Thin section analysis suggests there is no systematic variation in mineralogy for most of the sandstones from different facies (Table 4.3). Based upon point count data, the proportion of quartz falls between 33-52%, composed of monocrystalline grains; total feldspar contribution falls between 21-31%, and lithic content remains constant, between 4-22%. XRD data corroborates the point count data with quartz percentages between 38-56%, however a large variation of feldspar percentages from 7-51%, see appendix C.

Table 4-3 Overview of sampled facies beds from each location with associated textural properties (Qz-Quartz, Fsp-Feldspar, Lith-Lithics, Bio-Biotite, Musc-Muscovite, Chl-Chlorite, Glauc-Glauconite).

Sample Code	Facies	Mineral Percentages (%)									
		Qz	Fsp	Lith	Bio	Musc	Chl	Glauc	Cement	Matrix	Organic
OYPA1	Hl	36	27	7	17	4	0	0	3	5	0
PP	Sx	39	31	20	3	1	0	0	3	1	0
OYPBRS	Sx	40	28	9	10	4	0	0	8	3	0
OYPBRrS	Sx	45	31	12	3	1	0	0	6	1	0
CFBR	Sx	45	25	11	5	3	0	0	7	1	0
WKFGS	Sx	43	29	12	4	2	0	0	2	7	0
WRNA2S	Sx	48	26	12	3	1	2	2	5	1	0
OYPA2C	CS	34	29	7	5	2	1	0	0	23	0
OYPA3C	CS	39	27	5	13	3	0	0	0	13	0
WRNA2C	CS	51	30	4	3	7	0	0	0	1	0
WKBRC	CS	33	29	11	8	1	0	0	1	16	3
OYPLOS	Sw	32	23	7	6	3	1	0	5	14	8
OYPUSS	Sw	34	25	8	7	3	0	0	5	15	0
OYPNC L	Sw	38	24	22	12	2	0	0	5	1	0
OYPNC U	Sw	32	32	6	8	4	2	0	8	1	0
OYPBROL	Sw	25	21	6	8	12	0	0	5	0	13
WKBRS	Sw	37	29	10	5	2	0	0	4	13	0

Biotite mica is visible in thin section observed as coarse detrital grains, up to 12%, but only accounts for <2% of samples analysed by XRD. There is a consistently low degree of cementation across the sandstones between 1-8%, predominantly in the form of minor calcite or iron oxide cement. Matrix content is variable from 0-23%, locally concentrated within some carbonaceous sandstones and wavy bedded sandstones. Similarly, the presence of organic content is restricted to carbonaceous sandstones and wavy bedded sandstones.

Bulk chemistry data provided from XRD analysis demonstrates the constituent weight percentage for the various clay mineral types across the sandstone samples (Appendix C). XRD results show that kaolinite is the dominant clay mineral across all samples with localised traces of chlorite and illite. Kaolinite, a diagenetic clay, accounts for 80% of the total clay content. Illite is only detected in 3 samples from a single locality, Oyster Point, thus it is not possible to determine its true origin, where present illite is associated with a drop in the amount of kaolinite. Chlorite content is at a near constant background level across the different sandstones, present as both detrital grains and authigenic pore filling/rim coating cement as observed through thin section analysis. It represents approximately 5-10% of the total clay content; however, the content increases up to 20% in the heterolithic sandstone.

4.4.1.3. Porosity and Permeability

An overview of textural properties and physical property measurements associated with the sandstone facies sampled in this study are given in Table 4.4. Though the Hl sandstone facies is under-represented in this study, in-field permeability measurements acquired by Joyce (2018), are in agreement with the range.

Table 4-4 Overview of textural properties and physical properties associated with different sandstone facies

Facies	Facies Association	Grain Size (μm)	Grain Sorting	Dominant Pore Type	Porosity Fraction	Permeability (mD)
Hl	DF and SF	85	M-W	IG	0.25-0.27	0.25-12.6
Sx	DF, SF, DP and BR	100-300	P-M	IG and M	0.17-0.39	1.78-718
CS	DF, SF, DP and BR	40-100	P-M	IG	0.14-0.28	0.25-10.3
Sw	SF, DP and BR	120-235	P-M	IG, M and S	0.18-0.28	0.18-824

Porosity and permeability exhibit a correlation with considerable variability over a broad permeability, 0.04-824 mD, and porosity, 0.13 and 0.39, range (Figure 4.7a). A similar spatial distribution on the porosity-permeability plot is exhibited for the poorly-moderately sorted, fine to medium grained sandstones of the Sw and Sx facies. The fine to medium grained (100-300 μm) cross bedded sandstones (Sx) exhibit a good correlation between porosity (0.17-0.39) and permeability (1-718 mD). Similar to Sx, the fine to medium grained (120-235 μm) wavy bedded sandstones (Sw) exhibit a good correlation, but with a larger permeability range (0.18-824 md) attributed to a smaller porosity range (0.18-0.28). The poor-moderately sorted, very fine-fine grained carbonaceous sandstones (CS) cluster at the lower end of the graph with low permeabilities (0.25-10.3 mD) across a moderate porosity range (0.14-0.28). The Hl sandstones forms a tight cluster between 4.3-10 mD, however this is resultant from only a single unit sampled in this study, with a constant grain size (85 μm).

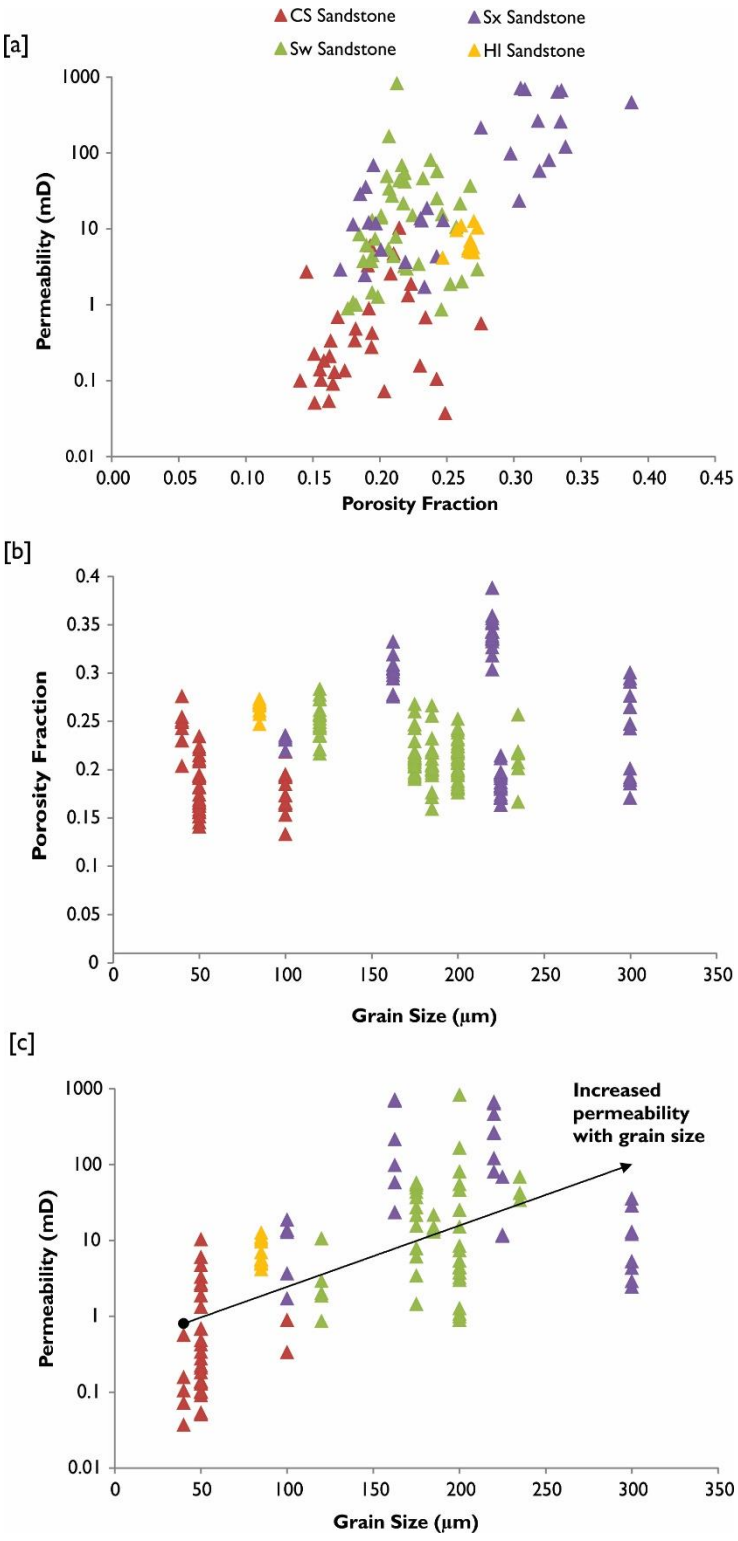

Figure 4-7[a] Linear relationship between the porosity-permeability trends as a function of sandstone facies. [b] No correlation exhibited between porosity fraction and grain size. [c] Positive linear trend with an increased permeability associated with coarser g rained sandstones.

Assessment of the porosity-permeability relationship on the basis of grain size demonstrates that the porosity fraction does not change as a function of grain size with a consistent porosity range from 0.15-0.30 observed across a grain size range from 40-300 μm (Figure 4.7b). There is a positive correlation between grain size and permeability, with higher permeabilities attributed to fine to medium grained sandstone facies, e.g. Sx (1.78-718 mD) and Sw (0.18-824 mD), and lower permeabilities attributed to siltstone/very fine-grained sandstone facies (0-10 mD) e.g. CS and Hl (Figure 4.7c). Regardless of Hl sandstones being underrepresented with data to represent the entire facies, the avaliable data does fall within the central permeability-grain size trend.

Permeability measurements were acquired as multi-directional components both parallel and perpendicular to assess for anisotropy in the sandstone facies (Figure 4.8). Overall, there are no major anisotropic trends across the different sandstone facies, with permeability ranges constrained to one or two orders of magnitude and displaying the expected trend of lower permeabilities orientated perpendicular to bedding in HI and Sx; the only exception to this trend is exhibited within the wavy bedded sandstone facies.

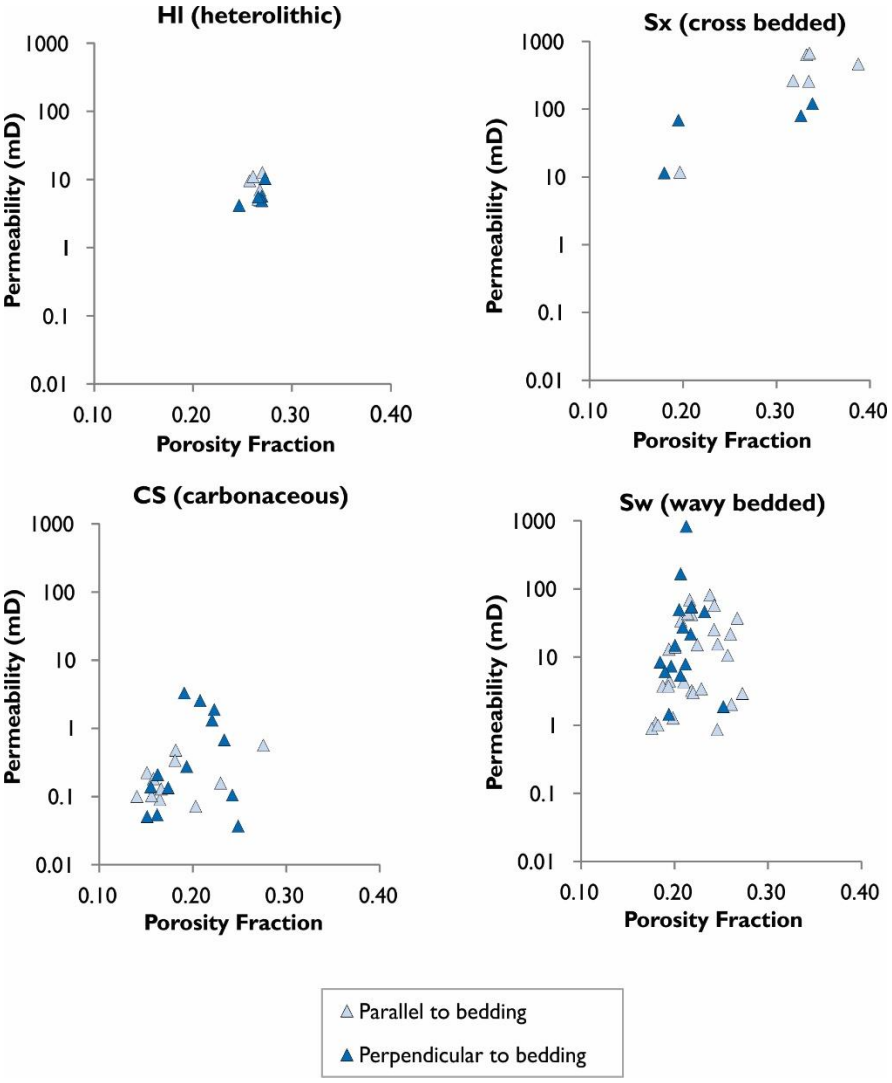

Figure 4-8 Porosity versus permeability plots, assessing for the presence of any permeability anisotropy. All sandstones display a certain amount of directional control on permeability, but this is considered negligible if contained to one or two orders of magnitude e.g. Hl and Sx.

4.5. Pore Structure Characterisation

MIP tests and SEM imagery were undertaken on four samples, DF-1, SF-2, DP-3 and BR-4. Results are used to develop an understanding of the pore network from different sandstones to determine the textural controls on porosity and permeability. The textural properties of the sandstones are summarised in Table 4.5.

Table 4-5 Comparison of textural properties and pore characteristics across four sandstones associated with the Sx facies (DF-1, SF-2, DP-3 and BR-4)

Sample	Facies Type	Grain Size (μm)	Grain Sorting	Pore throat diameter (μm)		Porosity Fraction	Permeability (mD)
				Mean	Modal		
DF-1	Hl	85	M	0.135	2.19	0.27	11.8
SF-2	Sw	200	P	0.10	0.62	0.19	7.9
DP-3	Sw	200	P-M	0.19	2.87	0.24	20.1
BR-4	Sw	175	P-M	0.23	2.37	0.26	29.6

4.5.1. **Results**

Results from the MIP tests provide information on the pore throat distribution and pore throat diameters of the four sandstones. The mean pore throat diameters for all sandstones measure between 0.10-0.23 μm. The modal (most frequent) pore throat diameters exhibit higher values from 2.18 μm to 2.87 μm in the DF-1, DP-3 and BR-4 samples compared to 0.6 μm in the SF-2 samples (Figure 4.9).

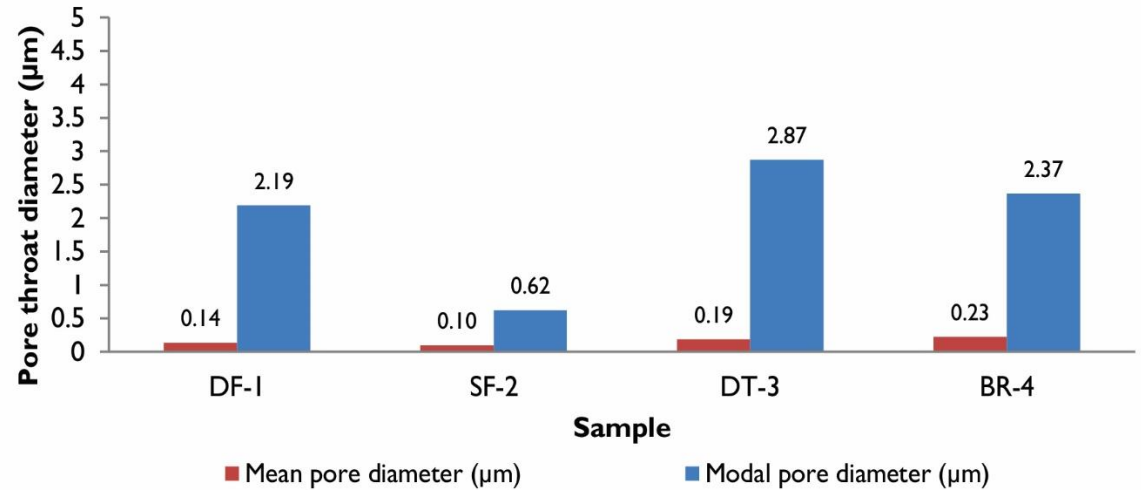

Figure 4-9 Comparison between mean pore throat diameter and modal pore throat diameter as determined during the MIP tests for each sandstone. The large modal pore throat diameter of the DF, ST and BR sandstones suggest large frequency of macropores; however, the lower mean pore throat diameters also suggest the retention of small pore throats in addition to the macropores.

A strong positive correlation is exhibited between the mean pore throat diameter and permeability; SF-2 with the lowest permeability of 7.9 mD is attributed to the smallest pore throat diameter of 0.10 µm (Figure 4.10). BR-4 with the highest permeability of 29.6 mD is attributed to the widest mean pore throat diameter of 0.23 µm. A tentative positive correlation is observed between modal pore diameter and permeability; the widest modal pore diameter of 2.87 µm is attributed to the second highest permeability sample, DP-3.

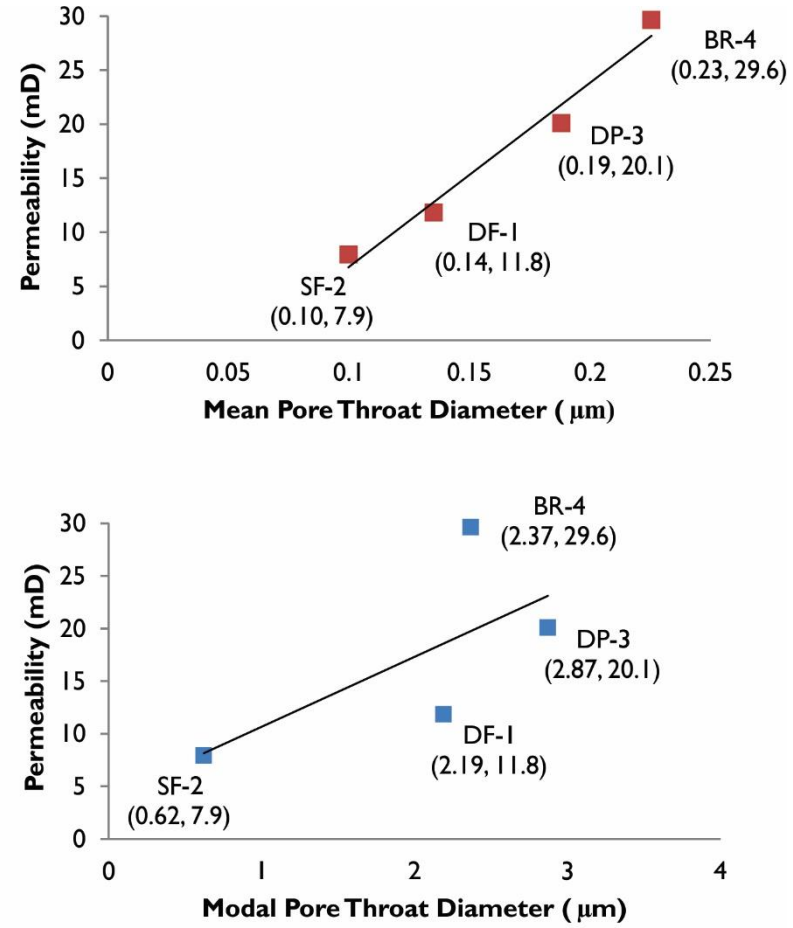

Figure 4-10 Positive relationships exhibited between the average pore throat diameters (mean/modal) and permeability. Strong correlation between micropore throat diameters (<1µm) and permeable flow.

Figure 4.11 represents a comparison of pore volume distribution curves from the MIP tests on the four sandstone samples. Data is presented in the form of cumulative (dV) and log differential (dV/dlogD) pore volume distribution curves. Cumulative curves can be used to provide an overview of total pore volume distribution, with steeper gradient of the slope indicative of an increase of pore volume concentrated within the associated pore throat diameters (Meyer & Klobes, 1999). Pore volume will increase with decreasing pore throat diameter, as large pores are the first to fill. The cumulative distribution is the least biased way of presenting pore volume distribution data as the there is no mathematical transformation of the data prior to plotting (Diamond, 1970); The cumulative log is described on the plots from right to left, from the mega to nano range (Figure 4.11). Above 5 µm (macro-megapores), there is a negligible amount of

pore volume attributed to all four sandstones. Between 1.5-5 µm (mesopores), DF-1, DP-3 and BR-4 exhibit similar steep gradients; The DF-1 gradient with a slight reduction in steepness continues to 0.6 µm, before gradually transforming into a low stepped gradient down to 0.0075 µm. DP-3 and DP-4 trends display a similar gently inclined slope from below 0.5 µm to 0.0075 µm (lower test limit). SF-2 only deviates from horizontal between 1-2 µm, at which a gently inclined gradient, with similar form to DP-3 and BR-4, is observed down to 0.03 µm. Between 0.3-0.0075 µm the SF-2, DF-3 and BR-4 exhibit a plateaued gradient with no increase in pore volume.

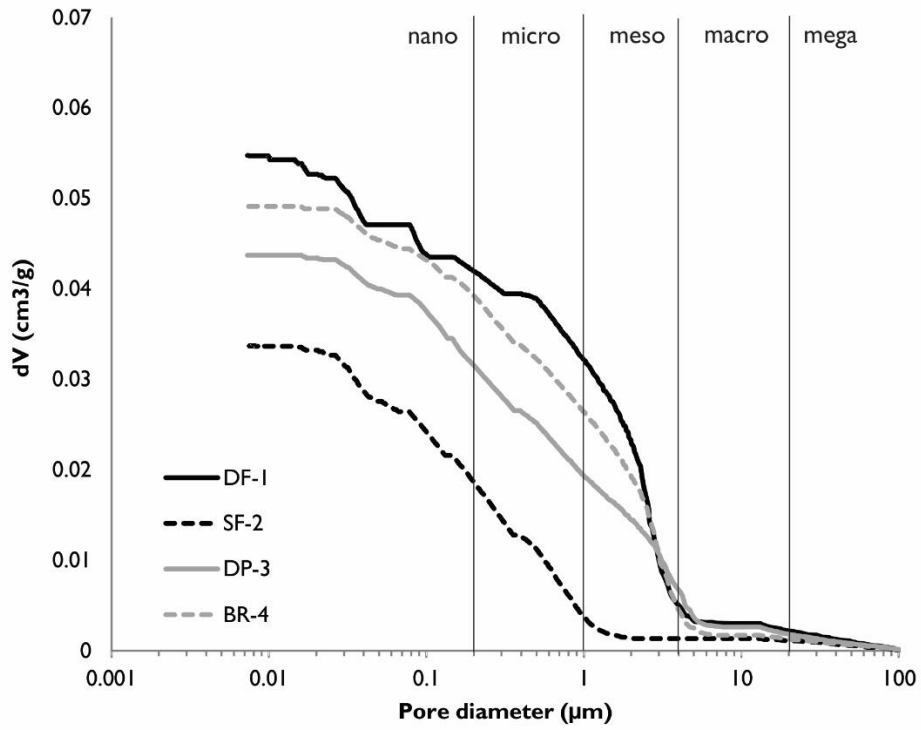

Figure 4-11 Cumulative pore volume distribution curves for DF-1, SF-2, DP-3 and BR-4 exhibiting pore volume attributed to different pore throat diameter ranges e.g. micro and mesopores.

The dV/dlogD represents the differential pore volume (dV) normalised to the logarithm of the pore throat diameter interval (D) in each interval, which accounts for the uneven spacing of these pore throat diameter intervals during testing (Meyer and Klobes, 1999)(Figure 4,12). The DF-1 pore structure exhibits a bimodal distribution, with a large amount of pore volume falling within 0.01-0.1 µm and 1-10 µm pore throat diameters. The SF-2, DP-3 and BR-4 sandstones exhibit similar volume distribution patterns across

between 0.01-1 μm, defined by a relatively consistent level of pore and no distinct peaks attributed to the micro-mesopore range. The absence of distinct peaks between 0.01 and 1 μm on the SF-2, DP-3 and BR4 curves indicates pore volumes are evenly distributed, though DP-3 and BR-4 show an increase in abundance of pore volume to the peak between 1-10 μm. DF-1 has the largest proportion of meso-macropores (>1 μm), followed by BR-4 and DP-3 and SF-2 has the lowest proportion of meso-macropores, this in agreement with the pore throat diameter measurements. In DF-1, DP-3 and BR-4, the largest peaks are positioned in proximity to the modal pore throat diameters (>1 μm). The meso-macropore dominated sandstones, as illustrated in both distribution curves correspond with highest porosity fractions, DF-1(0.26), DP-3(0.24) and BR-4(0.26).

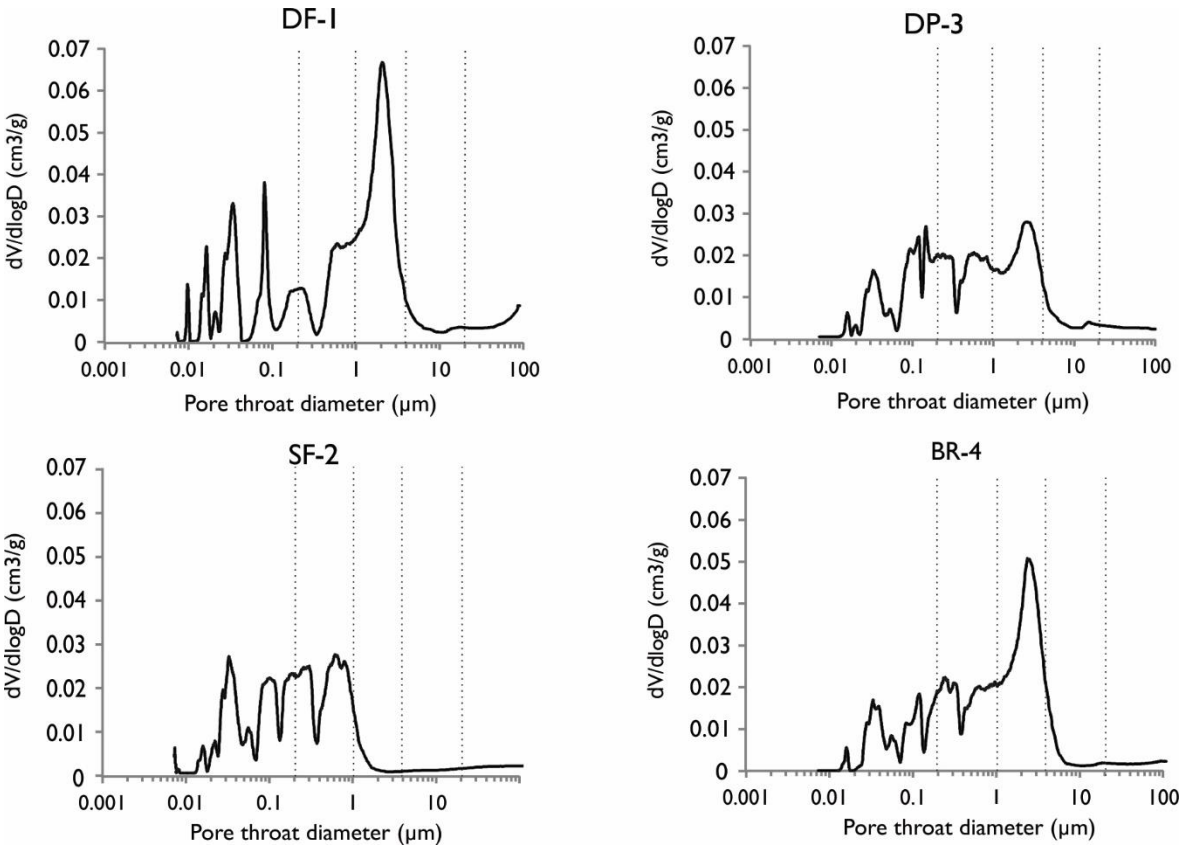

Figure 4-12 Pore volume distribution curves of DF-1, SF-2, DP-3 and BR-4 displaying the differential distribution of pore volume attributed to each pore throat diameter interval. The largest peaks for pore throat diameters cumulate in the meso-macro region for DF-1, DP-3 and BR-4. Within the nano-micro region SF-2, DP-3 and BR-4 exhibit similar distribution patterns.

SEM imagery used to capture the pore structure supports the results observed in the MIP tests (Figure 4.13). Very fine grained, moderately sorted, DF-1 sandstone exhibits substantial amount of intergranular pores between detrital grains, with additional pore space attributed to localised dissolution pores and splayed intragranular pores along splayed cleavage planes within buckled mica grains. SF-2 exhibits uniformly distributed micropores (d<5 μm) located within matrix which has infilled the pre-existing larger intergranular pores. Medium grained, poorly moderately sorted DP-3 and BR-4 sandstones exhibit a dominant presence of intergranular pores between detrital grains, although the pores are commonly infilled. For BR-4 with localised matrix, and for DP-3 with clay precipitate, increasing the contribution of micropores. Grain dissolution pores are observed in DF-1 and BR-4 but are more dominant in DP-3.

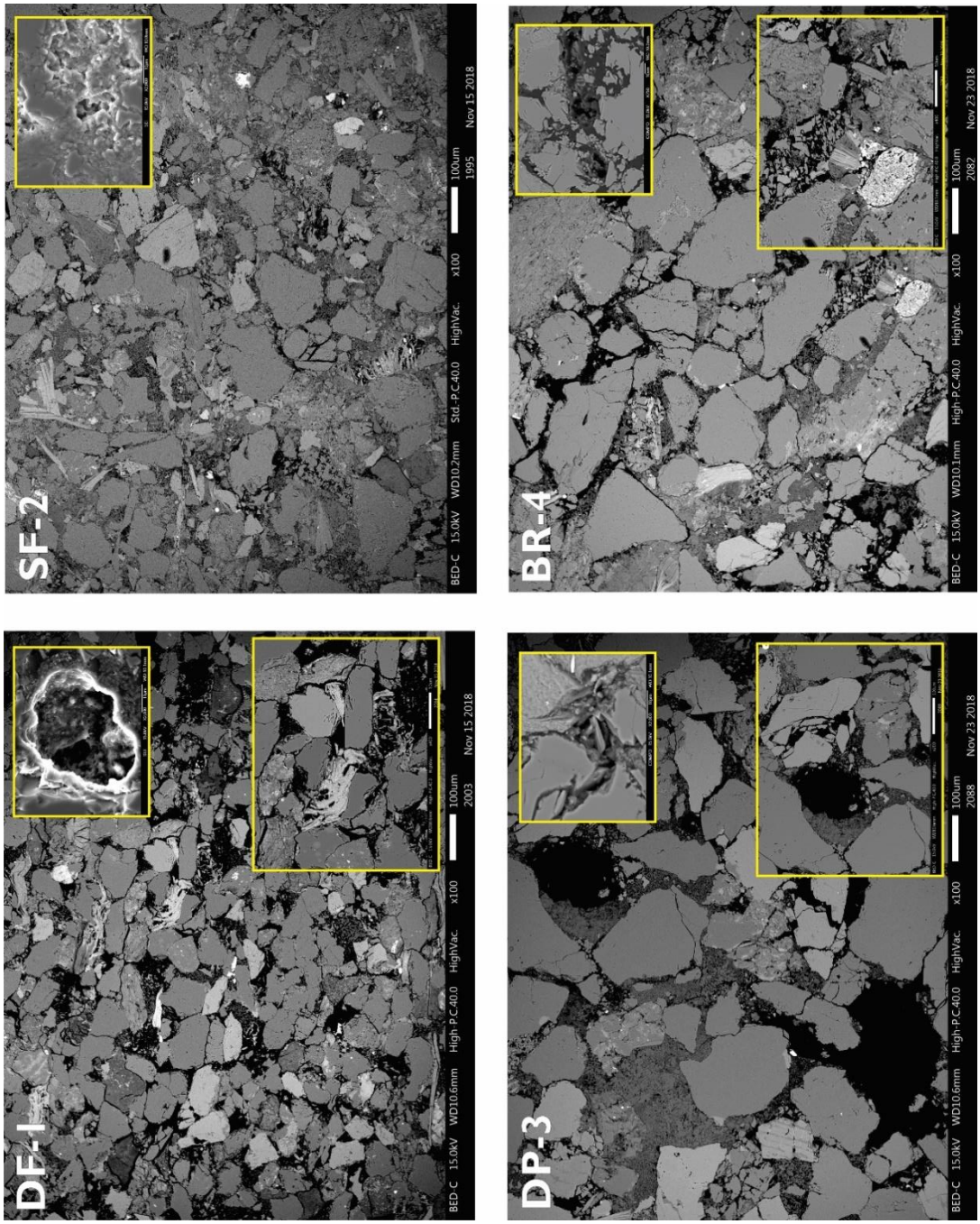

Figure 4-13 BSEM images of DF-1, SF-2, DT-3 and BR-4 sandstones. Dominant pore types are highlighted at higher magnification in yellow boxes. DF-1: Large intergranular pore spaces (d=25 μm; main image), localised grain dissolution pores (upper inset) and splayed intragranular pores between buckled mica grains (lower inset). SF-2: Majority of pore space is infilled with matrix (inset), producing well distributed micropores (d<5 μm) between fine detrital grains. DT-3: – Some intergranular pores (main image) but dominated by large secondary pores from grain dissolution (d=30 μm; lower inset), and infilled clay precipitate (upper inset). BR-4 – Large intergranular pores (d>100 μm; main image) locally infilled with a mix of matrix and or clay precipitate (upper inset), significant contribution of pore volume from micropores (lower inset).

4.6. Interpretation – Pore Structure

The pore structure characterisation of four sandstones (DF-1, SF-2, DP-3 and BR-4) presents a range of high porosities (0.19-0.27) and permeabilities (7.9-29.6 mD) which could be inferred as good reservoir properties. However, porosity and permeability do not sufficiently describe the pore volume distribution of sandstone. The variable textural properties characterising the sandstones result in varied pore volume distributions, which are described as a function of pore types and pore throat diameters.

DF-1 is a moderately sorted, subangular to subrounded, very fine-grained sandstone with the highest porosity fraction; the pore structure is characterised by small intergranular pores (d=25 μm) and localised secondary grain dissolution pores. DP-3 and BR-4 are both poor-moderately sorted, subangular-subrounded, fine to medium grained sandstones; the pore structure is characterised by large intergranular pores, and secondary grain dissolution pores, both locally infilled with matrix and clay infiltrate. SF-2 is a poorly sorted, subangular to subrounded, fine grained sandstone with a substantial matrix presence between detrital grains, attributed the lowest porosity fraction; the pore structure is characterised by a dominance of nano-micropores with pore throat diameters ranging up to 1μm. SF-2 exhibits a minimal amount of micro-fractured quartz grains, buckled mica grains and secondary pores from grain dissolution, in comparison to the macropore dominated sandstones DF-1, DP-3 and BR-4 sandstones. The combinations of textural properties suggest that grain sorting is a significant control on dominant pore type. The meso-macropore dominated sandstones (DF-1, DP-3 and BR-4) demonstrate the highest porosity fractions (0.24-0.29).

A positive correlation exists between the smaller mean pore throat diameters and permeability, with the lowest permeability of 7.9 mD attributed to the smallest pore throat diameter of 0.1 μm (Figure 4.10); this suggests the smaller micropores are contributing to effective flow. The positive relationship between mean pore throat diameter and permeability is exhibited regardless of grain size and grain sorting. In this instance, regardless of the variable textural properties and pore types across the

different sandstone facies, porosities and permeabilities are relatively high suggesting pore spaces are well connected.

A tentative positive correlation between the modal pore diameters and permeability (Figure 4.10) with meso-macro dominated sandstones attributed the highest permeabilities e.g. DP-3 and BR-4. The increased modal pore throat diameter of DP-3 (2.87 μm) could be attributed to exhibits increased amounts of grain dissolution within the sandstone, confirmed by SEM images (Figure 4.13). The dissolution of framework grains provides improved porosity and enhanced permeability if pores are well-connected, by enlarging of pores and pore throats (Mozley et al., 2016). When dissolution pores are interconnected with intergranular pores, the effectiveness of the pore system is improved (Ali et al., 2010). It is suggested a proportion of the larger macropore throat diameters are attributed to secondary pores in DF-1, DP-3 and BR-4. However, a relatively permeability (20.1 mD) associated with DP-3 could be resultant of increased clay precipitates clustered at the pore entrance reducing permeability.

The choice of parameter used to summarize the measured pore throat diameters (mean or modal) can considerably influence any projection made from the results (Table 4.5). The modal pore throat diameters in DF-1, DP-3 and BR-4 (2.19-2.87 μm) describe a high proportion of meso-macropores within the sandstones. However, independently this parameter incorrectly depicts three sandstones dominated by large, uniform, well-connected pores. The mean pore throat diameters range between 0.10-0.23 μm for all four sandstones. Used independently this incorrectly describes four sandstones with similar pore volume distributions, dominated by nano-micropores, omitting critical information regarding meso-macropores. Used in conjunction, modal and mean pore throat diameter, these parameters can be used to develop a much clearer image of pore volume distributions across the entire pore structure scale. Regardless of the high modal pore diameters observed in DF-1, DP-3 and BR-4, a significantly lower mean pore throat diameter suggests the presence of nano-micro pore throats in addition to the larger meso-macropores. The SF-2 sandstone has a modal pore throat diameter of 0.63 μm that is closer to its corresponding mean pore throat diameter of 0.099 μm, suggesting a

complete lack of meso-macropores, in contrast to micropore dominance with some meso-macropores. This is supported by the uniformly distributed micropores observed within the SEM image (Figure 4.13).

4.7. Interpretation - Primary Controls on Porosity and Permeability

Porosity and permeability are controlled by the characteristics the pore structure notably dominant pore types and the distribution of pore throats. The pore structure is developed based upon the textural rock properties of sandstone.

The dominant pore types are controlled by grain sorting. Intergranular pores are observed across all sandstone facies: Carbonaceous sandstone (CS), cross-bedded sandstone, wavy bedded sandstone (Sw) and heterolithic sandstones (Hl) but are commonly infilled with matrix and/or clays in poor-moderately sorted sandstone facies (Sx and Sw), increasing the contribution of micropores. Grain size does not affect dominant pore type and has no influence on total pore volume (Figure 4.7b), however finer grained sandstones e.g. Hl and CS exhibit smaller intergranular pores, in comparison to coarser grained sandstones e.g. Sx and Sw sandstones which exhibit larger intergranular pores.

Diagenetic alteration can significantly influence the flow capabilities of a reservoir, with increased secondary porosity from chemical and mechanical deformation e.g. microfractured grains and feldspar dissolution. Secondary pores from grain dissolution are exhibited in the Hl and Sx facies, and more prominently in the Sw facies. Intragranular pores are exhibited along cleavages of buckled mica grains and within microfracture quartz grain in coarser grained sandstones. In poorly sorted sandstones, the reduced pore space from matrix infill between detrital grains may act to restrict the amount of chemical and mechanical deformation. Grain dissolution is often absent from samples with generally small throat sizes as they exhibit poor sorting, close packing and high interstitial clay contents (Strong, 1993, Strong and Milodowski, 1987).

Permeability is controlled by both grain size and grain sorting demonstrated across different sandstone facies; finer grained sandstones exhibit lower permeabilities due to

a reduction in pore throat diameters; poorly sorted sandstones with increased microporosity act to reduce the average pore throat diameter.

Permeability can be affected by the distribution of clay precipitates, often clustered at the pore entrance, which can significantly reduce pore throat diameters (Figure 4.13). The dominant clay type of the sandstones is kaolinite; the presence of the inter-pore authigenic kaolinite, the vermicule and booklet texture of the clays can retain micropore space, ranging from 15-61% (Hurst and Nadeau, 1995). Kaolinite is sourced from either allogenic material or authigenic clay derived from weathering, early/uplift-related diagenesis (Burley and Worden, 2009). Smithies (2019) suggest a large proportion of authigenic kaolinite within the outcropping North Cape and Farewell formations are resultant from surface weathering at the time of deposition, observing an increased weathering pattern through up the stratigraphic section. Our data does suggest an increase in kaolinite clay from the upper Farewell Formation samples, which are stratigraphically above the lower North Cape Formation; however, this trend is not consistent across the entire data set.

Enhanced rates of kaolinization can occur at shallower depths during early diagenesis within reducing environments due to an abundance of carbon dioxide within the interstitial pore waters (Chen, 2011). We hypothesise that environments with organic rich sandstone facies e.g. Sw, CS and Sx could have contributed to local acidification of interstitial pore waters, which in turn enhanced the rate of chemical alteration of feldspars (Burley and Worden, 2009). Authigenic kaolinite can be derived from the alteration of detrital feldspars, unstable in diagenetic environments, thus commonly alter via grain dissolution and/or replacement (Morad and Aldahan, 1987). This is supported by the highest kaolinite levels being found the Sx, CS and Sw facies associations, in comparison to the Hl facies. In order for kaolinite to form via grain dissolution of feldspars, reservoir rocks require sufficient porosity and permeability to allow for fluid flow. The Sw sandstone facies display the highest levels of detrital feldspar dissolution, with secondary pores providing sufficient space for infilling of intergranular pores with kaolinite clays.

4.8. Discussion

4.8.1. Optimum Pore Diameter for Quantifying Permeable Flow

During an MIP test, mercury will only saturate a pore when the external pressure exceeds that of the capillary pressure at the pore entrance. The different levels of mercury saturation (0-100%) during the MIP test have been used to express the flow capability through a pore system as a function of pore throat diameter (Table 4.6).

Table 4-6 Pore throat diameters corresponding to 35% (R_{35}) and 50% (R_{50}) mercury saturation.

Sample	R35 (µm)	R50 (µm)
DF-1	2.33	1.54
SF-2	0.46	0.24
DP-3	1.79	0.73
BR-4	2.29	1.23

Sing (1985) developed a classification which utilizes the median pore throat diameter (R_{50}), represented by mercury saturation levels of 50%, where capillary pores are defined by an R_{50} of 0.2-5 µm. Conventional sandstone reservoirs are typically defined by capillary pores. In capillary pores fluids do not flow freely due to friction along pore walls, but if a change in pressure overcomes the acting capillary forces at the pore wall fluids can pass through (Hu et al., 2017). DF-1, SF-2, DP-3 and BR-4 sandstones can all be classified as having capillary pores with the median pore throat diameters ranging between 0.24-1.5µm (Figure 4.14a). Subcapillary pores, classified by R_{50}<0.2 µm, represent a pore throat diameter that becomes ineffective for fluid movement due to restriction by intermolecular forces at the pore entrance. SF-2 has the lowest median pore throat diameter, with an R_{50} of 0.24 µm, suggesting a strong subcapillary pore presence. However, the ability of subcapillary pores to act as a conduit for petroleum migration can be misjudged. In this study, a strong correlation between mean pore diameters and permeability suggests that even the subcapillary pores are contributing to effective flow (Figure 4.10).

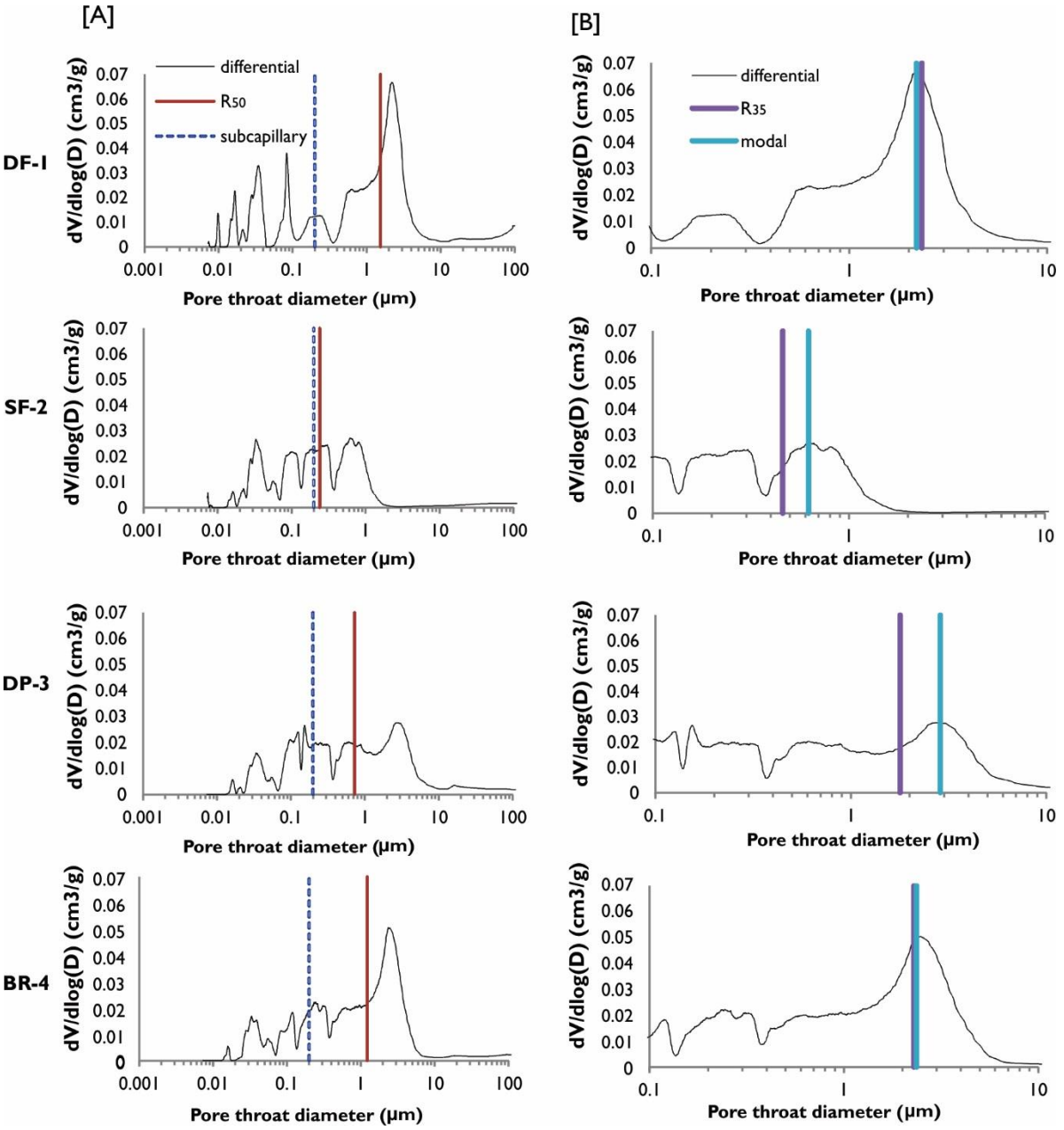

Figure 4-14 [a] Median pore throat diameter (R_{50}) positioned with respect to the sub-capillary-capillary boundary (0.2 µm); R_{50} for SF-2 is in close proximity to boundary, suggesting a strong subcapillary pore contribution. [b] Optimum pore throat diameter (R_{35}) positioned with respect to the modal pore throat diameters. Pore throat diameters below R_{35} do not contribute to flow.

Winland (1972) stated that fluid flows through a rock within an effective pore system which corresponds to a certain pore throat diameter, called the optimum pore throat diameter. In general, larger pore throats are a dominant control on permeable flow as they are first to fill during pore saturation. Winland (1972) found the optimum pore

throat diameter, which dominates flow through a rock, is represented by a mercury saturation level of 35% (R_{35}); pore throat diameters below R_{35} do not contribute to flow and instead contribute to storage. The R_{35} values closely correspond with their associated modal pore throat diameters, this would infer an optimum pore throat diameter for effective flow is attributed to the most common pore throat diameter in these sandstones; this is important for effective porosity as large pores are the first to fill, thus a dominant control on permeable flow (Figure 4.14b).

Multiple studies have demonstrated the permeability of rock is closely correlated to pore throat dimensions (Katz and Thompson, 1986, Nelson et al., 2006, Pittman, 1992, Purcell, 1949, Swanson, 1981). Winland (1972) developed an empirical relationship between porosity, permeability and pore throat diameter by investigating fluid flow at different levels of reservoir saturation, through the use of MIP tests, see Equation 4.3:

$$\log K_a = \frac{\log R_{35} + (0.864 \log \emptyset) - 0.732}{0.588} \quad (4.3)$$

Where,

Ka is air permeability (mD)

n is porosity (%)

R_{35} = optimum pore throat diameter (μm)

Permeabilities of the DF-1, SF-2, DP-3 and BR-4 can be predicted using Winland's Equation. Figure 4.15a compares the predicted permeabilities (from Equation 4.3), with the corresponding laboratory measured permeabilities. For SF-2, DP-3 and BR-4, the predicted permeabilities fall within a close range to the measured permeabilities; this suggests that the assumption of R_{35} as the optimum pore throat diameter for an effective flow is correct. permeabilities However, DF-1 demonstrates a higher predicted permeability of 29.7 mD, compared to the measured permeability of 11.8 mD.

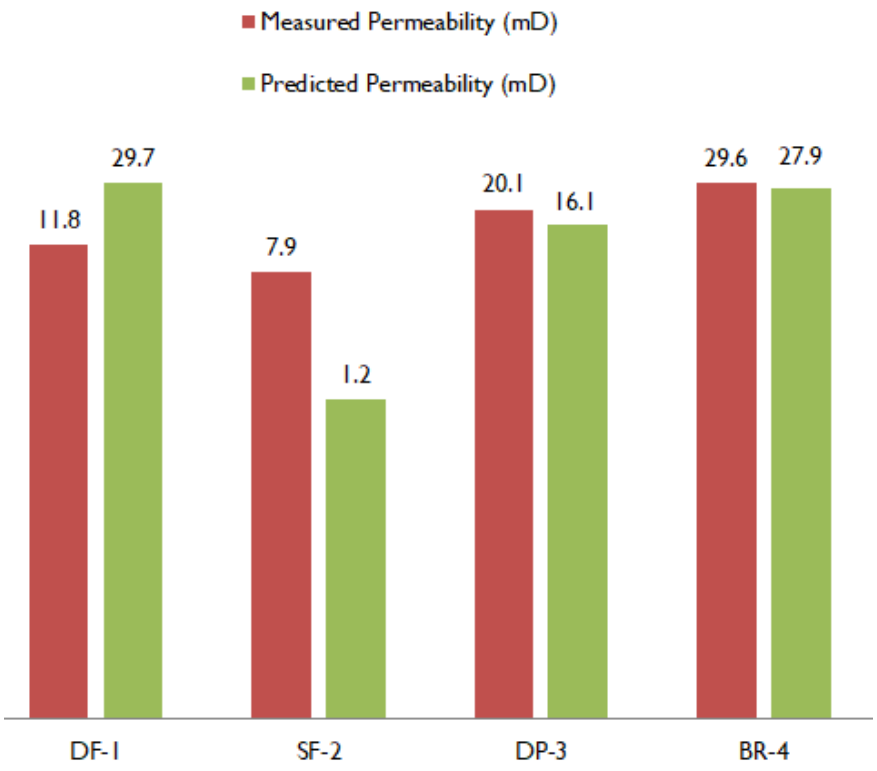

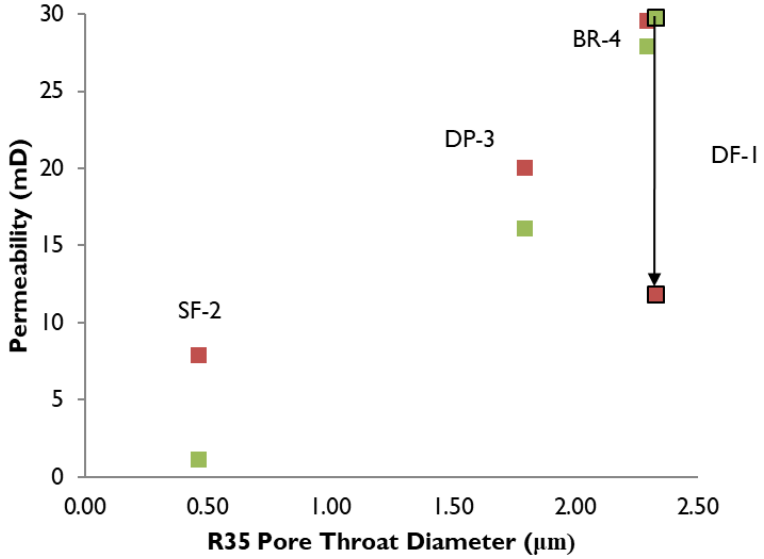

Figure 4-15[a] Comparison of laboratory measured permeability and predicted permeability from Equation 4.3, utilising the optimum pore throat diameter, R35. [b] Optimum pore throat diameter and permeability displayed a proportional relationship for a constant grain size, DF-1 sandstone exhibits an unexpectedly low measured permeability of 11.8 mD.

If a correct measure of optimum pore diameter, R_{35} should yield a strong correlation with measured and predicted permeabilities (Figure 4.15b). The predicted permeabilities exhibit a linear relationship with R_{35} for all four sandstones, DF-1, SF-2, DP-3 and BR-4, independent of the textural rock properties e.g. grain size and grain sorting. The slightly higher measured permeabilities can be attributed to flow contribution from sub-capillary pores. The measured permeabilities exhibit a linear relationship with R_{35} for the medium grained sandstones, SF-2. DP-3 and BR-4; the correlation between measured and predicted permeabilities improves as a function of better grain sorting. DF-1 is presented as an outlier with a much lower measured permeability of 11.8 mD; this is attributed to reduction in grain size which acts to reduce the optimum pore throat diameter for effective flow in a moderate-well sorted sandstone. This suggests for a grain size variable is required for accurate prediction of permeabilities within pore throat calculations.

4.8.2. **Sandstone Facies from Onshore and Offshore Reservoirs**

Hitchings and Chatellier (1987) undertook a geological investigation into the Eocene Mangahewa 'C' Sands and Kaimiro 'D' reservoirs in the offshore Maui A (Maui A1G and Maui 6) and Maui B (Maui 5 and 7) fields. They assessed core from four boreholes to develop a depositional model for the reservoir interval across the Maui Field. The 'C' and 'D' sands of the Mangahewa and Kaimiro Formations are characterized by a similar deltaic-coastal plain environment interpreted for the Pakawau sub-basin. The 'C' sands are representative of a lower delta plain environment, dominated by cross bedded channel sandstones and minor coastal bar features. The 'D' sands are representative of a non-marine upper delta plain environment, resulting in heterolithic sandstone channels between lake, swamp and over-bank deposits. Adopting a similar approach to our study, Hitchings and Chatellier (1987) determined average physical reservoir properties which were attributed to different sandstone facies composing the reservoir interval. Their aim was to establish if a relationship existed to predict permeability from porosity-derived logs.

Table 4-7 Average textural properties and pore characteristics from cross bedded and heterolithic sandstone facies within the 'C' and 'D' sands of the Maui Field (Hitchings and Chatellier, 1987)

Lithofacies	Depositional Setting	Porosity Fraction	Permeability (mD)	Mean Grain Size (μm)	Grain Sorting
Cross-bedded Sandstones (Sx)	Channel Complexes	0.17	174	335	6.16
Heterolithic Sandstones (Hl)	Crevasse Splays/ Overbank Deposits	0.17	33.9	161	6.19

General trends can be observed in the results from this study in Table 4.4 and from Hitchings and Chatellier (1987) in Table 4.7: Porosity fractions and mean grain size are relatively similar for the different facies, with only a small variation. However, there is stark difference in permeability across the different facies. This shows that high porosity does not necessarily translate to good reservoir quality. Both the Hl and Sx sandstones from the different regions have similar permeability magnitudes. For the Hl sandstone facies, an average in-situ field permeability of 37 mD in the Pakawau Sub-basin (Joyce, 2018) correlates closely with an average permeability of 34 mD from the Maui Field (Hitchings and Chatellier, 1987). For the Sx sandstone facies, an average in-situ field permeability of 227 mD in the Pakawau Sub-basin (Joyce, 2018) correlates closely with an average permeability of 174 mD from the Maui Field (Hitchings and Chatellier, 1987); In-situ field permeabilities measured by Joyce (2018) were conducted using the TinyPerm, In both instances, these averages fall within or near the ranges found in this study, 0.25-12.6 mD and 1.78-718 mD, respectively.

Detailed textural information such as grain sorting and size, or information regarding pore structure is rarely considered when assessing reservoir quality (Clelland et al., 1993). Hitchings and Chatellier (1987) demonstrated that statistically significant relationships were found to exist between porosity, permeability, grain size and grain

sorting. This is in agreement with our results, which suggest that any function used to determine permeability must consider both grain size and sorting as input parameters. Grain sorting provides the main indicator of dominant pore type e.g. intergranular versus micropores. Regardless of this, even the micropore-dominated sandstones demonstrated a modal pore throat diameter close to the optimum pore throat diameter for flow (R_{35}), thus exhibiting relatively high porosity fractions because pore throat diameter and porosity fraction exhibit a proportional relationship. Whereas the porosity fraction is independent of grain size, we find the permeability and R_{35} only demonstrate a proportional relationship across a constant grain size. Thus, the permeability range of sandstone facies will be more variable with a greater grain size variation.

4.9. Conclusions

A systematic approach to understanding the variation in physical properties across a reservoir requires recognition of the microscale heterogeneities within the different sedimentary facies (I-IV).

I. Grain sorting provides the dominant control on dominant pore type; pore throat diameter and porosity fraction exhibit a proportional relationship. If the modal pore throat diameter remains above the optimum pore throat diameter (R_{35}) for flow, this will correspond to a high porosity fraction.

II. Grain size is independent of the porosity fraction but can significantly affect permeability. For a constant grain size there is a proportional relationship between the optimum pore throat diameter and permeability.

III. Sandstone facies can be used as a first order assessment for the presence of reservoir heterogeneities which may control flow capabilities e.g. grain size and grain sorting. For example, low energy settings such as mudflats and floodplains are more prone to developing facies containing fine grained deposits e.g. CS and Hl.

IV. The application of facies used to quantify physical reservoir properties allows for comparable data between onshore reservoir analogues and offshore reservoirs. The highest permeabilities are attributed to the cross bedded sandstone facies both in the Pakawau Sub-basin and offshore Maui reservoirs.

Chapter Five – Physical and Mechanical Characteristics of Late-Cretaceous to Eocene Reservoir Rocks in the Maui, Maari and Manaia Fields

5.1. Introduction

Rock strength is an important input parameter utilized in geomechanical modelling, in particular used for understanding regional scale basin interactions and assessing reservoir stability (Chang et al., 2006) The compressive rock strength of an interval is a key component for understanding the geomechanical characterisation of a region. The unconfined compressive strength is utilized as an input parameter for in-situ stress field calculations, thus require accurate prediction. In drilling assessment, a linear poro-elasticity stress model in conjunction with a rock strength criterion is used to assess the strength of the rock and determine the optimum mud pressure to stabilise a wellbore (Gholami et al., 2013; Zhang et al., 2010). An enhanced knowledge of the compressive rock strength will help to address geomechanical problems such as borehole breakouts and sand production (Zhang, 1998).

The southern Taranaki Basin represents a region of extensive petroleum development in New Zealand, with many exploratory boreholes. Geomechanical studies previously undertaken in the Taranaki region are limited to wellbore stability by industry highlighting the need for increased laboratory testing to better constrain the rock strength across the basin (Shell Todd Oil Services Limited, 2001; Shell Todd Oil Services Limited, 2002; New Zealand Overseas Petroleum Limited, 2005; OMV New Zealand Limited, 1998-2006; Swift Energy, 2007a; Swift Energy, 2007b; Todd Energy, 2010). In agreement with this, there remains an absence of a geomechanical database for reference when considering wellbore design and drilling in the Taranaki basin. In cases where the availability of rock strength laboratory measurements is limited, rock

strength is often approximated using empirical relationships utilizing other physical properties e.g. compressional wave velocity and/or porosity (Fjaer et al.,1992; Moos et al., 1999; Chang et al., 2006). The most common parameters utilized in these empirical strength relations include porosity fraction (n) and compressional wave velocity (Vp)/ compressional slowness (DTC), (Chang et al., 2006). However, without calibration of the empirical strength relations to the local reservoirs, rock strength predictions are often poorly constrained and unreliable. In addition, empirical rock strength relations rarely consider petrographical properties such as grain size as input parameters (Ulusay et al., 1994; Atapour, 2018), despite grain size providing a dominant control on rock strength.

A physical property-rock strength relationship was developed for the southern Taranaki Basin reservoirs, utilizing two independent variables, porosity fraction and mean grain size, to predict the dependent variable, UCS. Validation of the empirical model was accomplished using existing petroleum report data. Strength envelopes were determined from triaxial data, categorise by grain size, for both the Mohr-Coulomb and Generalised Hoek-Brown Criteria and used to assess the in-situ stresses acting in the southern Taranaki Basin. Statistical analysis was used for quantitative assessment of derived empirical relations to provide a level of confidence for further extrapolation.

5.2. Geological Setting

5.2.1. Tectonic History

The Taranaki Basin is divided into two main structural components, the Western Stable Platform and the Eastern Mobile Belt (King et al., 1991, McBeath, 1977, Pilaar and Wakefield, 1978); separated by the Cape Egmont Fault (Figure 5.1). The Western Stable platform has remained undeformed since the Late Cretaceous, whilst the Eastern Mobile Belt has experienced significant Neogene Deformation (King and Thrasher, 1996, Nicol et al., 2007). The Late Cretaceous-Early Palaeocene strata reflect the onset and continuation of early basin rifting and thermal rift subsidence associated with the West Coast-Taranaki rift phase (Figure 5.2). Thick depo-centres associated with NE/SW

trending fault bound sub-basins controlled the rate of sedimentation of the Pakawau Group deposits (King and Thrasher, 1996, Thrasher, 1990, Thrasher, 1992).

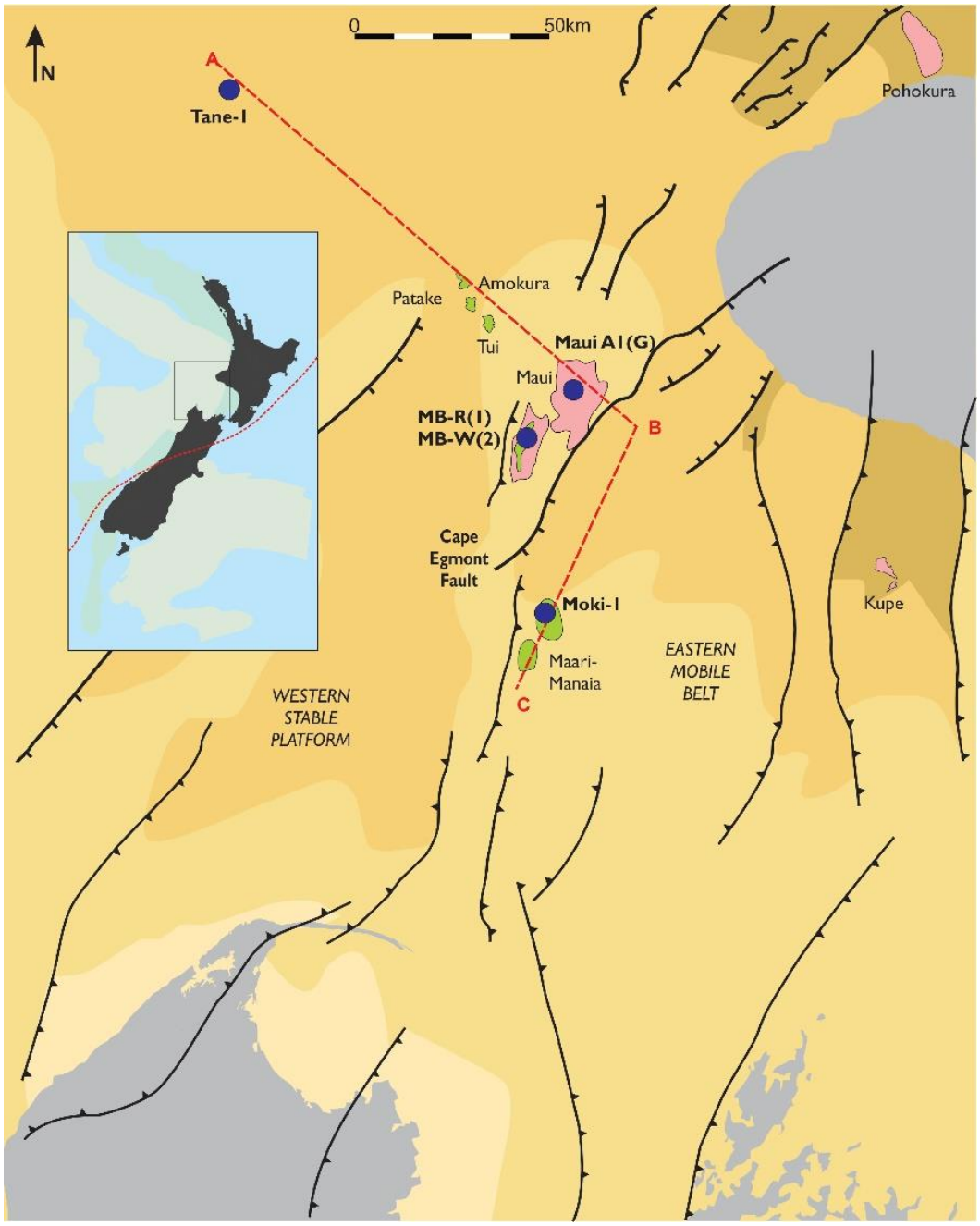

Figure 5-1 Regional map of southern Taranaki Basin with structural controlling faults separating the Western Stable Platform and Eastern Mobile Belt. Petroleum fields and wellbores referenced in text are indicated, and cross section line for Figure 5.3 (ABC') is delineated.

During the Palaeocene-Eocene, passive margin development was associated with the development of a NE-SW trending wide marine-influenced shoreline belt across the

central Taranaki Basin (King and Thrasher, 1996); sedimentation kept pace with passive margin subsidence with an intermittent regressive and transgressive movement of the Paleogene shoreline (Higgs, 2012). In the Late Eocene, a slow in subsidence rates resulted in a southwards transgression and marine inundation across the Central and Southern Taranaki Basin. early rift tectonics are later overprinted by Neogene convergent margin related tectonics (King and Thrasher, 1992).

5.2.1.1. Maui and Maari-Manaia Fields

The Maui and Maari-Manaia Fields contain large accumulations of hydrocarbon reserves and are significant producers in the Taranaki Basin. The Maui Field is bound by the western Whitiki Fault and the eastern Cape Egmont Fault. The geological structure consists of a dual crested low relief anticline with a spatial extent of 150km^2. Formed in response to Neogene compression, inversion along the Whitiki Fault during the Miocene resulted in the fault bent folding structure. Subsequent activation of normal movement along the Cape Egmont Fault from extension during the Middle Pliocene acted to enhance structure expression (King and Thrasher, 1996). The dual crested anticline delineates two regions, the north eastern gas bearing Maui A and south western gas and oil-bearing Maui B. The Maari-Manaia Field, positioned directly south of the Maui Field, is currently New Zealand's largest offshore oil field and covers an area of 80km^2. The Maari-Manaia Field is composed of two moderate anticlines with north south trending dip closures, termed the Maari and Manaia structures (New Zealand Petroleum Basins, 2014-5). The field is bound to the east by the Manaia Fault, and the Manaia anticlinal trap is associated with significant inversion lineament during the Miocene from Neogene shortening (King and Thrasher 1996).

5.2.2. **Stratigraphy**

The Late Cretaceous to Eocene offshore reservoirs are widely distributed across the Taranaki Basin (Figure 5.2). The Kapuni Group subdivides into the upper Mid-Eocene Mangahewa Formation, Early to Mid-Eocene Kaimiro Formation and lower Paleocene Farewell Formation. This strata is based upon deposition within a broadly defined NE-SW trending shoreline belt across the basin, following the paleo-shoreline of the Paleogene, superimposed on passive margin succession (Higgs, 2012, Higgs et al., 2017, Strogen, 2011); Strogen, 2011); this passive margin succession is observed within the Maari-Manaia and Maui Fields. Most of the petroleum reserves in the Taranaki Basin are constrained to this NE-SW trending fairway, which represents marginal marine-shallow marine sandstones and coastal plain sandstones (Higgs et al., 2017). The entire Kapuni Group succession from the Mangahewa 'C' sands to the Lower Farewell F' sands comprise of laterally equivalent sedimentation; the movement of the shoreline back and forth across the Maui area, and fluctuations in the rate and locus of sediment supply, have resulted in highly cyclic, intercalated coastal plain and shallow marine strata (New Zealand Petroleum Basins 2014/15). The Mangahewa 'C' sands consist of both non-marine and marine sediments, interpreted as deposits of a braid delta or delta plain (Chantellier and Hitching 1987). The upper interval of the 'C' sands is comprised of shoreface and tidal sandstones, with inner shelf shales consistent with propagation of braid plain into the marine environment (Bryant et al., 1994; Chantellier and Hitching 1987). The lower interval is represented by coastal plain sandstones and lagoonal mudstones consistent with a braid delta plain. The 'D' sands of the Kaimiro Formation consist of mostly nom-marine sediments deposited with an upper delta plain or fluvial estuarine environment (King and Thrasher, 1996). The 'C' sands and 'D' sand deposits have a high degree of lateral continuity (Chantellier and Hitching 1987). The 'F' sands of the Farewell Formation are considered significantly more homogenous than the overlying 'C' and 'D' sands. The 'F' Sands consist of stacked fining-upwards sequences interbedded with thin coal-shale intervals that are often extensive intra-formation seals (Bryant et al., 1994).

The uppermost unit of the Pakawau Group is the Late Cretaceous North Cape Formation. The North Cape Formation is comprised of shallow marine and coastal sandstones, and localised conglomerates and coal measures (Bal and Lewis, 1994, Browne, 2009, Strogen et al., 2017, Titheridge, 1977). The localised coal rich facies of the North Cape Formation are a known generating source rock for many producing fields in the Taranaki Basin (Sykes and Dow 2000; Sykes and Raine 2008).

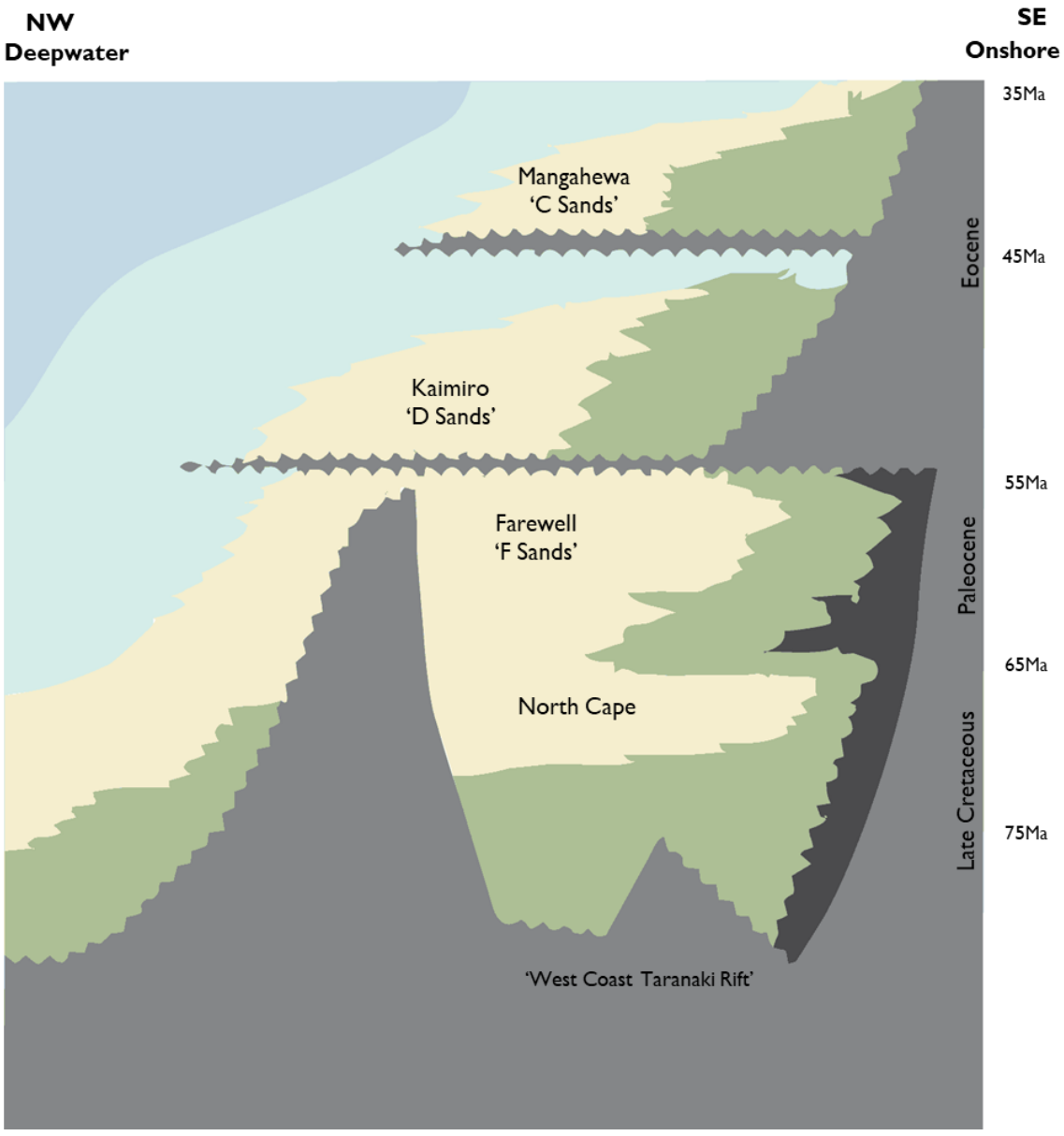

Figure 5-2 Generalized stratigraphy of the southern Taranaki Basin, with indication of gross depositional environment. The onset and continuation of the West Coast Taranaki Rift is denoted by the coal rich coastal plain and shallow marine sandstones of the Pakawau group. The marginal marine-shallow marine sandstones of the Kapuni Group contain most of the petroleum reserves in the Taranaki Basin (C, D and F sands).

5.3. Methods and Materials

This chapter presents quantitative geomechanical data from local reservoirs to better constrain rock strength parameters in order to refine predictive rock failure models for the Taranaki Basin. The samples were sourced from the Maui-Maari Fields of the southern Taranaki Basin, focussing on the Late Cretaceous-Eocene reservoir intervals for laboratory testing and analysis.

5.3.1. Sampled Reservoir Intervals

The North Cape Formation is a recognised potential reservoir, but despite weak-moderate oil shows in several wells there is no current production to date from the formation (Shell BP Todd Oil Services Ltd, 1982; Shell Todd Oil Services Ltd (STOS), 1992; New Zealand Overseas Petroleum Ltd, 2004). The Farewell Formation is recognised as an important producing reservoir interval and incorporates the better known 'F' sands of the Maui Field; oil and gas discoveries are found in the Maui, Tui, Amokura, Pateke and Kupe Fields (STOS Development Department, 1993a; STOS Development Department, 1993b; Stroud et al., 2004; Crowley et al., 1989; Martin. 1989). The Kaimiro Formation is a popular exploration target and is host for the gas-condensate reserves within the 'D' and 'E' shallow marine sands of the Maui Field. The Mangahewa Formation is also host for gas-condensate reserves within the 'C' sands of the Maui Field, with small accumulations in the Maari-Manaia and Pohokura Fields (Shell Todd Oil Services Limited, 2001; Halliburton Australia Pty Ltd, 1999; Koninklijke/Shell Exploratie. 1986; Chantellier and Hitchings. 1987).

Preliminary appraisal of scarce drill core available for subsampling exacerbated the level of apprehension against destructive strength testing. Due to the absence of an elementary rock property database, sample selection was approached in a systematic manner and incorporates four reservoir horizons, Mangahewa 'C' sands, Kaimiro 'D' sands. Farewell 'F' sands and the North Cape formation. Permission was granted from New Zealand Petroleum and Minerals (NZP&M) to sub-sample core plugs for destructive

strength testing from five petroleum wells: Moki-1, Maui-A1(G), MBW(2), MBR(2) and Tane-1 (Table 5.1). The position of the petroleum wells are predominantly focused in the Southern Taranaki Basin within the Maui and Maari-Manaia Fields, omitting Tane-1 positioned further northwest in the offshore Taranaki region (Figures 5.1 and 5.3). There are minimal well penetrations attributed to the North Cape Formation due to depths in excess of 3500m, thus limited core availability (Figure 5.3).

Table 5-1 Summary of sampled reservoir interval from each wellbore with associated depth range

Wellbore		Formation	Depth Range (m)	Reference
Moki-1		Mangahewa Formation	2134-2139	Tricentrol Exploration Overseas Ltd (1984)
Maui A1(G)		Mangahewa Formation	2771-2779	Shell BP Todd Oil Services Ltd (1979)
		Kaimiro Formation	3068-3078	Shell BP Todd Oil Services Ltd (1979)
Maui B	MBR (1)	Farewell Formation	3516-3524	STOS Development Department (1993a)
	MBW (2)	Farewell Formation	4124-4133	STOS Development Department (1993b)
Tane-1		North Cape Formation	3689-3694	Shell BP Todd Oil Services Ltd (1976)

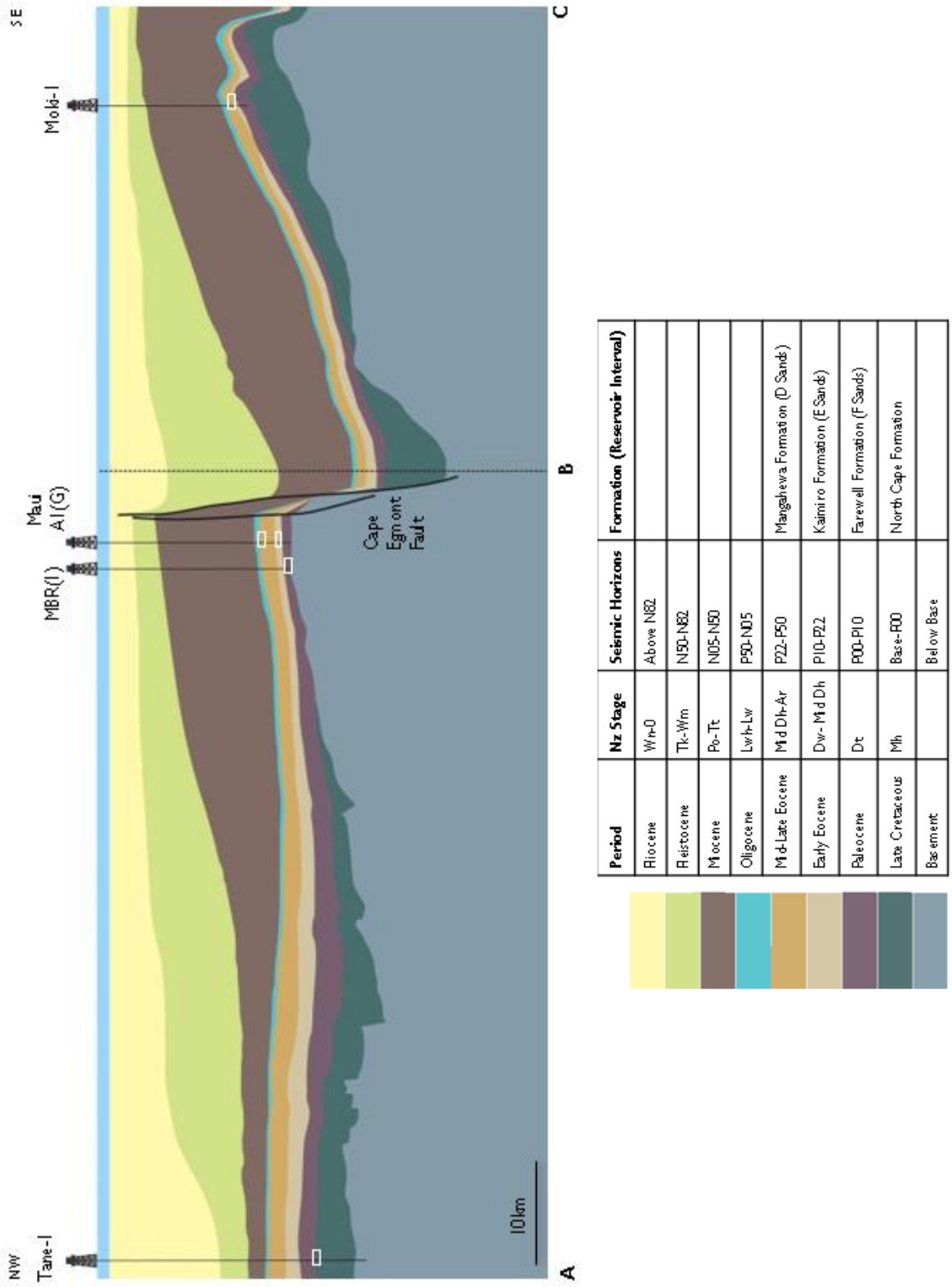

Figure 5-3 Cross section ABC as positioned in Figure 5.1. Transect developed from GNS PBE 3D Taranaki Map across study area exhibiting the spatial distribution of wellbores and sampled reservoir intervals. Chronostratigraphy is constrained based upon seismic horizons, with reference to equivalent formation.

5.3.2. **Non-Destructive Testing**

Core plugs were subsampled following the ASTM standard practice D4543-08 at the NZP&M Featherston Core Store, New Zealand. The 80 cylindrical cores, 25 mm in diameter, were sampled in two orientations were possible, vertical (following the borehole axis) and horizontal (perpendicular to the borehole axis). Core analysis was undertaken at the University of Canterbury's Rock Mechanics Laboratory. Prior to testing samples were oven-dried for at least 48 hours at 60°C. Sample dimensions and recorded masses were used to determine bulk density measurements (Ulusay and Hudson, 2007). Grain volume (V_s) measurements were undertaken using a AccuPyc II 134 nitrogen pycnometer (Micrometrics Instrument Corporation), which were used to calculate pore volume (V-V_s), then to calculate the porosity as the ratio of the pore volume to the bulk volume. Ultrasonic wave velocities were recorded using the GCTS ULT-100 Ultrasonic Velocity Measurement System under an applied load of 2000 N, in accordance with (Ulusay, 2014). Compressional wave velocities, Vp (m/s), were converted to imperial units (ft/s) and used to determine the compressional slowness, DTC, using Equation 5.1:

$$\mathrm{DTC} = \frac{1}{\mathrm{V_P}} \tag{5.1}$$

Where DTC (μs/ft) is the reciprocal of Vp

The wave velocities were used to determine the dynamic elastic moduli (GPa) of the rock. The calculations for these parameters are defined below in terms of density, sonic wave velocities V_p and V_s. and dry bulk density (kg/m^3). See Equation 5.2.

$$\mathrm{E} = \frac{\rho \mathrm{V_s^2}(3\mathrm{V_p^2} - 4\mathrm{V_s^2})}{\left(\mathrm{V_p^2} - \mathrm{V_s^2}\right)} \tag{5.2}$$

All quantifiable physical data attributed to this chapter can be found in Appendix G.

5.3.3. **Destructive Testing**

Of the original 80 drill core plugs used for non-destructive testing 45 were then used for destructive strength testing. The strength testing procedures followed guidelines from the ASTM standard D7012-14; this standard incorporates guidelines for unconfined compressive tests, triaxial compressive strength tests, and associated elastic moduli calculation from the two tests. For all test specimens, a length to width ratio 2:1 is desirable, however restrictions arose from the inability to drill core plugs of weaker material to a suitable length. For strength data acquired with a smaller ratio a considered approach with proper judgement is required before application.

Uniaxial Compressive Strength (UCS) tests were carried out using a 100 kN load frame (S178 Multi-Tester) commissioned by CMT Equipment, Australia. Experiments were run under a continuously applied axial load until rock failure, with a fixed axial strain rate of $1x10^{-5}$ s^{-1}. Real time data of axial load and deformation were collected using LabVIEW software. Due to limited material, all test specimens were non-conformable with a diameter under the suggested minimum sample diameter of 50 mm for UCS testing. Thus, a correction is applied to all UCS laboratory data, using the formula proposed by Hoek and Brown (1980), see section 3.3.6.2.

$$\sigma_{cd} = \sigma_{c50}\left(\frac{50}{d}\right)^{0.18} \tag{5.3}$$

Where,

σ_{cd} = measured UCS value (MPa)

d is the sample diameter (mm) and σ_{c50} is the corrected UCS value for an equivalent 50 mm diameter.

Deformation experiments were conducted under conventional triaxial conditions whereby $\sigma_1 > \sigma_2 = \sigma_3$. For triaxial tests, each specimen was placed in a rubber sleeve within a hoek cell, with top and bottom platens in contact with the specimen edge surfaces (Hoek and Franklin, 1967). A small amount of axial load was applied with the

100 kN S178 multitester to hold the platens in place, followed by a manually applied confining pressure via a hydraulic pump to secure the pressure vessel in place. For triaxial tests each specimen was hydrostatically loaded up to a selected confining pressure between 5 and 30 MPa ($\sigma_2 = \sigma_3$); the axial load (σ_1) was then continually applied at a fixed rate of $1x10^{-5}$ s^{-1} until the sample failed.

Due to sparse core availability from the wellbores there is an uneven distribution of test specimens attributed to each formation. The Mangahewa, Farewell and North Cape formations are better represented by UCS data and triaxial data points in terms of sample variation (>20 data points). The Kaimiro Formation is only attributed to 3 UCS and 2 triaxial data points; this is satisfactory to develop a failure criterion but is a poor representation of variation. This uneven sample distribution results in the use of formations as the basis for classifying strength profiles unreliable and biased. For this reason, classifications were conducted based upon physical characteristics. Grain size analysis was undertaken by a petrographic study on 44 thin sections and corroborated to existing petroleum reports. For each thin section a consistent method for grain size determination was taken whereby 100-120 grains were measured along the long axis; sample data is presented as a mean grain size (D).

5.3.4. **Empirical Strength Relationships**

Different physical parameters (porosity, mean grain size, compressional slowness and Youngs modulus) were plotted against the rock strength parameters to determine empirical strength relationships. Statistical analysis is undertaken on the empirical strength relationship to determine the ability for each physical parameter to act as a predictor for strength. A 'P' value was calculated for simple linear bivariate regression using the least square method; where 'P' is a probability factor that quantitatively assesses for the statistical significance of a linear correlation between two variables (Milton and Arnold, 1994). A null hypothesis states there is no relationship between the independent variable (x) and the dependent variable (y). The alternative hypothesis states that if there is a significant linear relationship between the independent variable and the dependent variable the linear regression slope is not equal to zero. A

small 'P' value (we use <0.05) suggests a statistically significant correlation and that the null hypothesis should be rejected, in support for an alternative hypothesis (Rawlings et al., 2001).

5.3.5. **Development of Failure Criteria**

An empirical failure criterion can be used to establish the strength of a rock in terms of the minor and major principal stresses σ_1 and σ_3. The Generalised Hoek-Brown criterion (Equation 5.4) uses a non-linear relationship and is defined by the major and minor principal stresses based upon the unconfined compressive strength of intact rock (σ_{ci}) and material constants (m_i) (Hoek and Brown, 2018). Both empirical fit parameters, which are unique to each lithology, are derived using the uniaxial and triaxial test data. Note that σ_{ci} is derived from empirical fitting to test data and is not the same as the mean UCS from laboratory testing, although the values should be similar.

$$\boldsymbol{\sigma_1 = \sigma_3 + \sigma_{ci}\left(m_i \frac{\sigma_3}{\sigma_{ci}} + 1\right)^{0.5}} \tag{5.4}$$

Many geo-engineering programs utilize the Mohr-Coulomb failure criterion for input parameters. The Mohr Coulomb failure criterion (5.5) imposes a linear relationship and is defined by an angle of internal friction (ϕ) and cohesion (C).

$$\sigma_1 = \frac{2C\cos\phi}{1-\sin\phi} + \frac{1+\sin\phi}{1-\sin\phi}\sigma_3 \tag{5.5}$$

RocData (RocScience 2019) was used to employ a regression of the triaxial data to derive the Hoek-Brown and Mohr-Coulomb parameters. The regressions for Hoek-Brown and Mohr-Coulomb can also be completed manually; for the Hoek-Brown parameters, the following equations (5.6 and 5.7) are used (Hoek and Brown, 1997):

$$\boldsymbol{\sigma_{ci}} = \sqrt{\frac{\sum \mathbf{y}}{\mathbf{n}} - \left[\frac{\sum \mathbf{xy} - \left(\frac{\sum \mathbf{x} \sum \mathbf{y}}{\mathbf{n}}\right)}{\sum \mathbf{x^2} - \left(\frac{(\sum \mathbf{x})^2}{\mathbf{n}}\right)}\right] \frac{\sum \mathbf{x}}{\mathbf{n}}} \quad (5.6)$$

$$m_i = \frac{1}{\sigma_{ci}} - \left[\frac{\sum xy - \left(\frac{\sum x \sum y}{n}\right)}{\sum x^2 - \left(\frac{(\sum x)^2}{n}\right)}\right] \quad (5.7)$$

Where $x = \sigma_3$, $y = (\sigma_1 - \sigma_3)^2$, and n is the number of triaxial tests. Note that Equation 5.6 is based on the worked example, not Equation B2, in Hoek and Brown (1997).

To determine the Mohr-Coulomb parameters the triaxial data were plotted in radius space (Labuz and Zang, 2012), where the x axis is representative of mean normal stress $(\sigma_m) = (\sigma_1 + \sigma_3)/2$, and the y axis is the maximum shear stress $(\tau_m) = (\sigma_1 - \sigma_3)/2$ such that a linear fit through the data points will give two fitting parameters, e and f such that: $\tau_m = \sigma_m m + s$. The Mohr-Coulomb failure criterion expressed in radius space as $\tau_m = \sigma_m \sin\phi + c\cos\phi$ and the parameters 'e' and 'f' are used to solve for internal friction angle, ϕ, and cohesion, c, using Equations 5.8 and 5.9:

$$\boldsymbol{\phi} = \mathbf{sin^{-1}\, e} \quad (5.8)$$

$$C = \frac{f}{\cos\phi} \quad (5.9)$$

5.4. Experimental Results

5.4.1. Physical and Uniaxial Compressive Strength Measurements

The UCS values range from 9-67MPa, porosity fractions fall between 0.05-0.24, compressional slowness varies from 75-150 μs/ft and Young's moduli between 7.9-28.8GPa (Table 5.2). Mean grain size (D) varies from 55 to 363 μm (Table 5.2), representative of coarse-grained silts to medium grained sands (Folk, 1963). Where experiments were conducted on vertical and horizontal samples for the same interval, the ratio of vertical to horizontal strength was found to range from 0.56 to 2.6, with one outlying ratio of 5, showing no systematic anisotropy. The UCS shows a general negative correlation with increasing porosity fraction (Figure 5.4a), increasing compressional slowness (Figure 5.4b) and increasing mean grain size (Figure 5.4c); a general positive correlation between UCS and increasing Young's modulus (Figure 5.4d).

The linear relationship for porosity fraction-UCS has a 'P' value of 3.92×10^{-5}, the linear relationship for Compressional slowness-UCS series has a 'P' value of 0.196, the linear relationship for mean grain size-UCS series has a 'P' value of 4.42×10^{-6} and the linear relationship for Young's Modulus-UCS series has a 'P' value of 0.370. The small 'P' value attributed to the porosity fraction-UCS and mean grain size-UCS series provides strong support for correlation. The higher 'P' value attributed to the Compressional slowness-UCS series and Young's Modulus-UCS is above the 0.05 threshold, making the test inconclusive. For this reason, the porosity fraction-UCS data and mean grain size-UCS series provide the strongest empirical relations for our data set.

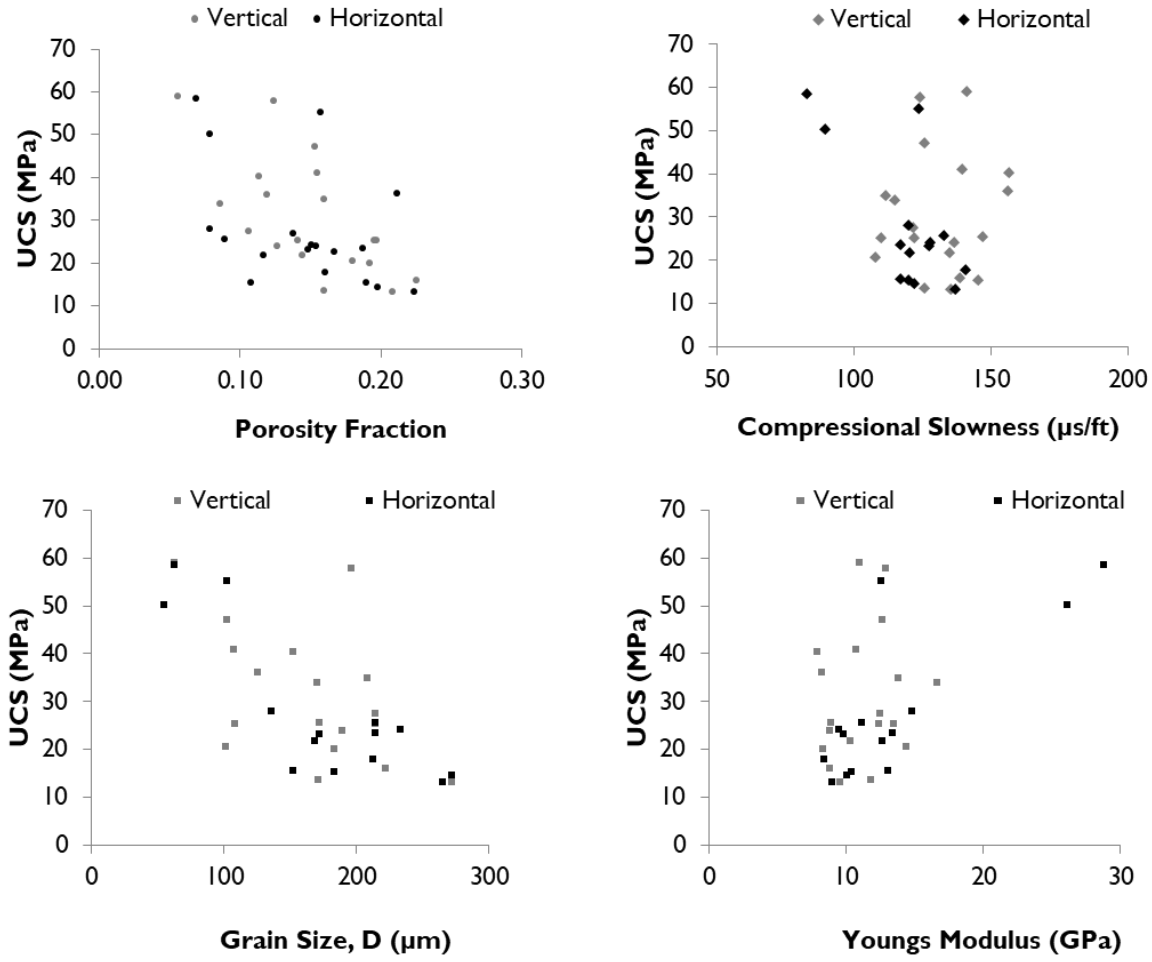

Figure 5-4 Physical property-UCS data series, a) porosity fraction-UCS; b) compressional slowness-UCS; c) mean grain size-UCS; d) Young's modulus-UCS.

Table 5-2 Summary of physical rock properties and uniaxial compressive strength tests for each test specimen

	Depth (m)	Formation	Core plug direction	Mean Grain Size D (μm)	Porosity Fraction n	Vp Dry (m/s)	Compressional Slowness DTC (μs/ft)	Young's Modulus (GPa)	Corrected UCS σ_{c50} (MPa)
MK1-B14	2138.5	Mangahewa	h2	136	0.08	2543	119.86	14.8	27.90
MK1-B13	2137.4	Mangahewa	v	189	0.13	2231	136.62	8.8	23.91
MK1-B12	2136.4	Mangahewa	v	169	0.14	2258	134.99	10.4	21.68
MK1-B12	2136.4	Mangahewa	h1	169	0.12	2528	120.57	12.7	21.69
MK1-B11	2135.6	Mangahewa	h1	213	0.16	2165	140.79	8.5	17.77
MK1-B10	2134.3	Mangahewa	v	215	0.11	2506	121.63	12.5	27.38
MK1-B10	2134.6	Mangahewa	h2	215	0.09	2296	132.75	11.2	25.52
A1G-B10B	2777.9	Mangahewa	v	209	0.16	2734	111.49	9.5	34.83
A1G-B10B	2777.9	Mangahewa	h2	209	0.15	2845	107.14	9.6	23.95
A1G-B10A	2776.7	Mangahewa	v	172	0.16	2420	125.95	10.1	13.47
A1G-B10A	2776.7	Mangahewa	h1	172	0.17	2737	111.36	10.8	22.48
A1G-B7	2774.0	Mangahewa	v	109	0.20	2498	122.02	12.7	25.17
A1G-B6B	2771.3	Mangahewa	v	101	0.18	2824	107.93	12.6	20.48
A1G-B6B	2771.3	Mangahewa	h1	101	0.21	2614	116.6	8.8	36.20
A1G-B2	3069.7	Kaimiro	v	171	0.09	2653	114.89	9.0	33.82
A1G-B1	3068.5	Kaimiro	v	197	0.12	2457	124.05	13.5	57.76
A1G-B1	3068.5	Kaimiro	h1	197	0.14	2912	104.67	13.4	26.94
MBR-B2	3516.9	Farewell	h1	233	0.15	2381	128.01	8.4	24.13
MBR-B7	3521.8	Farewell	v	272	0.21	2249	135.53	10.5	13.17
MBR-B7	3521.8	Farewell	h1	272	0.20	2498	122.02	8.9	14.44
MBR-B8	3522.8	Farewell	v	108	0.15	2183	139.62	9.8	40.91
MBR-B9	3523.4	Farewell	v	102	0.15	2420	125.95	8.2	47.05
MBR-B9	3523.4	Farewell	h1	102	0.16	2460	123.9	7.9	55.11
MBW-B16	4132.5	Farewell	v	222	0.23	2195	138.86	13.1	15.88
MBW-B14	4130.4	Farewell	h1	265	0.22	2226	136.93	11.0	13.17
MBW-B12	4128.1	Farewell	v	215	0.20	2773	109.92	28.8	25.18
MBW-B12	4128.1	Farewell	h1	215	0.19	2606	116.96	26.2	23.45
MBW-B8	4124.7	Farewell	v	183	0.19	2099	145.21	13.9	20.01
MBW-B8	4124.7	Farewell	h2	183	0.19	2541	119.95	16.0	15.27
T1-B5	3693.7	North Cape	v	173	0.14	2075	146.89	11.8	25.39
T1-B5	3693.7	North Cape	h1	173	0.15	2390	127.53	12.4	23.20
T1-B4A	3692.4	North Cape	v	126	0.12	1950	156.31	12.4	35.98
T1-B4B	3692.0	North Cape	v	152	0.11	1944	156.79	14.4	40.23
T1-B4B	3692.0	North Cape	h1	152	0.11	2606	116.96	8.9	15.44
T1-B3	3689.9	North Cape	v	63	0.06	2160	141.11	16.7	58.89
T1-B3	3689.9	North Cape	h1	63	0.07	3683	82.759	12.9	58.43
T1-B2	3689.2	North Cape	h2	55	0.08	3409	89.41	16.1	50.23

5.4.2. **Triaxial Experiments**

Triaxial experimental data is summarised in Table 5.3. The increase of confining pressure results in an increase of axial stress required to cause rock failure, as observed in previous studies of triaxial deformation of sandstone (e.g., Wong et al., 1997; Baud et al., 2000; Bésuelle et al., 2003; Heap et al., 2019).

Table 5-3 Summary of triaxial data

Sample Code	Depth (m)	Formation	Core plug direction	Maximum Principal (Axial) Stress (σ_1)	Minimum Principal (confining) stress ($\sigma_2 = \sigma_3$)	Mean Grain Size D (μm)	Porosity Fraction n
MK1-B11	2135.6	Mangahewa	h2	101	15	213	0.15
MK1-B12	2136.4	Mangahewa	h2	75	5	169	0.13
MBR-B2	3516.9	Farewell	h2	128	15	233	0.17
MBR-B7	3521.8	Farewell	h2	67	5	272	0.19
MBR-B8	3522.8	Farewell	h1	139	20	108	0.15
MBR-B9	3523.4	Farewell	h2	134	10	102	0.13
MBW-B8	4124.7	Farewell	h1	93	10	183	0.20
MBW-B14	4130.4	Farewell	h2	57	5	265	0.22
MBW-B16	4132.5	Farewell	h2	68	7	222	0.24
T1-B4A	3692.4	North Cape	h1	114	15	126	0.12
T1-B4B	3692.0	North Cape	h2	134	20	152	0.10
T1-B3	3689.9	North Cape	h2	115	10	63	0.09
T1-B2	3689.2	North Cape	h1	147	25	55	0.08

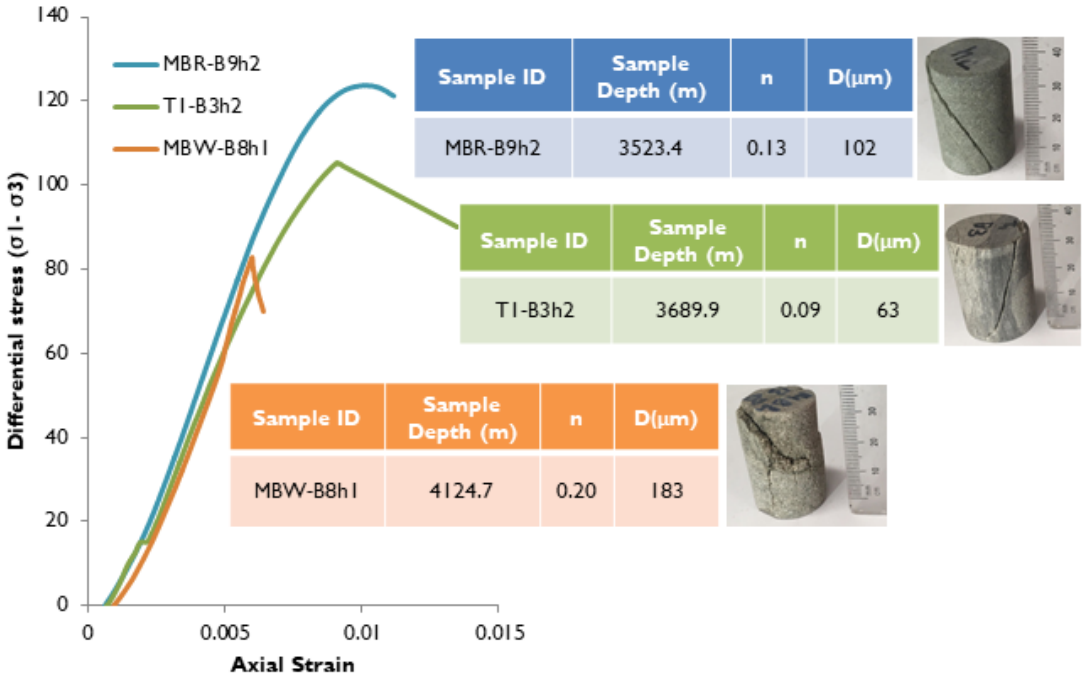

Figure 5-5 Differential stress versus axial strain curves for different rock types under a confining stress of 10 MPa, exhibiting different modes of yield

Figure 5.5 compares differential stress versus axial strain curves for different sandstones from the MBR(1), MBW(2), and Tane 1 at a confining pressure of 10MPa (~0.5 UCS). The stress-strain curves exhibit similar initial linear trends but different yield shapes; MBW-B8h2 and T1-B3h2 display more abrupt failures, yielding behaviour that is indicative of dilatant microcracking dominant deformation (Heap et al., 2015; Siratovich et al., 2016). MBR-B9h2 exhibits a more gradual yielding behaviour that is indicative of mixed dilatant microcracking and compaction deformation (Heap et al., 2015; Siratovich et al., 2016). The brittle deformation displayed in MBW-B8h2, MBR-B9h2 and T1-B3h2 is by a defined plane of failure along a shear fracture inclined approximately 60˚. This suggests there is no implication for variance in either grain size or porosity on the deformational behaviour of rock under a low compression.

5.4.3. **Failure Criteria**

The triaxial data are plotted in two different stress spaces to derive the Hoek-Brown failure criterion parameters (Figure 5.6a) and the Mohr Coulomb failure criterion parameters (Figure 5.6b), while the resulting parameters are given in Table 5.4. These results are in agreement with Robertson (1970), that whilst recognising considerable variation, the cohesion is between 16-27% of the average UCS value.

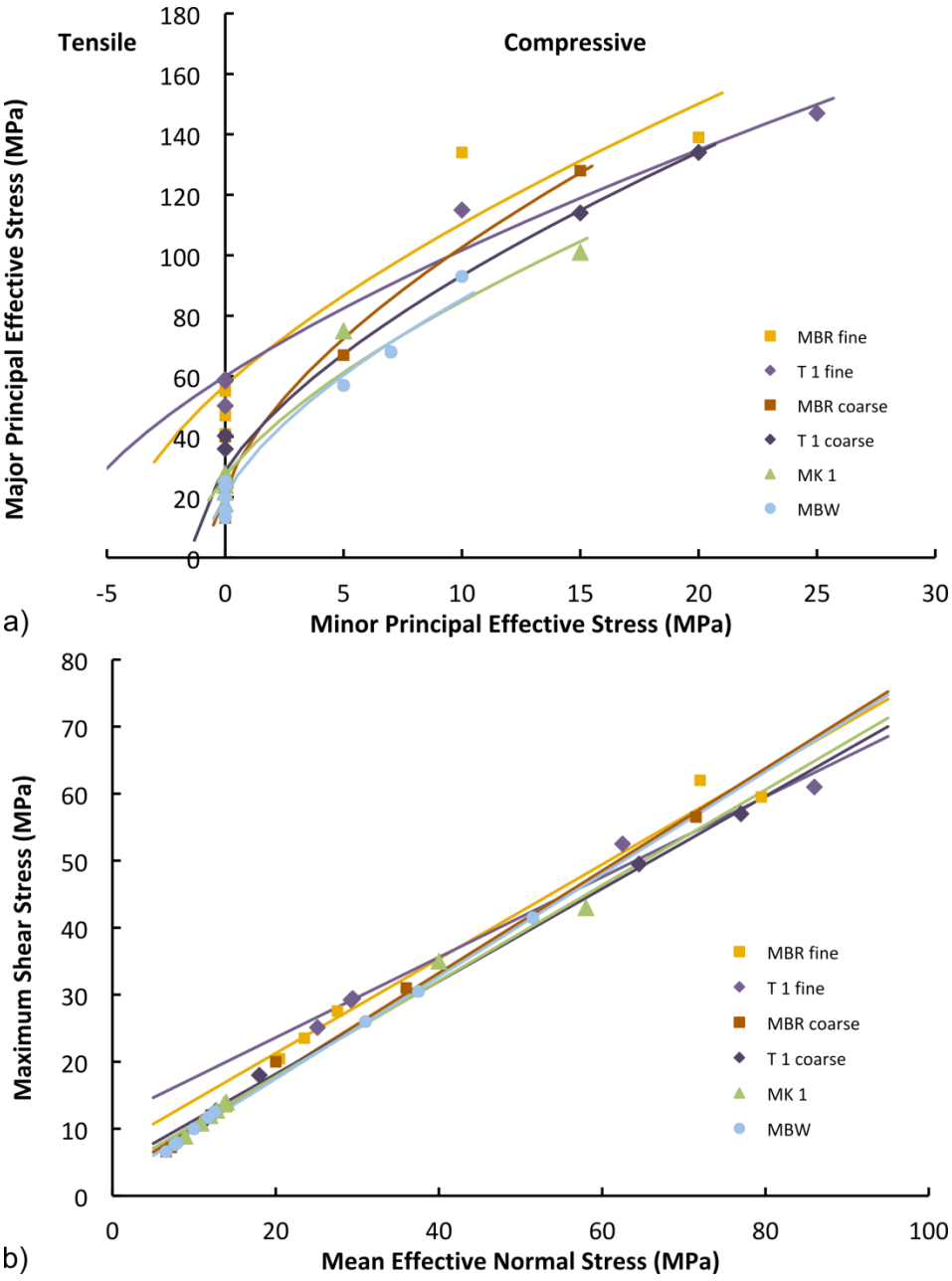

Figure 5-6 All triaxial test series plotted in a) principal stress space to derive the Hoek-Brown failure criteria; b) radius stress space to derive the Mohr-Coulomb failure criteria according to Labuz and Zang (2012).

Table 5-4 Failure criterion parameters for reservoir intervals

Well	Depth Interval	Mean Grain Size (μm)	Porosity Fraction	UCS range (MPa)	Number		Hoek Brown			Mohr Coulomb	
					UCS	Triaxial	σ_{ci} (MPa)	m_i	Normalised m_i (m_{in})	C (MPa)	Ø
Tane-1	3692.0-3693.7	126-173	0.11-0.15	15.4-40.2	5	2	29	21	0.7	6	44
Tane-1	3689.2-3689.9	55-63	0.06-0.09	50.2-58.9	3	2	60	8	0.1	15	36
Moki-1	2134.6-2138.5	136-215	0.08-0.16	17.7-27.9	7	2	27	18	0.7	5	44
MBW(2)	4124.7-4132.5	183-265	0.19-0.24	13.2-25.2	6	3	17	34	2.0	3	49
MBR (1)	3516.9-3521.8	233-272	0.15-0.21	13.2-24.1	3	2	23	35	1.5	5	49
MBR (1)	3522.8-3523.4	102-108	0.13-0.16	40.9-55.1	3	2	57	12	0.2	12	42

For the MBR interval (porosity fraction 0.13-0.21) the two grain size fractions: silts-very fine sand (102-108 μm) and fine-medium sand (233-272 μm) demonstrate that the finer samples have higher strength than the coarser samples (Figure 5.6). This is further demonstrated in Figure 5.7 where grain size for samples with porosity fraction ranging from 0.12-0.21 is compared to the two Hoek-Brown failure criterion parameters and the two Mohr-Coulomb failure parameters. The m_i and ϕ (which describe the curvature and slope of the failure criteria, respectively) increase with increasing grain size (Figure 5.7a), while σ_{ci} and cohesion (which describe the low-confinement strength components of the failure criteria) decrease with increasing grain size (Figure 5.7b). Our dataset did not contain a series with similar grain size and varying porosity fraction, however, and no relationships could be observed between porosity fraction and the Hoek-Brown criterion parameters σ_{ci} and m_i, nor the Mohr-Coulomb parameters, c and ϕ.

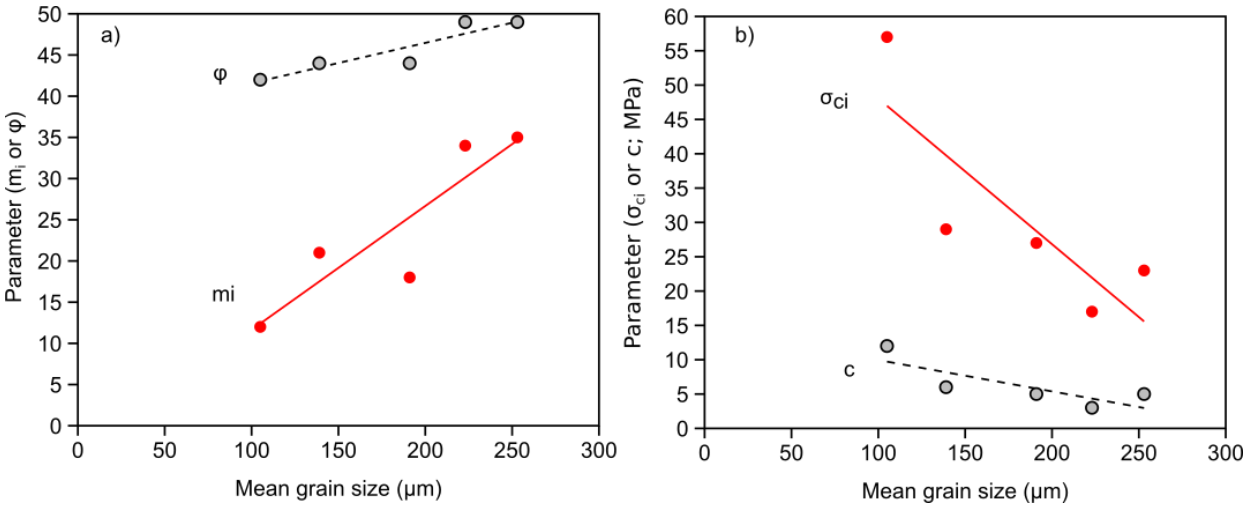

Figure 5-7 Hoek-Brown and Mohr-Coulomb failure criterion parameters for samples with porosity fraction 0.12-0.21 plotted according to a) curve parameters (ϕ and m_i); and b) strength parameters (c and σ_{ci}).

5.5. Discussion

5.5.1. Empirical Strength Relationships derived for Sandstone Reservoirs

The use of empirical relations utilizing more than one independent variable for sandstone rock strength prediction is infrequent (Fjaer et al.,1992; Moos et al., 1999; (Chang et al., 2006)); particularly with the incorporation of petrographical property parameters (Ulusay et al., 1994; Atapour, 2018). Our results indicate porosity provides a strong control on UCS (Figure 5.4b); however, a strong control on rock strength is also attributed to mean grain size (Figures 5.4c and 5.7).

Most studies agree that porosity and UCS exhibit an inverse relationship (Bell, 1978; Vernik, 1993; Ulusay, 1994). Previously proposed porosity-UCS relationships have utilized linear, logarithmic, power, exponential and second order polynomial laws (Vernik et al., 1993; Palchik, 1999; Chang et al., 2006; Reyer and Philipp, 2014). Localised calibration through laboratory testing manipulates the correlation coefficients in the regressions to increase the accuracy to better fit the data series. Data from this study suggest that the porosity-UCS series could be defined by multiple regression types,

all displaying similar regression coefficients (R^2), in accordance with Palchik (1999) and Atapour et al. (2018). Most published findings use an exponential fit, however, and we have adopted a similar fit, calibrated to our data (Figure 8a; Equation 5.10).

$$\mathbf{UCS = 108e^{-10n}} \tag{5.10}$$

This formulation uses the formulation for the exponent given in Chang et al. (2006) and follows the general form for the porosity-UCS relationship used in many other studies on sandstones (Reyer and Philipp, 2014; Atapour et al., 2018). A linear version of the fit was used in order to simplify for multivariate linear regression and test for goodness of fit, as follows: UCS = 108i, where $i = e^{(-10n)}$, e is the natural logarithm and n is the porosity as a decimal, not a percentage. Using linear regression of the linear version results in an r^2 value of 0.34 with a 'P' value of 1.557×10^{-4}, showing that the correlation is valid, but with considerable scatter (Figure 5.8b).

The role of mean grain size affecting rock strength is a disputed subject, with researchers reporting conflicting results. Previous investigations on low porosity rocks e.g. limestone and marble, have implied rock strength is inversely related to grain size, with a good linear correlation between UCS and the inverse square root of mean grain size (Fredrich et al., 1990; Wong et al.,1996). Studies focused on sandstones have demonstrated a weak correlation between mean grain size and UCS (Shakoor and Bonelli, 1991; Palchik, 1999; Atapour et al., 2018). Our results exhibit an inverse relationship between mean grain size and UCS, defined as a function of inverse square root mean grain size in accordance with Fredrich et al. (1990) and Wong et al. (1996) (Figure 5.8c; Equation 5.11).

$$\mathrm{UCS} = 366\left(\frac{1}{\sqrt{\mathrm{D}}}\right) \tag{5.11}$$

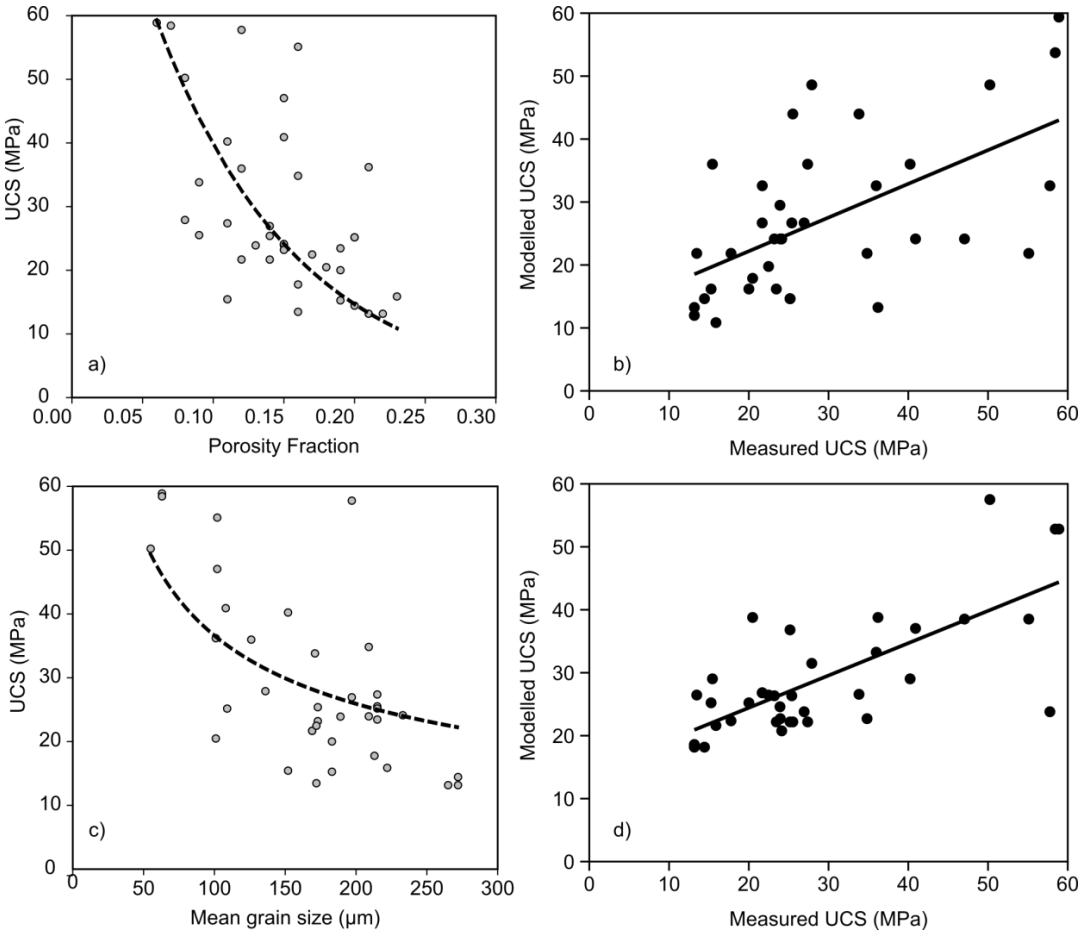

Figure 5-8 Plots for a) porosity-UCS model; b) porosity-UCS model prediction performance; c) mean grain size-UCS model; d) mean grain size-UCS model prediction performance

To enable a linear regression and goodness of fit tests, UCS is linearized as UCS = 366j where $j = D^{-0.5}$. In this formulation, the r^2 value is 0.51 and the 'P' value is 6.14×10^{-7}, which similarly to the porosity-UCS function is statistically valid, but with some scatter (Figure 5.8d). The discrepancies between different studies suggest grain size alone is not a suitable indicator of compressive strength in sandstone. Atapour et al. (2018) suggests higher porosity reduces the influence of grain size on UCS.

Formulating an empirical relation for UCS prediction requires a best fit regression attributed to both the porosity fraction-UCS and mean grain size-UCS data series. In order to obtain a stronger empirical formula, a multivariate regression was undertaken, which requires the input parameters to be considered independent variables. Theoretically porosity is independent of grain size, and it is the role of

alternative petrographical properties that control the availability of pore space e.g. grain sorting, grain shape/packing and the degree of cementation (Bell, 1978; Shakoor and Bonelli, 1991); however, several studies have found this is not the case with a tendency for porosity to increase with mean grain size (Ulusay et al., 1994). The linear relationship of porosity fraction and mean grain size is attributed an r^2 value of 0.22 with a 'P' value of 0.003, which is smaller than the 0.05 threshold suggesting a statistically significant correlation between the two variables. This is a much weaker relationship and for the purpose of the analysis the two parameters are considered independent variables. Figure 5.9 exhibits the spatial distribution of data points from the porosity fraction-mean grain size-UCS data series in xyz space. In practical terms, direct measurements of both porosity and grain size are straightforward and achievable. For the purpose of a multivariate linear regression, UCS is expressed as a function of porosity fraction and inverse square root mean grain size, with fitting parameters calibrated to the dataset presented herein. Regression coefficients calibrated to the dataset were determined using multiple linear regression analysis in SPSS.

$$\mathrm{UCS} = 430\left(\frac{1}{\sqrt{\mathrm{D}}}\right) - 90\mathrm{n} + 7 \tag{5.12}$$

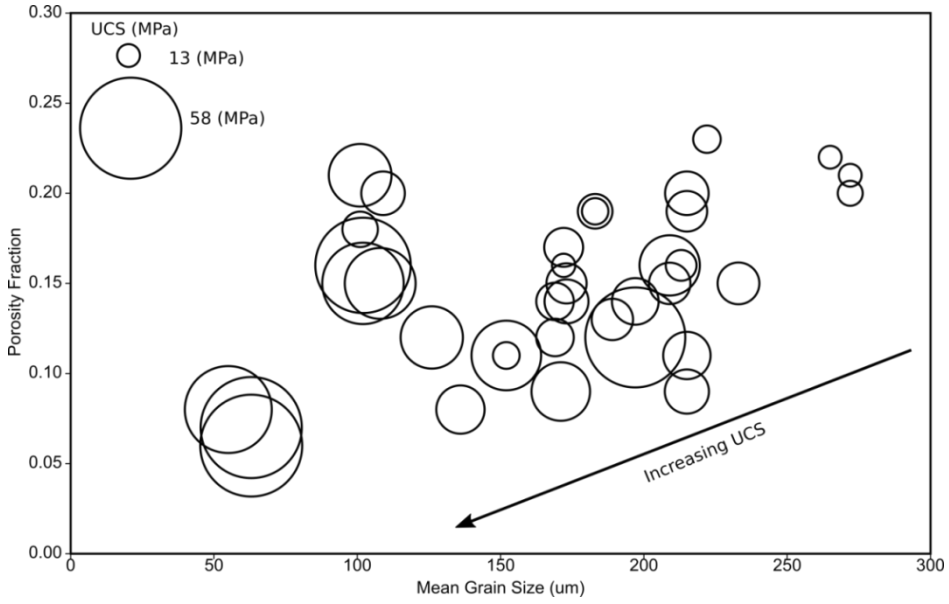

Figure 5-9 3D spatial distribution of the multivariate relationship between independent variables porosity fraction and mean grain size, and dependent variable UCS

To provide an overall measure of how well the model proposed in Equation 5.12 fits the data, laboratory measured UCS and corresponding predicted UCS are compared in Figure 5.10. The first data series represents the laboratory measured and predicted UCS values from our data set; this is defined by a linear relationship with an r^2 value of 0.58 with a 'P' value of 4.92×10^{-8} providing confidence in the model.

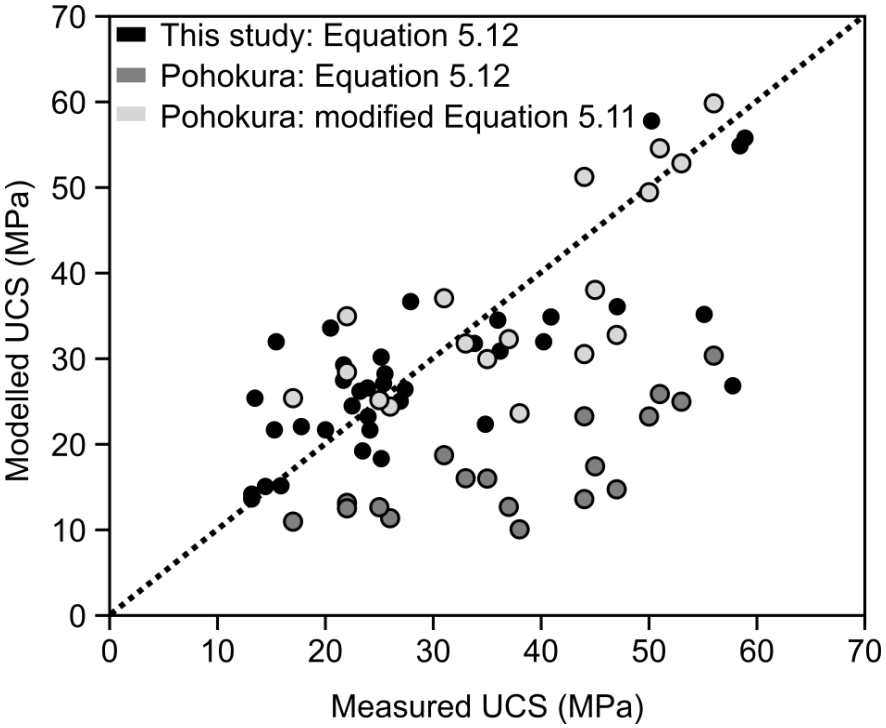

Figure 5-10 Comparison of measured to modelled UCS for the training data in this study using Equation 5.12 and the test data from Pohokura using Equation 5.12 and modified Equation 5.11 using fitting parameters 666.42 and +8.4. Dashed line represents the 1:1 line

In order to assess the validity of the model, existing UCS data was acquired from petroleum reports of the Eocene sands from the Pohokura Field (Shell Todd Oil Services Limited, 2002); in the north eastern Taranaki Basin (Figure 5. 1). The test data are summarised in Table 5.5 including mean grain size, porosity fraction and laboratory measured UCS. The modelled UCS compared to the measured UCS exhibits a r^2 value of 0.37 with a 'P' value of 6.4×10^{-4} (Figure 5.10) and underestimates UCS; this could be due to the narrow range of porosity, such that grain size has a much stronger impact ('P' value of 7.1×10^{-4}) on strength than porosity ('P' value of 0.87). The relationship with grain size for the Pohokura dataset is also different from Equation 5.11, where the fitting

parameters are 666.42 and +8.4. Despite the disparate location of reservoir samples, this suggests the calibration of correlation coefficients to Taranaki reservoirs in this study, can provide a first estimate of strength for other reservoir intervals, however local calibration will provide more robust relationships.

Table 5-5 Physical and geomechanical properties used for strength prediction of Pohokura-1 and Pohokura-2 (Martin, 200; Shell Todd Oil Services Limited, 2001; Shell Todd Oil Services Limited, 2002)

Wellbore	Depth (m)	Formation	Sample Code	Core Plug Direction	Mean Grain Size (μm)	Porosity Fraction n	Laboratory UCS (MPa)
Pohokura-1	3528.3	Maui	U01	Horizontal	660	0.10	47
Pohokura-1	3546.8	Maui	U02	Horizontal	198	0.08	56
Pohokura-2	3576.8	Maui	U04	Horizontal	680	0.12	37
Pohokura-2	3577.4	Maui	U05	Horizontal	760	0.10	44
Pohokura-2	3578.5	Maui	U06	Horizontal	580	0.13	22
Pohokura-2	3579.7	Maui	U07	Horizontal	877	0.10	22
Pohokura-2	3581.2	Maui	U08	Horizontal	790	0.07	35
Pohokura-2	3582.6	Maui	U09	Horizontal	516	0.08	31
Pohokura-2	3591.5	Maui	U10	Horizontal	1190	0.09	26
Pohokura-2	3591.9	Maui	U11	Horizontal	1270	0.10	38
Pohokura-2	3593.1	Maui	U12	Horizontal	1120	0.08	25
Pohokura-2	3595.4	Maui	U13	Horizontal	1100	0.10	17
Pohokura-2	3613.5	Maui	U15	Horizontal	490	0.10	45
Pohokura-2	3617.6	Maui	U16	Horizontal	702	0.08	33
Pohokura-2	3617.9	Maui	U17	Horizontal	290	0.10	50
Pohokura-2	3623.3	Maui	U18	Horizontal	254	0.10	53
Pohokura-2	3624.2	Maui	U19	Horizontal	238	0.10	51
Pohokura-2	3629.1	Maui	U20	Horizontal	270	0.11	44

5.5.2. **Failure Criteria**

Failure criteria can be used to predict the state stress that results in rock failure, presented as a function of normal (σ) and shear stress (τ), or the minimum (σ_1) and maximum (σ_3) principal stresses. The Mohr-Coulomb and Hoek Brown failure criteria are plane stress failure criteria and ignore the effect of the intermediate principal stress (σ_2) (Zoback, 2007). The Mohr-Coulomb criterion is commonly favoured in reservoir geomechanical application due its simplicity as an effective linear prediction tool, expressed in terms of a constant value of cohesion (C) and friction angle (ϕ). The Hoek-Brown failure criterion is a commonly used criterion for rock geotechnics, particularly for slope stability analysis and tunnelling, though its application in reservoir geomechanics is not as extensive. Each failure criterion has advantages and disadvantages in their applications. A practical disadvantage of the Hoek-Brown criterion is the absence of published literature relating the material constant, m_i, to commonly measured physical properties from geophysical logs (Zoback, 2007); an advantageous factor is the ability to incorporate rock mass properties into the failure criterion (Hoek and Brown, 2018) with material constants that vary by lithotype for rock mass characterisation of reservoirs (e.g. Villeneuve et al., 2018; Heap et al., 2019).
Failure criteria assume isotropic conditions in order to function. In general, sandstones are classified as isotropic or low anisotropy rocks (Ramamurthy 1933), regardless of internal structure. Although triaxial experiments were undertaken on samples orientated perpendicular to the wellbore axis (horizontal), the UCS series incorporated core plugs orientated both parallel (vertical) and perpendicular (horizontal) and show no strength anisotropy on the laboratory scale.

The values for m_i span from 8 to 35 (Table 5.3), which is much wider than the 17+/- 4 proposed by Hoek and Marinos (2000), but similar to the range given in Douglas (2002) and Sabatakakis et al. (2018). Given the wide range of m_i values, rather than proposing a range for the sandstones in the Taranaki Basin, the approach developed by Shen and Karakus (2014) to define m_i based on UCS was explored for this dataset. The m_{in} (normalized $m_i = m_i/\sigma_{ci}$) is plotted against σ_{ci} (Figure 5.11a) and a power function is fit to the data to derive two fitting parameters, a and b, corresponding to Equation 5.13:

$$m_{in} = a\sigma_{ci}^{b} \quad (5.13)$$

The m_{in} was also plotted against average UCS to compare the power function fit to the UCS data to the power function fit to the σ_{ci} data. The 'a' and 'b' fitting parameters for both functions are: 791 and -2.08 for the σ_{ci} fit compared to 2018 and -2.39 for the UCS fit. These fitting parameters are quite different from the parameters derived for sandstone in Shen and Karakus (2014) and analysed in Vásárhelyi et al. (2016), however the strengths of the sandstones in this study are in the low end of the range of sandstones examined in Shen and Karakus (2014) and Vásárhelyi et al. (2016). Vásárhelyi et al. (2016) also showed that the fitting parameters for a single lithology types (e.g. limestone, sandstone, granite, coal) can vary significantly from one locality to another. By assuming that UCS is $\sim\sigma_{ci}$, m_i could then be estimated using Equation 5.13 and the Hoek-Brown failure criterion could be derived for reservoir sandstones in offshore Taranaki without necessitating triaxial strength data. Note that σci is derived from empirical fitting to test data and is not the same as the mean UCS from laboratory testing, although the values should be similar. In cases where UCS is not available, it can be estimated using Equation 5.12.

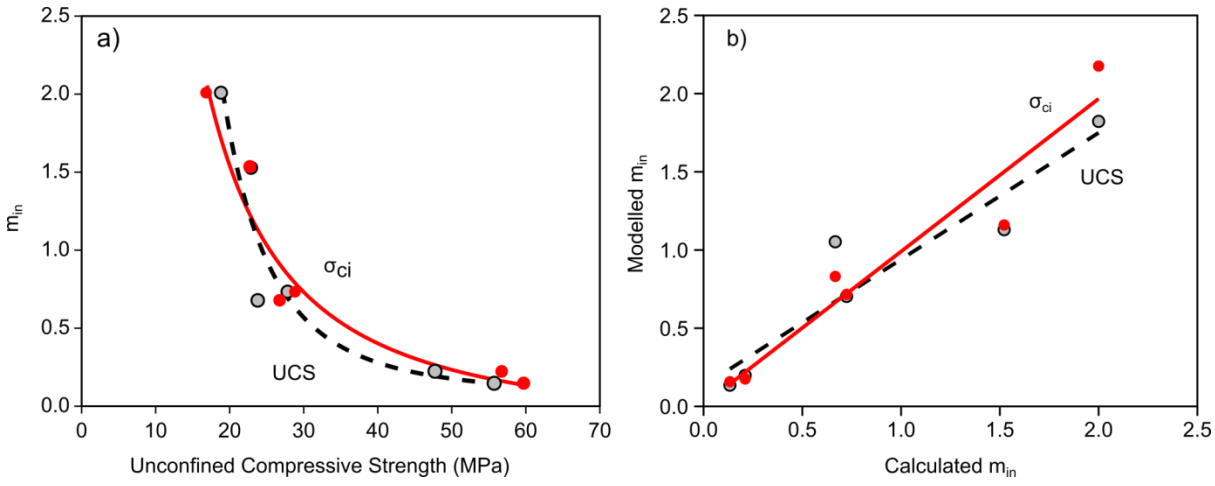

Figure 5-11 Plot of a) relationship between m_{in} and both σ_{ci} and UCS; b) calculated versus modelled m_{in} using the fitting parameters for modelled min based on σ_{ci} and based on UCS

5.5.3. Application to Offshore Reservoirs in the Maui Field

To predict the distribution of mechanical properties across a reservoir interval requires a fundamental understanding of the controls on the rock properties used for strength prediction. In the previous chapter, we determined the dominant control on porosity and permeability is from the textural rock properties, grain size and grain sorting. The The small variation of porosity exhibited across the different lithofacies, suggests there in no general trend between these parameters, however a noticeable trend is exhibited by the grain size distribution (Table 5.6). Stochastic modelling utilizes the distribution of sedimentary facies to extrapolate the quantifiable physical property data across a reservoir interval. Based on the assumption of the dominant control on rock strength attributed to mean grain size and porosity, we can infer that the mechanical properties of a reservoir should follow a similar spatial distribution pattern. For the two sandstone lithofacies by Chantellier and Hitchings (1987), described in chapter 4, we have ascribed an average UCS and Hoek Brown material constant (mi), derived using Equations 5.12 and 5.13 (Table 5.6). This technique can be utilized for an approximate rock strength prediction across un-cored reservoir intervals. It is expected that the cross bedded sandstones will be weaker in comparison to the heterolithic sandstones.

Table 5-6 Comparison of textural and geomechanical properties across two sandstone facies interpreted within the 'C' sands of the Maui Field.

Lithofacies	Depositional Setting	Average Porosity Fraction	Permeability (mD)	D (μm)	UCS (MPa)	m_i
Cross-bedded Sandstones (Sx)	Channel Complexs and minor Coastal	0.19	174	335	13	55
Heterolithic Sandstones (Hl)	Crevasse Splays/ Overbank Deposits	0.17	33.9	161	26	22

5.6. Conclusions

- UCS is inversely proportional to both porosity fraction and mean grain size. We propose an empirical rock strength relationship, locally calibrated to the reservoir rocks of the Taranaki basin, using both porosity fraction and grain size as input parameters. For the purpose of this empirical rock strength relationship grain size is considered independent of porosity fraction. We show that the proposed empirical strength relationship can be extrapolated across a wide spatial and age distribution to other reservoir intervals e.g. Pohokura Field to provide a first estimate of strength.
- The response of the Hoek-Brown and Mohr-Coulomb strength parameters to change in grain size suggest that these criteria can be utilized as a predictive tool for reservoir failure in petroleum geomechanics. However, if triaxial data are not available we show that σ_{ci} can be estimated using average UCS, which can then be used to derive the Hoek-Brown parameters, m_i, and thus build the Hoek-Brown failure criterion for geomechanical analysis.
- As more UCS and triaxial data become available in the Taranaki basin, these empirical relationships can continue to be calibrated to provide improved predictive tools for strength estimates and development of failure criteria.

Chapter Six – Mechanical Property Characterisation of the Maui-Maari Region, Southern Taranaki Basin; Appraisal of Whio-1

6.1. Introduction

Unplanned geomechanical issues cost the petroleum industry billions of dollars a year due to non-productive time. The major cause of non-productive time is wellbore instability resulting in borehole collapse, lost circulation, stuck pipe, lost hole and sand production during the producing life of the well (Moazzeni et al., 2010). To address such geomechanical problems, one-dimensional mechanical earth models (1D MEMs) can be constructed which using logging data, inform the variation of mechanical properties and stress concentrations in proximity to a given wellbore (Ali et al., 2003). Wireline data e.g. density, porosity and sonic velocities are utilized to quantify and assess the mechanical properties (elastic and strength parameters) defining the deformational behaviour of formations being drilled through. Building a 1D MEM during the well planning phase allows for effective operation of petroleum fields during early production, prediction of optimal mud weight windows, stability of wells from pore pressure and fracture gradient prediction, and design of optimal well trajectories. ID MEMs have proven to be valuable in delivering complex wells safely whilst minimising the non-productive time due to wellbore instability (Plumb et al., 2000; Goodman, 2005). The 1D MEM can be particularly useful in a region with minimal geomechanical information such as the Taranaki Basin, as a first-order level assessment of the region. Such issues are noted to occur in the Goss & Trapper wellbores within the TAWN fields of the Taranaki Basin (Swift Energy, 2007a). Furthermore, the 1D MEMs used in conjunction with seismic inversion data can provide input parameters to build a 3D geomechanical model (Wendt et al., 2013). To date, petroleum reports detailing comprehensive 1D MEMS for the Taranaki Basin are all located onshore e.g. Pohokura

Field, Mangahewa Field, TAWN (Tariki, Ahuroa, Waihapa and Ngaere) fields, Kauri field and the Te Kiri Prospect (Shell Todd Oil Services Limited, 2001; Swift Energy, 2007a; Swift Energy, 2007b; Todd Energy, 2010; Todd Energy, 2015).The offshore region of the Taranaki Basin is poorly represented, despite more complex and deeper petroleum prospects. In turn, no comprehensive 3D geomechanical model has ever been developed within the Taranaki region.

The aim of this paper is to present the mechanical rock property component of a 1D MEM for the Maui-Maari-Tui region of the southern Taranaki Basin, attributed across two stratigraphic intervals from the Whio-1 well trajectory. A typical workflow for the rock property component of a 1D MEM utilizes well data from physical properties, density and sonic velocities, which provide the basis for prediction of the elastic and strength parameters. This paper proposes the incorporation of porosity logs into the model, used for the prediction of strength of clean and shaly sandstones. The strength parameter logs allow for failure criterion development at any depth without the need for laboratory testing and when used in conjunction with local stress measurements this allows for reservoir stability assessment. This paper discusses the impact of strength prediction on the assessment of the contemporary stress field.

6.2. Geological Setting

6.2.1. Tectonic History

The southern Taranaki Basin straddles two structural domains, the Western Stable Platform (Tui Field) and the Eastern Mobile Belt (Maui and Maari-Manaia Fields), separated by the Cape Egmont Fault (King et al., 1991; McBeath, 1977; Pilaar and Wakefield, 1978), Figure 6.1. In the mid to Late Cretaceous, basin development initiated from extensional rifting associated with the break-up of Gondwana and the opening of the Tasman Sea. The Western Stable Platform has remained relatively undeformed since the Late Cretaceous, whilst the Eastern Mobile Belt is composed of complex structures from continued tectonic activity to the present (King and Thrasher, 1996; Nicol et al.,

2007). During the Palaeocene-Eocene, passive margin subsidence was associated with the development of a NE-SW trending wide marine-influenced shoreline belt across the central Taranaki Basin (King and Thrasher, 1996); sedimentation kept pace with passive margin subsidence with an intermittent regressive and transgressive movement of the Paleogene shoreline (Higgs, 2012).

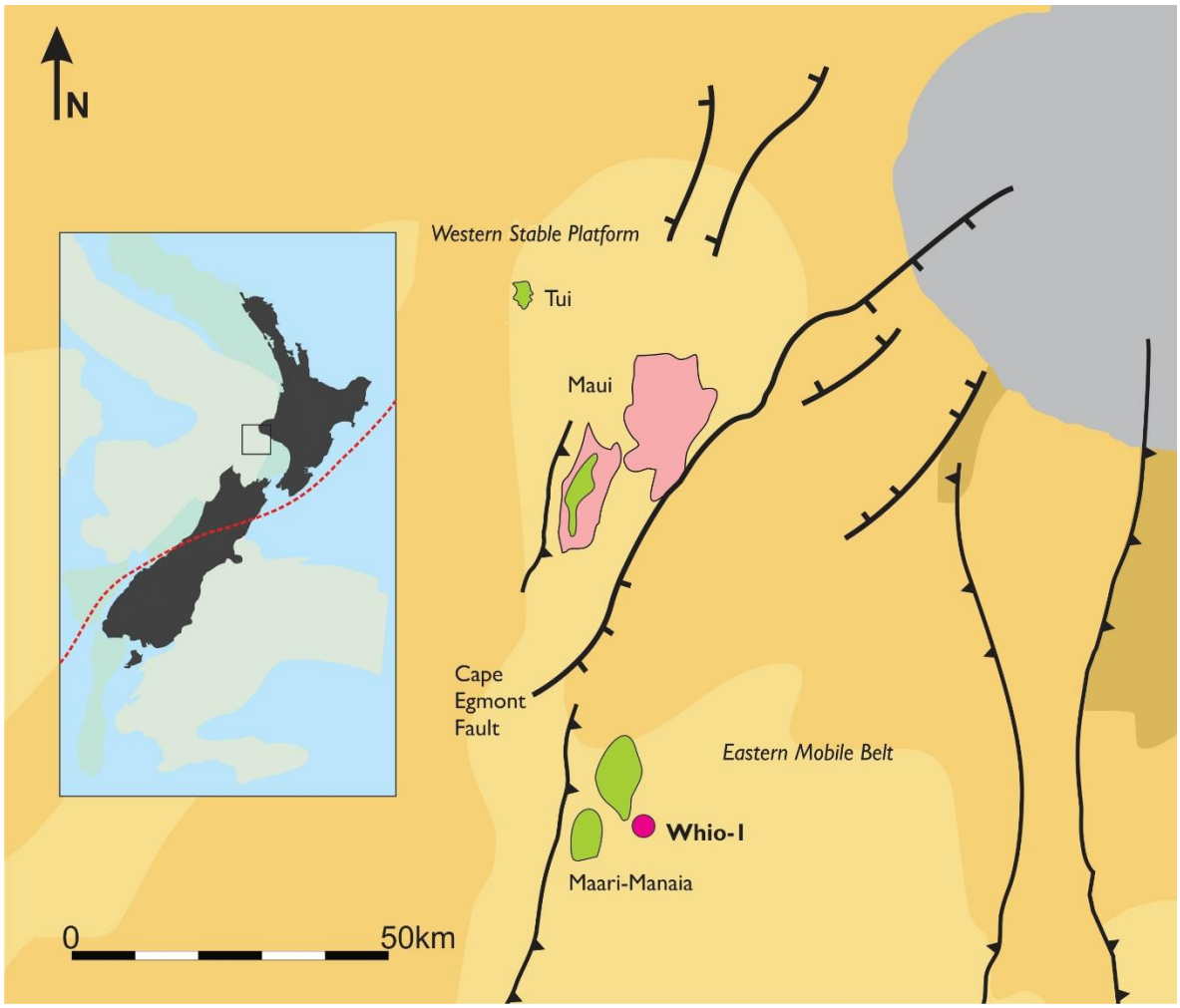

Figure 6-1 Regional map of Maui-Maari and Tui region of the southern Taranaki Basin with position of study well Whio-1; structural controlling faults separating the Western Stable Platform and Eastern Mobile Belt

In the Late Eocene, a slow in subsidence rates resulted in a southwards transgression and marine inundation across the Central and Southern Taranaki Basin. Early rift tectonics were later overprinted by Neogene convergent margin related tectonics (King and Thrasher, 1992). The westwards propagation of contractional deformation into the

Late Miocene resulted in reactivation and inversion along Late Cretaceous normal faults (King and Thrasher, 1996; Reilly et al., 2015), with subsequent extension and collapse of some inversion structures during the Pliocene (King and Thrasher, 1996).

6.2.1.1. Whio Prospect

The Whio Prospect is positioned adjacently east of the Maari-Manaia Field and south of the Maui region. The Whio Prospect is interpreted to lie on a migration fairway from the Maui Sub-basin source, which has in turn charged both the Maui and Maari-Manaia Fields. The proximity to other producing fields led to the suggestion of petroleum prospects identified at several levels (OMV NZ, 2015). Reservoir horizons can be constrained to two chronostratigraphic intervals: Miocene and Eocene-Paleocene. Each stratigraphic interval has a stark difference in depositional environment, due to the rapidly changing stress regime across the Eastern Mobile Belt. During the Miocene, the propagation of the continental shelf gave rise to a thick succession of continental slope and basinal mudstones, with intercalated toe-of-slope to basin floor submarine fan sandstone reservoir intervals; the largest of which is attributed to the Moki Formation, where sand-dominated sequences are 250-350 m thick (King & Thrasher, 1996; King & Browne, 2001); further reservoir intervals include the Whio A Sand and M2A Sandstone. The inter-fingering submarine fan sandstones are laterally extensive across the region, with the M2A Sandstone and Moki Formation acting as dominant reservoirs for the Maari-Manaia Field. The sandstones are often clean, very fine- to fine-grained and are interbedded with siltstones and mudstones of variable thickness, with common limestone stringers and concretion horizons (King & Thrasher, 1996).

During the Paleocene-Eocene, thermally induced subsidence provided accommodation space for a succession of highly cyclic, intercalated coastal plain and shallow marine strata attributed to the Mangahewa, Kaimiro and Farewell Formation (King and Thrasher, 1996; Higgs, 2012; Higgs et al., 2017; Strogen, 2011). The sediment deposition was contained within a NE-SW fairway across the Maui-Maari-Tui region, which followed the regressive and progradational paleo-shoreline. This resulted in laterally

equivalent sedimentation (Higgs et al., 2017); the sequences consist of highly interbedded sequences of sandstones, siltstones and mudstones, often with coal layers (Bryant et al., 1994). Also extensive across the region, the Mangahewa, Kaimiro and Farewell sands are dominant reservoirs for the Maui Field and Tui fields (OMV NZ, 2016).

The Whio structure is represented by a small anticline with four-way dip closure; Whio-1 is positioned at the crest of the anticline. Though originally part of the down-dip southern limb of the Maari-Manaia structure from substantial Late Miocene inversion, the Whio structure developed as a result of structural readjustment during the Pliocene, independent of the Maari structure (OMV NZ, 2016).

6.3. Methods and Materials

The methodology presented herein provides the workflow to develop the rock property logs utilized as a component within a 1D-MEM, for the Maui-Maari-Tui region of the Southern Taranaki Basin. Two stratigraphic intervals were selected along the Whio-1 trajectory for analysis: Miocene strata (1430-1535 mMDRT) and Late Paleocene-Early Eocene strata (2610-2730 mMDRT). The two main lithologies recognised along the Whio-1 trajectory are sand and shale. The rock property logs from wireline tools can provide mechanical stratigraphy (gamma and shale volume), index properties (porosity and sonic velocities), and engineering properties (elastic parameters e.g. Youngs' Modulus and Poissons' Ratio, and strength parameters e.g. compressional strength and angle of internal friction). Table 6.1 contains a summary of the properties derived from wireline logs presented herein.

6.3.1. Mechanical Stratigraphy

The Gamma Ray log (GR) is used as a first-order level index to distinguish reservoir from non-reservoir, with a cut-off of 60 API (sand < 60 < shale). For further evaluation, the GR

log is used to derive the total volume of shale. Firstly, the gamma ray index (I_{GR}) is derived from Equation 6.1:

$$\mathbf{I_{GR}} = \frac{\mathbf{GR_{log}} - \mathbf{GR_{min}}}{\mathbf{GR_{max}} - \mathbf{GR_{min}}} \quad (6.1)$$

I_{GR} = gamma ray index

GR_{log} = gamma ray (log measurement)

GR_{min} = minimum gamma ray reading (mean minimum through a clean sandstone)

GR_{max} = maximum gamma ray reading (mean maximum through a shale or clay formation).

A nonlinear response developed for Tertiary rocks from Larionov (1969) is then selected for the shale volume (Vsh) calculation, Equation 6.2:

$$V_{sh} = 0.083\left(2^{3.7(I_{GR})} - 1\right) \quad (6.2)$$

Using these indices, each stratigraphic interval is separated into lithology categories (shale, sandstone and shaly sandstone).

6.3.2. **Physical Rock Properties**

Table 6.1 provides an outline of wireline data utilized in this section for rock property characterisation.

Table 6-1 Wireline logging tools used to derive rock properties, showing conventional units

Logging Tools	Symbol	Units	Calculated Logs	Units
HNGS Gamma Ray	GR	API	Shale Volume (Vsh)	-
RHOZ Formation Density	ρ	kg/m	Porosity Fraction (n_ρ)	-
Sonic Scanner – Sonic Velocities	Vp	(m/s)	Compressional Slowness Young's Modulus (E) Poisson's Ratio (v)	µs/ft GPa -

Porosity

The formation bulk density tool is a function of matrix density, porosity, and the density of fluid in the pores. The Formation Density Log (RHOZ) is used to calculate the density derived porosity (n_ρ) according to Equation 6.3:

$$n_\rho = \frac{\rho_{ma} - \rho_b}{\rho_{ma} - \rho_f} \quad (6.3)$$

Where,

n_ρ = density derived porosity fraction

ρ_{ma} = matrix density (grain density)

ρ_b = Formation bulk density (log measurement)

ρ_f = Fluid density

For porosity calculation from the density log, assumptions must be applied regarding matrix and fluid density properties. Matrix densities for each interval are determined from grain density measurements taken on sidewall core samples. However, if these are unavailable, average values are used based upon the lithology categories identified using the mechanical stratigraphy method in section 6.3.1.1. As no moveable hydrocarbons were discovered within the reservoirs, the fluid density is assumed to be represented by the 'mud weight' of the drilling fluid; this information can be assumed (1.1g/cm^3 for salt mud and 1.0g/cm^3 for fresh mud), or more accurate values can be determined from drilling reports.

Sonic Velocity

The sonic logging tool provides information about the speed at which waveforms travel through a formation, in terms of compressional wave (V_p) and shear wave (V_s) velocities, often expressed as a measure of compressional slowness (Δt), Equation 6.4:

$$\Delta t = \frac{1}{V_P} \quad (6.4)$$

6.3.3. **Mechanical Rock Properties**

Elastic Parameters

The elastic parameters provide a measure of recoverable deformational behaviour prior to rock failure and are expressed in terms of Dynamic Young's Modulus (Equation 6.5) and Poisson's Ratio (Equation 6.6). These are derived from the sonic velocities:

$$E_{dyn} = \frac{\rho V_s^2 (3V_p^2 - 4V_s^2)}{(V_p^2 - V_s^2)} \quad (6.5)$$

$$\nu_{dyn} = \frac{V_p^2 - 2V_s^2}{2(V_p^2 - V_s^2)} \quad (6.6)$$

Where,

E_{dyn} = Dynamic Elastic Modulus

ν_{dyn} = Dynamic Poissons' Ratio

V_p = Compressional wave Velocity

V_s = Shear wave Velocity

ρ_b = Bulk Density

Unconfined Compressive Strength

Two physical property-strength empirical relations were used to develop a UCS log within the stratigraphic intervals for assessment of sands and shales. The proposed formulae were developed for the Taranaki Basin, and calibrated with laboratory testing on cores from local stratigraphy.

For shales, compressional slowness used to predict UCS (Kazianis, 2018 using the formulation from McNally, 1987), is expressed in Equation 6.7:

$$\mathrm{UCS} = 3226.7\mathrm{e}^{-0.054\,\Delta t} \tag{6.7}$$

Where,

σ_c = Unconfined compressive strength (MPa)

Δt = compressional slowness (μs/ft)

For sandstones, porosity fraction used to predict UCS (Chapter 5; Chang et al., 2006) is expressed in Equation 6.8:

$$\mathrm{UCS} = 108\mathrm{e}^{-10n} \tag{6.8}$$

Where,

σ_c = Unconfined compressive strength (MPa)

n = porosity fraction

Angle of internal friction

The angle of internal friction is assessed using Equation 6.9 (Chang et al., 2006):

$$\phi = \tan^{-1}\left(\frac{(\mathrm{GR} - \mathrm{GR}_{\mathrm{sand}})\mu_{\mathrm{shale}} + (\mathrm{GR}_{\mathrm{shale}} - \mathrm{GR})\mu_{\mathrm{sand}}}{\mathrm{GR}_{\mathrm{shale}} - \mathrm{GR}_{\mathrm{sand}}}\right) \tag{6.9}$$

Where,

ϕ = Angle of internal friction

GR = gamma ray (log measurement)

GR_{sand} = gamma ray measurement for clean sand

GR_{shale} = gamma ray measurement for shale

Values of GR for clean sand and shale are assumed from log calibration, represented by the mean minimum and mean maximum gamma readings in adjacent intervals. The angle of internal friction can be expressed in terms of coefficient of friction (μ), Equation 6.10:

$$\mu = \tan\phi \tag{6.10}$$

Values of μ_{shale} and μ_{sand} were approximated at 0.7 and 0.6, respectively.

Incorporation of the UCS and angle of internal friction to derive the cohesion coefficient (c) , Equation 6.11, allows for the development of a complete Mohr-Coulomb failure criterion for a depth of interest:

$$c = UCS\frac{1\text{-}\sin\phi}{2\cos\phi} \quad (6.11)$$

Strength parameters used in conjunction with contemporary stress measurements can be utilized to assess the likelihood of rock failure.

6.3.4. **Data Calibration**

Physical laboratory measurements on cores are used for calibration of mechanical properties from log data. Sidewall core acquisition along the Whio-1 wellbore axis provides regularly spaced sampling of the stratigraphic column. A total of 50 SWC samples were collected over two runs; 10 of which were recovered within the stratigraphic intervals of interest. Core analysis of the SWC samples was undertaken at the University of Canterbury's Rock Mechanics Laboratory to provide density and porosity measurements. The porosity measurements on the oven dried cores were undertaken using a Micrometrics AccuPyc II 1340 nitrogen pycnometer, which provides the sample's grain volume. Porosity is calculated as the ratio of the pore volume to sample bulk volume (V). Saturated bulk density is calculated as the ratio of saturated mass (g) to bulk volume (cm^3). Due to the dimensions of the SWCs, mechanical strength testing could not be performed.

6.4. Results

6.4.1. Mechanical Stratigraphy

The responsive changes in the gamma and density logs are used in conjunction with the well completion report to delineate shale, sand and shaly sandstone units. In most cases, the mechanical stratigraphy divisions follow the formation boundaries. In general, the Miocene strata exhibit less internal variability within an individual unit and are shale dominated (Figure 6.2a). In contrast, the Eocene-Paleocene strata display significant internal variation demonstrated by the highly fluctuating pattern of wireline logs within an individual unit (Figure 6.2b).

In the Miocene stratigraphic section three reservoir prospects are identified based upon the GR response (Figure 6.2a): Whio-A Sand (1436-1444.5 m), M2A sandstone (1459-1464 m), and Moki 1.1 (1525.5-1535 m). These are interbedded between a dominant shale succession, termed the Upper Manganui Formation. The Whio-A Sand (10 m) has GR values ranging between 55-84 API (focused around the sand-shale boundary) and a formation density between 2.30-2.53 g/cm^3; this corresponds to shaly sand. A saw-tooth serrated log pattern for GR, and the calculated shale volume relates to the presence of thinly interbedded layers of shaly sand and shale. At the top of the Whio-A Sand no distinctive contact is observed with the overlying Manganui Formation, due to a gradational fining upwards of grain size into the shale. A marked change is observed at the base of Whio A Sand with a noticeable increase of GR denoting the continuation of the Manganui Formation (100 API). In contrast, the M2A sandstone (5 m) is represented with a uniform, non-serrated GR log ranging from 47-58 API and formation density of 2.24-2.33 g/cm^3, coinciding with a much cleaner sand formation with a maximum shale volume of 0.17. Atop of the M2A sandstone, a slight gradational fining upwards transition is observed into the overlying Manganui Formation. The continuation of the Manganui Formation at the base of M2A is denoted by a sharp contact and increase of GR values, though the shale volume remains relatively low (0.3).

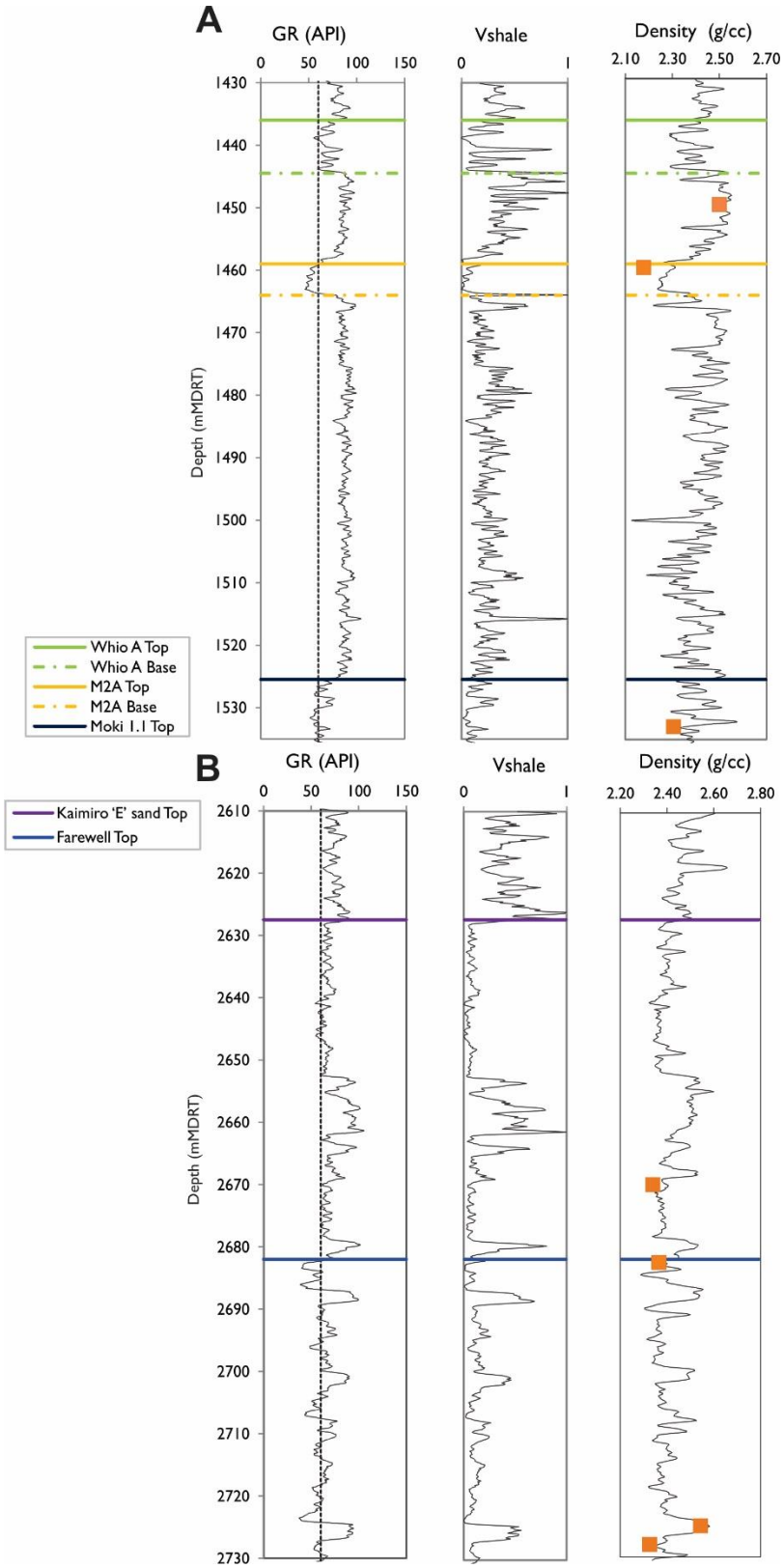

Figure 6-2 Mechanical stratigraphy delineated along Whio-1 trajectory, based upon GR, shale volume and formation density. Laboratory measurements were used to calibrate Formation Density Log (Orange Squares). [a] Miocene stratigraphic interval (1430-1535 mMDRT). [b] Late Paleocene-Eocene stratigraphic interval (2610-2730 mMDRT).

The uppermost Moki 1.1 reservoir (10 m) is comprised of shaly sandstones, with a small GR range between 54-72 API and formation densities between 2.30-2.57 g/cm^3. The jagged serrated pattern of the GR log indicates thicker packages of interbedded sandstone and shale, with maximum shale content of 0.31. The upper boundary of the Moki 1.1 reservoir exhibits a gradational fining upwards transition into the overlying Manganui Formation, similarly to the Whio-A Sand and M2A sandstone.

In the Late Paleocene-Eocene stratigraphic section two reservoir intervals are identified (Figure 6.2b): the underlying Farewell Formation (2682-2824 m) and the Kaimiro 'E' sand (2627.5-2679 m) capped by the overlying Kaimiro 'E' shale (2606-2627.5 m). The 'E' sand can be further divided into an upper and lower reservoir portion, separated by a shale-dominated interval (2652-2665 m), marked by a rapid increase in GR (<100 API) and formation density. Both the upper and lower portions of the 'E' sand exhibit relatively high GR readings of 57-75 API and 61-85 API, respectively, with an average formation density of 2.37 g/cm^3, indicative of shaly sands. The uppermost Farewell Formation (45 m) displays GR values ranging between 39-94 API, and a formation density between 2.34-2.58 g/cm^3; with the maximum values assigned to the high shale content layers (Vshale = 0.5-0.8). The wide range in the GR log correlates with the cyclicity of 10 m thick fining upwards packages from clean sandstones (39 API) to shaly sandstones (77 API). A similar pattern is exhibited across the boundary between the Farewell Formation and overlying Kaimiro 'E' sand. Table 6.2 provides a summary of mechanical stratigraphic intervals and the associated lithology category e.g. sand, shale or shaly sand.

The wireline log of formation density is overlain with the laboratory measured saturated bulk densities from the sidewall cores; the overlay of data points across both stratigraphic intervals shows the log data is suitably calibrated to the laboratory data (Figure 6.2).

Table 6-2 Overview of mechanical stratigraphy subdivided on the basis of sand, shale and shaly sands using GR response

Stratigraphic Division	Depth (mMDRT)	GR(API)	Lithology
Upper Manganui	1430-1525.5m	>100	Shale
Whio A Sand	1436-1444.5m	55-84	Shaly sand
M2A Sand	1459-1464m	47-58	Sand
Moki 1.1 Sand	1525.5-1535m	54-72	Shaly sand
Kaimiro 'E' Shale	2606-2627.5m	70-90	Sandy Shale
Kaimiro 'E' Sand	2627.5652m	57-75	Shaly sand
	2652-2665m	>100	Shale
	2665-2679m	61-85	Shaly sand
Farewell Formation	2682-2730m	39-94	Clean/Shaly sand

6.4.2. **Rock Properties**

The physical properties e.g. density, porosity and sonic velocities, provide a quantifiable measure used to describe and characterise the properties across different lithologies, providing the basis for predictive strength functions.

6.4.2.1. Sonic Velocities

Within the Miocene stratigraphic interval, compressional slowness increases for sandier intervals e.g. M2A sands (99 µsec/ft), compared to the shale-dominated intervals e.g. Upper Manganui (85 µsec/ft). For the Late Paleocene-Eocene stratigraphic interval, a decrease in compressional slowness is attributed to sand-dominated layers e.g. Kaimiro 'E' Sand (75 µsec/ft), in comparison to shale dominated layers (87 µsec/ft). The consistent compressional slowness attributed to shale dominated layers (85-87µsec/ft) is in contrast with a decrease of compressional slowness for sandstones with depth (Figure 6.3).

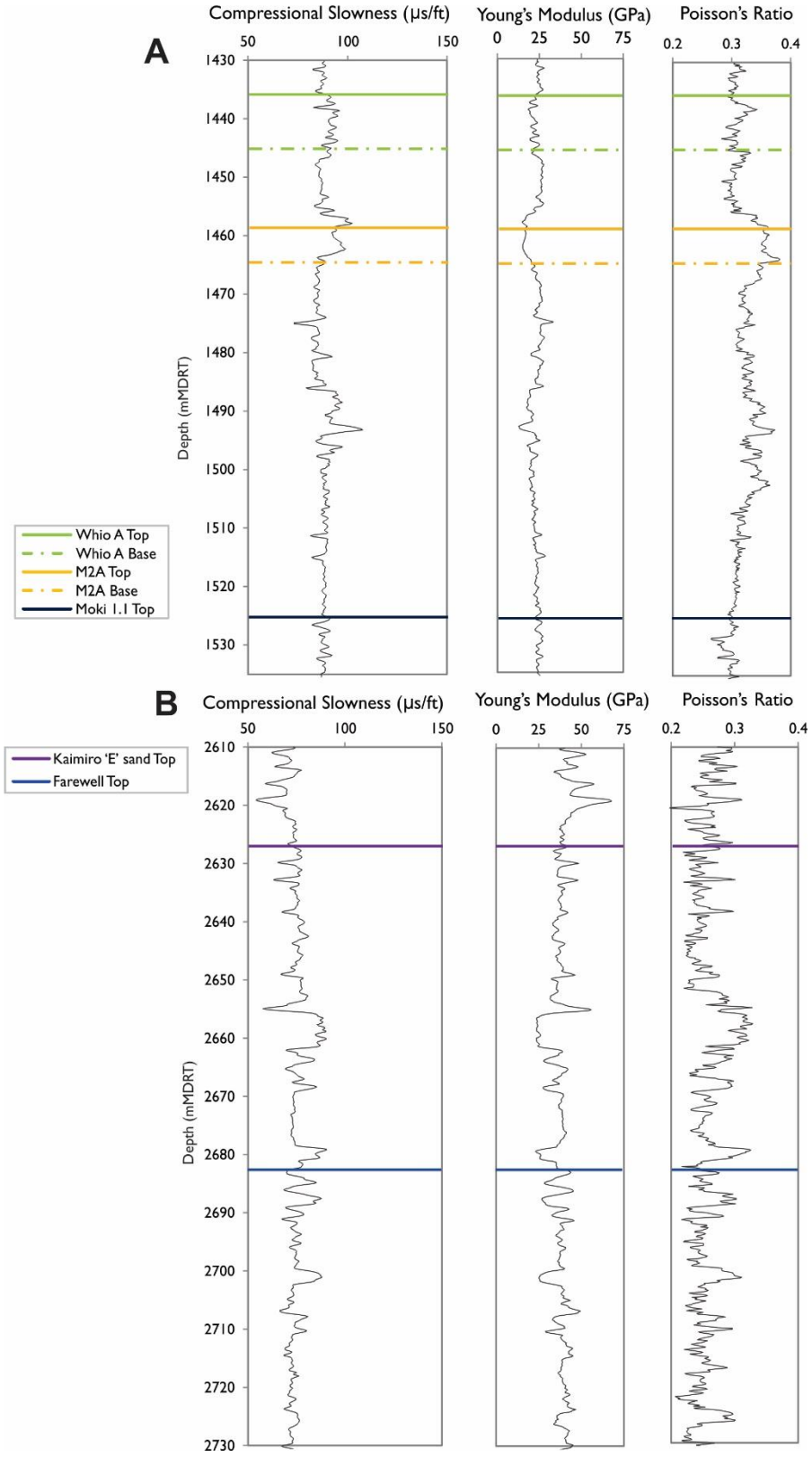

Figure 6-3 Compressional slowness log (1/Vp) along Whio-1 trajectory, used to determine elastic parameter logs - Dynamic Young's Modulus and Poisson's Ratio based upon Equation's 6.5 and 6.6. [a] Miocene aged stratigraphic interval (1430-1535 mMDRT). [b] Late Paleocene-Eocene stratigraphic interval (2610-2730 mMDRT).

The elastic properties, dynamic Young's Modulus and Poisson's Ratio, are based on measures of density and sonic velocities. For the Miocene stratigraphic section, the sandier unit e.g. M2A sandstone, with a high compressional slowness, exhibits a Poisson's Ratio of 0.35 and a Young's Modulus of 15 GPa. In contrast, for the Late Paleocene-Eocene stratigraphic section, the sandier unit e.g. Kaimiro Sand, with a low compressional slowness, has a lower Poissons Ratio of 0.24 and higher Young's Modulus of 40 GPa. This suggests that, for sandstone intervals, there is a marked increase in Young's Modulus, and decrease in Poisson's Ratio with depth. In comparison, shale-dominated intervals remain consistent across the measured stratigraphic section, with an average Poisson's Ratio of 0.31, and a Young's Modulus of 25 GPa.

6.4.2.2. Porosity

A consistent general trend is exhibited whereby higher porosities are found in sand-dominated horizons (Figure 6.4). The Miocene stratigraphic interval exhibits a large porosity range between 0.09-0.35, in contrast to the Late Paleocene-Eocene stratigraphic interval, which exhibits much lower porosity values between 0-0.23, showing an overall porosity reduction with depth.

The porosity log mirrors the variation observed within the mechanical stratigraphy; low density, low GR and low shale volume layers are associated with higher porosities (e.g. M2A sandstone, and the base of fining upwards packages in the Farewell Formation). For interbedded units of sands and shales the serration of the porosity log reflects the variation of lithology across the interval e.g. Whio A and Upper Moki 1.1. Attention is a paid to noticeable low density (2.1 g/cm^3) correlating to organic-rich layers (as indicated from the composite log (OMV NZ, 2015)), which can lead to overestimating porosity on the graphs (e.g. at 1500 mMDRT). The density log derived porosity fraction is compared with the porosity fraction measured in the laboratory on the SWC; the close correlations between the values across both stratigraphic intervals show the log data is suitably calibrated (Figure 6.4).

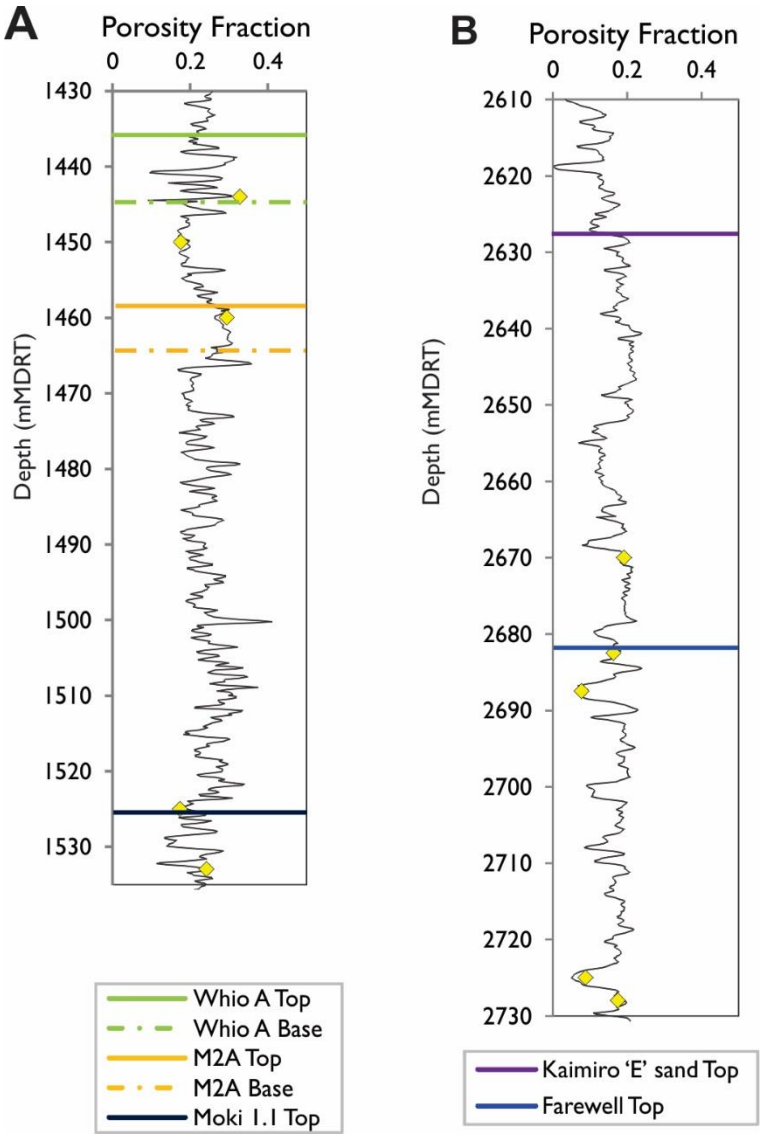

Figure 6-4 Density derived-Porosity log along Whio-1 trajectory used for subsequent strength parameter predictions. Laboratory measurements were used to calibrate porosity values between core and log (Yellow Points). [a] Upper Miocene aged stratigraphic interval (1430-1535 mMDRT). [b] Lower Paleocene-Eocene stratigraphic interval (2610-2730 mMDRT).

6.4.2.3. Strength Parameters

Two physical property relationships were used to assess strength: porosity-UCS for sandstones, and compressional slowness-UCS for shale (Figure 6.5). For sandstones, the porosity-UCS log exhibits an increase in strength with depth from the Miocene and to the Late Paleocene-Eocene intervals, from 10-40 MPa to 15-60 MPa respectively. For the Miocene sandstone reservoirs, the clean sandstone M2A displays the smallest strength range from 5-10 MPa, with larger variations attributed to shaly dominated sandstones and interbedded sandstones e.g. M2A and Moki 1.1 ranging from 5-40 MPa. For Eocene-Late Paleocene reservoirs, the Kaimiro 'E' Sand and Farewell Formation demonstrate a consistent strength profile of approximately 25 MPa often with deviations up to 60 MPa. The porosity-UCS profile follows a similarly serrated pattern to the GR log, correlating with the mechanical stratigraphy; lower strength is assigned to sandier intervals with a lower GR e.g. M2A sand and Kaimiro 'E' sand. For shales, the compressional slowness-UCS log displays an increase of strength predictions with depth from the Miocene (25-64MPa) to the Late Paleocene-Eocene (50-150MPa) stratigraphic intervals. The UCS log exhibits a consistent strength profile with only a few local variations e.g. decreased strength values coinciding with organic layers at 1500 mMDRT. In general, higher angles of internal friction are attributed to sandstones (35˚) than to the shale dominated layers (31˚); this trend is more clearly defined within the Late Paleocene-Eocene stratigraphic interval.

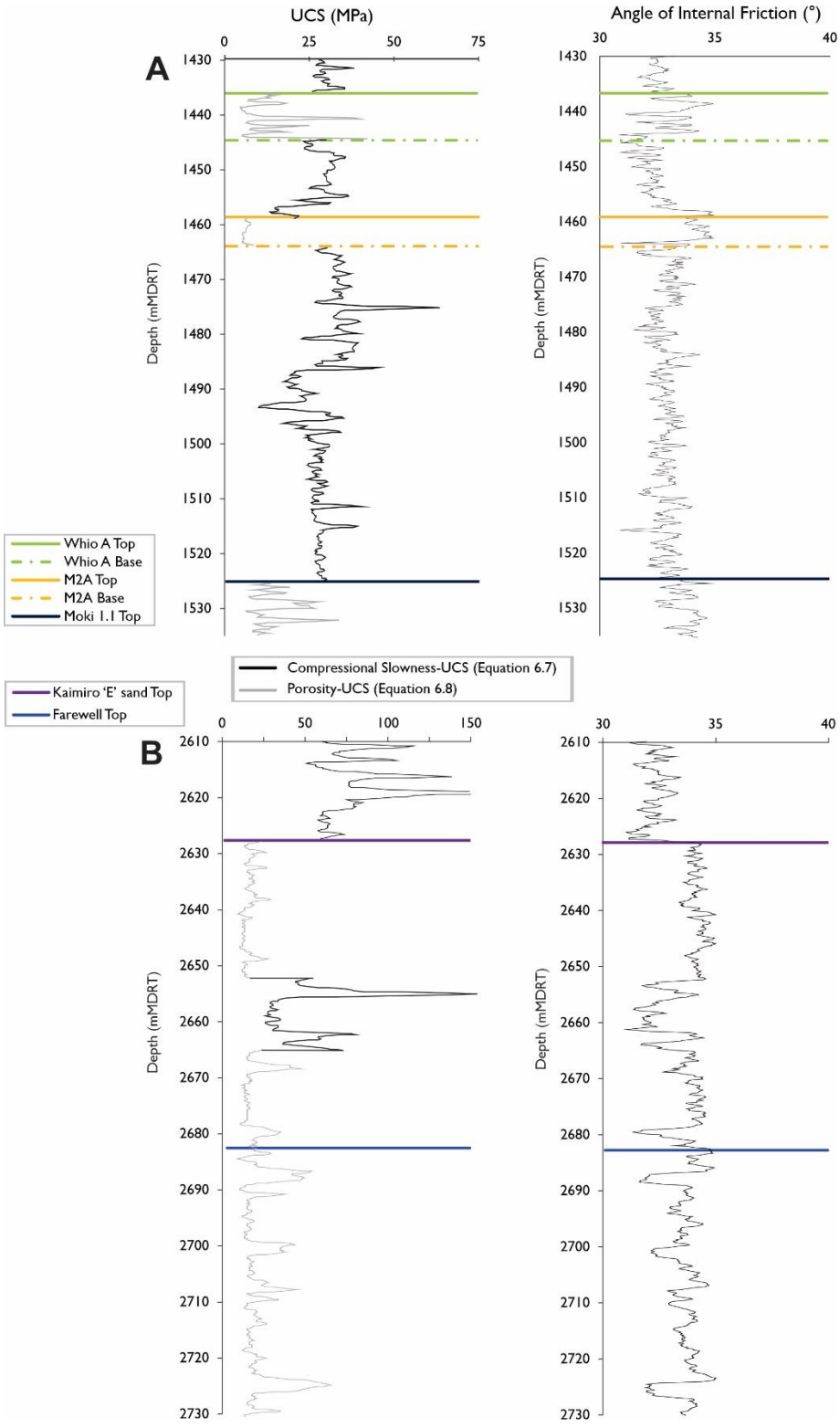

Figure 6-5 Strength parameter logs used to define the Mohr Coulomb criterion: UCS logs – compressional slowness (Equation 6.7) and porosity (Equation 6.8), and Angle of internal Friction (Equation 6.9). [a] Miocene aged stratigraphic interval (1430-1535 mMDRT). [b] Late Paleocene-Eocene stratigraphic interval (2610-2730 mMDRT),

6.4.3. **Rock Property Characterisation**

Figures 6.6 and 6.7 show a complete rock property characterisation for the Miocene stratigraphic interval (1430-1535 mMDRT) and Late Paleocene-Eocene stratigraphic interval (2610-2730 mMDRT), respectively. Each stratigraphic interval is subdivided into discrete mechanical units on the basis lithology (determined from GR logs and validated through drilling reports).

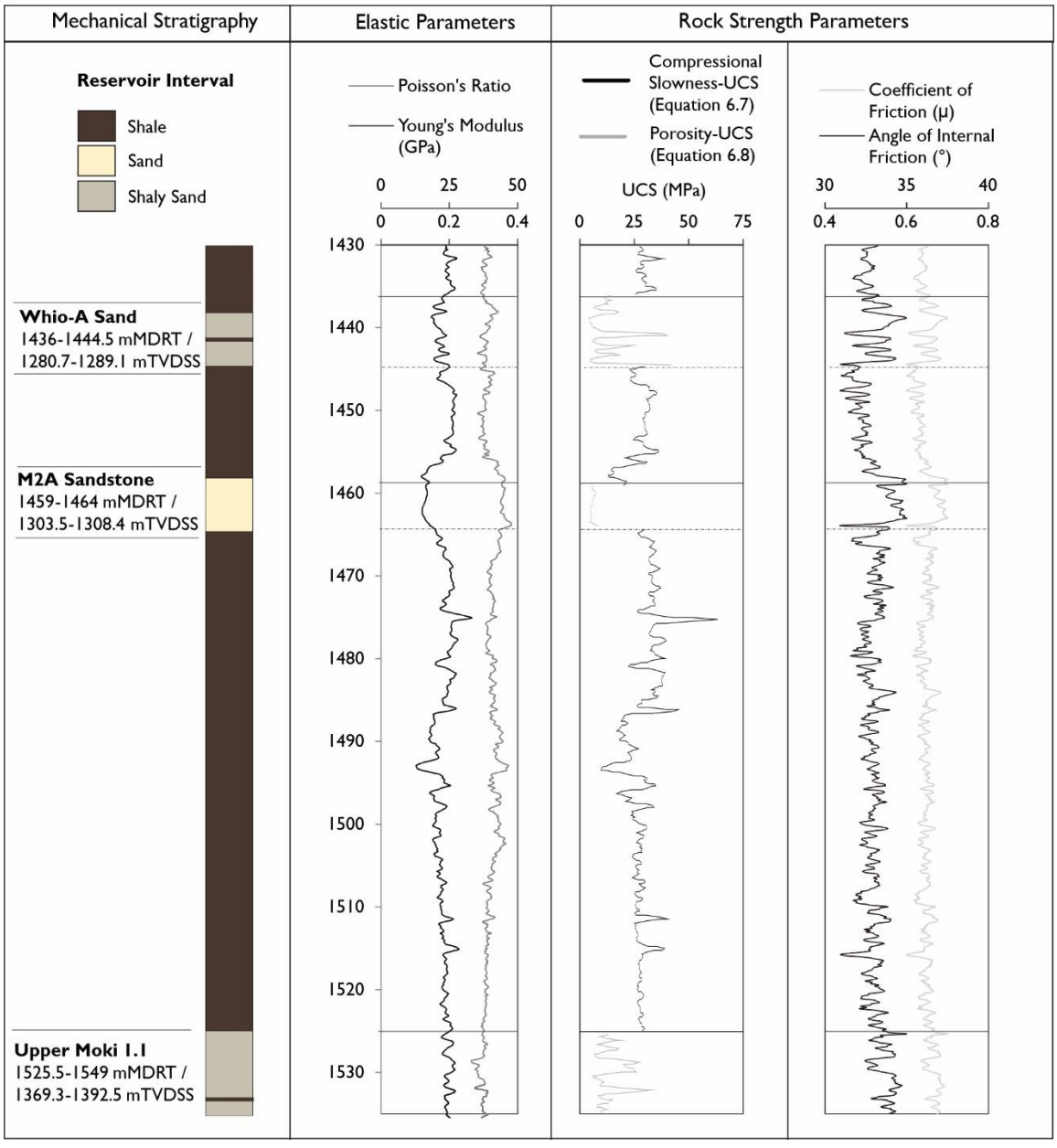

Figure 6-6 Mechanical property characterisation for the Miocene stratigraphic interval (1430-1535 mMDRT)

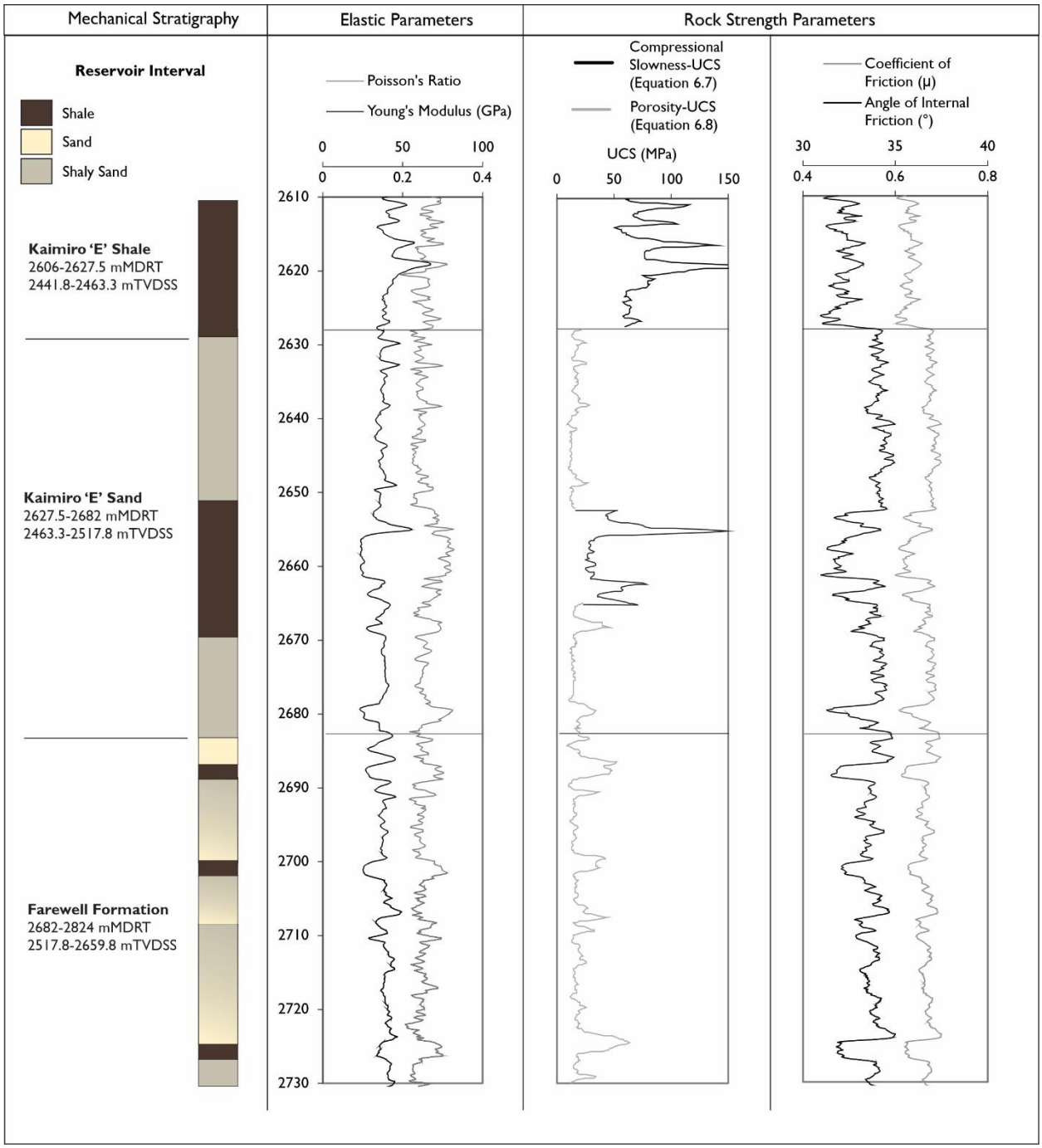

Figure 6-7 Mechanical property characterisation for the Late Paleocene-Eocene stratigraphic interval (2610-2730 mMDRT)

6.5. Discussion - Application for Geomechanical Modelling

6.5.1. Defining Mechanical Units from Rock Shaliness

The mechanical stratigraphy subdivides the stratified rock into discrete mechanical units on the basis of lithology categories from GR logs (Laubach et al., 2009). In most cases, the divisions follow the formation boundaries separated by the dominant lithologies of sand and shale; however, if in many instances the two lithologies are not well differentiated, with a dominant presence of shaly sands and interbedded sands/shales (OMV NZ, 2015). The gamma ray log response increases based upon a concentration of radioactive material as observed in shales. However, it is possible for a clean sandstone (with a low shale content) to provide a heightened gamma ray response if the sandstone contains high concentrations of radioactive minerals e.g. potassium feldspar, micas and glauconite. In contrast to the Miocene interval, the Eocene-Paleocene sandstones consist of predominantly feldspathic quartz arenites, with the Farewell Formation demonstrating more feldspathic sandstones than the overlying Kapuni Group sandstones. Thus, determination of sandstones, shaly sandstones and shales intervals from the gamma ray log (60API) was corroborated with cuttings descriptions and the composite log from the Whio-1 petroleum report.

In reality, the shaliness of a unit does not change suddenly, but rather gradually with depth. Such gradual changes are indicative of the litho-facies and are associated with changes in grain size and sorting that are controlled by the depositional environment (Chapter 4; Potter et al., 2012). We suggest the delineation of mechanical units can be represented by depositional cycles within the stratigraphy, termed ‘mechanical facies’; this is not an innovative idea, though the concept is not widely adopted (Yale & Jamieson, 1994; Khaksar et al., 2009).

The shapes of the GR log, often used as a proxy for grain size trends, can provide an indication of depositional setting of sedimentary cycles (Rider, 1986). The principal GR log shapes are bell shape (fining upwards), funnel (coarsening upward), cylindrical

(consistent), bow (systematic increase and decrease) and irregular trend (Figure 6.8). The Upper Manganui Formation represents a clay- and silt-dominated continental slope and basinal unit that is characterised by a consistent cylindrical, but highly serrated saw-tooth pattern gamma response. Whio-A, M2A sandstone and Moki Formation all demonstrate a 'bell shape' GR curve fining upwards into the overlying shale formation. Considered a dirtying up trend, within a marine setting this is indicative of the waning of submarine fans. In contrast, the Late Paleocene-Eocene stratigraphic interval is described as fluvial-dominated lower coastal plain to near shore sandstones and siltstones. Within the Kaimiro 'E' sand, progradation and retrogradation of the shoreface is denoted by an hourglass shaped GR response. The upper 76 m of the Farewell Formation at Whio-1 (2682-2758 mMDRT) consists of a stacked sequence of upwards-fining sandstones separated by 1-4 m thick calcareous cemented siltstones. This sequence is denoted in the GR log by a highly serrated, cyclic bell-shaped pattern.

In reservoir characterisation, stochastic modelling utilizes the distribution of sedimentary facies to extrapolate the quantifiable physical property data e.g. porosity and permeability across an interval (Doyle & Sweet, 1995). Based on the assumption that a dominant control on strength of the sands is attributed to mean grain size and porosity (Chapter 5), we can infer that the mechanical properties of a reservoir should follow a similar spatial distribution pattern. The use of sedimentary facies to delineate mechanical stratigraphy in the development of a 1D MEM can allows for extrapolation of mechanical properties away from the wellbore in a systematic manner.

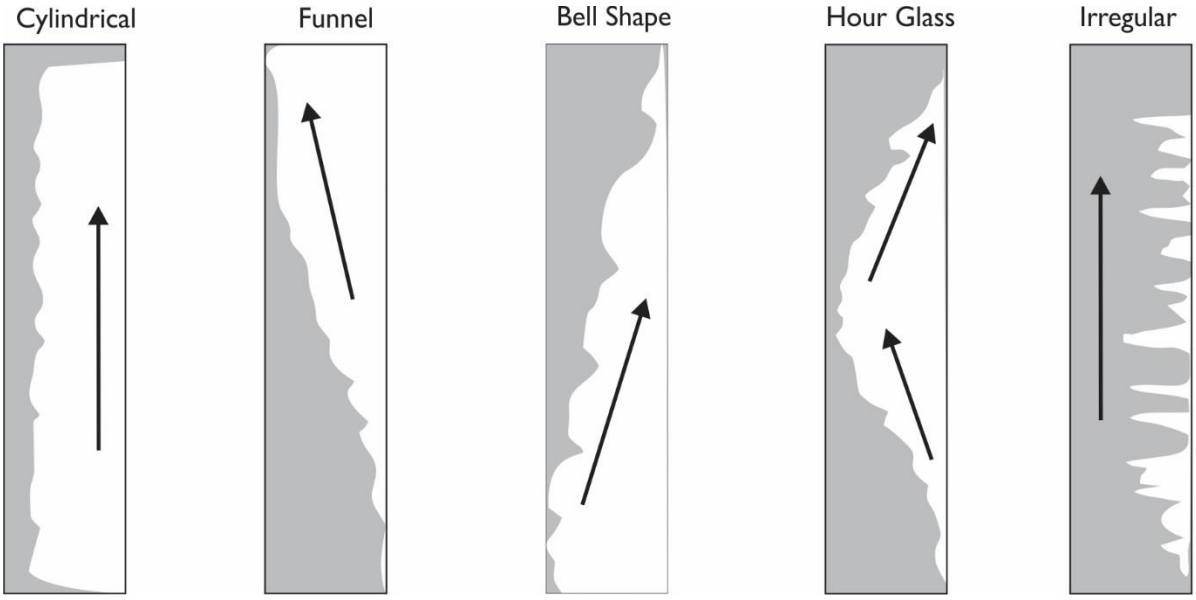

Figure 6-8 Principle shapes recognised in GR logs, indicative of depositional cycle; bell shape (fining upwards), funnel (coarsening upward), cylindrical (consistent), bow (systematic increase and decrease) and irregular trend. Adapted from Emery & Myers (1996)

6.5.2. **Importance of Local Calibration for Rock Strength Prediction**

The use of physical property-strength relationships is a robust technique used to provide a lower bound estimate of in-situ strength (Chang et al., 2006). A physical property-strength relationship is developed on the premise of a strong correlation between variables for a data subset. The calculation of a first order strength approximation can be beneficial for applications related to borehole stability, though overgeneralisation of proposed empirical relations can result in poor guidance regarding strength predictions. For example, an empirical relation developed for sandstone in the North Sea may in principal behave similarly to sandstone in the Taranaki Basin; however localised variation in sediment input, diagenesis and textural properties, etc., will alter the correlation coefficients defining the physical property-strength relationship.

McNally (1987) and Chang et al. (2006) presented empirical relations developed for the prediction of rock strength, using compressional slowness, and porosity fraction

respectively. Two formulae utilized for strength prediction of shale and sandstone in this study (Equation 6.7 and 6.8) were developed according to the methods in McNally (1987) and Chang et al. (2006), then calibrated using laboratory testing on cores from local stratigraphy within the for the Taranaki Basin (Kazianis, 2018 for the shale; Chapter 5 for the sandstone). McNally (1987) and Equation 6.7 both adopt exponential formulae with compressional slowness as the input variable for the calculation of shale UCS. Chang et al. (2006) and Equation 6.8 both adopt exponential formulae with porosity fraction as the input variable for the calculation of sandstone UCS.

For both the shales and sandstones, the formulae locally calibrated to the Taranaki Basin (Equation 6.7 and 6.8) exhibit a leftwards shift of the UCS profile (Figure 6.9) predicting lower rock strengths than the uncalibrated relationships. This suggests that irrespective of the relationship chosen for strength prediction, without calibration of the prediction tool for the Taranaki, the lower bound strength estimate is likely to be over predicted; for Chang et al. (2006) and Equation 6.8 the difference can be in excess of 50% within shaly sandstone intervals e.g. Whio-A and Moki 1.1.

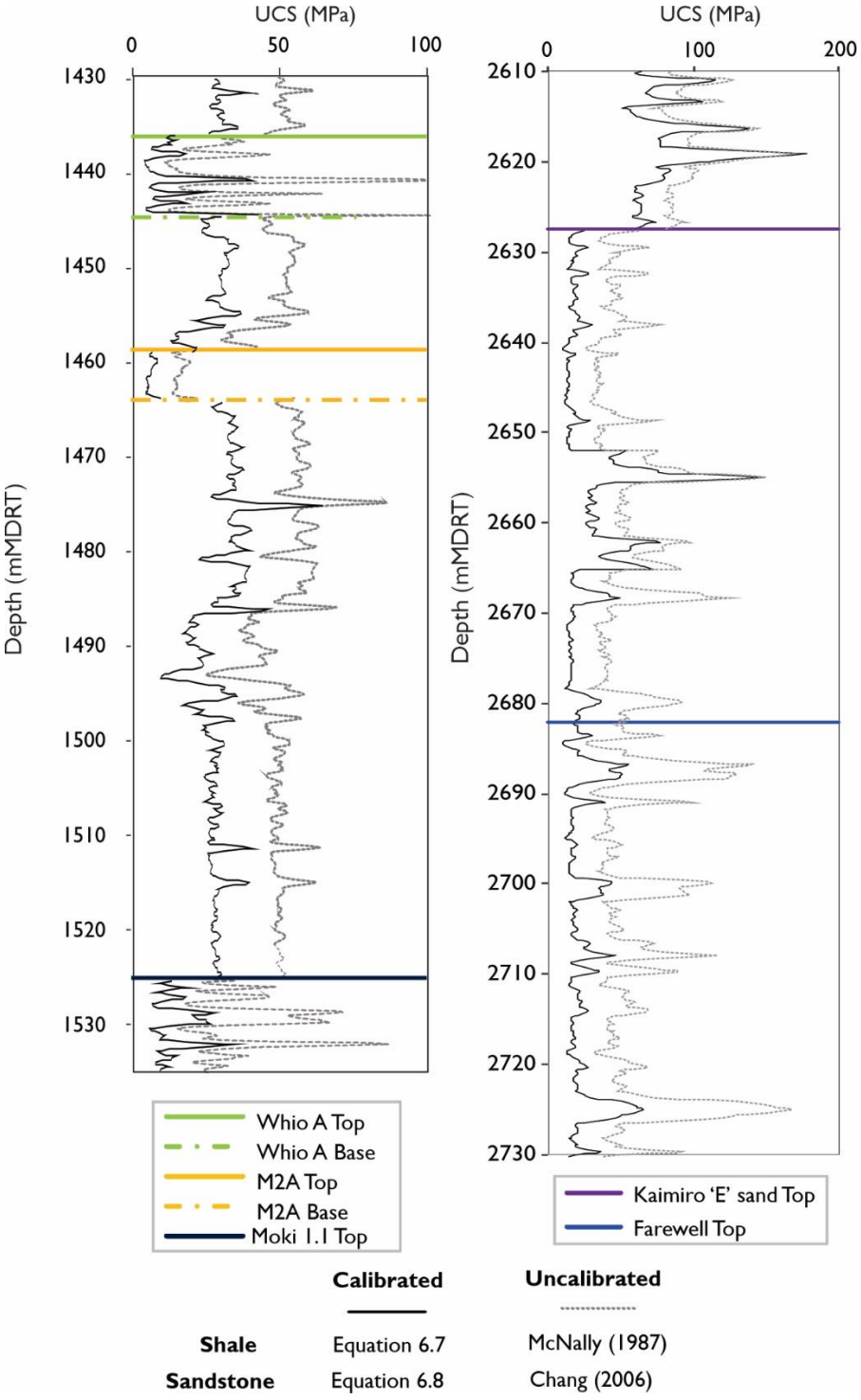

Figure 6-9 Miocene aged stratigraphic interval (1430-1535 mMDRT) and Late Paleocene-Eocene stratigraphic interval (2610-2730 mMDRT). Uncalibrated physical property-UCS log compared to the calibrated log (McNally, 1987; Chang et al., 2006) compared to calibrated logs for the Southern Taranaki Basin (Equation 6.7 (Kazianis, 2018)); (Equation 6.8 (Chapter 5)). Note leftwards shift between logs suggesting overestimation of strength using uncalibrated relationships.

6.5.3. Determination of Appropriate Relation for Strength prediction

6.5.3.1. Grain Size Variable

The deformational behaviour of sandstones is different from that of shale (Jizba, 1992). Empirical strength relationships are defined for individual rock types e.g. sandstones and shales, as summarised by Chang et al. (2006); this is applicable for a region consisting of well differentiated lithologies e.g. Gulf of Mexico and North Sea. In the Southern Taranaki Basin, lithologies commonly consist of muddy (shaly) sandstones and sandy mudstones (shales) (Massiot et al., 2019). Classification of an interval with a fluctuating shale volume within a sandstone can be difficult, as an increase of shaliness will affect the elastic and strength parameters. For both clean and shaly sandstones there is a decrease in Poisson's Ratio and increase of Young's Modulus with increasing burial depth and consolidation. The porosity–UCS log follows the configuration of the mechanical stratigraphy in response to the GR log, suggesting that a correlation between porosity and the fluctuation of sands and shaly sands exists.

In order to assess strength variation across different sandstone reservoirs, an input variable of grain size can be used in predictive tools to better constrain strength between clean and shaly sandstones. The GR log, often used as a proxy for grain size, provides a measure of shale/clay volume (Vsh or Vclay), which can be used to delineate between clean and shaly sandstones (Equation 6.2).

Coates and Denoo (1981) developed a mechanical properties evaluation programme based upon correlations between Young's modulus and UCS. This was further developed for sandstones with varying clay content (Anderson et al., 1986). Fjaer et al. (1992) reorganised this relation in terms of Poisson's Ratio (v), density (ρ) and compressional sonic velocity (Vp) as follows (Equation 6.12):

$$UCS = 3.3x10^{-20}\rho^2 V_p^4 \left(\frac{1+\nu}{1-\nu}\right)^2 (1-2\nu)\left(1+0.78V_{clay}\right) \quad (6.12)$$

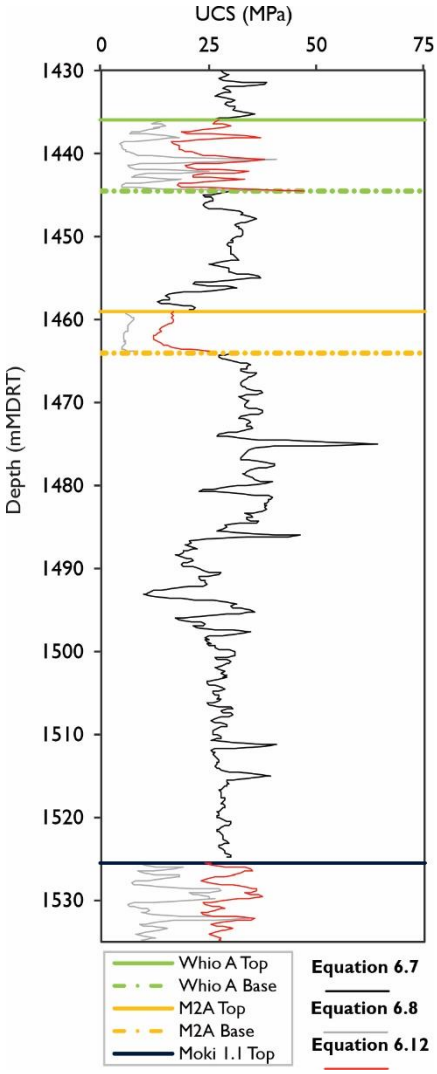

Figure 6-10 Comparison of strength predictions for clean and shaly sandstone intervals (Whio-A, M2A and Moki 1.1) using a clay volume parameter.

Figure 6.10 displays the strength predictions from Equation 6.12 and compares with original UCS log across clean and shaly sandstone intervals. Following the previous discussion topic, the strength predictions are expected to be marginally overestimated due to the use of an uncalibrated relationship that was developed for use in the Gulf Coast (Fjaer et al., 1992); thus, a rightwards shift of strength predictions. For the Miocene interval, the strength log for the clean M2A sandstone (clay volume of <10%) displays similar form to the porosity-UCS log. In comparison, the shaly sandstones, Whio-A and Moki 1.1 (clay volume up to 45%) exhibit a narrower range of strength values between 20-37 MPa. This suggests the use of clay volume acts to constrain strength predictions.

6.5.3.2. Comparison of Strength Predictions and Laboratory Data

The UCS log is compared with laboratory data of equivalent intervals from wells in the Maui-Maari region for assessment of strength prediction. The Late Paleocene-Eocene stratigraphic interval from Whio-1 corresponding to the Kaimiro 'E' shale, Kaimiro 'E' sand and Upper Farewell Formation is comparable to deposits from the Maui region (Table 6.3). For example, within the Whio region the 'E' sand is interpreted to have been deposited contemporaneously with the E Sand coastal facies in the Maui Field to the northwest (OMV NZ, 2015). This stratigraphic interval is considerably deeper to the north within the Maui Field (MBR-1/MBW-2) with a Kaimiro 'E' sand - Farewell Formation contact situated at a true vertical depth of 3181 mTVDSS, in comparison to the shallower 2517.8 mTVDSS interpreted from Whio-1.

For sandstone, strength prediction assigned to the sand dominated Upper Farewell Formation (2682-2730 m), the porosity-UCS log varies from 20-80 MPa. Two wellbores were used for strength testing of the Farewell Formation, MBR-1 and MBW-2, from the Maui Field are positioned approximately 40 km north of Whio-1 (Figure 6.1). The strength predictions from the porosity-UCS log are more aligned with laboratory strength measurements from the corresponding wells, MBR-1 and MBW-2 from 13-55MPa (Table 6.3). This suggests porosity based UCS predictions provide the most accurate values for sandstones. For shale, the compressional slowness-UCS profile provides more consistent strength attributed to the shale layers (~30 MPa). The shale strength predictions from the compressional slowness-UCS log are supported by strength data from Amokura-1 in the Tui region, with a UCS of 58MPa for the Kaimiro 'E' shale (New Zealand Overseas Petroleum Limited, 2005). All available strength data attributed to the Taranaki Basin can be found in Appendix A.

Table 6-3 Rock strength data for the lower stratigraphic interval corresponding to the Kaimiro 'E' shale and Farewell Formation, from wells (MBR-1, MBW-2 and Amokura-1) within the Southern Taranaki Basin

Wellbore	Depth (mMDRT)	UCS	Lithotype	Formation
MBR-1	3476-3635	13-55MPa	Sand	Farewell
MBW-2	4077-4186	13-25MPa	Sand	Farewell
Amokura-1	3664.25	58MPa	Shale	Kaimiro 'E' shale

As presented in chapter 5, we demonstrated an inversely proportional relationship of UCS with both porosity and mean grain size. The maximum UCS measurement attained for the Farewell Formation of 55 MPa (MBR-1) was attributed to the smallest grain size of 102 µm, with a porosity fraction of 0.16. The minimum UCS measurement of 13 MPa attained for both MBR-1 and MBW-2 was attributed to the largest grain sizes of 272 µm and 265 µm, respectively, both with a porosity fraction of 0.22 and 0.21. We suggest that to better constrain strength prediction between clean sands and shaly sandstones that an input variable of grain size should be incorporated into empirical relations (Chapter 5; Chang et al., 2006; Fjaer et al., 1992); this is supported by the constrained strength values predicted using Equation 6.12 for the Miocene interval.

6.5.4. **Implication for Contemporary Stress Field Assessment**

Stress magnitudes can be challenging to obtain but are essential for the application of geomechanical modelling. According to single focal mechanism data, a predominant strike slip tectonic stress regime exists across the Taranaki region ($S_{HMax} > S_v > S_{hmin}$), with a localised normal faulting regime ($S_v > S_{HMax}$) (Rajabi et al., 2016). Assessment of individual petroleum reports highlights the Pohokura, Moana, Kauri, TAWN fields and Te Kiri Prospect, are positioned within a strike-slip regime (Shell Todd Oil Services Limited, 2001; OMV NZ, 2006; Swift Energy, 2007a; Swift Energy, 2007b; Todd Energy, 2010). However, Massiot et al. (2019), delineating the in-situ stress field across the southern Taranaki Basin (Tui, Maui and Maari-Manaia regions), suggest a transitional strike-slip to normal stress regime, with similar magnitudes for S_{Hmax} and S_v ($S_{Hmax}/S_v \sim$

1); similar to the Mangatoa and Mangahewa fields (Mildren, 2009; Todd Energy, 2015). The variation from strike-slip to a transitional strike slip/normal regime may be resultant from deviation of S_{Hmax} from its regional trend; alternatively, potential miscalculation of SHmax stress magnitude using poorly calibrated σc in Equation 6.12 could result in false interpretation of the local stress regime. A major drawback of the S_{Hmax} calculation is the inability to confidently predict strength as an input parameter from uncalibrated logs, as acknowledged by Massiot et al. (2019).

$$S_{Hmax} = \frac{UCS + 2P_p + \Delta P + \sigma^{\Delta T} - S_{hmin}(1 + 2\cos(2\theta))}{1 - 2\cos(2\theta)}$$

Where,

σ_c = Uniaxial compressive strength (MPa)

P_p = Pore Pressure (MPa)

ΔP = Pressure difference between formation and borehole

$\sigma^{\Delta T}$ = Thermal stress effect

2Θ = π-Ø, Ø is the angle of borehole breakout (width) in radians

Massiot et al. (2019) adopted a two-step approach for estimating UCS, selecting a preferred relation based upon dominant lithology and providing a range of UCS predictions from different empirical relations; this approach provides an increased level of confidence for first order approximations of UCS. This investigation has shown that the use of compressional slowness for the development of the UCS-depth profile works most effectively for shaly intervals; and the porosity-UCS log, which follows the configuration of the mechanical stratigraphy (GR log), is better utilized for strength characterisation of clean and shaly sandstones. Lower UCS values attributed to the porosity-UCS result in a lower S_{Hmax} magnitude calculation.

The use of uncalibrated prediction tools in the Taranaki Basin is likely to overestimate the strength. Many empirical equations used to convert compressional wave slowness

from downhole measurements into UCS were mainly developed in the Gulf of Mexico and North Sea, where sandstones and mudstones are well differentiated (Chang et al., 2006). As previously mentioned, rocks in the southern Taranaki Basin are represented by mixed lithologies, with a dominant presence of shaly sandstones (Massiot et al., 2019). Over-prediction of strength, suggested from comparison of calibrated and uncalibrated logs, and use of Figure 6.9, could result in the designation of a false stress regime interpretation. An overestimation of S_{Hmax} from overestimated UCS predictions could result in assumption of strike-slip conditions ($S_{Hmax}>S_v$), while in reality a normal faulting regime exists. Inaccurate assessment of present-day stresses can lead to expensive instability or collapse of boreholes (Zoback, 2007). This concern is emphasised when evaluating a region with a known transitioning stress regime; Massiot et al. (2019) calculated a median S_{Hmax}/S_v ratio of 1.1 for both Whio-1, and nearby Maari-1. This research corroborates the work of Massiot et al. (2019), suggesting a transitional strike-slip/normal stress regime in proximity to Whio-1 with a S_{Hmax}/S_v ratio ranging from 0.9-1.6. Over-prediction of S_{Hmax} in transitional stress regimes could underestimate the extent of rock surrounding the wellbore that is subjected to a partial normal stress regime.

6.6. Conclusions

- The use of sedimentary facies to delineate mechanical stratigraphy in the development of a 1D MEM allows for extrapolation of mechanical properties away from the wellbore in a systematic manner. This is based upon the assumption that porosity and grain size provide dominant controls on the mechanical rock properties.
- In general, the use of compressional slowness is most suited for the prediction of shale strength, while for clean and shaly sandstones, porosity provides better strength indicators. The use of a grain size variable within porosity-UCS prediction can act to further constrain strength measurements between clean and shaly sands. Additional research could be used to develop an empirical

function incorporating the GR log (proxy for grain size) for an improved strength prediction into the porosity-UCS relationship.

- Irrespective of the relationship chosen for strength prediction, without localised calibration of the prediction tool the strength estimate is likely to be under or over predicted. The under or overestimation of rock strength can lead to misrepresentation of the stress regimes, especially in a transitional regime setting. In this instance, an over-prediction of UCS from uncalibrated logs acts to underestimate the rock surrounding the wellbore subjected to a partial normal stress regime.

Chapter Seven – Concluding Remarks

7.1. Research Summary

Key findings of this research have highlighted the textural properties of siliciclastic rocks, noticeably grain size and grain sorting, should provide the principal basis for mechanical rock property characterisation of reservoirs. Sedimentary facies are associated with changes in grain size and sorting as a result of the depositional environment, and thus can provide the basis for quantifiable units of physical rock properties and mechanical strength parameter.

1. **What are the dominant microscale controls on physical rock properties, and can sedimentary facies be used to allocate quantifiable data to a reservoir unit?**

   This study has demonstrated that reservoir physical properties are regulated by the textural properties of the rock e.g. grain size and grain sorting. Grain sorting provides the dominant control on dominant pore type e.g. intergranular pores and micropores; pore throat diameter and porosity fraction exhibit a proportional relationship with grain sorting. Grain size is deemed independent of porosity fraction but demonstrates a control on permeability with smaller grain sizes attributed to lower flow rates; under a constant grain size there is a proportional relationship between pore throat diameter and permeability. Sandstone facies can be used as a first order assessment for the presence of reservoir heterogeneities which may control flow capabilities e.g. grain size and grain sorting.

   In order to reduce the inaccuracy of reservoir models, physical properties need to be quantified in a systematic way which incorporates as much fine detail as possible. Stochastic modelling utilizes the distribution of sedimentary facies to extrapolate the quantifiable physical property data across a reservoir interval. Comparison of sandstone facies within the onshore Pakawau Sub-basin and

offshore Maui Field both attribute the highest permeabilities to the cross bedded sandstone facies.

2. **Which are the dominant controls on the mechanical rock properties of sandstones, and how can these be incorporated to accurately predict rock strength?**

Statistical analysis undertaken on physical property-rock strength relationships from measurements derived in the laboratory demonstrates the most statistically significant relationship is attributed to porosity-UCS, expressed as:

$$\mathrm{UCS} = 108\mathrm{e}^{-10\mathrm{n}}$$

This empirical relation was validated using previously measured rock strength data from the Pohokura Field. In addition, textural analysis presented a dominant control of mean grain size on UCS; grain size (D) and porosity (n) are considered independent in this study, and could be incorporated into a multivariate relationship, expressed as:

$$\mathrm{UCS} = 430\left(\frac{1}{\sqrt{\mathrm{D}}}\right) - 90\mathrm{n} + 7$$

An input variable of grain size, or GR (often used a proxy for grain size), allows for refined strength prediction between clean and mixed lithologies e.g. shaly sands. Based on the assumption of the dominant control on rock strength attributed to mean grain size and porosity, we can infer that the mechanical properties of a reservoir should follow a similar spatial distribution pattern to that used for flow properties in stochastic models.

3. **How is the assessment of formation stability improved from accurate determination of mechanical strength and failure parameters using locally calibrated relationships?**

   The responsiveness of both the Hoek-Brown and Mohr-Coulomb strength parameters to change in grain size suggest that both these criteria can be utilized as a predictive tool for reservoir failure in petroleum geomechanics. An advantage of the Hoek-Brown failure criterion is the ability to incorporate rock mass properties (Hoek and Brown, 2018) with material constants that vary by lithotype for rock mass characterisation of reservoirs (e.g. Villeneuve et al., 2018; Heap et al., 2019). However, a practical disadvantage of the Hoek Brown Criterion is the current absence of literature relating the material parameter, m_i, to commonly measured physical properties on wireline logs (Zoback, 2007); by defining m_i as a function upon UCS, a method is proposed to derive a Hoek-Brown failure criterion for Southern Taranaki Basin reservoirs without necessitating triaxial strength data. Rock strength predictions from locally calibrated relationships reduce the likelihood of under/overestimation of UCS. The under or overestimation of rock strength can lead to misrepresentation of the stress regimes, especially in a transitional regime setting such as the Southern Taranaki Basin. In the example of the strike-slip regime proposed for the Maui-Maari region, over-prediction of UCS from uncalibrated logs leads to underestimation of the rock surrounding the wellbore subjected to a partial normal stress regime.

7.1.1. **Proposed Workflow Characterisation**

Based upon the research presented in this thesis, the following steps are recommended for improving rock strength predictions to incorporate into geomechanical models.

I. Evaluation of laboratory data through statistical analysis to develop locally calibrated physical property-rock strength relations for improved UCS predictions. Independent empirical relations to be developed for individual lithotypes. For the Southern Taranaki Basin, porosity-UCS provides better

estimates for sandstones, and compressional slowness-UCS provides better estimates for shales.

II. Detailed textural analysis of sedimentary rocks to be utilized as input variables within multivariate physical property-rock strength relations e.g. grain size and grain sorting. The use of a grain size variable within porosity-UCS prediction will act to further constrain strength measurements between clean and shaly sands.

III. Application of numerous physical-property rock strength relations provides bounds for UCS log prediction; calibrated with laboratory strength data.

IV. Development of failure criterion parameter logs e.g. UCS, angle of internal friction and cohesion, allow for the development of a failure criterion at any depth of interest.

7.2. Potential Future Advances

The Taranaki Basin is poorly represented with geomechanical investigation of the offshore region in its early stages, despite more complex and deeper petroleum prospects than the onshore region; the only offshore geomechanical reports are attributed to the Amokura Field, and the Kaupokonui Prospect in the Southern Taranaki Basin (New Zealand Overseas Petroleum Limited, 2005; New Zealand Oil and Gas, 2010). Existing onshore geomechanical studies were undertaken to ensure a minimal risk of formation damage and wellbore instability during drilling, or to provide sand failure, pore pressure and fracture gradient predictions (Shell Todd Oil Services Limited, 2002; New Zealand Oil and Gas, 2010; Todd Energy, 2014). Future work could build upon this understanding focused on wellbore stability assessment of other offshore regions. As more UCS and triaxial data become available in the Taranaki basin, empirical relationships can continue to be calibrated to provide improved predictive tools for strength estimates and development of failure criteria. In turn, no comprehensive 3D geomechanical model has ever been developed within the Taranaki region; seismic inversions could be used in conjunction with the rock property characterisation and knowledge of contemporary stress field to develop this.

In 2018, the New Zealand government declared an end to offshore exploration permits including the Taranaki Basin, producing a negative forecast for petroleum exploration in New Zealand. In turn, New Zealand's target for a carbon neutral environment by 2050 is likely to see investment in CO_2 reduction technologies including Carbon Capture Storage (CCS); whilst petroleum reservoirs may become obsolete as energy sources, they are uniquely positioned for carbon storage. CCS requires an understanding of the responsive behaviour of rock properties under evolving stresses. For a true geomechanical assessment of rock behaviour under an evolving stress field requires true-triaxial experiments with three independently controlled principal stresses; this would allow modelling of in-situ basin conditions. In turn, it would allow for determination of different failure criterion where σ_2 is assessed separately from σ_3, which some researchers consider essential for representative geomechanical modelling. A separate element of controlled pore pressure would also allow for assessment of coupled processes.

Chapter Eight - References

Addis, M.A., 2017. The geology of geomechanics: petroleum geomechanical engineering in field development planning. Geological Society, London, Special Publications, 458(1), pp.7-29.

Al-Ajmi, A.M. and Zimmerman, R.W., 2005. Relation between the Mogi and the Coulomb failure criteria. International Journal of Rock Mechanics and Mining Sciences, 42(3), pp.431-439.

Alexander, J., 1993. A discussion on the use of analogues for reservoir geology. Geological Society, London, Special Publications, 69(1), pp.175-194.

Ali, A.H.A., Brown, T., Delgado, R., Lee, D., Plumb, D., Smirnov, N., Marsden, R., Prado-Velarde, E., Ramsey, L., Spooner, D. and Stone, T., 2003. Watching rocks change—Mechanical earth modelling. Oilfield Review, 15(1), pp.22-39.

Anderson, E.M., 1905. The dynamics of faulting. Transactions of the Edinburgh Geological Society, 8(3), pp.387-402.

ASTM D4404–18, 2018. Standard Test Method for Determination of Pore Volume and Pore Volume Distribution of Soil and Rock by Mercury Intrusion Porosimetry. Annual Book of ASTM Standards, American Society for Testing Materials, West Conshohocken, PA.

ASTM D4543-19, 2019. Standard Practices for Preparing Rock Core as Cylindrical Test Specimens and Verifying Conformance to Dimensional and Shape Tolerances. Annual Book of ASTM Standards. West Conshohocken, PA: ASTM International.

ASTM D7012-14. Standard Test Methods for Compressive Strength and Elastic Moduli of Intact Rock Core Specimens under Varying States of Stress and Temperatures. Annual Book of ASTM Standards. West Conshohocken, PA: ASTM International.

Atapour, H. and Mortazavi, A., 2018. The influence of mean grain size on unconfined compressive strength of weakly consolidated reservoir sandstones. Journal of Petroleum Science and Engineering, 171, pp.63-70.

Bal, A., 1992. Cessation of Tasman Sea spreading recorded as a sequence boundary. Evolution of the Tasman Sea Basin. Proceedings of the Tasman Sea Conference, Christchurch, New Zealand, 23-30.

Bal, A. and Lewis, D. W., 1994. A cretaceous - early tertiary Macrotidal estuarine-fluvial succession: Puponga coal measures in Whanganui inlet, onshore Pakawau sub-basin, Northwest Nelson, New Zealand, New Zealand Journal of Geology and Geophysics, 37(3), pp. 287-307.

Barton, C. A., Zoback, M. D. and Burns, K. L. 1988. In-situ stress orientation and magnitude at the Fenton Geothermal Site, New Mexico, determined from wellbore breakouts. Geophysical Research Letters, 15, 467-470.

Baud, P., Zhu, W., Wong, T.F., 2000. Failure mode and weakening effect of water on sandstone. Journal of Geophysical Research: Solid Earth 105(B7), 16371–16389.

Bell, F.G., 1978. The physical and mechanical properties of the fell sandstones, Northumberland, England. Engineering Geology, 12, pp.1-29.

Benz, T., Schwab, R., Kauther, R.A. and Vermeer, P.A., 2008. A Hoek–Brown criterion with intrinsic material strength factorization. International Journal of Rock Mechanics and Mining Sciences, 45(2), pp.210-222.

Bésuelle, P., Baud, P., Wong, T.F., 2003. Failure mode and spatial distribution of damage in Rothbach sandstone in the brittle-ductile transition. Pure and Applied Geophysics 160(5–6), 851–868

Biot, M.A., 1941. General three-dimensional theory of poroelasticity. J. Appl. Phys, 12, pp.155-164.

BJ Services Technology Center, 2007. Elastic Properties of Mangahewa Formation Core from the Mangahewa-3 Well, Mangahewa Field, New Zealand. BJ Services Technology Center report 07-07-0163. Tomball Technology Center, Perth, Australia.

Bradford, I.D.R., Fuller, J., Thompson, P.J., Walsgrove, T.R., 1998. Benefits of assessing the solids production risk in a North Sea reservoir using elastoplastic modelling. SPE/ISRM Eurock '98 held in Trondheim, Norway, 8–10 July 1998, pp. 261–269.

Bridge, J.S. and Lunt, I.A., 2006. Depositional models of braided rivers. Braided rivers: Process, deposits, ecology and management, 36, p.11e50.

Browne, G.H., Kennedy, E.M., Constable, R.M., Raine, J.I., Crouch, E.M. and Sykes, R., 2008. An outcrop-based study of the economically significant Late Cretaceous Rakopi Formation, northwest Nelson, Taranaki Basin, New Zealand. New Zealand Journal of Geology and Geophysics, 51(4), pp.295-315.

Browne, G. H., 2009. First New Zealand record of probable dinosaur footprints from the Late Cretaceous North Cape Formation, northwest Nelson, New Zealand Journal of Geology and Geophysics, 52(4), pp. 367-377.

Bryant, I.D., Marshall, M.G., Greenstreet, C.W., Voggenreiter, W.R., Cohen, J.M. and Stroemmen, J.F., 1994. Integrated geological reservoir modelling of the Maui field, Taranaki Basin, New Zealand. In 1994 New Zealand petroleum conference proceedings: the post Maui challenge-investment and development opportunities. Wellington: Energy and Resources Division (pp. 256-281).

Burley, S. and Worden, R. eds., 2009. Sandstone diagenesis: recent and ancient (Vol. 24). John Wiley & Sons.

Cant, J. L., Siratovich, P. A., Cole, J. W., Villeneuve, M. C. and Kennedy, B. M., 2018. Matrix permeability of reservoir rocks, Ngatamariki geothermal field, Taupo Volcanic Zone, New Zealand. Geothermal Energy, 6(1), pp. 1-28.

Chang, C., Zoback, M. D. and Khaksar, A., 2006. Empirical relations between rock strength and physical properties in sedimentary rocks, Journal of Petroleum Science and Engineering, 51(3), pp. 223-237.

Chantellier, J.Y. & Hitchings, V.H., 1987. Geological investigations of cores from the C and D reservoirs in well Maui-7, Maui Field, New Zealand. PML 381012. New Zealand unpublished open file petroleum report 1302. Ministry of Economic Development, Wellington.

Chen, G., Du, Guichao., Zhang, Gongcheng., Wang, Qi., Lv, Chengfu., 2011. Chlorite cement and its effect on the reservoir quality of sandstones from the Panyu low-uplift, Pearl River Mouth Basin. Petroleum Science, 8(2), pp. 143-150.

Coates, G.R. and Denoo, S.A., 1981. Mechanical properties program using borehole analysis and Mohr's circle. In SPWLA 22nd Annual Logging Symposium. Society of Petrophysicists and Well-Log Analysts.

Colmenares, L.B. and Zoback, M.D., 2002. A statistical evaluation of intact rock failure criteria constrained by polyaxial test data for five different rocks. International Journal of Rock Mechanics and Mining Sciences, 39(6), pp.695-729.

Crowley, J., Way, C.J. & Purcell, D., 1989. Kupe South-4 well completion report. PPL38116. New Zealand unpublished open file petroleum report 1483. Ministry of Economic Development, Wellington.

Diederichs, M., 2003. Manuel Rocha Medal Recipient Rock Fracture and Collapse Under Low Confinement Conditions. Rock Mechanics and Rock Engineering 36, pp.339–381

Douglas, K.J., 2002. The shear strength of rock masses. PhD thesis, School of Civil and Environmental Engineering, University of New South Wales, Sydney, Australia.

Doyle, J.D., and Sweet, M.L., 1995. Three-dimensional distribution of lithofacies, bounding surfaces, porosity, and permeability in a fluvial sandstone--Gypsy Sandstone of Northern Oklahoma. AAPG bulletin, 79(1), pp.70-95.

Drucker, D.C. and Prager, W., 1952. Soil mechanics and plastic analysis or limit design. Quarterly of applied mathematics, 10(2), pp.157-165.

Eberhardt, E., 2012. The hoek–brown failure criterion. Rock mechanics and rock engineering, 45(6), pp.981-988.

Emery, D and Myers, K.J., 1996. Sequence stratigraphy. Blackwell Science Limited, pp. 297.

Fischer, K. and Henk, A., 2013. A workflow for building and calibrating 3-D geomechanical models–a case study for a gas reservoir in the North German Basin. Solid Earth, 4(2), pp.347-355.

Fjaer, E., Holt, R.M., Horsrud, P., Raaen, A.M., Risnes, R., 1992. Petroleum Related Rock Mechanics. Elsevier, Amsterdam.

Fredrich, J.T., Evans, B. and Wong, T.F., 1990. Effect of grain size on brittle and semibrittle strength: Implications for micromechanical modelling of failure in compression. Journal of Geophysical Research: Solid Earth, 95(B7), pp.10907-10920.

Freyburg, E., 1972. Der Untere und mittlere Buntsandstein SW Thuringen in seinen gesteinstechnischen Eigenschaften, Ber. Dte. Ges. Geo!. Wiss. A; Berlin, 176,911-919

Ghazvinian, A.H., Fathi, A. and Moradian, Z.A., 2008. Failure behaviour of marlstone under triaxial compression. International Journal of Rock Mechanics and Mining Sciences, 5(45), pp.807-814.

Gholami, R., Moradzadeh, A., Rasouli, V. and Hanachi, J., 2014. Practical application of failure criteria in determining safe mud weight windows in drilling operations. Journal of Rock Mechanics and Geotechnical Engineering, 6(1), pp.13-25.

Goodman, H.E., 2005. Bridging the Gap Between the Earth Science and Engineering Disciplines: The Strategy of Using Acoustics Technology To Characterize Rock Mechanical Properties for Optimal Well Design—Reliability and Placement. In International Petroleum Technology Conference. International Petroleum Technology Conference.

Greer, G., Marquet, M. and Saunders, C., 2013. Petroleum Exploration and Extraction Study. Agribusiness and Economics Research Unit. Report prepared for the Gisborne District Council.

Guerra, C., Fischer, K. and Henk, A., 2019. Stress prediction using 1D and 3D geomechanical models of a tight gas reservoir—A case study from the Lower Magdalena Valley Basin, Colombia. Geomechanics for Energy and the Environment, 19, p.100113.

Halliburton Australia Pty Ltd, 1999. Maari-1 & 1A well completion report, PPL 38413. New Zealand unpublished openfile petroleum report 1572. Ministry of Economic Development, Wellington.

Heap, M.J., Farquharson, J.I., Baud, P., Lavallée, Y., Reuschlé, T., 2015. Fracture and compaction of andesite in a volcanic edifice. Bulletin of Volcanology 77, 55.

Heap, M. J., Reuschlé, T., Farquharson, J. I. and Baud, P., 2018. Permeability of volcanic rocks to gas and water. Journal of Volcanology and Geothermal Research, 354, pp. 29-38.

Heap, M., Villeneuve, M., Kushnir, A., Farquharson, J., Baud, P. and Reuschlé, T., 2019. Rock mass strength and elastic modulus of the Buntsandstein: An important lithostratigraphic unit for geothermal exploitation in the Upper Rhine Graben. Geothermics 77, 236–256.

Heidbach, O., Tingay, M., Barth, A., Reinecker, J., Kurfeß, D., and Müller B., 2010. Global crustal stress pattern based on the World Stress Map database release 2008. Tectonophysics, 482(1-4), pp.3-15.

Henk, A. and Frischbutter, A., 2009, June. Predicting Stress and Fracture Orientations with Geomechanical Reservoir Models–Lessons Learned from a Case Study. In 71st EAGE Conference and Exhibition incorporating SPE EUROPEC 2009.

Henk, A., Frischbutter, A. and Tawengi, K.S., 2010. Geomechanical reservoir models–a case study from the Sirte Basin, Libya. Oil Gas-Eur, pp.18-22.

Herwanger, J., 2014, December. Seismic geomechanics: How to build and calibrate geomechanical models using 3D and 4D seismic data. In Education Days Stavanger 2014.

Higgs, K. E., Arnot, M. J., Browne, G. H. and Kennedy, E. M., 2010. Reservoir potential of Late Cretaceous terrestrial to shallow marine sandstones, Taranaki Basin, New Zealand. Marine and Petroleum Geology, 27(9), pp. 1849-1871.

Higgs, K. E., Strogen, D., Griffin, A., Ilg, B., Arnot, M., 2012. Reservoirs of the Taranaki Basin. In: 2012/13a, D.S. (ed.). GNS Science

Higgs, K. E., Crouch, E. M. and Raine, J. I., 2017. An interdisciplinary approach to reservoir characterization; an example from the early to middle Eocene Kaimiro Formation, Taranaki Basin, New Zealand, Marine and Petroleum Geology, 86, pp. 111-139.

Hoek, E., Brown, E.T., 1980. Underground excavations in rock. CRC Press.

Hoek, E. and Brown, E.T., 1980. Empirical strength criterion for rock masses. Journal of Geotechnical and Geoenvironmental Engineering, 106(ASCE 15715).

Hoek, E. and Brown, E.T., 1997. Practical estimates of rock mass strength. International journal of rock mechanics and mining sciences, 34(8), pp.1165-1186.

Hoek, E. and Brown, E.T., 2019. The Hoek–Brown failure criterion and GSI–2018 edition. Journal of Rock Mechanics and Geotechnical Engineering, 11(3), pp.445-463.

Hoek, E., Carranza-Torres, C. and Corkum, B., 2002. Hoek-Brown failure criterion-2002 edition. Proceedings of NARMS-Tac, 1(1), pp.267-273.

Hoek, E. and Franklin, J.A., 1967. A simple triaxial cell for field or laboratory testing of rock. Imperial College of Science and Technology, University of London.

Hoek, E., Marinos, P., 2000. Predicting tunnel squeezing problems in weak heterogeneous rock masses. Tunnels and tunnelling international, Part 1 – November 2000, Part 2 – December 2000.

Hoek, E., Wood, D. and Shah, S., 1992. A modified Hoek–Brown failure criterion for jointed rock masses. In Rock Characterization: ISRM Symposium, Eurock'92, Chester, UK, 14–17 September 1992 (pp. 209-214). Thomas Telford Publishing.

Holt, R.M., Ingsoy, P. and Mikkelson, M., 1989. Rock mechanical analysis of North Sea reservoir formations. SPE Formation Evaluation, 4(01), pp.33-37

Hu, X., Hu, S., Jin, F. and Huang, S., 2017. Physics of petroleum reservoirs. Springer.

Hurst, A. and Nadeau, P. H., 1995. Clay microporosity in reservoir sandstones: an application of quantitative electron microscopy in petrophysical evaluation. AAPG bulletin, 79(4), pp. 563-573.

Jaeger, J.C. and Cook, N.G.W., 1979. Fundamentals of Rock Mechanics, Chapman and Hall, Ltd. London.

Jizba, D.L., 1992. Mechanical and acoustical properties of sandstones and shales.

Joyce, R., 2018. Assessment of paleo-depositional environments and reservoir potential of the Late Cretaceous North Cape Formation, Nelson, New Zealand. Unpublished MSc Thesis, University of Canterbury, Christchurch, New Zealand.

Katz, A. J. and Thompson, A. H., 1986. Quantitative prediction of permeability in porous rock. Physical Review B, 34(11), pp. 8179-8181.

Kazianis, C., 2018. Rock strength Characteristics of Pliocene and Miocene Aged Marine Sediments in the Taranaki Basin, New Zealand. New Zealand unpublished open-file petroleum report 5595. Ministry of Economic Development, Wellington

Khaksar, A., Taylor, P.G., Fang, Z., Kayes, T.J., Salazar, A. and Rahman, K., 2009. Rock strength from core and logs, where we stand and ways to go. In EUROPEC/EAGE Conference and Exhibition. Society of Petroleum Engineers.

Kirsch, E.G., 1898. Die Theorie der Elastizität und die Bedürfnisse der Festigkeitslehre. Zeitschrift des Vereines deutscher Ingenieure, 42, 797–807

King, P., Naish, T. and Thrasher, G., 1991. Structural cross sections and selected palinspastic reconstructions of the Taranaki Basin, New Zealand, New Zealand Geological Survey Report G, 150.

King, P. and Thrasher, G., 1992. Post-Eocene Development of the Taranaki Basin, New Zealand: Convergent Overprint of a Passive Margin, Southwest Pacific and Eastern Indian Ocean Margins.

King, P. R. and Thrasher, G. P., 1996. Cretaceous Cenozoic geology and petroleum systems of the Taranaki Basin, New Zealand. Institute of Geological & Nuclear Sciences.

Klinkenberg, L.,1941. The permeability of porous media to liquids and gases. Drilling and production practice.

Knox, G. J., 1982. Taranaki Basin, Structural Style and Tectonic Setting. New Zealand Journal of Geology and Geophysics, 25(2), pp. 125-140.

Koninklijke/Shell Exploratie, 1986. Geological investigations of cores from the C1 and D1 reservoirs in well Maui A1 (G) Maui Field New Zealand. New Zealand unpublished open file petroleum report 818. Ministry of Economic Development, Wellington

Labuz, J.F. and Zang, A., 2012. Mohr-Coulomb Failure Criterion. Rock. Mech. Rock. Eng., 45, 975.

Larionov, V.V., 1969. Radiometry of boreholes (in Russian). Nedra, Moscow, p.127.

Last, N., Plumb, R., Harkness, R., Charlez, P., Alsen, J. and McLean, M., 1995. An integrated approach to evaluating and managing wellbore instability in the Cusiana field, Colombia, South America. In SPE annual technical conference and exhibition. Society of Petroleum Engineers.

Laubach, S.E., Olson, J.E. and Gross, M.R., 2009. Mechanical and fracture stratigraphy. AAPG bulletin, 93(11), pp.1413-1426.

Longuemare, P., Mainguy, M., Lemonnier, P., Onaisi, A., Gérard, C. and Koutsabeloulis, N., 2002. Geomechanics in reservoir simulation: overview of coupling methods and field case study. Oil & gas science and technology, 57(5), pp.471-483.

Lunt, I.A., Bridge, J.S. and Tye, R.S., 2004. A quantitative, three-dimensional depositional model of gravelly braided rivers. Sedimentology, 51(3), pp.377-414.

Martin, K.R., 1989. Petrology, diagenesis and reservoir quality of the Farewell Formation in Kupe South No. 4, Taranaki Basin. In: Crowley, J., Way, C.J. & Purcell, D., 1989.

Martin, K.R., 2001. Petrology, diagenesis and reservoir quality of Kapuni Group sandstones in Pohokura-1 and Pohokura-2, PEP38459, Taranaki Basin. New Zealand unpublished open file petroleum report 2601. Ministry of Economic Development, Wellington.

Massiot, C., Seebeck, H., Nicol, A., McNamara, D.D., Lawrence, M.J., Griffin, A.G., Thrasher, G.P., O'Brien, G. and Viskovic, G.P.D., 2019. Effects of regional and local stress variabilities on fault slip tendency in the southern Taranaki Basin, New Zealand. Marine and Petroleum Geology.

McBeath, D. M., 1977. Gas-condensate fields of the Taranaki Basin, New Zealand. New Zealand Journal of Geology and Geophysics, 20(1), pp. 99-127.

McNally, G.H., 1987. Estimation of coal measures rock strength using sonic and neutron logs. Geoexploration, 24(4-5), pp.381-395.

Meyer, K. and Klobes, P., 1999. Comparison between different presentations of pore size distribution in porous materials. Fresenius' journal of analytical chemistry, 363(2), pp.174-178.

Mildren, S., 2009. Mangatoa wellbore stability and fracture susceptibility assessment. New Zealand unpublished open-file petroleum report 4011. Ministry of Economic Development, Wellington

Milton, J.S. and Arnold, J.C., 1994. Schaum's Outline of Introduction to Probability & Statistics: Principles & Applications for Engineering & the Computing Sciences. McGraw-Hill Higher Education.

Moazzeni, A.R., Nabaei, M., Shahbazi, K. and Shadravan, A., 2010. Mechanical Earth Modelling Improves Drilling Efficiency and Reduces Non-Productive Time (NPT). In SPE Deep Gas Conference and Exhibition. Society of Petroleum Engineers.

Mogi, K., 1971. Fracture and flow of rocks under high triaxial compression. Journal of Geophysical Research, 76(5), pp.1255-1269.

Moos, D., Zoback, M.D. and Bailey, L., 1999. Feasibility study of the stability of openhole multilaterals, Cook Inlet, Alaska. 1999 SPE Mid-Continent Operations Symposium held in Oklahoma City, Oklahoma, 28–31 March 1999, SPE 52186.

Moos, D. and Barton, C., Baker Hughes Inc, 2014. Method to improve reservoir simulation and recovery from fractured reservoirs. U.S. Patent 8,898,046.

Morad, S. and Aldahan, A.A., 1987. Diagenetic replacement of feldspars by quartz in sandstones. Journal of Sedimentary Research, 57(3), pp.488-493.

Nelson, P. H., Batzle, M. L. and Fanchi, J., 2006. Single-phase permeability. Petroleum engineering handbook: General engineering: Richardson, Texas, Society of Petroleum Engineers, 1, pp. 687-726.

New Zealand Overseas Petroleum Ltd, 2004. Pukeko-1 well completion report. New Zealand unpublished open file petroleum report 2928. Ministry of Economic Development,

New Zealand Overseas Petroleum Limited, 2005. Amokura-1 Advanced Core Analysis Study. New Zealand unpublished open-file petroleum report 3150. Ministry of Economic Development, Wellington

New Zealand Oil and Gas, 2010. 1D Pore Pressure and Fracture Gradient Prediction for Well Planning, Kaupokonui Prospect. New Zealand unpublished open-file petroleum report 4422. Ministry of Economic Development, Wellington

New Zealand Petroleum and Minerals, 2014/15. New Zealand's Petroleum Basins

Nicol, A., Mazengarb, C., Chanier, F., Rait, G., Uruski, C. and Wallace, L., 2007. Tectonic evolution of the active Hikurangi subduction margin, New Zealand, since the Oligocene, Tectonics, 26(4), pp. TC4002.

OMV New Zealand Limited, 1998-2006. Maari Platform Geotechnical Information. New Zealand unpublished open-file petroleum report 3312. Ministry of Economic Development, Wellington

OMV NZ, 2006. Moana Prospect Cross-Fault Pressure Difference Analysis, Northern Taranaki Graben, New Zealand. New Zealand unpublished open-file petroleum report 3647. Ministry of Economic Development, Wellington

OMV NZ, 2015. PEP 51313- Whio-1 Well Completion Report New Zealand unpublished open-file petroleum report 5207. Ministry of Economic Development, Wellington

OMV NZ, 2015. PEP 51313- Composite Petrophysical Log (Appendix G), Whio-1 Well Completion Report New Zealand unpublished open-file petroleum report 5207. Ministry of Economic Development, Wellington

OMV NZ, 2016. PEP 51313- Stage 2 Prospectivity Interpretation Report. New Zealand unpublished open-file petroleum report 5332. Ministry of Economic Development, Wellington

Ongley, M. and Macpherson, E. O., 1923. The geology and mineral resources of the Collingwood Subdivision, Karamea Division, New Zealand Geological Survey, B: Dept. of Mines, Geological Survey, New Zealand.

Oyler, D.C., Mark, C. and Molinda, G.M., 2010. In situ estimation of roof rock strength using sonic logging. International Journal of Coal Geology, 83(4), pp.484-490.

Palchik, V., 1999. Influence of porosity and elastic modulus on uniaxial compressive strength in soft brittle porous sandstones. Rock Mechanics and Rock Engineering, 32(4), pp.303-309.

Pan, X.D. and Hudson, J.A., 1988. A simplified three-dimensional Hoek-Brown yield criterion. In ISRM International Symposium. International Society for Rock Mechanics and Rock Engineering.

Pilaar, W. and Wakefield, L., 1978. Structural and stratigraphic evolution of the Taranaki Basin, offshore North Island, New Zealand. The APPEA Journal, 18(1), 93-101.

Pittman, E. D., 1992. Relationship of porosity and permeability to various parameters derived from mercury injection-capillary pressure curves for sandstone. AAPG bulletin, 76(2), pp. 191-198.

Plumb, R., Edwards, S., Pidcock, G., Lee, D. and Stacey, B., 2000. The mechanical earth model concept and its application to high-risk well construction projects. In IADC/SPE Drilling Conference. Society of Petroleum Engineers.

Potter, P.E., Maynard, J.B. and Pryor, W.A., 2012. Sedimentology of shale: study guide and reference source. Springer Science & Business Media.

Purcell, W., 1949. Capillary pressures-their measurement using mercury and the calculation of permeability therefrom. Journal of Petroleum Technology, 1(2), pp. 39-48.

Rajabi, M., Ziegler, M., Tingay, M., Heidbach, O. and Reynolds, S., 2016. Contemporary tectonic stress pattern of the Taranaki Basin, New Zealand. Journal of Geophysical Research: Solid Earth, 121(8), pp.6053-6070.

Rattenbury, M. S., Cooper, R. A. and Johnston, M. R., 1998. Geology of the nelson area. Lower Hutt, New Zealand: Institute of Geological & Nuclear Sciences Limited.

Rattenbury, M. S. and Isaac, M. J., 2012. The QMAP 1:250 000 Geological Map of New Zealand project. New Zealand Journal of Geology and Geophysics, 55(4), pp. 393-405.

Rawlings, J.O., Pantula, S.G. and Dickey, D.A., 2001. Applied regression analysis: a research tool. Springer Science & Business Media.

Reading, H.G. ed., 2009. Sedimentary environments: processes, facies and stratigraphy. John Wiley & Sons.

Reilly, C., Nicol, A., Walsh, J.J. and Seebeck, H., 2015. Evolution of faulting and plate boundary deformation in the Southern Taranaki Basin, New Zealand. Tectonophysics, 651, pp.1-18.

Reyer, D., Philipp, S., 2014. Empirical relations of rock properties of outcrop and core samples from the Northwest German Basin for geothermal drilling. Geotherm Energy Sci 2, 21–37.

Rider, M., 1986. The geological interpretation of well logs. Blackie, Halsted Press, New York, 175 pp.

Robertson, A., 1970. Interpretation of geological factors for use in slope theory. In Planning Open Pit Mines-Symp. on the theoretical background to the planning of open pit mines with special reference to slope stability (pp. 55-71).

Sabatakakis, N., Tsiambaos, G., Ktena, S., Bouboukas, S., 2018. The effect of microstructure on mi strength parameter variation of common rock types. Bulletin of Engineering Geology and the Environment 77, 1673–1688. https://dx.doi.org/10.1007/s10064-017-1059-7

Scheidegger, A. E., 1974. The physics of flow through porous media. 3rd edn.: University of Toronto Press.

Sech, R. P., Jackson, M. D. and Hampson, G. J. 2009. Three-dimensional modeling of a shoreface-shelf parasequence reservoir analogue: Part 1. Surface-based modeling to capture high-resolution facies architecture. AAPG bulletin, 93, 1155-1181.

Settari, A. and Mourits, F.M., 1998. A coupled reservoir and geomechanical simulation system. Spe Journal, 3(03), pp.219-226.

Settari, A. and Walters, D.A., 2001. Advances in coupled geomechanical and reservoir modeling with applications to reservoir compaction. Spe Journal, 6(03), pp.334-342.

Shakoor, A. and Bonelli, R.E., 1991. Relationship between petrographic characteristics, engineering index properties, and mechanical properties of selected sandstones. Bulletin of the Association of Engineering Geologists, 28(1), 55-71.

Shell BP Todd Oil Services Ltd, 1976. Well resume Tane-1 (Offshore). New Zealand unpublished open file petroleum report 698. Ministry of Economic Development, Wellington.

Shell BP Todd Oil Services Ltd, 1979. Maui Field Platform A development well drilling and completion reports. New Zealand unpublished open file petroleum report 800. Ministry of Economic Development, Wellington.

Shell BP Todd Oil Services Ltd, 1982. Well resume, Wainui-1. Taranaki offshore. PPL 38049. New Zealand unpublished open file petroleum report 869. Ministry of Economic Development, Wellington.

Shell Todd Oil Services Ltd, 1992. Taranga-1 well completion report. PPL38444. New Zealand unpublished open file petroleum report 1864. Ministry of Economic Development, Wellington.

Shell Todd Oil Services Limited, 2001. Pohokura Field ERD Wellbore Stability Study. New Zealand unpublished open-file petroleum report 2651. Ministry of Economic Development, Wellington

Shell Todd Oil Services Limited, 2002. Rock Strength Measurements from Pohokura-1 and Pohokura-2. New Zealand unpublished open-file petroleum report 2778. Ministry of Economic Development, Wellington

Shen, J., Karakus., M., 2014. Simplified method for estimating the Hoek-Brown constant for intact rocks. Journal of Geotechnical and Geoenvironmental Engineering, 140(6), 04014025.

Sherburn, S. and White, R.S., 2006. Tectonics of the Taranaki region, New Zealand: earthquake focal mechanisms and stress axes. New Zealand journal of geology and geophysics, 49(2), pp.269-279.

Sing, K. S. W., 1985. Reporting physisorption data for gas/solid systems with special reference to the determination of surface area and porosity (Recommendations 1984. Pure and Applied Chemistry, 57(4), pp. 603-619.

Siratovich, P.A., Heap, M.J., Villeneuve, M.C., Cole, J.W., Kennedy, B.M., Davidson, Reuschlé, 2016. Mechanical behaviour of the Rotokawa Andesites (New Zealand): Insight into permeability evolution and stress-induced behaviour in an actively utilised geothermal reservoir. Geothermics 64, 163–179.

Smith, S., Ismail, I.Y., Brehm, A., & Castillo, D., 2006. Impact of Tectonic Stress Variation on Field Development Planning in The Temana and Bazan Fields, Sarawak Basin, GEO Asia 2006, Kuala Lumpur

Smithies, S. L., 2018. Provenance analysis of the Late Cretaceous to Paleocene Rakopi, North Cape, and Farewell formations, northwest Nelson, New Zealand. Unpublished MSc Thesis, University of Canterbury, Christchurch, New Zealand.

Stagpoole, V., Uruski, C., Funnell, R. and Darby, D., 2001. Petroleum potential of the deepwater Taranaki Basin.

Stark, C. J., 1996. Interpretation of some Paleocene fluvial sediments from the Upper Pakawau and Kapuni groups, Pakawau Sub-basin, North-West Nelson.

Strogen, D. P., 2011. Updated paleogeographic maps for the Taranaki Basin and surrounds. Lower Hutt, N.Z: GNS Science.

Strogen, D. P., Seebeck, H., Nicol, A. and King, P. R., 2017. Two-phase Cretaceous-Paleocene rifting in the Taranaki Basin region, New Zealand; implications for Gondwana break-up. Journal of Geological Society, 174(5), pp. 929-946.

Strong, G.E. and Milodowski, A.E., 1987. Aspects of the diagenesis of the Sherwood Sandstones of the Wessex Basin and their influence on reservoir characteristics. Geological Society, London, Special Publications, 36(1), pp.325-337.

Strong, G.E., 1993. Diagenesis of Triassic Sherwood Sandstone Group rocks, Preston, Lancashire, UK: a possible evaporitic cement precursor to secondary porosity?. Geological Society, London, Special Publications, 73(1), pp.279-289.

STOS Development Department, 1993a. MB-R (1) well completion report, Maui B Field, PML381012. Offshore Taranaki Basin. New Zealand unpublished open file petroleum report 1912. Ministry of Economic Development, Wellington.

STOS Development Department, 1993b. MB-W (2) well completion report, Maui B Field, PML 381012. Offshore Taranaki Basin. New Zealand unpublished open file petroleum report 1932. Ministry of Economic Development, Wellington.

Stroud, T., Miller, D., Leask, B., 2004. Amokura-1 well completion report. New Zealand unpublished open file petroleum report 2920. Ministry of Economic Development, Wellington.

Swanson, B. F., 1981. Simple correlation between permeabilities and mercury capillary pressures. JPT, Journal of Petroleum Technology, 33(12), pp. 2498-2504.

Swift Energy, 2007a. Geomechanical analysis and wellbore Stability study of the Goss & Trapper Wells, Tawn Trend NZ. New Zealand unpublished open-file petroleum report 3751. Ministry of Economic Development, Wellington

Swift Energy, 2007b. Geomechanical modelling, fracture permeability and drilling options analysis of the Kauri Field NZ. New Zealand unpublished open-file petroleum report 3752. Ministry of Economic Development, Wellington

Sykes, R., and Dow, M. J., 2000. Petroleum source rock potential of North Cape Formation (Late Cretaceous) coaly sediments, Taranaki Basin. In 2000 New Zealand Petroleum Conference Proceedings, Ministry of Commerce, Wellington (pp. 264-286).

Sykes, R., and Raine, J.I., 2008. Organofacies controls on the oil potential of coaly source rocks in the Late Cretaceous North Cape Formation, Taranaki Basin. PESA eastern Australasian Basins Symposium III, Sydney, 14–17 September 2008. Pp. 219–224.

Takahashi, M. and Koide, H., 1989. Effect of the intermediate principal stress on strength and deformation behaviour of sedimentary rocks at the depth shallower than 2000 m. In ISRM international symposium. International Society for Rock Mechanics and Rock Engineering.

Terzaghi, K., 1925. Erdbaumechanik auf bodenphysikalischer Grundlage.

Thrasher, G.P., 1990. Tectonics of the Taranaki rift. In New Zealand Oil Exploration Conference Proceedings (pp. 124-133). Ministry of Commerce Wellington.

Thrasher, G. P., 1992. Last Cretaceous Geology of Taranaki Basin, New Zealand, Unpublished PhD thesis.

Titheridge, D. G., 1977. Stratigraphy and sedimentology of the Upper Pakawau and Lower Westhaven groups: (Upper Cretaceous - Oligocene), northwest Nelson.

Todd Energy, 2007. Mangahewa 3 well completion report. New Zealand unpublished open-file petroleum report 3518. Ministry of Economic Development, Wellington

Todd Energy, 2010. Te Kiri Prospect Geomechanical Analysis, PEP51149. New Zealand unpublished open-file petroleum report 4278. Ministry of Economic Development, Wellington

Todd Energy, 2014. Wellbore Stability Analysis for the Planned Te Kiri North1 Well, Onshore Taranaki Basin PEP51149 New Zealand unpublished open-file petroleum report 5070. Ministry of Economic Development, Wellington

Todd Energy, 2015. Geomechanical Modelling for Mangahewa Field Development Well Planning and Reservoir Stimulation PMP 38150. New Zealand unpublished open-file petroleum report 5085. Ministry of Economic Development, Wellington

Townend, J., Sherburn, S., Arnold, R., Boese, C. and Woods, L., 2012. Three-dimensional variations in present-day tectonic stress along the Australia–Pacific plate boundary in New Zealand. Earth and Planetary Science Letters, 353, pp.47-59

Tricentrol Exploration Overseas Ltd., 1984. Well completion report Moki-1 PPL 38114. New Zealand unpublished open file petroleum report 987. Ministry of Economic Development, Wellington.

Ulusay, R., Türeli, K. and Ider, M.H., 1994. Prediction of engineering properties of a selected lit arenite sandstone from its petrographic characteristics using correlation and multivariate statistical techniques. Engineering Geology, 38(1-2), pp.135-157.

Ulusay, R. and Hudson, J., 2007. The complete ISRM suggested methods for rock characterization, testing and monitoring. ISRM Turkish National Group, Ankara, Turkey.

Ulusay, R., 2014. The ISRM Suggested Methods for Rock Characterization, Testing and Monitoring: 2007-2014. Springer.

Vernik, L., Bruno, M. and Bovberg, C., 1993. Empirical relations between compressive strength and porosity of siliciclastic rocks. International journal of rock mechanics and mining sciences & geomechanics abstracts, 30(7), pp. 677-680. Pergamon.

Villeneuve, M., Heap, M., Kushnir, A., Qin, T., Baud, P., Zhou, G., Xu, T., 2018. Estimating in situ rock mass strength and elastic modulus of granite from the Soultz-sous-Forêts geothermal reservoir (France). Geothermal Energy 6, 11.

Walsh, J.B. and Brace, W.F., 1964. A fracture criterion for brittle anisotropic rock. Journal of Geophysical Research, 69(16), pp.3449-3456.

Washburn, E. W., 1921. The dynamics of capillary flow. Physical Review 17(3), pp. 273.

Webb, P. A., 2001. An Introduction to the Physical Characterization of Materials by Mercury Intrusion Porosimetry with Emphasis on Reduction and Presentation of Experimental Data.. Micromeritics Instrument Corp, Norcross, Georgia

Weingarten, J.S. and Perkins, T.K., 1995. Prediction of sand production in gas wells: methods and Gulf of Mexico case studies. Journal of Petroleum Technology, 47(07), pp.596-600.

Wendt, A.S., Khazanehdari, J., Murineddu, A., Rasmussen, A., Mohamed, F.R., Westeng, K. and Voskamp, A., Schlumberger Technology Corp, 2013. Three-dimensional mechanical earth modeling. U.S. Patent 8,577,660.

White, C. D., Willis, B. J., Dutton, S. P., Bhattacharya, J. P. and Narayanan, K. 2004. Sedimentology, statistics, and flow behaviour for a tide-influenced deltaic sandstone, Frontier Formation, Wyoming, United States.

Winland, H., 1972. Oil accumulation in response to pore size changes, Weyburn field, Saskatchewan. Amoco Production Company report F72-G-25 (unpublished), 20.

Wiprut, D. and Zoback, M. D. 2000. Constraining the stress tensor in the Visund field, Norwegian North Sea: Application to wellbore stability and sand production. International Journal of Rock Mechanics and Mining Sciences, 37, 317-336.

Wong, R.H., Chau, K.T. and Wang, P., 1996. Microcracking and grain size effect in Yuen Long marbles. In International journal of rock mechanics and mining sciences & geomechanics abstracts, 33(5), pp. 479-485. Pergamon.

Wong, T.-F., David, C. and Zhu, W., 1997. The transition from brittle faulting to cataclastic flow in porous sandstones: mechanical deformation. Journal of Geophysical Research: Solid Earth 102(B2), 3009–3025.

Yale, D.P. and Jamieson Jr, W.H., 1994. Static and dynamic mechanical properties of carbonates. In 1st North American Rock Mechanics Symposium. American Rock Mechanics Association.

Zhang, J., Rai, C.S. and Sondergeld, C.H., 1998. Mechanical strength of reservoir materials: key information for sand prediction. In SPE/ISRM Rock Mechanics in Petroleum Engineering. Society of Petroleum Engineers.

Zhang, L. and Zhu, H., 2007. Three-dimensional Hoek-Brown strength criterion for rocks. Journal of Geotechnical and Geoenvironmental Engineering, 133(9), pp.1128-1135.

Zhang, L., 2008. A generalized three-dimensional Hoek–Brown strength criterion. Rock mechanics and rock engineering, 41(6), pp.893-915.

Zhang, L., Cao, P. and Radha, K.C., 2010. Evaluation of rock strength criteria for wellbore stability analysis. International journal of rock mechanics and mining sciences, 47(8), pp.1304-1316.

Zhao, J., 2000. Applicability of Mohr–Coulomb and Hoek–Brown strength criteria to the dynamic strength of brittle rock. International Journal of Rock Mechanics and Mining Sciences, 37(7), pp.1115-1121.

Zoback, M.L., 1992. First-and second-order patterns of stress in the lithosphere: The World Stress Map Project. Journal of Geophysical Research: Solid Earth, 97(B8), pp.11703-11728.

Zoback, M. D., Barton, C., Brudy, M., Castillo, D., Finkbeiner, T., Moos, D., Peska, P., Ward, C. and Wiprut, D. 2003. Determination of stress orientation and magnitude in deep wells. International Journal of Rock Mechanics and Mining Sciences, 40, 1049-1076.

Zoback, M. D., 2007. Reservoir Geomechanics, Stanford University, California.

Chapter Nine - Appendices

9.1. Appendix A – Strength data attributed to the Taranaki Basin

Location	Depth (m)	Test Type	Lithotype	Compressive Strength (MPa)	CP (MPa)	Petroleum Report Reference
Pohokura-1	3528.3	UCS	Sandstone	47	0	2778
Pohokura-1	3546.8	UCS	Sandstone	56	0	2778
Pohokura-1	3552.7	UCS	Sandstone	92	0	2778
Pohokura-2	3576.8	UCS	Sandstone	37	0	2778
Pohokura-2	3577.4	UCS	Sandstone	44	0	2778
Pohokura-2	3578.5	UCS	Sandstone	22	0	2778
Pohokura-2	3579.7	UCS	Sandstone	22	0	2778
Pohokura-2	3581.2	UCS	Sandstone	35	0	2778
Pohokura-2	3582.6	UCS	Sandstone	31	0	2778
Pohokura-2	3591.5	UCS	Sandstone	26	0	2778
Pohokura-2	3591.9	UCS	Sandstone	38	0	2778
Pohokura-2	3593.1	UCS	Sandstone	25	0	2778
Pohokura-2	3595.4	UCS	Sandstone	17	0	2778
Pohokura-2	3597.6	UCS	Sandstone	89	0	2778
Pohokura-2	3613.5	UCS	Sandstone	45	0	2778
Pohokura-2	3617.6	UCS	Sandstone	33	0	2778
Pohokura-2	3617.9	UCS	Sandstone	50	0	2778
Pohokura-2	3623.3	UCS	Sandstone	53	0	2778
Pohokura-2	3624.2	UCS	Sandstone	51	0	2778
Pohokura-2	3629.1	UCS	Sandstone	44	0	2778
Amokura-1	3664.25	UCS	Shale	58	0	3150
Amokura-1	3664.25	Triaxial	Shale	78	4.5	3150
Amokura-1	3664.25	Triaxial	Shale	87	9.3	3150
Amokura-1	3664.25	Triaxial	Shale	106	14.5	3150
Amokura-1	3673.96	UCS	Sandstone	32	0	3150
Amokura-1	3673.96	Triaxial	Sandstone	72	4.5	3150
Amokura-1	3673.96	Triaxial	Sandstone	101	9.3	3150
Amokura-1	3673.96	Triaxial	Sandstone	127	14.5	3150

Kauri-E4	2564.7	Triaxial	Sandstone	31	4.1	3752
Kauri-E4	2577.0	Triaxial	Sandstone	107	4.1	3752
Kauri-E4	2577.8	Triaxial	Sandstone	153	18.6	3752
MHW05	3899.9	UCS	Shale	54	0	5085
MHW05	3905.3	UCS	Shale	104	0	5085
MHW05	3914.9	UCS	Sandstone	89	0	5085
MHW05	3919.0	UCS	Sandstone	89		5085
MHW05	3922.2	UCS	Sandstone	70	0	5085
MHW05	3927.0	UCS	Sandstone	79	0	5085
MHW05	3930.1	UCS	Sandstone	77	0	5085
MHW05	3933.8	UCS	Sandstone	55	0	5085
MHW05	3937.1	UCS	Sandstone	37	0	5085
MHW05	3942.1	UCS	Sandstone	87	0	5085
MHW11	4552.4	UCS	Shale	41	0	5085
MHW11	4555.9	UCS	Sandstone	87	0	5085
MHW11	4559.0	UCS	Sandstone	110	0	5085
MHW11	4561.8	UCS	Sandstone	106	0	5085
MHW11	4566.9	UCS	Sandstone	103	0	5085
MHW11	4573.2	UCS	Sandstone	61	0	5085
MHW11	4578.9	UCS	Sandstone	70	0	5085
MHW11	4586.8	UCS	Sandstone	77	0	5085
MHW11	4639.4	UCS	Sandstone	79	0	5085
MHW11	4644.6	UCS	Sandstone	62	0	5085
MHW11	4654.6	UCS	Sandstone	77	0	5085
MHW11	4669.9	UCS	Sandstone	49	0	5085
MHW11	4671.0	UCS	Sandstone	56	0	5085
MHW11	4674.6	UCS	Sandstone	101	0	5085
Cheal-2	1370.6	UCS	Shale	5	0	5595
Cheal-2	1372.7	UCS	Shale	5	0	5595
Cheal-2	1372.75	UCS	Shale	5	0	5595
Cheal-2	1372.5	UCS	Shale	7	0	5595
Cheal-2	1372.65	UCS	Shale	4	0	5595
Cheal-2	1372.45	UCS	Shale	7	0	5595
Ngatoro-11	1717.6	UCS	Shale	11	0	5595
Ngatoro-11	1717.8	UCS	Shale	12	0	5595
Ngatoro-11	1717.35	UCS	Shale	20	0	5595
Ngatoro-11	1717.55	UCS	Shale	14	0	5595

Ngatoro-11	1717.47	UCS	Shale	23	0	5595
Ngatoro-11	1717.3	UCS	Shale	19	0	5595
Ngatoro-11	1717.4	UCS	Shale	8	0	5595
Ngatoro-11	1717.45	UCS	Shale	20	0	5595
Rimu-1	2064.15	UCS	Shale	25	0	5595
Rimu-1	2064.3	UCS	Shale	18	0	5595
Rimu-1	2064	UCS	Shale	29	0	5595
Rimu-1	2064.1	UCS	Shale	29	0	5595
Rimu-1	2064.4	UCS	Shale	18	0	5595
Rimu-1	2064.35	UCS	Shale	18	0	5595
Rimu-1	2064.55	UCS	Shale	92	0	5595
Rimu-1	2064.45	UCS	Shale	95	0	5595
Cheal-2	1373.6	UCS	Shale	5	0	5595
Cheal-2	1373.6	UCS	Shale	4	0	5595
Cheal-2	1373.6	UCS	Shale	10	0	5595
Cheal-2	1373.5	UCS	Shale	4	0	5595
Cheal-2	1373.5	UCS	Shale	7	0	5595
Cheal-2	1370.7	UCS	Shale	3	0	5595
Cheal-2	1370.65	UCS	Shale	5	0	5595
Cheal-2	1373.8	UCS	Shale	3	0	5595
Rimu-1	2064.5	UCS	Shale	92	0	5595
Rimu-1	2064.2	UCS	Shale	56	0	5595
Rimu-1	2064.1	UCS	Shale	93	0	5595
Rimu-1	2064.4	UCS	Shale	36	0	5595
Rimu-1	2064.75	UCS	Shale	50	0	5595
Rimu-1	2064.9	UCS	Shale	74	0	5595
Ngatoro-11	1717.9	UCS	Shale	29	0	5595
Ngatoro-11	1717.7	UCS	Shale	18	0	5595
Ngatoro-11	1717.7	UCS	Shale	30	0	5595
Ngatoro-11	1717.7	UCS	Shale	31	0	5595
Ngatoro-11	1717.9	UCS	Shale	31	0	5595
Ngatoro-11	1717.9	UCS	Shale	15	0	5595
Manutahi-1	663	UCS	Shale	2	0	5595
Manutahi-1	661	UCS	Shale	3	0	5595
Manutahi-1	658	UCS	Shale	2	0	5595
Manutahi-1	652.35	UCS	Shale	1	0	5595
Manutahi-1	264.6	UCS	Shale	3	0	5595

Manutahi-1	263.7	UCS	Shale	3	0	5595
Manutahi-1	255.76	UCS	Shale	6	0	5595
Manutahi-1	255.56	UCS	Shale	5	0	5595
Manutahi-1	255.28	UCS	Shale	6	0	5595
Moki 2A	1312.8	UCS	Shale	23	0	This study
Moki 2A	1312.8	UCS	Shale	19	0	This study
Moki-1	2138.5	UCS	Sandstone	28	0	This study
Moki-1	2138.3	UCS	Sandstone	43	0	This study
Moki-1	2137.4	UCS	Sandstone	24	0	This study
Moki-1	2136.4	UCS	Sandstone	22	0	This study
Moki-1	2136.4	UCS	Sandstone	22	0	This study
Moki-1	2136.4	Triaxial	Sandstone	75	5	This study
Moki-1	2135.6	UCS	Sandstone	18	0	This study
Moki-1	2135.6	UCS	Sandstone	14	0	This study
Moki-1	2135.6	Triaxial	Sandstone	101	15	his study
Moki-1	2134.3	UCS	Sandstone	27	0	This study
Moki-1	2134.6	UCS	Sandstone	26	0	This study
Maui A-1G	2777.9	UCS	Sandstone	35	0	This study
Maui A-1G	2777.9	UCS	Sandstone	24	0	This study
Maui A-1G	2776.7	UCS	Sandstone	13	0	This study
Maui A-1G	2776.7	UCS	Sandstone	22	0	This study
Maui A-1G	2774.0	UCS	Sandstone	25	0	This study
Maui A-1G	2771.3	UCS	Sandstone	20	0	This study
Maui A-1G	2771.3	UCS	Sandstone	36	0	This study
Maui A-1G	3069.7	UCS	Sandstone	34	0	This study
Maui A-1G	3068.5	UCS	Sandstone	58	0	This study
Maui A-1G	3068.5	UCS	Sandstone	27	0	This study
MBR-1	3516.9	UCS	Sandstone	57	0	This study
MBR-1	3516.9	UCS	Sandstone	24	0	This study
MBR-1	3516.9	Triaxial	Sandstone	128	15	This study
MBR-1	3519.4	UCS	Sandstone	40	0	This study
MBR-1	3519.4	UCS	Sandstone	8	0	This study
MBR-1	3521.8	UCS	Sandstone	13	0	This study
MBR-1	3521.8	UCS	Sandstone	14	0	This study
MBR-1	3521.8	Triaxial	Sandstone	67	5	This study
MBR-1	3522.8	UCS	Sandstone	41	0	This study
MBR-1	3522.8	Triaxial	Sandstone	139	20	This study

MBR-1	3523.4	UCS	Sandstone	47	0	This study
MBR-1	3523.4	UCS	Sandstone	55	0	This study
MBR-1	3523.4	Triaxial	Sandstone	134	10	This study
MBW-2	4132.5	UCS	Sandstone	16	0	This study
MBW-2	4132.45	UCS	Sandstone	7	0	This study
MBW-2	4132.5	Triaxial	Sandstone	68	7	This study
MBW-2	4130.4	UCS	Sandstone	13	0	This study
MBW-2	4130.4	UCS	Sandstone	10	0	This study
MBW-2	4130.4	Triaxial	Sandstone	57	5	This study
MBW-2	4128.1	UCS	Sandstone	25	0	This study
MBW-2	4128.1	UCS	Sandstone	23	0	This study
MBW-2	4126.46	UCS	Sandstone	12	0	This study
MBW-2	4124.7	UCS	Sandstone	20	0	This study
MBW-2	4124.7	UCS	Sandstone	15	0	This study
MBW-2	4124.7	Triaxial	Sandstone	93	10	This study
Tane-1	3693.7	UCS	Sandstone	25	0	This study
Tane-1	3693.7	UCS	Sandstone	23	0	This study
Tane-1	3692.4	UCS	Sandstone	36	0	This study
Tane-1	3692.4	Triaxial	Sandstone	114	15	This study
Tane-1	3692.0	UCS	Sandstone	40	0	This study
Tane-1	3692.0	UCS	Sandstone	15	0	This study
Tane-1	3692.0	Triaxial	Sandstone	134	20	This study
Tane-1	3689.9	UCS	Sandstone	59	0	This study
Tane-1	3689.9	UCS	Sandstone	58	0	This study
Tane-1	3689.9	Triaxial	Sandstone	115	10	This study
Tane-1	3689.2	UCS	Sandstone	50	0	This study
Tane-1	3689.2	Triaxial	Sandstone	147	25	This study

9.2. Appendix B – Locality map for outcrop facies samples

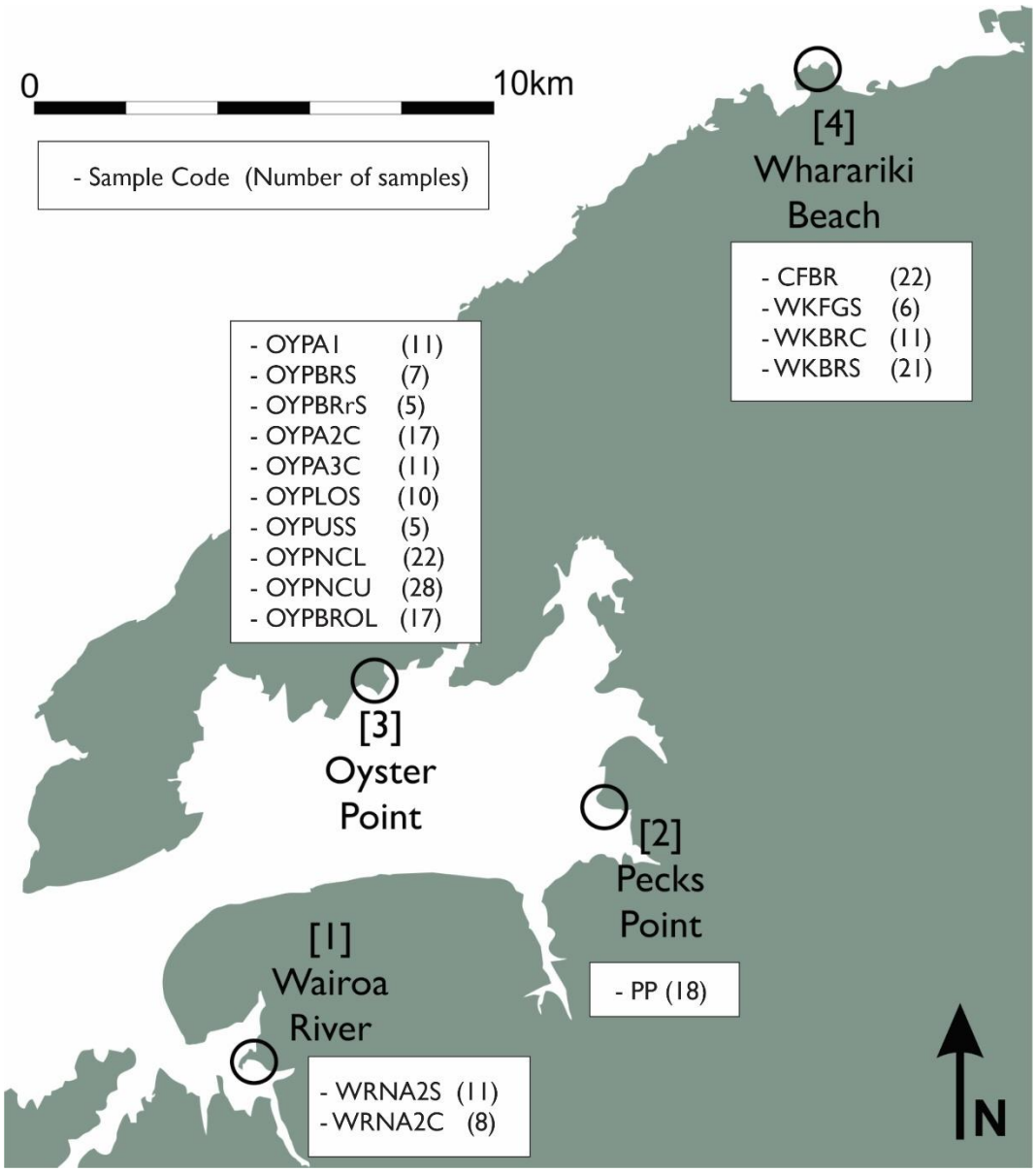

9.3. Appendix C – XRD Data for Outcrop Samples (Mineral Percent)

Samples	Sandstone Facies	Quartz	Albite	Orthoclase	Muscovite	Kaolinite	Chlorite	Calcite	Illite	Biotite
OYPA1	Hl	38	39	12	5	4	1	1		Trace
PP	Sx	41	21	14	8	14	1	1		Trace
OYPBRS	Sx	52	15	6	9	11	2	Trace	4	1
OYPBRrS	Sx	46	22	7	7	13	1	Trace	4	Trace
CFBR	Sx	59	1	9	9	22	Not detected	Trace	Not detected	Trace
WKFGS	Sx	62	3	4	7	23		Not detected	Not detected	1
WRNA2S	Sx	50	26	6	6	11	Not detected	1		Not detected
OYPA2C	CS	56	18	1	13	12	Not detected	Trace	Not detected	Trace
OYPA3C	CS	54	10	Not detected	17	17	1	Trace	Not detected	1
WRNA2C	CS	51	23	5	8	12	Not detected	Trace	Not detected	1
WKBRC	CS	39	9	8	14	27	1	1		1
OYPLOS	Sw	45	17	3	13	20	1	Trace	Not detected	1
OYPUSS	Sw	55	11	1	15	16	1	Trace	Not detected	1
OYPNC L	Sw	44	22	3	15	15	Trace	1	Not detected	Poss. Trace
OYPNC U	Sw	44	16	7	12	18	1	1	Not detected	1
OYPBROL	Sw	48	11	3	11	18	2	Trace	6	1
WKBRS	Sw	53	16	6	9	13	2	Trace	Not detected	1

9.4. Appendix D –Sedimentary facies, and textural/physical rock properties for outcrop samples

Sample	Facies	Association	Direction	Sorting	Rounding	Grain Size (μm)	Perm (mD)	Porosity Fraction
OYPA1/1	Hl	DF	Perpendicular	Well	SA-SR	85	5.7	0.27
OYPA1/2	Hl	DF	Perpendicular	Well	SA-SR	85	4.2	0.25
OYPA1/3	Hl	DF	Perpendicular	Well	SA-SR	85	4.9	0.27
OYPA1/4	Hl	DF	Perpendicular	Well	SA-SR	85	10.3	0.27
OYPA1/5	Hl	DF	Perpendicular	Well	SA-SR	85	5.5	0.27
OYPA1/6	Hl	DF	Parallel	Well	SA-SR	85	6.9	0.27
OYPA1/7	Hl	DF	Parallel	Well	SA-SR	85	4.9	0.27
OYPA1/8	Hl	DF	Parallel	Well	SA-SR	85	9.6	0.26
OYPA1/9	Hl	DF	Parallel	Well	SA-SR	85	5.1	0.27
OYPA1/10	Hl	DF	Parallel	Well	SA-SR	85	11.1	0.26
OYPA1/11	Hl	DF	Parallel	Well	SA-SR	85	12.6	0.27
WRNA2S/1	Sx	SF	Parallel	Poor	A-SA	162.5	58.1	0.32
WRNA2S/2	Sx	SF	Parallel	Poor	A-SA	162.5	688.0	0.31
WRNA2S/3	Sx	SF	Parallel	Poor	A-SA	162.5	98.0	0.30
WRNA2S/4	Sx	SF	Parallel	Poor	A-SA	162.5	23.4	0.30
WRNA2S/5	Sx	SF	Parallel	Poor	A-SA	162.5	214.5	0.28
WRNA2S/6	Sx	SF	Parallel	Poor	A-SA	162.5	718.5	0.30
WRNA2S/7	Sx	SF	Perpendicular	Poor	A-SA	162.5		0.29
WRNA2S/8	Sx	SF	Perpendicular	Poor	A-SA	162.5		0.28
WRNA2S/9	Sx	SF	Perpendicular	Poor	A-SA	162.5		0.30
WRNA2S/10	Sx	SF	Parallel	Poor	A-SA	162.5		0.31
WRNA2S/11	Sx	SF	Parallel	Poor	A-SA	162.5		0.33
OYPBRS/1	Sx	BR	Parallel	Poor-Mod	SA-SR	300	12.9	0.25
OYPBRS/2	Sx	BR	Parallel	Poor-Mod	SA-SR	300	4.3	0.24
OYPBRS/3	Sx	BR	Parallel	Poor-Mod	SA-SR	300		0.28
OYPBRS/4	Sx	BR	Parallel	Poor-Mod	SA-SR	300		0.29
OYPBRS/5	Sx	BR	Parallel	Poor-Mod	SA-SR	300		0.29
OYPBRS/6	Sx	BR	Parallel	Poor-Mod	SA-SR	300		0.30
OYPBRS/7	Sx	BR	Parallel	Poor-Mod	SA-SR	300		0.26
OYPBRrS/1	Sx	BR	Parallel	Poor-Mod	SA-SR	100	3.6	0.22
OYPBRrS/2	Sx	BR	Parallel	Poor-Mod	SA-SR	100	1.7	0.23
OYPBRrS/3	Sx	BR	Parallel	Poor-Mod	SA-SR	100	13.6	0.23
OYPBRrS/4	Sx	BR	Parallel	Poor-Mod	SA-SR	100	18.6	0.24
OYPBRrS/5	Sx	BR	Parallel	Poor-Mod	SA-SR	100	12.8	0.23
WKFGS/1	Sx	BR	Parallel	Moderate	A-SA	300	5.3	0.20
WKFGS/2	Sx	BR	Parallel	Moderate	A-SA	300	2.4	0.19
WKFGS/3	Sx	BR	Parallel	Moderate	A-SA	300	2.9	0.17
WKFGS/4	Sx	BR	Parallel	Moderate	A-SA	300	28.6	0.19
WKFGS/5	Sx	BR	Parallel	Moderate	A-SA	300	12.1	0.19
WKFGS/6	Sx	BR	Parallel	Moderate	A-SA	300	35.4	0.19
CFBR/1	Sx	BR	Perpendicular	Poor	A-SA	225		0.19
CFBR/2	Sx	BR	Perpendicular	Poor	A-SA	225		0.20
CFBR/3	Sx	BR	Perpendicular	Poor	A-SA	225	68.5	0.20
CFBR/4	Sx	BR	Perpendicular	Poor	A-SA	225		0.19
CFBR/5	Sx	BR	Parallel	Poor	A-SA	225	11.8	0.20
CFBR/6	Sx	BR	Parallel	Poor	A-SA	225		0.19
CFBR/7	Sx	BR	Parallel	Poor	A-SA	225		0.19
CFBR/8	Sx	BR	Perpendicular	Poor	A-SA	225		0.17
CFBR/9	Sx	BR	Perpendicular	Poor	A-SA	225		
CFBR/10	Sx	BR	Perpendicular	Poor	A-SA	225		0.17
CFBR/11	Sx	BR	Perpendicular	Poor	A-SA	225		0.16
CFBR/12	Sx	BR	Perpendicular	Poor	A-SA	225		0.18
CFBR/13	Sx	BR	Perpendicular	Poor	A-SA	225		0.18

CFBR/14	Sx	BR	Perpendicular	Poor	A-SA	225		0.19
CFBR/15	Sx	BR	Perpendicular	Poor	A-SA	225	11.4	0.18
CFBR/16	Sx	BR	Perpendicular	Poor	A-SA	225		0.17
CFBR/17	Sx	BR	Perpendicular	Poor	A-SA	225		0.19
CFBR/18	Sx	BR	Perpendicular	Poor	A-SA	225		0.18
CFBR/19	Sx	BR	Perpendicular	Poor	A-SA	225		0.18
CFBR/20	Sx	BR	Perpendicular	Poor	A-SA	225		0.21
CFBR/21	Sx	BR	Perpendicular	Poor	A-SA	225		0.21
CFBR/22	Sx	BR	Perpendicular	Poor	A-SA	225		0.20
PP/1	Sx	DF	Parallel	Moderate	A-SA	220		0.30
PP/2	Sx	DF	Parallel	Moderate	A-SA	220	264.4	0.32
PP/3	Sx	DF	Parallel	Moderate	A-SA	220	256.8	0.33
PP/4	Sx	DF	Parallel	Moderate	A-SA	220		0.35
PP/5	Sx	DF	Parallel	Moderate	A-SA	220	635.7	0.33
PP/6	Sx	DF	Parallel	Moderate	A-SA	220		0.39
PP/7	Sx	DF	Parallel	Moderate	A-SA	220		0.36
PP/8	Sx	DF	Parallel	Moderate	A-SA	220	666.2	0.34
PP/9	Sx	DF	Parallel	Moderate	A-SA	220		0.34
PP/10	Sx	DF	Parallel	Moderate	A-SA	220		0.34
PP/11	Sx	DF	Parallel	Moderate	A-SA	220		0.35
PP/12	Sx	DF	Parallel	Moderate	A-SA	220	464.6	0.39
PP/13	Sx	DF	Parallel	Moderate	A-SA	220		0.34
PP/14	Sx	DF	Parallel	Moderate	A-SA	220		0.34
PP/15	Sx	DF	Perpendicular	Moderate	A-SA	220	80.0	0.33
PP/16	Sx	DF	Perpendicular	Moderate	A-SA	220		0.34
PP/17	Sx	DF	Perpendicular	Moderate	A-SA	220	120.7	0.34
PP/18	Sx	DF	Perpendicular	Moderate	A-SA	220		0.36
OYPA2C/1	CS	SF	Parallel	Moderate	SA-SR	50	0.7	0.17
OYPA2C/2	CS	SF	Parallel	Moderate	SA-SR	50	2.7	0.15
OYPA2C/3	CS	SF	Parallel	Moderate	SA-SR	50	0.4	0.19
OYPA2C/4	CS	SF	Parallel	Moderate	SA-SR	100		0.16
OYPA2C/5	CS	SF	Parallel	Moderate	SA-SR	100		0.13
OYPA2C/6	CS	SF	Parallel	Moderate	SA-SR	100	0.3	0.16
OYPA2C/7	CS	SF	Parallel	Moderate	SA-SR	100		0.15
OYPA2C/8	CS	SF	Parallel	Moderate	SA-SR	100		0.22
OYPA2C/9	CS	SF	Parallel	Moderate	SA-SR	100		0.17
OYPA2C/10	CS	SF	Parallel	Moderate	SA-SR	100		0.17
OYPA2C/11	CS	SF	Parallel	Moderate	SA-SR	100		0.19
OYPA2C/12	CS	SF	Parallel	Moderate	SA-SR	100		0.17
OYPA2C/13	CS	SF	Parallel	Moderate	SA-SR	100		0.17
OYPA2C/14	CS	SF	Parallel	Moderate	SA-SR	100	0.9	0.19
OYPA2C/15	CS	SF	Parallel	Moderate	SA-SR	100		0.19
OYPA2C/16	CS	SF	Parallel	Moderate	SA-SR	100		0.19
OYPA2C/17	CS	SF	Parallel	Moderate	SA-SR	100		0.18
OYPA3C/1	CS	DP	Perpendicular	Well	SA-SR	50	0.1	0.16
OYPA3C/2	CS	DP	Perpendicular	Well	SA-SR	50	0.1	0.16
OYPA3C/3	CS	DP	Perpendicular	Well	SA-SR	50	0.3	0.19
OYPA3C/4	CS	DP	Perpendicular	Well	SA-SR	50	0.2	0.16
OYPA3C/5	CS	DP	Perpendicular	Well	SA-SR	50	0.1	0.15
OYPA3C/6	CS	DP	Perpendicular	Well	SA-SR	50	0.1	0.17
OYPA3C/7	CS	DP	Parallel	Well	SA-SR	50	0.1	0.17
OYPA3C/8	CS	DP	Parallel	Well	SA-SR	50	0.1	0.16
OYPA3C/9	CS	DP	Parallel	Well	SA-SR	50	0.2	0.15
OYPA3C/10	CS	DP	Parallel	Well	SA-SR	50	0.2	0.16
OYPA3C/11	CS	DP	Parallel	Well	SA-SR	50	0.1	0.14
WRNA2C/1	CS	SF	Parallel	Moderate	SA-SR	40	0.2	0.23
WRNA2C/2	CS	SF	Parallel	Moderate	SA-SR	40	0.1	0.20
WRNA2C/3	CS	SF	Perpendicular	Moderate	SA-SR	40		0.25
WRNA2C/4	CS	SF	Perpendicular	Moderate	SA-SR	40	0.1	0.24
WRNA2C/5	CS	SF	Perpendicular	Moderate	SA-SR	40	0.0	0.25

WRNA2C/6	CS	SF	Perpendicular	Moderate	SA-SR	40		0.23
WRNA2C/7	CS	SF	Parallel	Moderate	SA-SR	40	0.6	0.28
WRNA2C/8	CS	SF	Parallel	Moderate	SA-SR	40		0.25
WKBRC/1	CS	BR	Parallel	Moderate	SA-SR	50	4.7	0.21
WKBRC/2	CS	BR	Parallel	Moderate	SA-SR	50	6.0	0.19
WKBRC/3	CS	BR	Parallel	Moderate	SA-SR	50	10.3	0.21
WKBRC/4	CS	BR	Perpendicular	Moderate	SA-SR	50	3.3	0.19
WKBRC/5	CS	BR	Perpendicular	Moderate	SA-SR	50	2.6	0.21
WKBRC/6	CS	BR	Perpendicular	Moderate	SA-SR	50	0.7	0.23
WKBRC/7	CS	BR	Perpendicular	Moderate	SA-SR	50	1.3	0.22
WKBRC/8	CS	BR	Perpendicular	Moderate	SA-SR	50	1.9	0.22
WKBRC/9	CS	BR	Parallel	Moderate	SA-SR	50	0.5	0.18
WKBRC/10	CS	BR	Parallel	Moderate	SA-SR	50	0.1	0.17
WKBRC/11	CS	BR	Parallel	Moderate	SA-SR	50	0.3	0.18
OYPLOS/1	Sw	SF	Perpendicular	Poor-Mod	A-SR	200	165.5	0.21
OYPLOS/2	Sw	SF	Perpendicular	Poor-Mod	A-SR	200	5.4	0.21
OYPLOS/3	Sw	SF	Perpendicular	Poor-Mod	A-SR	200	8.4	0.18
OYPLOS/4	Sw	SF	Perpendicular	Poor-Mod	A-SR	200	54.6	0.22
OYPLOS/5	Sw	SF	Perpendicular	Poor-Mod	A-SR	200	824.1	0.21
OYPLOS/6	Sw	SF	Parallel	Poor-Mod	A-SR	200	3.2	0.22
OYPLOS/7	Sw	SF	Parallel	Poor-Mod	A-SR	200	1.1	0.18
OYPLOS/8	Sw	SF	Parallel	Poor-Mod	A-SR	200	4.3	0.21
OYPLOS/9	Sw	SF	Parallel	Poor-Mod	A-SR	200	4.4	0.19
OYPLOS/10	Sw	SF	Parallel	Poor-Mod	A-SR	200	0.9	0.18
OYPUSS/1	Sw	SF	Parallel	Poor-Mod	SA-SR	200	1.0	0.18
OYPUSS/2	Sw	SF	Parallel	Poor-Mod	SA-SR	200	1.3	0.20
OYPUSS/3	Sw	SF	Parallel	Poor-Mod	SA-SR	200	3.0	0.22
OYPUSS/4	Sw	SF	Parallel	Poor-Mod	SA-SR	200	3.7	0.19
OYPUSS/5	Sw	SF	Parallel	Poor-Mod	SA-SR	200	3.7	0.19
OYPNCL/1	Sw	DP	Parallel	Poor-Mod	A-SA	185		0.16
OYPNCL/2	Sw	DP	Parallel	Poor-Mod	A-SA	185	13.0	0.19
OYPNCL/3	Sw	DP	Parallel	Poor-Mod	A-SA	185	14.0	0.20
OYPNCL/4	Sw	DP	Parallel	Poor-Mod	A-SA	185		0.22
OYPNCL/5	Sw	DP	Parallel	Poor-Mod	A-SA	185		0.20
OYPNCL/6	Sw	DP	Parallel	Poor-Mod	A-SA	185		0.23
OYPNCL/7	Sw	DP	Parallel	Poor-Mod	A-SA	185		0.27
OYPNCL/8	Sw	DP	Parallel	Poor-Mod	A-SA	185		0.21
OYPNCL/9	Sw	DP	Parallel	Poor-Mod	A-SA	185		0.17
OYPNCL/10	Sw	DP	Parallel	Poor-Mod	A-SA	185		0.22
OYPNCL/11	Sw	DP	Parallel	Poor-Mod	A-SA	185		0.21
OYPNCL/12	Sw	DP	Parallel	Poor-Mod	A-SA	185		0.20
OYPNCL/13	Sw	DP	Parallel	Poor-Mod	A-SA	185		0.19
OYPNCL/14	Sw	DP	Parallel	Poor-Mod	A-SA	185		0.18
OYPNCL/15	Sw	DP	Parallel	Poor-Mod	A-SA	185		0.20
OYPNCL/16	Sw	DP	Perpendicular	Poor-Mod	A-SA	185		0.20
OYPNCL/17	Sw	DP	Perpendicular	Poor-Mod	A-SA	185		0.20
OYPNCL/18	Sw	DP	Perpendicular	Poor-Mod	A-SA	185		0.20
OYPNCL/19	Sw	DP	Perpendicular	Poor-Mod	A-SA	185		0.26
OYPNCL/20	Sw	DP	Perpendicular	Poor-Mod	A-SA	185		0.22
OYPNCL/21	Sw	DP	Perpendicular	Poor-Mod	A-SA	185	21.6	0.22
OYPNCL/22	Sw	DP	Perpendicular	Poor-Mod	A-SA	185	14.8	0.20
OYPNCU/23	Sw	DP	Parallel	Poor-Mod	A-SA	235		0.17
OYPNCU/24	Sw	DP	Parallel	Poor-Mod	A-SA	235		0.26
OYPNCU/25	Sw	DP	Parallel	Poor-Mod	A-SA	235	33.9	0.21
OYPNCU/26	Sw	DP	Parallel	Poor-Mod	A-SA	235	68.6	0.22
OYPNCU/27	Sw	DP	Parallel	Poor-Mod	A-SA	235		0.20
OYPNCU/28	Sw	DP	Parallel	Poor-Mod	A-SA	235	41.9	0.22
OYPNCU/29	Sw	DP	Parallel	Poor-Mod	A-SA	235		0.22
OYPNCU/30	Sw	DP	Parallel	Poor-Mod	A-SA	200		0.22
OYPNCU/31	Sw	DP	Parallel	Poor-Mod	A-SA	200		0.24

OYPNCU/32	Sw	DP	Parallel	Poor-Mod	A-SA	200	80.8	0.24
OYPNCU/33	Sw	DP	Parallel	Poor-Mod	A-SA	200		0.22
OYPNCU/34	Sw	DP	Parallel	Poor-Mod	A-SA	200		0.23
OYPNCU/35	Sw	DP	Parallel	Poor-Mod	A-SA	200		0.22
OYPNCU/36	Sw	DP	Parallel	Poor-Mod	A-SA	200		0.25
OYPNCU/37	Sw	DP	Parallel	Poor-Mod	A-SA	200		0.22
OYPNCU/38	Sw	DP	Parallel	Poor-Mod	A-SA	200		0.20
OYPNCU/39	Sw	DP	Parallel	Poor-Mod	A-SA	200		0.18
OYPNCU/40	Sw	DP	Parallel	Poor-Mod	A-SA	200	25.1	0.24
OYPNCU/41	Sw	DP	Parallel	Poor-Mod	A-SA	200	15.1	0.22
OYPNCU/42	Sw	DP	Parallel	Poor-Mod	A-SA	200		0.18
OYPNCU/43	Sw	DP	Parallel	Poor-Mod	A-SA	200		0.21
OYPNCU/44	Sw	DP	Perpendicular	Poor-Mod	A-SA	200	7.3	0.20
OYPNCU/45	Sw	DP	Perpendicular	Poor-Mod	A-SA	200	46.2	0.23
OYPNCU/46	Sw	DP	Perpendicular	Poor-Mod	A-SA	200		0.23
OYPNCU/47	Sw	DP	Perpendicular	Poor-Mod	A-SA	200		0.21
OYPNCU/48	Sw	DP	Perpendicular	Poor-Mod	A-SA	200		0.20
OYPNCU/49	Sw	DP	Perpendicular	Poor-Mod	A-SA	200		0.22
OYPNCU/50	Sw	DP	Perpendicular	Poor-Mod	A-SA	200		0.20
OYPBROL/1	Sw	BR	Parallel	Moderate	SA-SR	120	2.9	0.27
OYPBROL/2	Sw	BR	Parallel	Moderate	SA-SR	120	2.0	0.26
OYPBROL/3	Sw	BR	Parallel	Moderate	SA-SR	120	0.9	0.25
OYPBROL/4	Sw	BR	Parallel	Moderate	SA-SR	120		0.28
OYPBROL/5	Sw	BR	Parallel	Moderate	SA-SR	120	10.6	0.26
OYPBROL/6	Sw	BR	Parallel	Moderate	SA-SR	120		0.24
OYPBROL/7	Sw	BR	Parallel	Moderate	SA-SR	120		0.22
OYPBROL/8	Sw	BR	Parallel	Moderate	SA-SR	120		0.24
OYPBROL/9	Sw	BR	Perpendicular	Moderate	SA-SR	120		0.28
OYPBROL/10	Sw	BR	Perpendicular	Moderate	SA-SR	120	1.9	0.25
OYPBROL/11	Sw	BR	Perpendicular	Moderate	SA-SR	120		0.26
OYPBROL/12	Sw	BR	Perpendicular	Moderate	SA-SR	120		0.26
OYPBROL/13	Sw	BR	Perpendicular	Moderate	SA-SR	120		0.23
OYPBROL/14	Sw	BR	Perpendicular	Moderate	SA-SR	120		0.27
OYPBROL/15	Sw	BR	Perpendicular	Moderate	SA-SR	120		0.25
OYPBROL/16	Sw	BR	Perpendicular	Moderate	SA-SR	120		0.22
OYPBROL/17	Sw	BR	Perpendicular	Moderate	SA-SR	120		0.24
WKBRS/1	Sw	BR	Perpendicular	Poor-Mod	SA-SR	175	27.2	0.21
WKBRS/2	Sw	BR	Perpendicular	Poor-Mod	SA-SR	175	53.9	0.22
WKBRS/3	Sw	BR	Perpendicular	Poor-Mod	SA-SR	175	49.2	0.21
WKBRS/4	Sw	BR	Perpendicular	Poor-Mod	SA-SR	175	6.1	0.19
WKBRS/5	Sw	BR	Perpendicular	Poor-Mod	SA-SR	175	7.8	0.21
WKBRS/6	Sw	BR	Parallel	Poor-Mod	SA-SR	175	43.2	0.21
WKBRS/7	Sw	BR	Parallel	Poor-Mod	SA-SR	175	36.9	0.27
WKBRS/8	Sw	BR	Parallel	Poor-Mod	SA-SR	175	57.2	0.24
WKBRS/9	Sw	BR	Parallel	Poor-Mod	SA-SR	175	3.4	0.23
WKBRS/10	Sw	BR	Parallel	Poor-Mod	SA-SR	175	15.4	0.25
WKBRS/11	Sw	BR	Parallel	Poor-Mod	SA-SR	175	21.6	0.26
WKBRS/12	Sw	BR	Parallel	Poor-Mod	SA-SR	175		0.20
WKBRS/13	Sw	BR	Parallel	Poor-Mod	SA-SR	175		0.21
WKBRS/14	Sw	BR	Parallel	Poor-Mod	SA-SR	175		0.21
WKBRS/15	Sw	BR	Parallel	Poor-Mod	SA-SR	175		0.19
WKBRS/16	Sw	BR	Perpendicular	Poor-Mod	SA-SR	175	1.4	0.19
WKBRS/17	Sw	BR	Perpendicular	Poor-Mod	SA-SR	175		0.21
WKBRS/18	Sw	BR	Perpendicular	Poor-Mod	SA-SR	175		0.20
WKBRS/19	Sw	BR	Perpendicular	Poor-Mod	SA-SR	175		0.20
WKBRS/20	Sw	BR	Perpendicular	Poor-Mod	SA-SR	175		0.21
WKBRS/21	Sw	BR	Perpendicular	Poor-Mod	SA-SR	175		0.22

9.5. Appendix E – Density, sonic velocities and strength properties for outcrop samples

Sample	Facies	Association	Direction	Dry Bulk Density (g/cm3)	Vp (m/s)	Vs (m/s)	UCS (MPa)
OYPA1/1	Hl	DF	Perpendicular	2.03	1652	1063	13.03
OYPA1/2	Hl	DF	Perpendicular	2.11	1609	971	
OYPA1/3	Hl	DF	Perpendicular	2.05	1635	1027	
OYPA1/4	Hl	DF	Perpendicular	2.04	1646	1054	
OYPA1/5	Hl	DF	Perpendicular	2.06	1621	963	
OYPA1/6	Hl	DF	Parallel	2.04	1726	1057	14.38
OYPA1/7	Hl	DF	Parallel	2.06	1841	1176	12.48
OYPA1/8	Hl	DF	Parallel	2.08	1791	1125	
OYPA1/9	Hl	DF	Parallel	2.07	1742	1063	
OYPA1/10	Hl	DF	Parallel	2.05	1727	1093	
OYPA1/11	Hl	DF	Parallel	2.05	1677	1056	
WRNA2S/1	Sx	1.85	Parallel			1.85	
WRNA2S/2	Sx	1.89	Parallel			1.89	
WRNA2S/3	Sx	1.87	Parallel		5.87	1.87	
WRNA2S/4	Sx	1.91	Parallel			1.91	
WRNA2S/5	Sx	1.99	Parallel			1.99	
WRNA2S/6	Sx	1.91	Parallel			1.91	
WRNA2S/7	Sx	2.00	Perpendicular			2.00	
WRNA2S/8	Sx	2.03	Perpendicular			2.03	
WRNA2S/9	Sx	1.97	Perpendicular			1.97	
WRNA2S/10	Sx	1.96	Parallel			1.96	
WRNA2S/11	Sx	1.89	Parallel			1.89	
OYPBRS/1	Sx	BR	Parallel	2.08	2037	1271	
OYPBRS/2	Sx	BR	Parallel	2.11	1978	1240	
OYPBRS/3	Sx	BR	Parallel	2.00		1128	
OYPBRS/4	Sx	BR	Parallel	1.95	1405	1040	
OYPBRS/5	Sx	BR	Parallel	1.97	1474	1753	
OYPBRS/6	Sx	BR	Parallel	1.92			
OYPBRS/7	Sx	BR	Parallel	1.99	1356		
OYPBRrS/1	Sx	BR	Parallel	2.08	2037	1271	
OYPBRrS/2	Sx	BR	Parallel	2.11	1978	1240	
OYPBRrS/3	Sx	BR	Parallel	2.00		1128	
OYPBRrS/4	Sx	BR	Parallel	1.95	1405	1040	
OYPBRrS/5	Sx	BR	Parallel	1.97	1474	1753	
WKFGS/1	Sx	BR	Parallel	1.92			
WKFGS/2	Sx	BR	Parallel	1.99	1356		
WKFGS/3	Sx	BR	Parallel	2.14	1905	1205	
WKFGS/4	Sx	BR	Parallel	2.12	1920	1210	
WKFGS/5	Sx	BR	Parallel	2.12	1856	1211	
WKFGS/6	Sx	BR	Parallel	2.13	1829	1132	
CFBR/1	Sx	BR	Perpendicular	2.12	1639	1028	
CFBR/2	Sx	BR	Perpendicular	2.20	1931	1197	10.68
CFBR/3	Sx	BR	Perpendicular	2.22	2101	1365	4.35
CFBR/4	Sx	BR	Perpendicular	2.27	1962	1265	
CFBR/5	Sx	BR	Parallel	2.22	2200	1435	
CFBR/6	Sx	BR	Parallel	2.25			6.60
CFBR/7	Sx	BR	Parallel	2.23	2096	1293	6.29
CFBR/8	Sx	BR	Perpendicular	2.23	1994	1298	
CFBR/9	Sx	BR	Perpendicular		2522	1596	
CFBR/10	Sx	BR	Perpendicular	2.30	1975	1251	
CFBR/11	Sx	BR	Perpendicular	2.31	2147	1365	
CFBR/12	Sx	BR	Perpendicular	2.23	2010	1285	8.20
CFBR/13	Sx	BR	Perpendicular	2.24			4.31

CFBR/14	Sx	BR	Perpendicular	2.23	1987	1146	9.66
CFBR/15	Sx	BR	Perpendicular	2.23	1913	1219	
CFBR/16	Sx	BR	Perpendicular	2.27			4.39
CFBR/17	Sx	BR	Perpendicular	2.20	2108	1317	7.23
CFBR/18	Sx	BR	Perpendicular	2.26	2041	1176	5.50
CFBR/19	Sx	BR	Perpendicular	2.25	1962	1158	6.55
CFBR/20	Sx	BR	Perpendicular	2.17			4.60
CFBR/21	Sx	BR	Perpendicular	2.18	2015	1322	
CFBR/22	Sx	BR	Perpendicular	2.23	1985	1033	
PP/1	Sx	DF	Parallel	2.72			
PP/2	Sx	DF	Parallel	2.71	1493		
PP/3	Sx	DF	Parallel	2.77	1478		
PP/4	Sx	DF	Parallel	2.82			2.62
PP/5	Sx	DF	Parallel	2.76			
PP/6	Sx	DF	Parallel	2.77			3.01
PP/7	Sx	DF	Parallel	2.80			
PP/8	Sx	DF	Parallel	2.77			
PP/9	Sx	DF	Parallel	2.79			
PP/10	Sx	DF	Parallel	2.76			
PP/11	Sx	DF	Parallel	2.78			2.18
PP/12	Sx	DF	Parallel	2.85			
PP/13	Sx	DF	Parallel	2.81			2.04
PP/14	Sx	DF	Parallel	2.72			2.71
PP/15	Sx	DF	Perpendicular	2.77			
PP/16	Sx	DF	Perpendicular	2.77			
PP/17	Sx	DF	Perpendicular	2.78			
PP/18	Sx	DF	Perpendicular	2.75			2.71
OYPA2C/1	CS	SF	Parallel	2.26	2357	1489	15.91
OYPA2C/2	CS	SF	Parallel	2.35	2206	1433	3.25
OYPA2C/3	CS	SF	Parallel	2.22	2195	1404	2.37
OYPA2C/4	CS	SF	Parallel	2.33			
OYPA2C/5	CS	SF	Parallel	2.41	2187	1433	
OYPA2C/6	CS	SF	Parallel	2.28	2255	1493	
OYPA2C/7	CS	SF	Parallel	2.22			
OYPA2C/8	CS	SF	Parallel	2.15	2332	1535	6.50
OYPA2C/9	CS	SF	Parallel	2.25	2173	1450	
OYPA2C/10	CS	SF	Parallel	2.27	2252	1529	5.34
OYPA2C/11	CS	SF	Parallel	2.21	2101	1413	
OYPA2C/12	CS	SF	Parallel	2.25	2327	1527	
OYPA2C/13	CS	SF	Parallel	2.22	2356	1583	
OYPA2C/14	CS	SF	Parallel	2.24	2226	1446	
OYPA2C/15	CS	SF	Parallel	2.21	2040	1368	
OYPA2C/16	CS	SF	Parallel	2.22			
OYPA2C/17	CS	SF	Parallel	2.25			
OYPA3C/1	CS	DP	Perpendicular	2.31	1949	1242	
OYPA3C/2	CS	DP	Perpendicular	2.33	2213	1357	39.72
OYPA3C/3	CS	DP	Perpendicular	2.23	1786	1092	24.26
OYPA3C/4	CS	DP	Perpendicular	2.32	1964	1272	
OYPA3C/5	CS	DP	Perpendicular	2.34	2475	1566	
OYPA3C/6	CS	DP	Perpendicular	2.29	1897	1199	
OYPA3C/7	CS	DP	Parallel	2.32	2272	1425	11.20
OYPA3C/8	CS	DP	Parallel	2.34	2031	1274	
OYPA3C/9	CS	DP	Parallel	2.34	2186	1405	21.48
OYPA3C/10	CS	DP	Parallel	2.34	2520	1601	
OYPA3C/11	CS	DP	Parallel	2.39	2219	1386	
WRNA2C/1	CS	SF	Parallel	2.11	2224	1408	
WRNA2C/2	CS	SF	Parallel	2.18	2223	1420	8.20
WRNA2C/3	CS	SF	Perpendicular	2.21	1960	1242	15.84
WRNA2C/4	CS	SF	Perpendicular	2.23	1838	1193	5.39
WRNA2C/5	CS	SF	Perpendicular	2.23	1857	1236	

WRNA2C/6	CS	SF	Perpendicular	2.26	2093	1372	
WRNA2C/7	CS	SF	Parallel	2.17	2131	1382	
WRNA2C/8	CS	SF	Parallel	2.19	2210	1498	7.34
WKBRC/1	CS	BR	Parallel	2.15	2057	1307	
WKBRC/2	CS	BR	Parallel	2.23	2033	1251	
WKBRC/3	CS	BR	Parallel	2.18	1992	1279	
WKBRC/4	CS	BR	Perpendicular	2.24	1972	1250	7.60
WKBRC/5	CS	BR	Perpendicular	2.20	1794	1081	5.79
WKBRC/6	CS	BR	Perpendicular	2.14	2100	1294	
WKBRC/7	CS	BR	Perpendicular	2.17	1868	1175	
WKBRC/8	CS	BR	Perpendicular	2.16	2002	1231	
WKBRC/9	CS	BR	Parallel	2.25	2098	1304	
WKBRC/10	CS	BR	Parallel	2.29	2127	1325	3.09
WKBRC/11	CS	BR	Parallel	2.27	2074	1317	
OYPLOS/1	Sw	SF	Perpendicular	2.16	2277	2277	
OYPLOS/2	Sw	SF	Perpendicular	2.16	2276	2276	8.14
OYPLOS/3	Sw	SF	Perpendicular	2.22	2552	2552	
OYPLOS/4	Sw	SF	Perpendicular	2.05			
OYPLOS/5	Sw	SF	Perpendicular	2.13	2268	2268	
OYPLOS/6	Sw	SF	Parallel	2.17	2079	2079	
OYPLOS/7	Sw	SF	Parallel	2.23	2079	2079	
OYPLOS/8	Sw	SF	Parallel	2.18	2069	2069	
OYPLOS/9	Sw	SF	Parallel	2.20	2080	2080	
OYPLOS/10	Sw	SF	Parallel	2.25	2252	2252	13.27
OYPUSS/1	Sw	SF	Parallel	2.24	2081	2081	
OYPUSS/2	Sw	SF	Parallel	2.21	2040	2040	6.67
OYPUSS/3	Sw	SF	Parallel	2.14	2165	2165	5.17
OYPUSS/4	Sw	SF	Parallel	2.23	2367	2367	2.76
OYPUSS/5	Sw	SF	Parallel	2.22	2082	2082	
OYPNCL/1	Sw	DP	Parallel	2.33	2259	1454	1.15
OYPNCL/2	Sw	DP	Parallel	2.26	2126	1395	
OYPNCL/3	Sw	DP	Parallel	2.28	1815	1216	
OYPNCL/4	Sw	DP	Parallel	2.22	1960	1287	
OYPNCL/5	Sw	DP	Parallel	2.29	1803	1162	5.84
OYPNCL/6	Sw	DP	Parallel	2.20	1925	1265	2.32
OYPNCL/7	Sw	DP	Parallel	2.11			5.77
OYPNCL/8	Sw	DP	Parallel	2.29			10.54
OYPNCL/9	Sw	DP	Parallel	2.39			6.34
OYPNCL/10	Sw	DP	Parallel	2.25			
OYPNCL/11	Sw	DP	Parallel	2.27			
OYPNCL/12	Sw	DP	Parallel	2.24			
OYPNCL/13	Sw	DP	Parallel	2.27			
OYPNCL/14	Sw	DP	Parallel	2.32			
OYPNCL/15	Sw	DP	Parallel	2.27			
OYPNCL/16	Sw	DP	Perpendicular	19.92	1740	1090	18.28
OYPNCL/17	Sw	DP	Perpendicular	20.36	2039	1217	8.55
OYPNCL/18	Sw	DP	Perpendicular	20.03			
OYPNCL/19	Sw	DP	Perpendicular	25.54			
OYPNCL/20	Sw	DP	Perpendicular	21.72	1931	1287	5.90
OYPNCL/21	Sw	DP	Perpendicular	21.75	2021	1381	
OYPNCL/22	Sw	DP	Perpendicular	20.09	1748.0		
OYPNCU/23	Sw	DP	Parallel	2.33	2143	1347	
OYPNCU/24	Sw	DP	Parallel	2.00	1914	1222	
OYPNCU/25	Sw	DP	Parallel	2.17	1967	1325	
OYPNCU/26	Sw	DP	Parallel	2.14	1869	1191	13.35
OYPNCU/27	Sw	DP	Parallel	2.16	2010	1332	
OYPNCU/28	Sw	DP	Parallel	2.13	1787	1143	
OYPNCU/29	Sw	DP	Parallel	2.15			10.75
OYPNCU/30	Sw	DP	Parallel	2.13			
OYPNCU/31	Sw	DP	Parallel	2.07			

OYPNCU/32	Sw	DP	Parallel	2.09			
OYPNCU/33	Sw	DP	Parallel	2.11			
OYPNCU/34	Sw	DP	Parallel	2.11			
OYPNCU/35	Sw	DP	Parallel	2.14			6.36
OYPNCU/36	Sw	DP	Parallel	2.05			4.06
OYPNCU/37	Sw	DP	Parallel	2.08			4.35
OYPNCU/38	Sw	DP	Parallel	2.16	2083	1329	
OYPNCU/39	Sw	DP	Parallel	2.27	2012	1251	
OYPNCU/40	Sw	DP	Parallel	2.10	1906	1176	
OYPNCU/41	Sw	DP	Parallel	2.19	1829	1162	
OYPNCU/42	Sw	DP	Parallel	2.14	2037	1287	
OYPNCU/43	Sw	DP	Parallel	2.23			
OYPNCU/44	Sw	DP	Perpendicular	2.27			4.63
OYPNCU/45	Sw	DP	Perpendicular	2.17			5.56
OYPNCU/46	Sw	DP	Perpendicular	2.21			
OYPNCU/47	Sw	DP	Perpendicular	2.25			
OYPNCU/48	Sw	DP	Perpendicular	2.27	1933	1233	
OYPNCU/49	Sw	DP	Perpendicular	2.24	1639	1040	11.60
OYPNCU/50	Sw	DP	Perpendicular	2.30	1784	1176	23.00
OYPBROL/1	Sw	BR	Parallel	1.95	1607	1055	
OYPBROL/2	Sw	BR	Parallel	1.98	1663	1110	
OYPBROL/3	Sw	BR	Parallel	2.04	1535	1008	
OYPBROL/4	Sw	BR	Parallel	1.97	1979	967	
OYPBROL/5	Sw	BR	Parallel	1.95	1924	958	5.13
OYPBROL/6	Sw	BR	Parallel	1.92	2012	804	
OYPBROL/7	Sw	BR	Parallel	1.98	2124	1257	
OYPBROL/8	Sw	BR	Parallel	1.97	1654	1239	
OYPBROL/9	Sw	BR	Perpendicular	1.91	1698	1279	
OYPBROL/10	Sw	BR	Perpendicular	1.95	1562	1355	5.09
OYPBROL/11	Sw	BR	Perpendicular	1.93	1584	1050	
OYPBROL/12	Sw	BR	Perpendicular	1.93	1623	1068	
OYPBROL/13	Sw	BR	Perpendicular	1.98	1597	1000	
OYPBROL/14	Sw	BR	Perpendicular	1.96	2184	1032	5.1
OYPBROL/15	Sw	BR	Perpendicular	1.98		1049	5.1
OYPBROL/16	Sw	BR	Perpendicular	2.02	1729	1037	
OYPBROL/17	Sw	BR	Perpendicular	2.01	1639	1393	
WKBRS/1	Sw	BR	Perpendicular	2.18	1803	1172	9.39
WKBRS/2	Sw	BR	Perpendicular	2.16	1735	1120	
WKBRS/3	Sw	BR	Perpendicular	2.10	1731	1141	
WKBRS/4	Sw	BR	Perpendicular	2.16	1839	1195	12.09
WKBRS/5	Sw	BR	Perpendicular	2.14	1778	1160	
WKBRS/6	Sw	BR	Parallel	2.13	1930	1227	4.39
WKBRS/7	Sw	BR	Parallel	1.99	1557	1009	
WKBRS/8	Sw	BR	Parallel	2.06	1509	971	
WKBRS/9	Sw	BR	Parallel	2.09	1611	1033	
WKBRS/10	Sw	BR	Parallel	2.06	1684	1092	
WKBRS/11	Sw	BR	Parallel	2.03	1641	1051	
WKBRS/12	Sw	BR	Parallel	2.15	2211	1457	
WKBRS/13	Sw	BR	Parallel	2.13	2180	1417	
WKBRS/14	Sw	BR	Parallel	2.14	2087	1374	
WKBRS/15	Sw	BR	Parallel	2.20	2190	1438	11.36
WKBRS/16	Sw	BR	Perpendicular	2.19	2072	1355	9.55
WKBRS/17	Sw	BR	Perpendicular	2.17	2127	1396	9.85
WKBRS/18	Sw	BR	Perpendicular	2.17	2191	1456	
WKBRS/19	Sw	BR	Perpendicular	2.16	2316	1521	6.86
WKBRS/20	Sw	BR	Perpendicular	2.14			
WKBRS/21	Sw	BR	Perpendicular	2.14	2177	1434	8.38

9.6. Appendix F -Further SEM images of DF-1, SF-2, DP-3 and BR-4

DF-1

[1A] x100

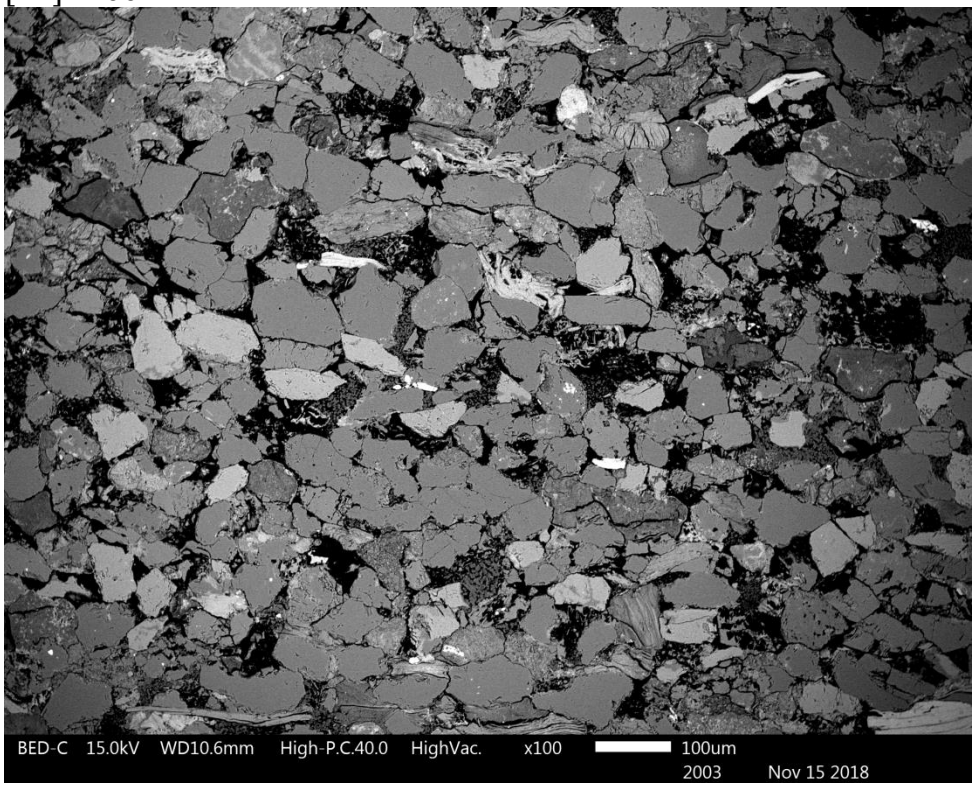

[1B] x400

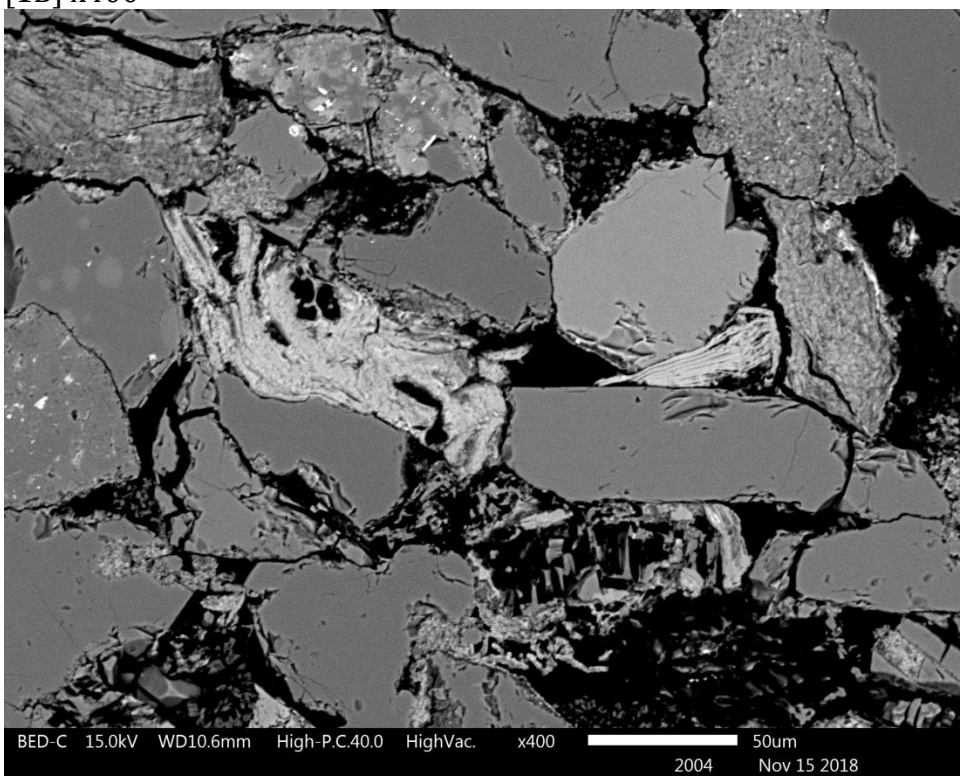

[1C] x2000

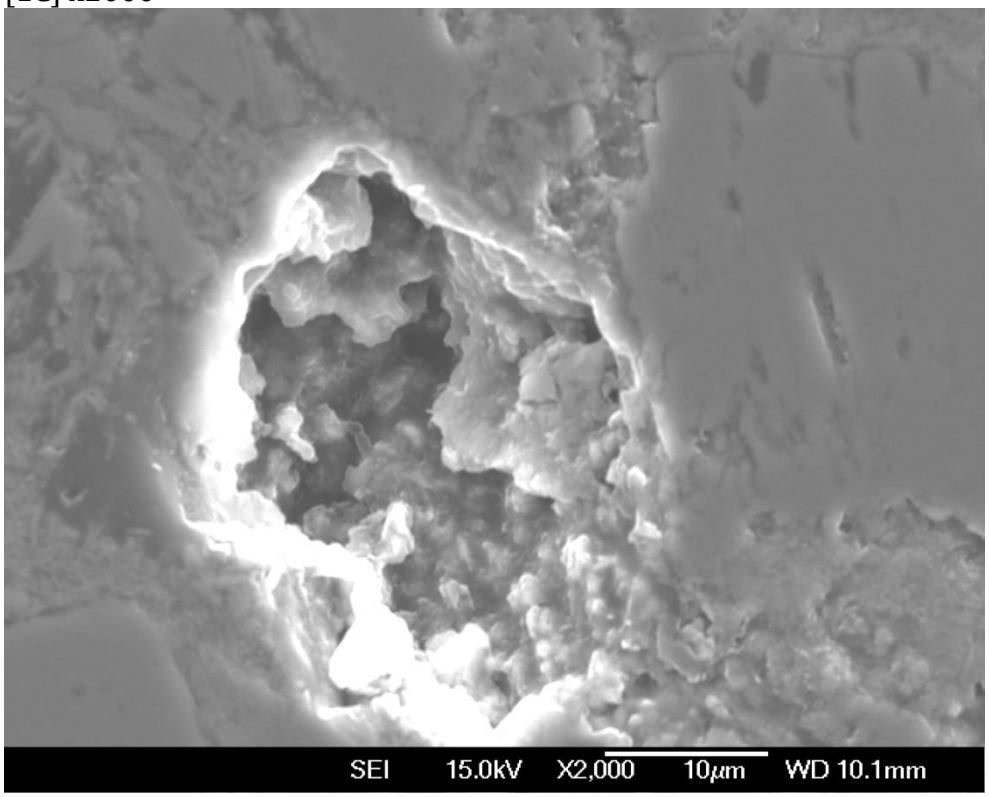

SF-2

[1A] x100

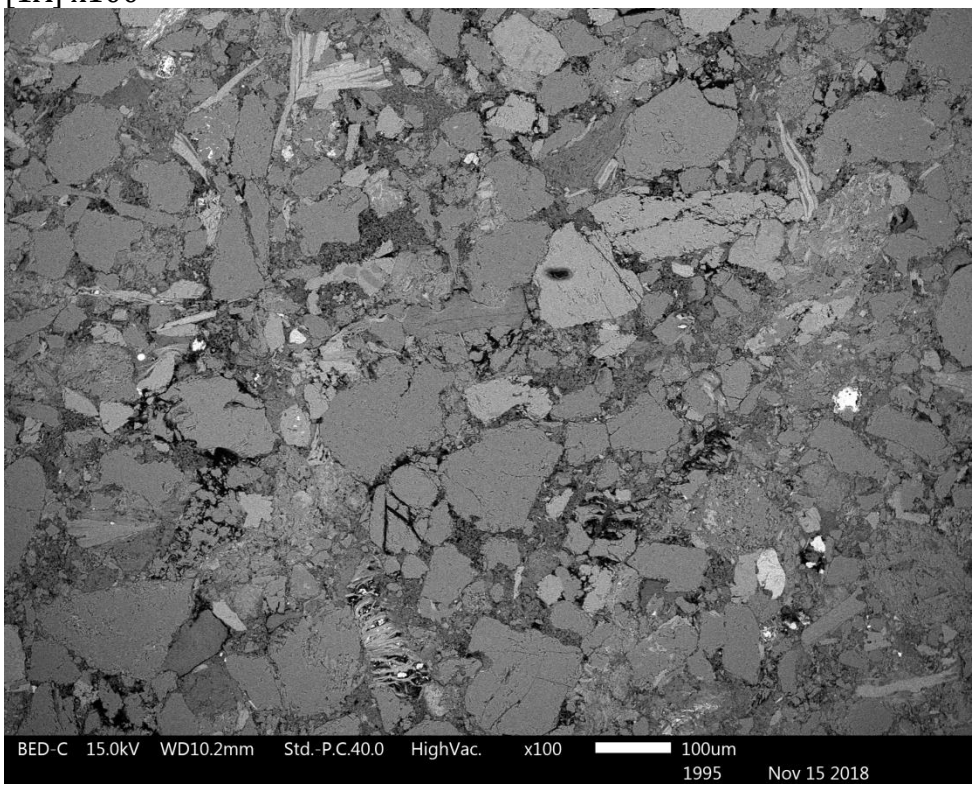

[1B] x200

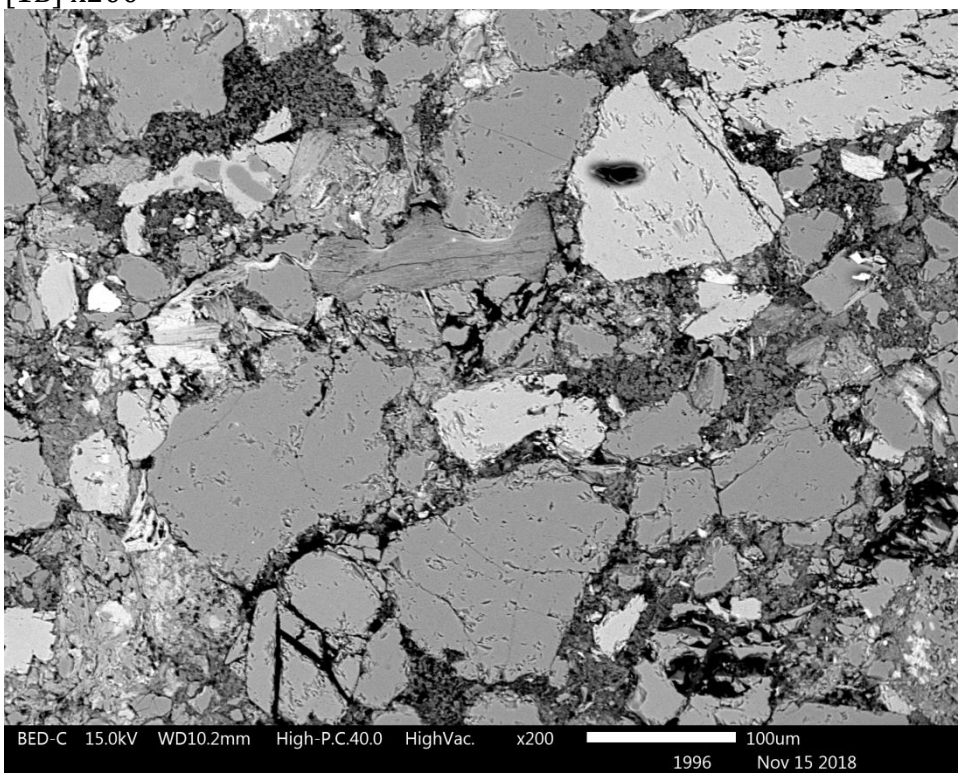

[1C] x500

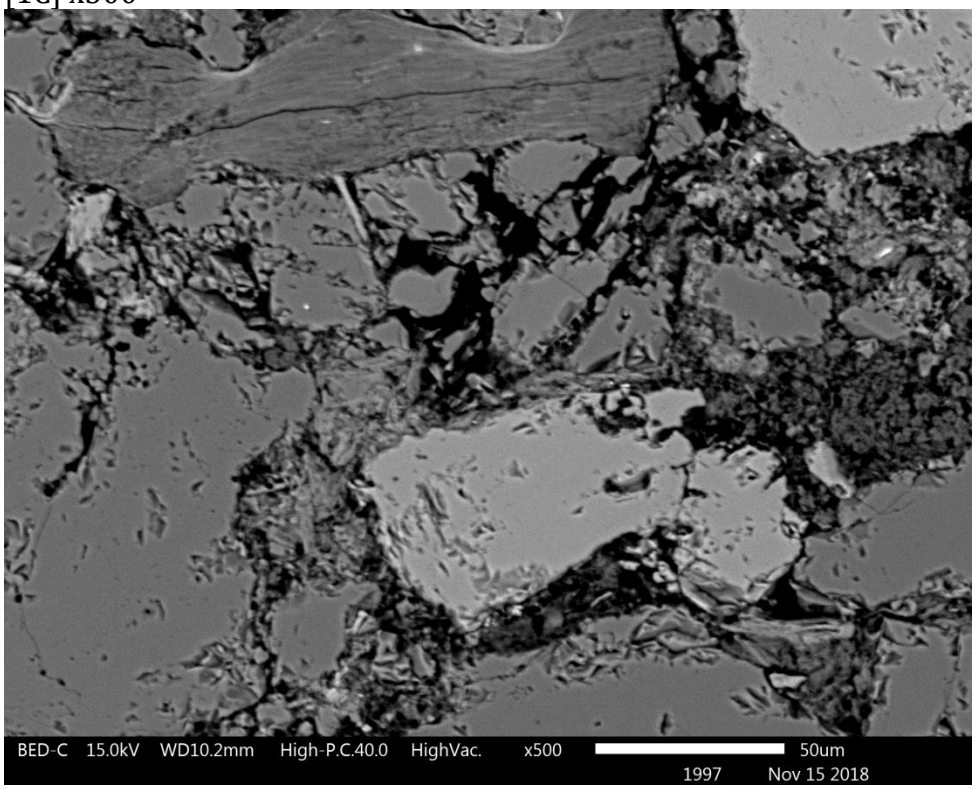

[1D] x2000

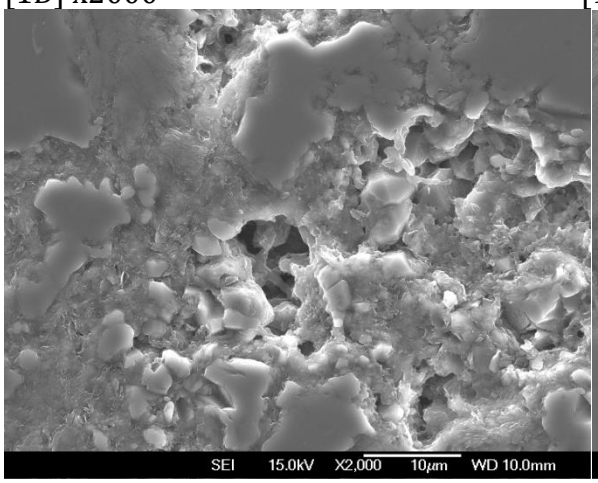

[1E] x3000

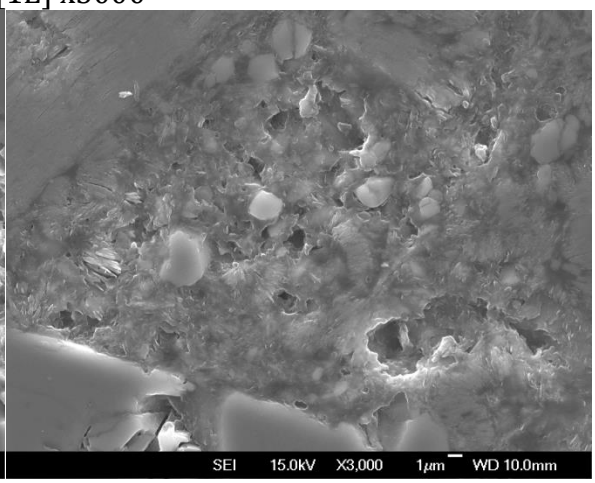

DP-3

[1A] x95

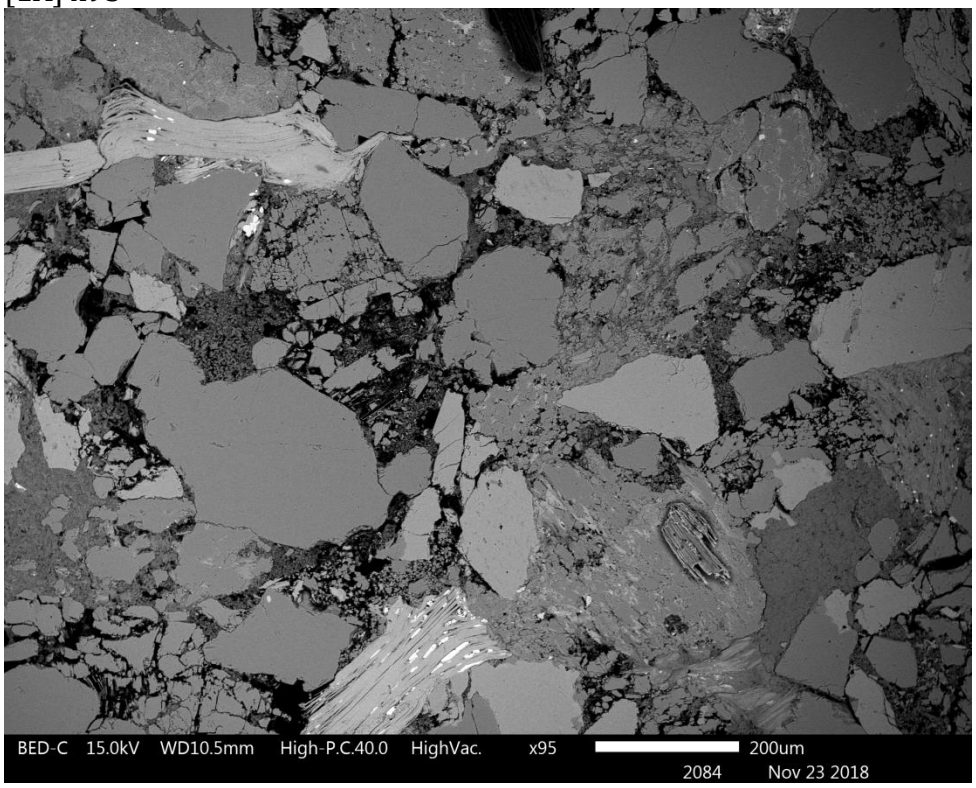

[1B] x200

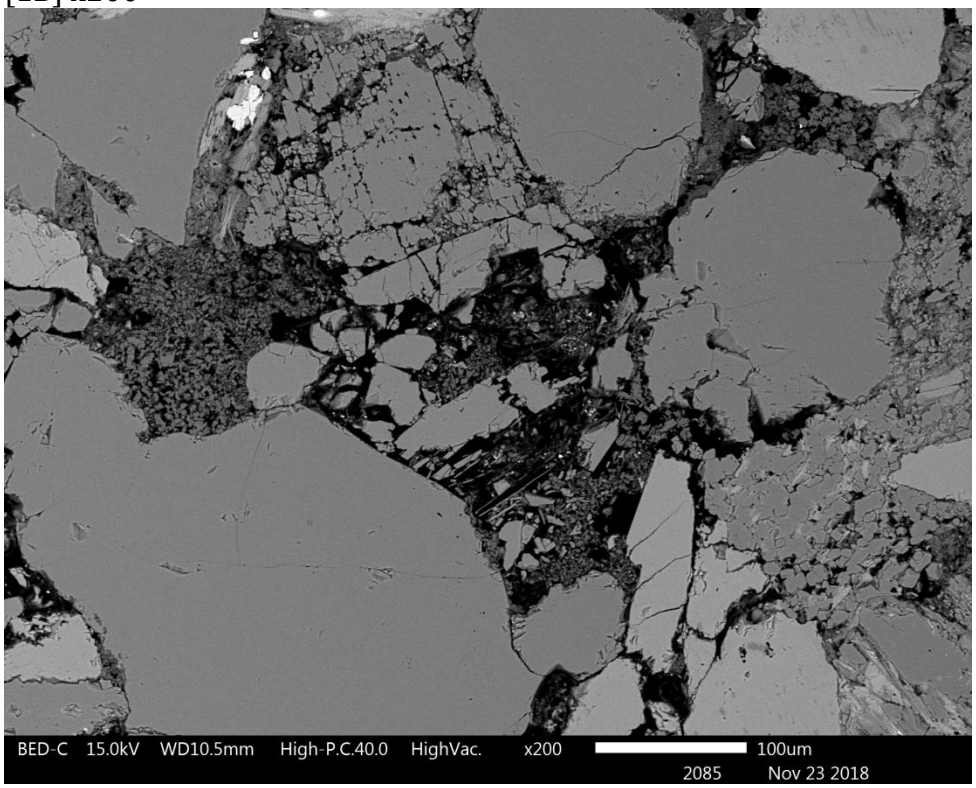

[1C] x2000

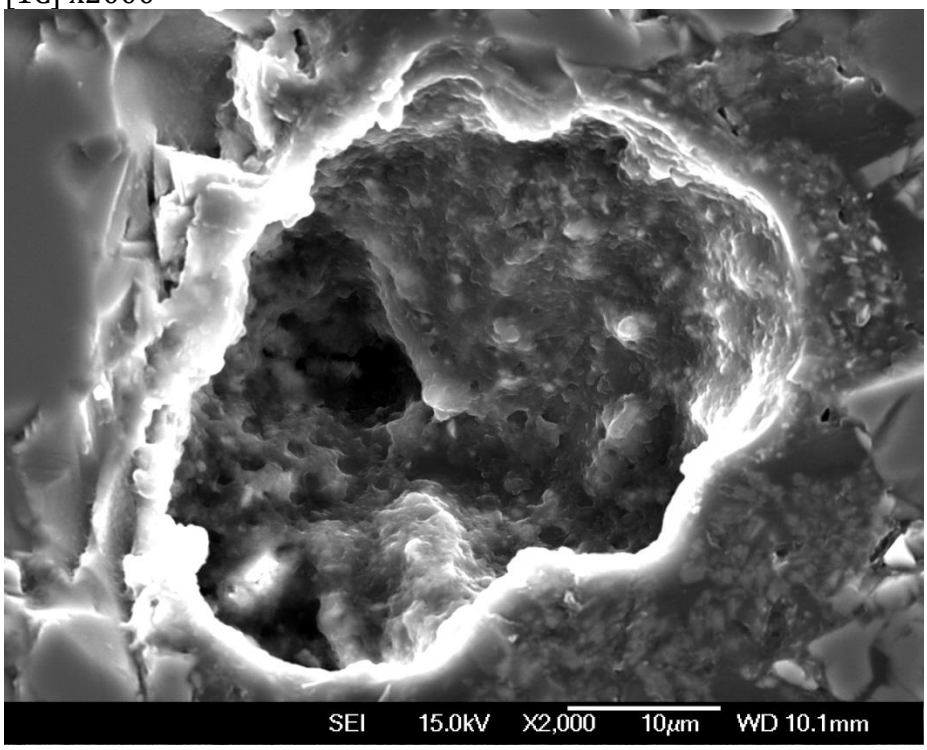

[2A] x100

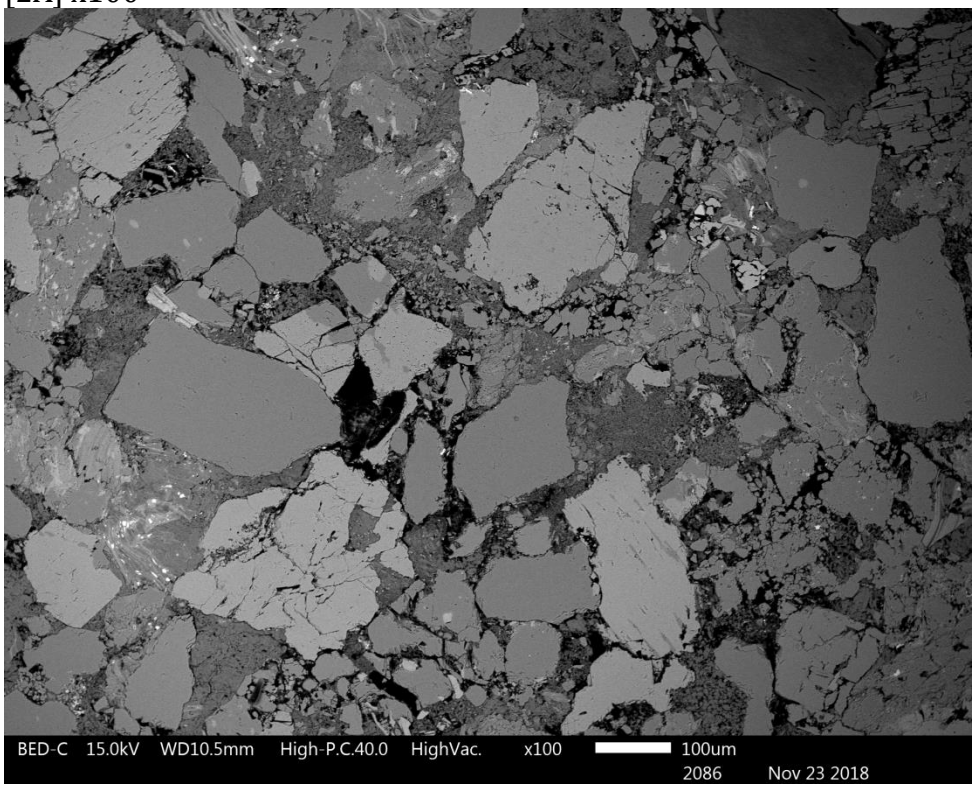

[2B] x200

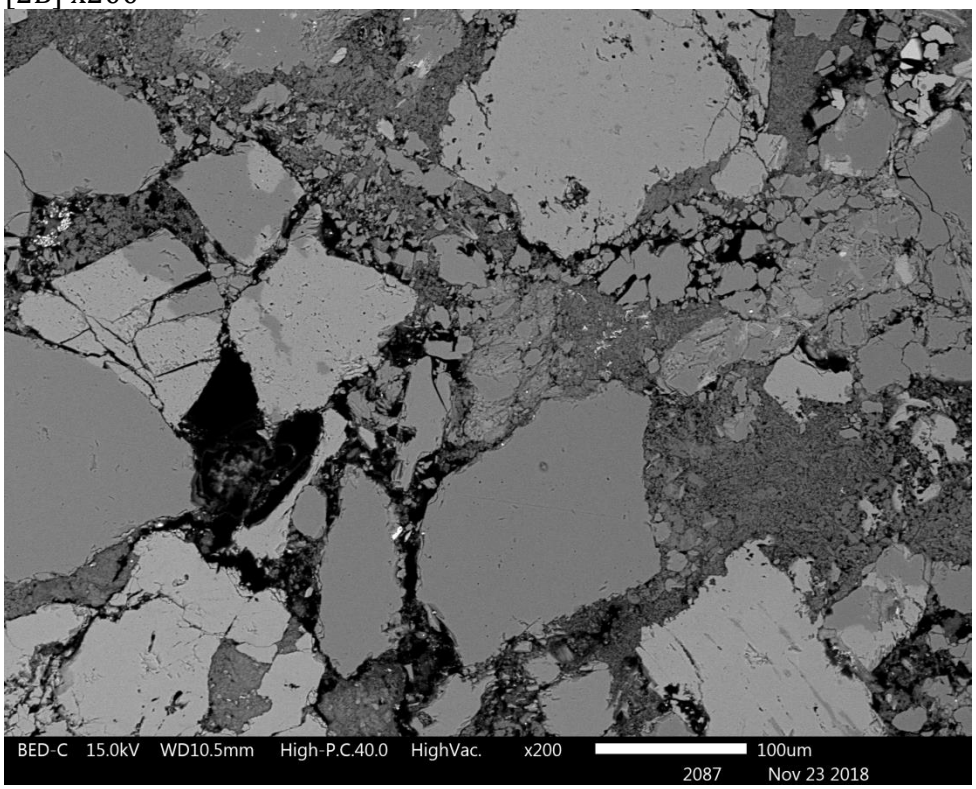

[2C] x2000

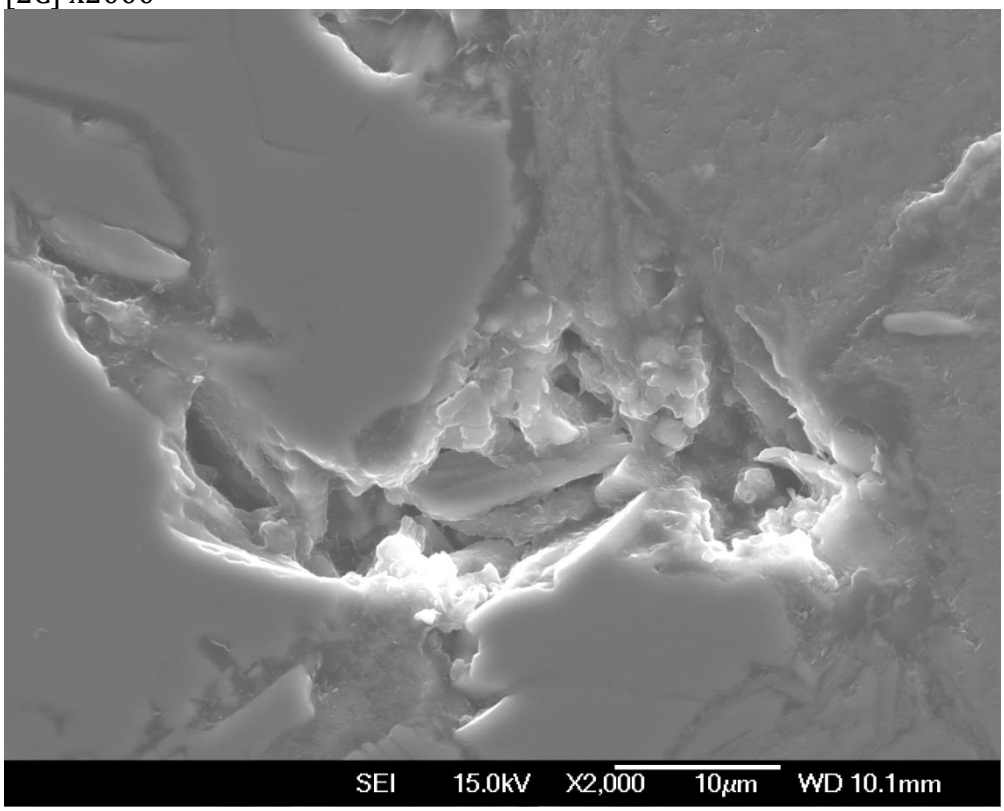

[3A] x100

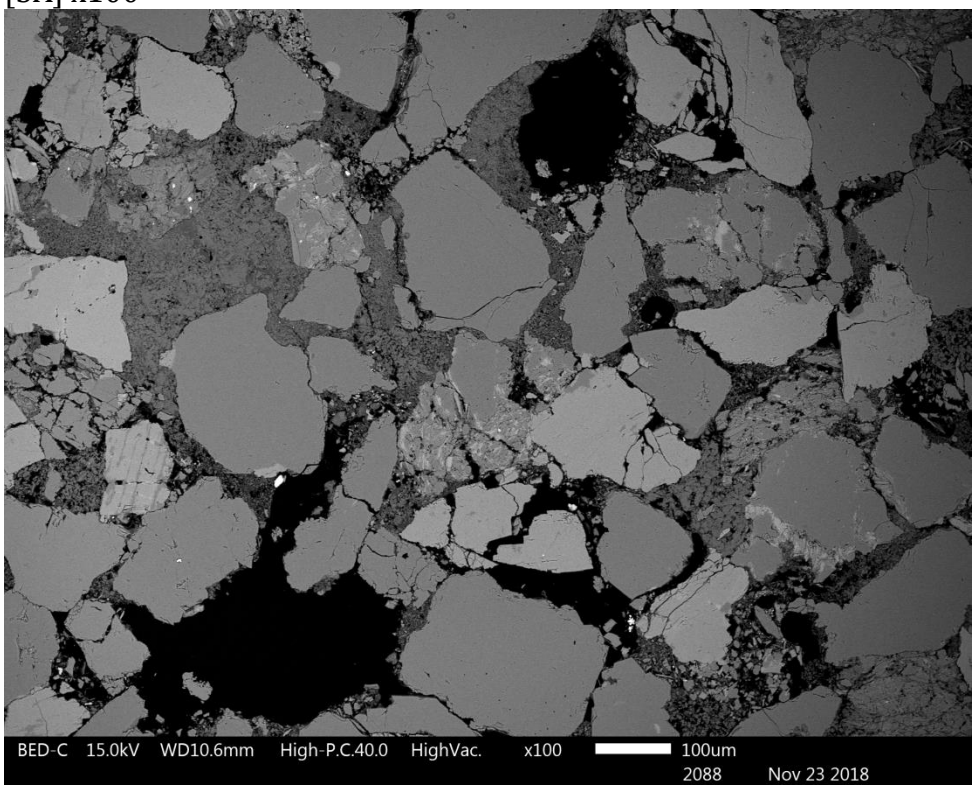

[3B] x200

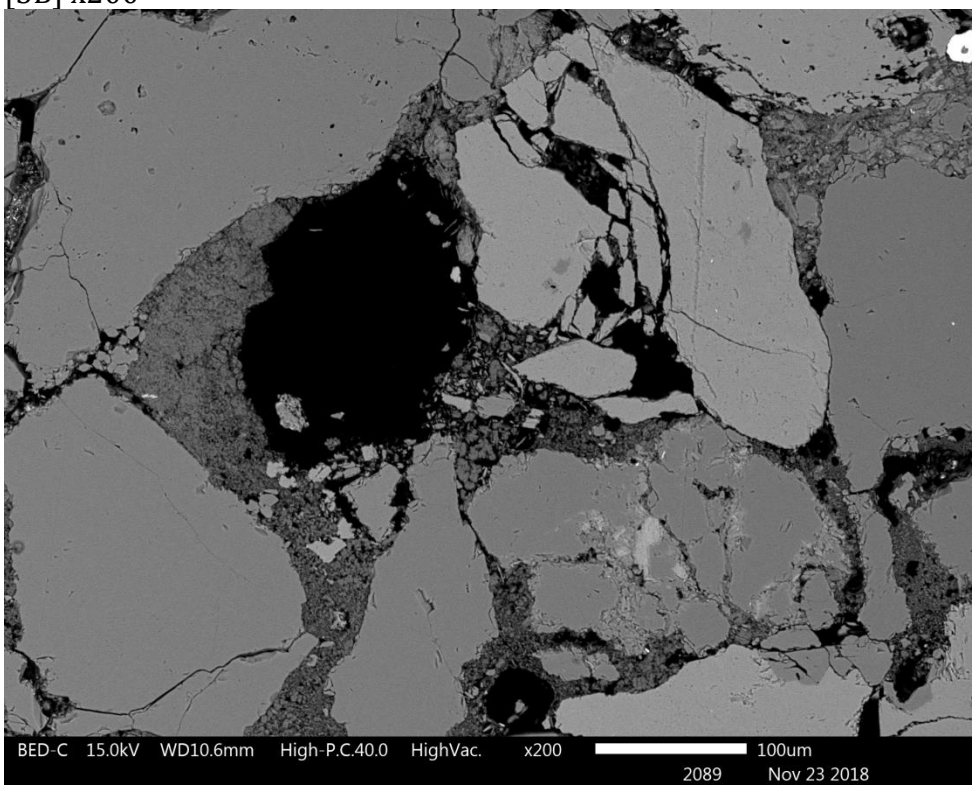

BR-4

[1A] x100

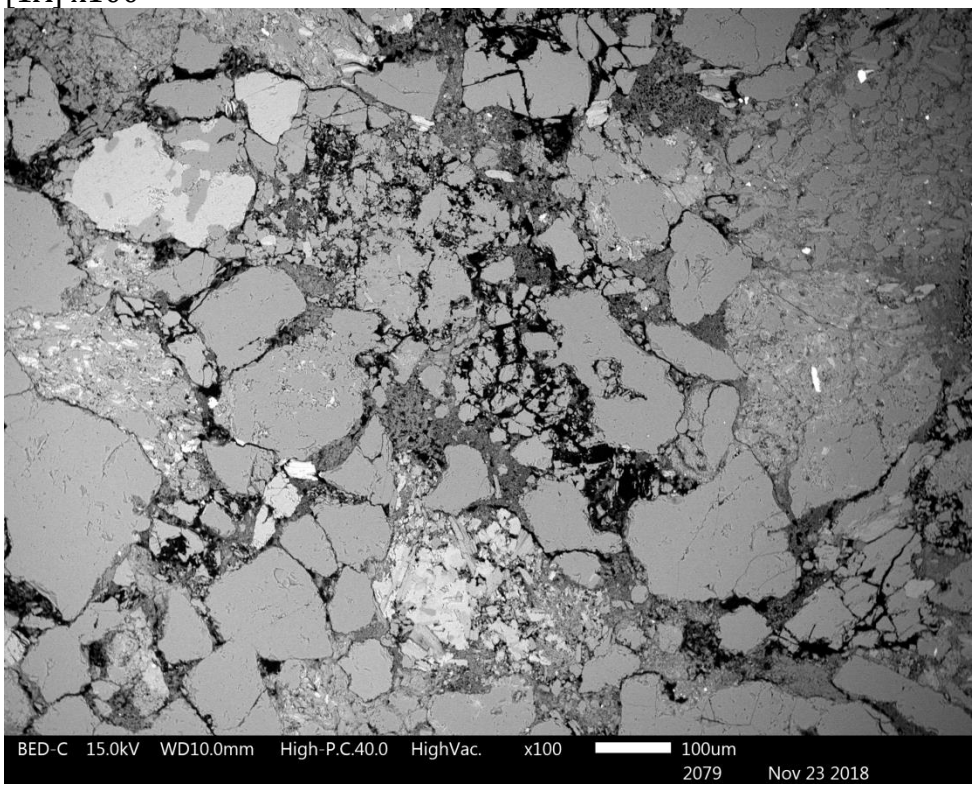

[1B] x190

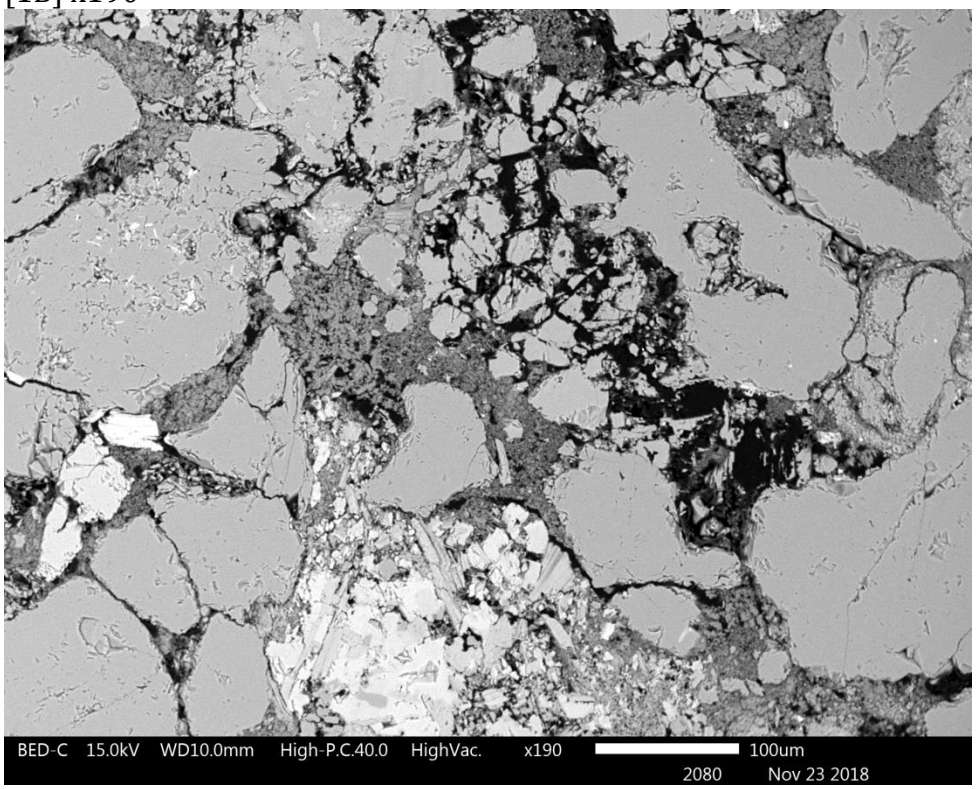

[C] x500

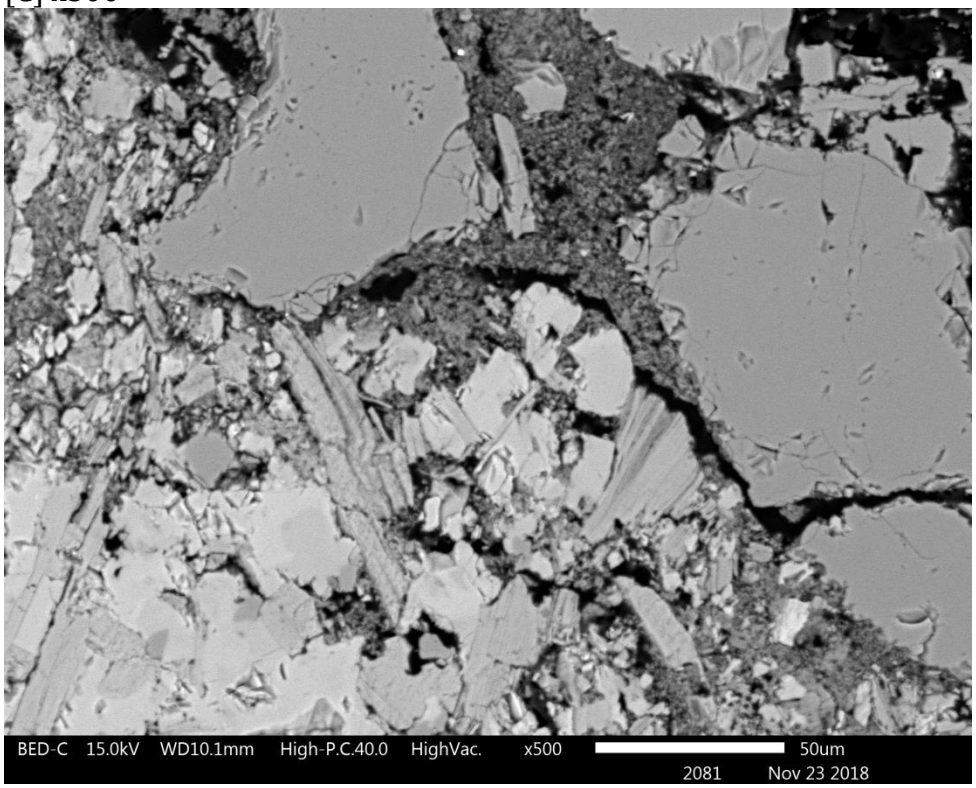

[1D] x750

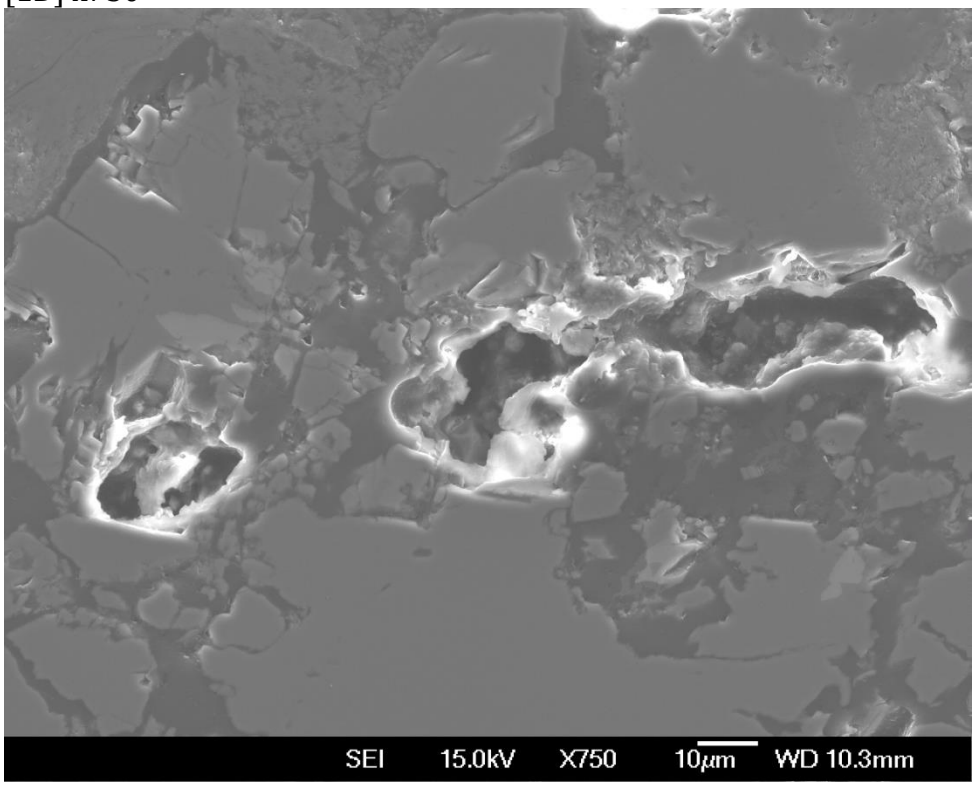

[2A] x100

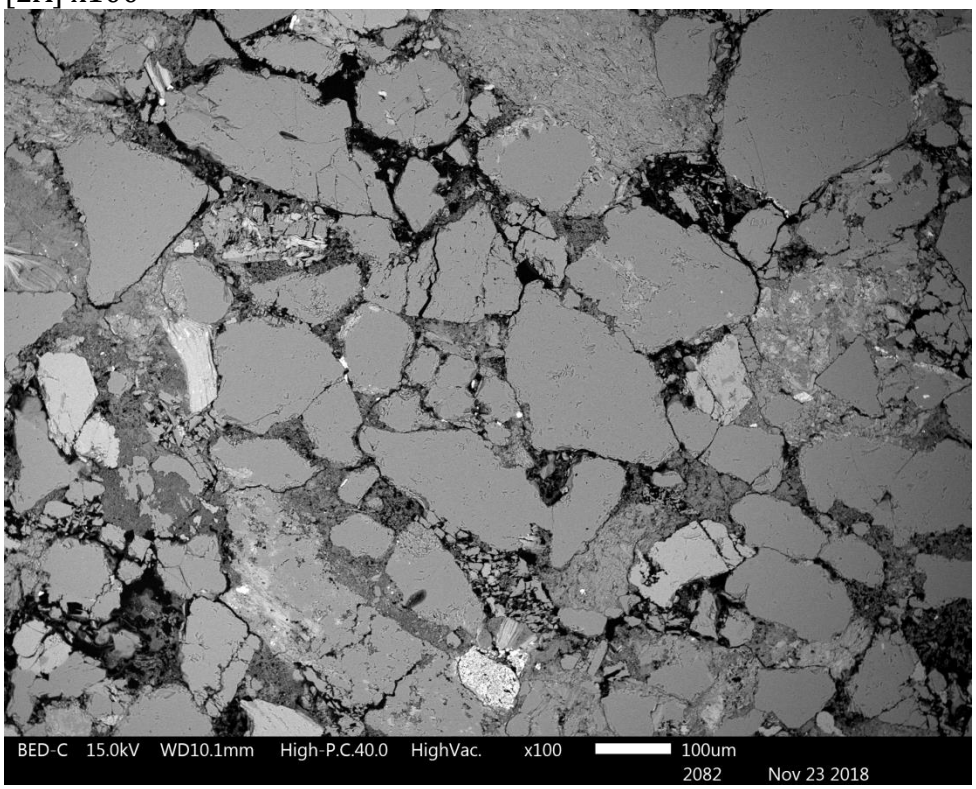

[2B] x400

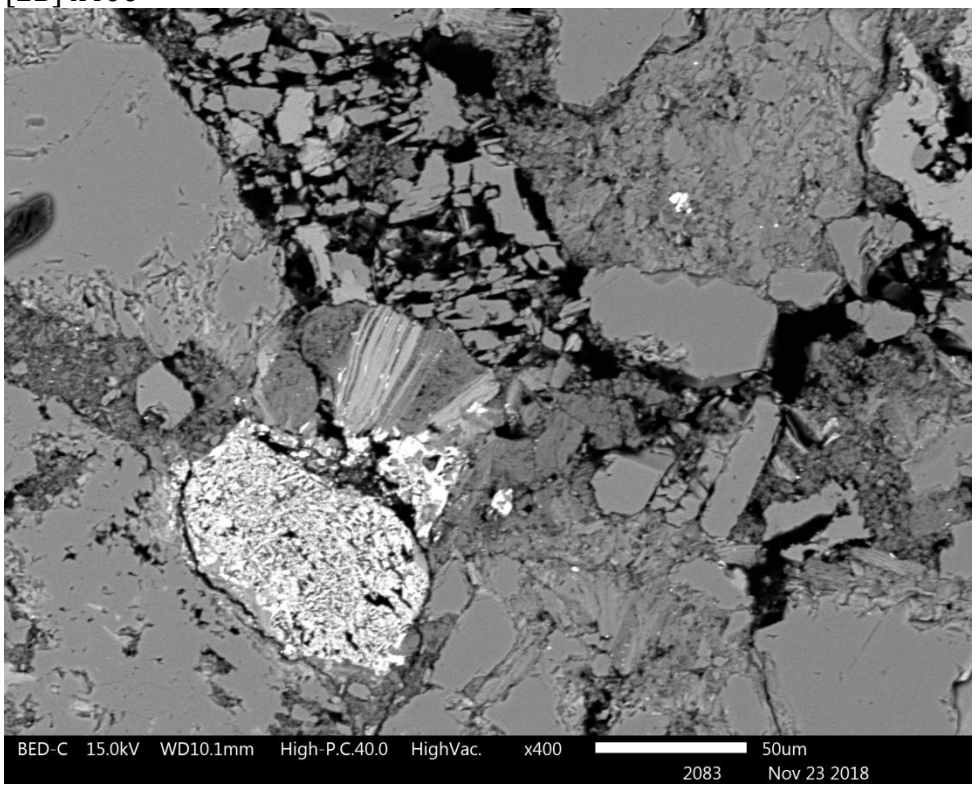

[2C] x1000

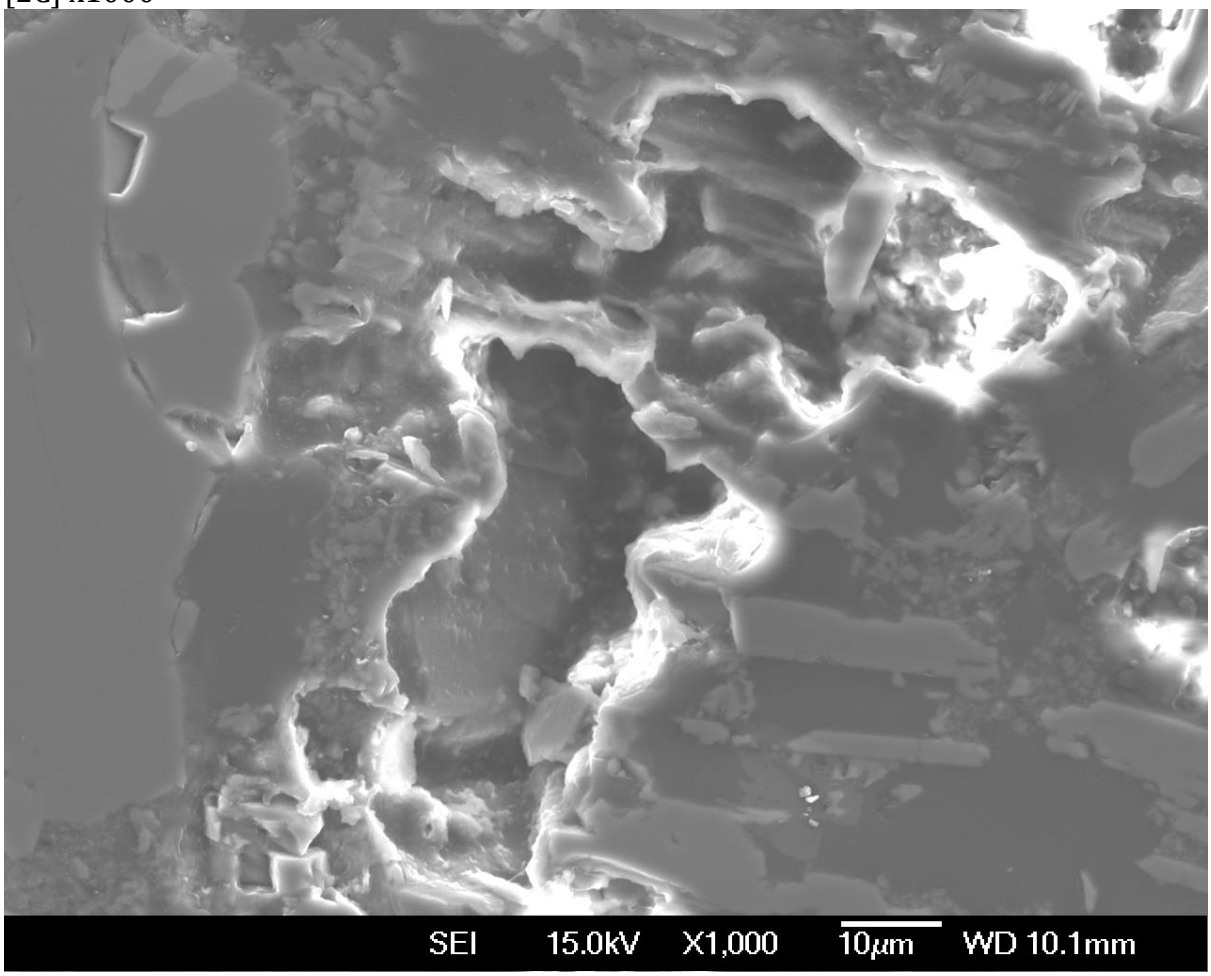

9.7. Appendix G - Physical and Mechanical Rock Properties for Reservoir Core Samples

Wellbore	Code	Plug Direction	From (m)	To (m)	Formation	Grain density (g/cm)	Porosity Fraction	Perm (mD)
Moki 2A	MK2-B8	v	1315	1315.1	Manganui	2.79	0.15	
Moki 2A	MK2-B8	h1	1315	1315.1	Manganui	2.83	0.16	
Moki 2A	MK2-B8	h2	1315	1315.1	Manganui	2.82	0.15	
Moki 2A	MK2-B6	h1	1313	1313.2	Manganui	2.79	0.13	
Moki 2A	MK2-B6	h2	1313	1313.2	Manganui	2.76	0.08	
Moki 2A	MK2-B5	v	1312.8	1313	Manganui	2.77	0.20	
Moki 2A	MK2-B5	h1	1312.8	1313	Manganui	2.76	0.22	
Moki 2A	MK2-B5	h2	1312.8	1313	Manganui	2.82	0.17	
Moki 1	MK1-B14	v	2138.3	2138.4	Mangahewa	2.72	0.03	0.003
Moki 1	MK1-B14	h1	2138.5	2138.6	Mangahewa	2.72	0.09	0.06
Moki 1	MK1-B14	h2	2138.5	2138.6	Mangahewa	2.66	0.08	0.04
Moki 1	MK1-B13	v	2137.4	2137.5	Mangahewa	2.64	0.13	0.21
Moki 1	MK1-B13	h1	2137.4	2137.5	Mangahewa	2.65	0.12	0.17
Moki 1	MK1-B13	h2	2137.4	2137.5	Mangahewa	2.65	0.10	0.12
Moki 1	MK1-B12	v	2136.4	2136.55	Mangahewa	2.64	0.14	0.19
Moki 1	MK1-B12	h1	2136.4	2136.55	Mangahewa	2.65	0.12	0.04
Moki 1	MK1-B12	h2	2136.4	2136.55	Mangahewa	2.65	0.13	0.10
Moki 1	MK1-B11	v	2135.6	2135.75	Mangahewa	2.66	0.16	0.09
Moki 1	MK1-B11	h1	2135.6	2135.75	Mangahewa	2.67	0.16	0.78
Moki 1	MK1-B11	h2	2135.6	2135.75	Mangahewa	2.63	0.15	0.76
Moki 1	MK1-B10	v	2134.3	2134.35	Mangahewa	2.65	0.11	0.06
Moki 1	MK1-B10	h1	2134.6	2134.7	Mangahewa	2.65	0.11	0.58
Moki 1	MK1-B10	h2	2134.6	2134.7	Mangahewa	2.66	0.09	0.85
Maui A1(G)	A1G-B10B	v	2777.9	2778.08	Mangahewa	2.68	0.16	0.56
Maui A1(G)	A1G-B10B	h1	2777.9	2778.08	Mangahewa	2.68	0.15	
Maui A1(G)	A1G-B10B	h2	2777.9	2778.08	Mangahewa	2.69	0.15	0.69
Maui A1(G)	A1G-B10A	v	2776.68	2777.03	Mangahewa	2.69	0.16	3.06
Maui A1(G)	A1G-B10A	h1	2776.68	2777.03	Mangahewa	2.69	0.17	0.29
Maui A1(G)	A1G-B10A	h2	2776.68	2777.03	Mangahewa	2.6930	0.15	0.26
Maui A1(G)	A1G-B7	v	2774	2774.26	Mangahewa	2.69	0.20	0.31
Maui A1(G)	A1G-B7	h1	2774	2774.26	Mangahewa	2.69	0.27	
Maui A1(G)	A1G-B7	h2	2774	2774.26	Mangahewa	2.68	0.19	0.69
Maui A1(G)	A1G-B6B	v	2771.3	2771.53	Mangahewa	2.71	0.18	0.11
Maui A1(G)	A1G-B6B	h1	2771.3	2771.53	Mangahewa	2.70	0.20	2.67
Maui A1(G)	A1G-B6B	h2	2771.3	2771.53	Mangahewa	2.69	0.21	0.32
Maui A1(G)	A1G-B6A	v	3077.71	3077.9	Kaimiro	2.67	0.28	
Maui A1(G)	A1G-B6A	h1	3076.22	3076.41	Kaimiro	2.66	0.27	
Maui A1(G)	A1G-B5	h1	3075.16	3075.36	Kaimiro	2.67	0.28	
Maui A1(G)	A1G-B5	h2	3075.16	3075.36	Kaimiro	2.66	0.21	25.02
Maui A1(G)	A1G-B2	v	3069.71	3070.01	Kaimiro	2.71	0.09	0.04
Maui A1(G)	A1G-B2	h1	3069.71	3070.01	Kaimiro	2.76	0.09	0.03
Maui A1(G)	A1G-B2	h2	3069.71	3070.01	Kaimiro	2.74	0.10	0.04
Maui A1(G)	A1G-B1	v	3068.48	3068.63	Kaimiro	2.79	0.12	0.03
Maui A1(G)	A1G-B1	h1	3068.48	3068.63	Kaimiro	2.79	0.14	0.11
Maui A1(G)	A1G-B1	h2	3068.48	3068.63	Kaimiro	2.82	0.14	0.08
MBR (1)	MBR-B2	v	3516.9	3517.2	Farewell	2.67	0.04	0.01
MBR (1)	MBR-B2	h1	3516.9	3517.2	Farewell	2.64	0.15	6.97

MBR (1)	MBR-B2	h2	3516.9	3517.2	Farewell	2.64	0.17	8.25
MBR (1)	MBR-B4	v	3519.4	3519.6	Farewell	2.62	0.19	25.86
MBR (1)	MBR-B4	h1	3519.4	3519.6	Farewell	2.64	0.21	75.95
MBR (1)	MBR-B4	h2	3519.4	3519.6	Farewell	2.64	0.23	1.89
MBR (1)	MBR-B7	v	3521.75	3521.9	Farewell	2.62	0.21	102.29
MBR (1)	MBR-B7	h1	3521.75	3521.9	Farewell	2.64	0.20	73.72
MBR (1)	MBR-B7	h2	3521.75	3521.9	Farewell	2.58	0.19	73.65
MBR (1)	MBR-B8	v	3522.8	3522.9	Farewell	2.87	0.15	0.02
MBR (1)	MBR-B8	h1	3522.8	3522.9	Farewell	2.86	0.15	0.03
MBR (1)	MBR-B8	h2	3522.8	3522.9	Farewell	2.87	0.14	0.07
MBR (1)	MBR-B9	v	3523.4	3523.65	Farewell	2.84	0.15	0.04
MBR (1)	MBR-B9	h1	3523.4	3523.65	Farewell	2.86	0.16	0.04
MBR (1)	MBR-B9	h2	3523.4	3523.65	Farewell	2.88	0.13	0.08
MBW (2)	MBW-B16	v	4132.45	4132.6	Farewell	2.62	0.23	161.88
MBW (2)	MBW-B16	h1	4132.45	4132.6	Farewell	2.66	0.23	110.55
MBW (2)	MBW-B16	h2	4132.45	4132.6	Farewell	2.66	0.24	82.45
MBW (2)	MBW-B14	v	4130.4	4130.6	Farewell	2.62	0.22	167.87
MBW (2)	MBW-B14	h1	4130.4	4130.6	Farewell	2.66	0.22	147.03
MBW (2)	MBW-B14	h2	4130.4	4130.6	Farewell	2.66	0.22	133.13
MBW (2)	MBW-B12	v	4128.05	4128.3	Farewell	2.66	0.20	51.22
MBW (2)	MBW-B12	h1	4128.05	4128.3	Farewell	2.69	0.19	21.27
MBW (2)	MBW-B12	h2	4128.05	4128.3	Farewell	2.67	0.20	44.76
MBW (2)	MBW-B10	v	4126.46	4126.66	Farewell	2.63	0.21	65.96
MBW (2)	MBW-B10	h1	4126.46	4126.66	Farewell	2.66	0.23	90.30
MBW (2)	MBW-B10	h2	4126.46	4126.66	Farewell	2.62	0.21	112.36
MBW (2)	MBW-B8	v	4124.65	4124.95	Farewell	2.62	0.19	52.82
MBW (2)	MBW-B8	h1	4124.65	4124.95	Farewell	2.65	0.20	26.96
MBW (2)	MBW-B8	h2	4124.65	4124.95	Farewell	2.66	0.19	23.33
Tane 1	T1-B5	v	3693.68	3693.78	North Cape	2.66	0.14	0.10
Tane 1	T1-B5	h1	3693.68	3693.78	North Cape	2.66	0.15	0.26
Tane 1	T1-B5	h2	3693.68	3693.78	North Cape	2.67	0.17	1.12
Tane 1	T1-B4A	v	3692.42	3692.65	North Cape	2.67	0.12	0.10
Tane 1	T1-B4A	h1	3692.42	3692.65	North Cape	2.67	0.12	0.22
Tane 1	T1-B4A	h2	3692.42	3692.65	North Cape	2.67	0.12	0.17
Tane 1	T1-B4B	v	3692	3692.15	North Cape	2.67	0.11	0.06
Tane 1	T1-B4B	h1	3692	3692.15	North Cape	2.67	0.11	0.15
Tane 1	T1-B4B	h2	3692	3692.15	North Cape	2.67	0.10	0.18
Tane 1	T1-B3	v	3689.91	3690.21	North Cape	2.66	0.06	0.03
Tane 1	T1-B3	h1	3689.91	3690.21	North Cape	2.66	0.07	0.005
Tane 1	T1-B3	h2	3689.91	3690.21	North Cape	2.68	0.09	0.02
Tane 1	T1-B2	h1	3689.15	3689.3	North Cape	2.63	0.08	0.004
Tane 1	T1-B2	h2	3689.15	3689.3	North Cape	2.68	0.08	0.003

Code		Dry Bulk Density (g/cm3)	Vp Dry m/s	Vs Dry m/s	Dynamic Poisson's Ratio	Dynamic Young's Modulus (GPa)	Dynamic Shear Modulus (GPa)	Dynamic Bulk Modulus (GPa)
MK2-B8	v	2.38	2253	1274	0.26	9.76	3.86	6.92
MK2-B8	h1	2.38	1942	1088	0.27	7.16	2.81	5.21
MK2-B8	h2	2.40	3199	1906	0.22	21.37	8.72	12.94
MK2-B6	h1	2.44	2683	1511	0.27	14.15	5.58	10.16
MK2-B6	h2	2.55	3515	1832	0.31	22.44	8.54	20.06
MK2-B5	v	2.23	2438	1455	0.22	11.54	4.72	6.95
MK2-B5	h1	2.16	2402	1364	0.26	10.14	4.02	7.10
MK2-B5	h2	2.33	2867	1724	0.22	16.84	6.92	9.91
MK1-B14	v	2.64	2484	1536	0.19	14.85	6.24	7.99
MK1-B14	h1	2.48	2465	1365	0.28	11.83	4.62	8.91
MK1-B14	h2	2.45	2543	1612	0.16	14.82	6.37	7.36
MK1-B13	v	2.30	2231	1219	0.29	8.81	3.42	6.90
MK1-B13	h1	2.34	2353	1258	0.30	9.62	3.70	8.01
MK1-B13	h2	2.37	2071	1097	0.30	7.45	2.86	6.37
MK1-B12	v	2.26	2258	1382	0.20	10.38	4.32	5.77
MK1-B12	h1	2.34	2528	1475	0.24	12.67	5.10	8.18
MK1-B12	h2	2.31	2748	1608	0.24	14.81	5.97	9.48
MK1-B11	v	2.22	2212	1233	0.27	8.62	3.38	6.38
MK1-B11	h1	2.25	2165	1218	0.27	8.45	3.33	6.08
MK1-B11	h2	2.24	2436	1436	0.23	11.42	4.63	7.15
MK1-B10	v	2.37	2506	1457	0.24	12.50	5.02	8.16
MK1-B10	h1	2.37	2941	1738	0.23	17.66	7.17	10.97
MK1-B10	h2	2.42	2296	1376	0.22	11.18	4.58	6.65
A1G-B10B	v	2.25	2734	1565	0.26	13.87	5.52	9.49
A1G-B10B	h1	2.28	3403	1724	0.33	17.97	6.77	17.35
A1G-B10B	h2	2.28	2845	1692	0.23	15.98	6.52	9.74
A1G-B10A	v	2.26	2420	1472	0.21	11.83	4.90	6.72
A1G-B10A	h1	2.24	2737	1460	0.30	12.44	4.78	10.42
A1G-B10A	h2	2.29	3042	1705	0.27	16.92	6.66	12.31
A1G-B7	v	2.16	2498	1557	0.18	12.41	5.25	6.51
A1G-B7	h1	1.98	2946	1727	0.24	14.61	5.90	9.30
A1G-B7	h2	2.17	2313	1327	0.25	9.60	3.82	6.52
A1G-B6B	v	2.22	2824	1605	0.26	14.41	5.71	10.07
A1G-B6B	h1	2.15	2562	1384	0.29	10.65	4.12	8.62
A1G-B6B	h2	2.12	2614	1243	0.35	8.87	3.27	10.12
A1G-B6A	v	1.91	2345	1414	0.21	9.30	3.83	5.42
A1G-B6A	h1							
A1G-B5	h1	1.92	2217	1346	0.21	8.41	3.48	4.80
A1G-B5	h2	2.09	1827	1086	0.23	6.06	2.47	3.70
A1G-B2	v	2.48	2653	1720	0.14	16.69	7.33	7.67
A1G-B2	h1	2.51	3438	2128	0.19	27.00	11.35	14.49
A1G-B2	h2	2.45	3138	1855	0.23	20.78	8.44	12.90
A1G-B1	v	2.44	2457	1476	0.22	12.94	5.31	7.64
A1G-B1	h1	2.40	2912	1622	0.28	16.13	6.32	11.95
A1G-B1	h2	2.42	3135	1838	0.24	20.23	8.17	12.88
MBR-B2	v	2.57	2905	1579	0.29	16.53	6.41	13.14
MBR-B2	h1	2.24	2381	1280	0.30	9.51	3.67	7.80
MBR-B2	h2	2.19	2597	1439	0.28	11.59	4.53	8.72
MBR-B4	v	2.12	2626	1671	0.16	13.72	5.91	6.72
MBR-B4	h1	2.09	2399	1405	0.24	10.20	4.12	6.51
MBR-B4	h2	2.02	2104	1332	0.17	8.35	3.58	4.16

MBR-B7	v	2.08	2249	1391	0.19	9.57	4.02	5.15
MBR-B7	h1	2.11	2498	1358	0.29	10.06	3.90	7.99
MBR-B7	h2	2.09	2538	1410	0.28	10.60	4.15	7.92
MBR-B8	v	2.42	2183	1379	0.17	10.76	4.61	5.40
MBR-B8	h1	2.45	2884	1721	0.22	17.72	7.24	10.68
MBR-B8	h2	2.48	2242	1287	0.25	10.31	4.11	6.99
MBR-B9	v	2.41	2420	1478	0.20	12.65	5.26	7.09
MBR-B9	h1	2.41	2460	1457	0.23	12.59	5.12	7.77
MBR-B9	h2	2.51	2632	1563	0.23	15.07	6.14	9.22
MBW-B16	v	2.03	2195	1350	0.20	8.84	3.70	4.84
MBW-B16	h1	2.04	2271	1300	0.26	8.66	3.45	5.92
MBW-B16	h2	2.03	2226	1287	0.25	8.39	3.36	5.57
MBW-B14	v	2.04	2482	1438	0.25	10.52	4.22	6.94
MBW-B14	h1	2.06	2226	1343	0.21	9.03	3.72	5.26
MBW-B14	h2	2.07	2323	1437	0.19	10.17	4.27	5.47
MBW-B12	v	2.14	2773	1587	0.26	13.52	5.38	9.25
MBW-B12	h1	2.18	2606	1605	0.19	13.45	5.63	7.33
MBW-B12	h2	2.15	2733	1708	0.18	14.81	6.28	7.70
MBW-B10	v	2.07	2259	1320	0.24	8.93	3.60	5.74
MBW-B10	h1	2.05	2334	1353	0.25	9.36	3.75	6.17
MBW-B10	h2	2.07	2525	1388	0.28	10.25	3.99	7.89
MBW-B8	v	2.11	2099	1283	0.20	8.36	3.48	4.67
MBW-B8	h1	2.13	2434	1300	0.30	9.37	3.60	7.82
MBW-B8	h2	2.16	2541	1368	0.30	10.46	4.04	8.54
T1-B5	v	2.29	2075	1279	0.19	8.94	3.74	4.86
T1-B5	h1	2.27	2390	1293	0.29	9.80	3.79	7.89
T1-B5	h2	2.22	2414	1300	0.30	9.71	3.75	7.93
T1-B4A	v	2.35	1950	1216	0.18	8.22	3.48	4.31
T1-B4A	h1	2.35	2491	1284	0.32	10.22	3.87	9.41
T1-B4A	h2	2.34	2362	1278	0.29	9.90	3.83	7.97
T1-B4B	v	2.37	1944	1175	0.21	7.93	3.27	4.59
T1-B4B	h1	2.38	2606	1476	0.26	13.12	5.19	9.26
T1-B4B	h2	2.40	2791	1550	0.28	14.71	5.76	11.00
T1-B3	v	2.51	2160	1377	0.16	11.04	4.77	5.38
T1-B3	h1	2.48	3683	2169	0.23	28.79	11.66	18.07
T1-B3	h2	2.44	3499	2164	0.19	27.15	11.40	14.61
T1-B2	h1	2.41	3557	2088	0.24	25.98	10.50	16.47
T1-B2	h2	2.47	3409	2113	0.19	26.15	11.01	13.97

Code		Saturated Bulk Density (g/cm3)	Vp Wet m/s	Vs Wet m/s	Dynamic Poisson's Ratio	Dynamic Young's Modulus (GPa)	Dynamic Shear Modulus (GPa)	Dynamic Bulk Modulus (GPa)
MK2-B8	v	2.55						
MK2-B8	h1	2.58						
MK2-B8	h2	2.57						
MK2-B6	h1	2.57						
MK2-B6	h2	2.62						
MK2-B5	v	2.42						
MK2-B5	h1	2.36						
MK2-B5	h2	2.51						
MK1-B14	v	2.68	3350	1367	0.40	14.04	5.01	23.43
MK1-B14	h1	2.56	2958	1192	0.40	10.22	3.64	17.58
MK1-B14	h2	2.53	3249	1417	0.38	14.03	5.07	19.91
MK1-B13	v	2.41	2570	1114	0.38	8.29	2.99	11.94
MK1-B13	h1	2.44	2489	1168	0.36	9.06	3.34	10.70
MK1-B13	h2	2.47	2588	1066	0.40	7.84	2.81	12.79
MK1-B12	v	2.39	2435	1296	0.30	10.48	4.02	8.83
MK1-B12	h1	2.45	2709	1309	0.35	11.33	4.20	12.40
MK1-B12	h2	2.43	2796	1518	0.29	14.45	5.60	11.52
MK1-B11	v	2.37	2610	1136	0.38	8.44	3.05	12.04
MK1-B11	h1	2.39	2903	1163	0.40	9.07	3.23	15.82
MK1-B11	h2	2.38	2633	1198	0.37	9.36	3.42	11.96
MK1-B10	v	2.46	3221	1427	0.38	13.83	5.02	18.88
MK1-B10	h1	2.47	3045	1597	0.31	16.50	6.30	14.50
MK1-B10	h2	2.50	3127	1363	0.38	12.83	4.64	18.23
A1G-B10B	v	2.39	2784	1278	0.37	10.65	3.90	13.29
A1G-B10B	h1	2.40						
A1G-B10B	h2	2.40	2600	1307	0.33	10.92	4.10	10.77
A1G-B10A	v	2.39	2469	1374	0.28	11.50	4.51	8.55
A1G-B10A	h1	2.37	2836	1383	0.34	12.17	4.53	13.00
A1G-B10A	h2	2.40	3055	1338	0.38	11.88	4.30	16.68
A1G-B7	v	2.33	2539	1293	0.32	10.34	3.90	9.84
A1G-B7	h1	2.14	2382	1068	0.37	6.71	2.44	8.89
A1G-B7	h2	2.34	2313	1148	0.34	8.24	3.08	8.40
A1G-B6B	v	2.37	3122	1370	0.38	12.27	4.44	17.15
A1G-B6B	h1	2.31	2617	1339	0.32	10.97	4.15	10.31
A1G-B6B	h2	2.28	2457	1218	0.34	9.05	3.38	9.26
A1G-B6A	v	2.12						
A1G-B6A	h1							
A1G-B5	h1	2.11	2294	1001	0.38	5.85	2.12	8.29
A1G-B5	h2	2.26	2340	1138	0.35	7.88	2.93	8.48
A1G-B2	v	2.54	3104	1341	0.39	12.68	4.58	18.42
A1G-B2	h1	2.57	3702	1419	0.41	14.64	5.18	28.34
A1G-B2	h2	2.55	3208	1377	0.39	13.40	4.83	19.77
A1G-B1	v	2.53	3233	1387	0.39	13.52	4.87	19.98
A1G-B1	h1	2.51	3074	1362	0.38	12.84	4.66	17.52
A1G-B1	h2	2.52	3195	1681	0.31	18.61	7.11	16.20
MBR-B2	v	2.61	4004	1427	0.43	15.15	5.31	34.70
MBR-B2	h1	2.38	2494	1060	0.39	7.43	2.67	11.24
MBR-B2	h2	2.34	2543	1235	0.35	9.62	3.57	10.39
MBR-B4	v	2.29	2870	1262	0.38	10.08	3.65	14.02
MBR-B4	h1	2.25	2462	1277	0.32	9.66	3.67	8.75
MBR-B4	h2	2.21	2260	1187	0.31	8.16	3.11	7.14

MBR-B7	v	2.27	2445	1115	0.37	7.73	2.82	9.81
MBR-B7	h1	2.30	2792	1240	0.38	9.72	3.53	13.19
MBR-B7	h2	2.28	2632	1283	0.34	10.10	3.76	10.80
MBR-B8	v	2.53	2635	1214	0.37	10.19	3.73	12.61
MBR-B8	h1	2.55	3184	1308	0.40	12.22	4.37	20.06
MBR-B8	h2	2.60	2788	1181	0.39	10.07	3.62	15.35
MBR-B9	v	2.51	2733	1263	0.36	10.92	4.00	13.40
MBR-B9	h1	2.51	3146	1316	0.39	12.13	4.35	19.06
MBR-B9	h2	2.61	3081	1241	0.40	11.26	4.01	19.38
MBW-B16	v	2.24	2544	1274	0.33	9.68	3.63	9.64
MBW-B16	h1	2.25	2460	1232	0.33	9.10	3.41	9.06
MBW-B16	h2	2.23	2397	1145	0.35	7.91	2.92	8.92
MBW-B14	v	2.24	2525	1264	0.33	9.53	3.57	9.50
MBW-B14	h1	2.26	2861	1241	0.38	9.63	3.48	13.85
MBW-B14	h2	2.27	3006	1371	0.37	11.67	4.26	14.80
MBW-B12	v	2.32	3221	1443	0.37	13.27	4.83	17.61
MBW-B12	h1	2.35	3242	1432	0.38	13.29	4.82	18.27
MBW-B12	h2	2.33	2936	1443	0.34	13.00	4.85	13.60
MBW-B10	v	2.27	2432	1174	0.35	8.43	3.13	9.25
MBW-B10	h1	2.25	2334	1108	0.35	7.48	2.76	8.57
MBW-B10	h2	2.27	2582	1308	0.33	10.32	3.89	9.97
MBW-B8	v	2.30	2875	1115	0.41	8.07	2.86	15.19
MBW-B8	h1	2.30	2850	1133	0.41	8.30	2.95	14.74
MBW-B8	h2	2.32	2823	1189	0.39	9.15	3.29	14.14
T1-B5	v	2.41	2490	1247	0.33	10.00	3.75	9.95
T1-B5	h1	2.39	2786	1232	0.38	10.00	3.63	13.71
T1-B5	h2	2.34	2805	1238	0.38	9.90	3.59	13.64
T1-B4A	v	2.45	2600	1313	0.33	11.25	4.23	10.95
T1-B4A	h1	2.45	2694	1178	0.38	9.41	3.40	13.26
T1-B4A	h2	2.46	2510	1150	0.37	8.88	3.25	11.14
T1-B4B	v	2.47	2568	1073	0.39	7.92	2.84	12.49
T1-B4B	h1	2.48	2657	1358	0.32	12.09	4.57	11.39
T1-B4B	h2	2.48	2800	1480	0.31	14.21	5.44	12.21
T1-B3	v	2.62	2617	1298	0.34	11.80	4.41	12.05
T1-B3	h1	2.53	3683	1846	0.33	23.00	8.63	22.85
T1-B3	h2	2.51	3568	1865	0.31	22.90	8.73	20.31
T1-B2	h1	2.48	3646	1660	0.37	18.69	6.82	23.82
T1-B2	h2	2.53	3429	1508	0.38	15.89	5.76	22.09

9.8. Appendix H – Core Photos

Moki-1	Mangahewa Formation	2135-2136m

Moki-1	Mangahewa Formation	2136-2137m

Moki-1	Mangahewa Formation	2137-2138m

Moki-1	Mangahewa Formation	2138-2139m

Maui-A1G	Mangahewa Formation	2770.8-2772.68m

Maui-A1G	Mangahewa Formation	2772.68-2774.53m

Maui-A1G	Mangahewa Formation	2776.28-2778.02m

Maui-A1G	Kaimiro Formation	3068.25-3069.38m

Maui-A1G	Kaimiro Formation	3069.38-3070.92m

Maui-A1G	Kaimiro Formation	3074.5-3076.22m

Maui-A1G	Kaimiro Formation	3076.22-3077.97m

MBR-1	Farewell Formation	3516.9-3517.8m

MBR-1	Farewell Formation	3518.7-3519.7m

MBR-1	Farewell Formation	3521.5-3522.3m

MBR-1	Farewell Formation	3522.3-3523.2m

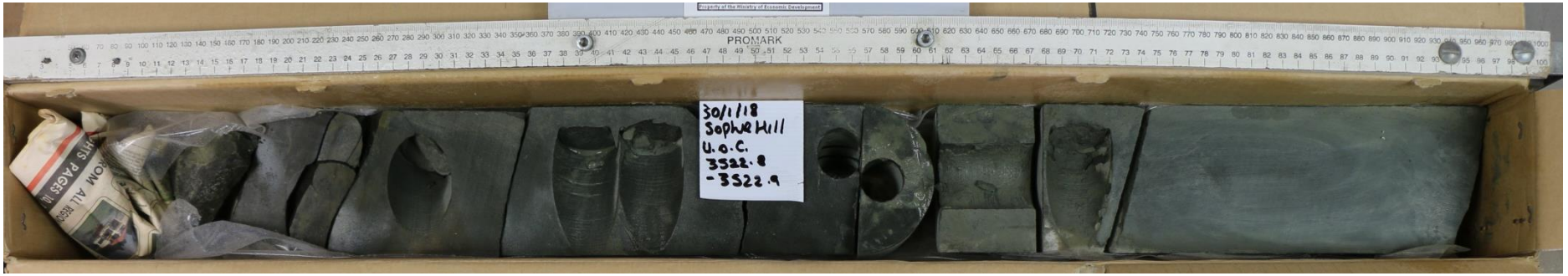

MBR-1	Farewell Formation	3523.2-3524.1m

MBW-2	Farewell Formation	4124.25-4125.1m

MBW-2	Farewell Formation	4126.26-4127.15m

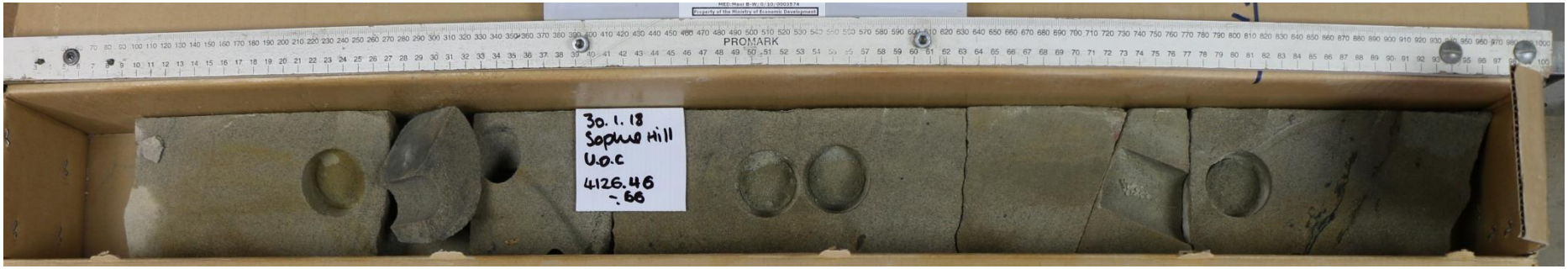

MBW-2	Farewell Formation	4128.05-4129.0m

MBW-2	Farewell Formation	4129.9-4131m

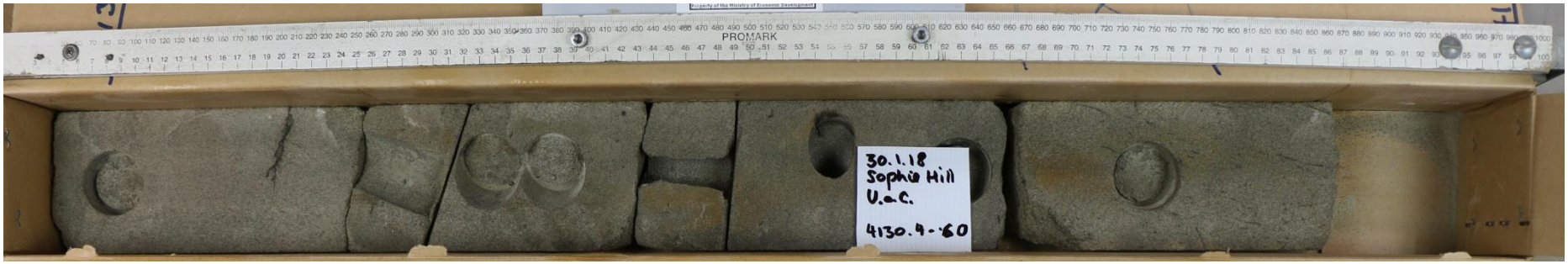

MBW-2	Farewell Formation	4131.95-4132.75m

Tane-1	North Cape Formation	3686.6-3688.12m

Tane-1	North Cape Formation	3688.12-3689.71m

Tane-1	North Cape Formation	3689.71-3691.5m

Tane-1	North Cape Formation	3691.5-3693.28m

Tane-1	North Cape Formation	3693.28-3694.73m

Tane-1	North Cape Formation	3694.73-3695.6m

9.1. Appendix I – Sidewall Core Data and Photos from Whio-1

OMV	NZP&M	Depth	Formation	Lithotype	Grain (Matrix) density (g/cm)	Porosity Fraction	Permeability
R2A1	#1	1460.00	M2A Sands	Sandstone	2.74	0.29	
R2A2	#2	2814.60	Farewell	Sandstone	2.67	0.12	0.11
R2A5	#5	2783.00	Farewell	Sandstone	2.71	0.14	7.48
R2A7	#7	2762.00	Farewell	Siltstone	2.56	0.07	0.08
R2A8	#8	2758.00	Farewell	Sandstone	2.66	0.19	98.63
R2A9	#9	2751.00	Farewell	Siltstone	2.64	0.06	0.00
R2A11	#11	2742.00	Farewell	Sandstone	2.68	0.17	0.93
R2A12	#12	2728.00	Farewell	Sandstone	2.67	0.17	18.44
R2A13	#13	2725.00	Farewell	Sandstone	2.72	0.09	0.01
R2A14	#14	2687.50	Farewell	Siltstone	2.62	0.08	
R2A15	#15	2682.50	Farewell	Sandstone	2.68	0.16	3.48
R2A17	#17	2670.00	Kaimiro	Sandstone	2.71	0.19	1.69
R2A22	#22	2601.00	Kaimiro	Sandstone	2.66	0.23	
R2A23	#23	2592.00	Kaimiro	Sandstone	2.63	0.09	
R2A25	#25	2507.00	Mangahewa	Sandstone	2.64	0.17	
R2A27	#27	2404.50	Mangahewa	Sandstone	2.64	0.15	1.35
R2A29	#29	2389.00	Mangahewa	Siltstone	2.63	0.03	
R2A31	#31	2371.00	Maui Sand	Sandstone	2.60	0.18	
R2A33	#33	2364.00	Maui Sand	Sandstone	2.58	0.25	
R2A35	#35	2354.00	Turi Shale	Siltstone	2.70	0.04	
R2A36	#36	2344.00	Turi Shale	Gl. Sandstone	2.94	0.13	
R2A38	#38	2337.50	Upper Turi	Sandstone	2.80	0.11	
R2A42	#42	2322.00	Otaraoa	Sandstone	2.70	0.05	
R2A43	#43	1533.00	Moki 1.1	Sandstone	2.80	0.24	
R2A44	#44	1525.00	Above Moki	Siltstone	2.91	0.17	
R2A47	#47	1450.00	Whio A to	Siltstone	2.84	0.17	
R2A48	#48	1444.00	Whio A	Sandstone	2.85	0.33	

OMV	Depth (m)	Formation	Lithotype	Dry bulk density (g/cm)	Vp Dry (m/s)	Vs Dry (m/s)	Poisson's Ratio	Young's Modulus (GPa)	Shear Modulus (GPa)	Bulk Modulus (GPa)
R2A1	1460.00	M2A Sands	Sandstone	1.94	1665	776	0.36	3.18	1.17	3.82
R2A2	2814.60	Farewell	Sandstone	2.34	1850	1114	0.22	7.07	2.91	4.14
R2A5	2783.00	Farewell	Sandstone	2.33	2161	1104	0.32	7.52	2.84	7.10
R2A7	2762.00	Farewell	Siltstone	2.38	2564	1123	0.38	8.28	3.00	11.63
R2A8	2758.00	Farewell	Sandstone	2.14	2174	1161	0.30	7.51	2.89	6.28
R2A9	2751.00	Farewell	Siltstone	2.48	2395	1168	0.34	9.09	3.38	9.71
R2A11	2742.00	Farewell	Sandstone	2.23	2306	1295	0.27	9.49	3.74	6.87
R2A12	2728.00	Farewell	Sandstone	2.20	1996	1176	0.23	7.52	3.05	4.71
R2A13	2725.00	Farewell	Sandstone	2.48	2137	1220	0.26	9.30	3.70	6.41
R2A15	2682.50	Farewell	Sandstone	2.24	1790	1031	0.25	5.96	2.38	4.00
R2A17	2670.00	Kaimiro	Sandstone	2.19	1923	1068	0.28	6.39	2.50	4.77
R2A22	2601.00	Kaimiro	Sandstone	2.05	2004	1156	0.25	6.85	2.74	4.58
R2A25	2507.00	Mangahewa	Sandstone	2.20	2421	1444	0.22	11.20	4.58	6.76
R2A27	2404.50	Mangahewa	Sandstone	2.24	2354	1325	0.27	9.96	3.93	7.16
R2A31	2371.00	Maui Sand	Sandstone	2.13	2146	1313	0.20	8.81	3.67	4.91
R2A35	2354.00	Turi Shale	Siltstone	2.59	2811	1604	0.26	16.75	6.66	11.57
R2A36	2344.00	Turi Shale	Sandstone	2.56	1895	1103	0.24	7.76	3.12	5.05
R2A38	2337.50	Upper Turi	Sandstone	2.50	1737	1063	0.20	6.78	2.82	3.77
R2A43	1533.00	Moki 1.1	Sandstone	2.12	2015	109	0.29	6.61	2.56	5.20
R2A47	1450.00	Whio A to M2A	Siltstone	2.35	2246	1201	0.30	8.80	3.39	7.33

OMV	Depth (m)	Formation	Lithotype	Saturated bulk density (g/cm)	Vp Wet (m/s)	Vs Wet (m/s)	Poisson's Ratio	Young's Modulus (GPa)	Shear Modulus (GPa)	Bulk Modulus (GPa)
R2A1	1460.00	M2A Sands	Sandstone	2.18						
R2A2	2814.60	Farewell	Sandstone	2.40	2413	1114	0.36	8.14	2.98	10.02
R2A5	2783.00	Farewell	Sandstone	2.42	2324	1010	0.38	6.83	2.47	9.77
R2A7	2762.00	Farewell	Siltstone	2.42	2234	954	0.39	6.12	2.21	9.15
R2A8	2758.00	Farewell	Sandstone	2.30	2294	1050	0.37	6.94	2.54	8.73
R2A9	2751.00	Farewell	Siltstone	2.52	3283	1481	0.37	15.19	5.53	19.81
R2A11	2742.00	Farewell	Sandstone	2.35	2368	1156	0.34	8.43	3.14	8.98
R2A12	2728.00	Farewell	Sandstone	2.33	2434	1014	0.39	6.67	2.39	10.59
R2A13	2725.00	Farewell	Sandstone	2.54	2824	1496	0.30	14.86	5.69	12.70
R2A15	2682.50	Farewell	Sandstone	2.37	2646	1496	0.27	13.39	5.29	9.50
R2A17	2670.00	Kaimiro	Sandstone	2.34	2693	1479	0.28	13.14	5.12	10.14
R2A22	2601.00	Kaimiro	Sandstone	2.23						
R2A25	2507.00	Mangahewa	Sandstone	2.33	2281	1248	0.29	9.36	3.64	7.30
R2A27	2404.50	Mangahewa	Sandstone	2.36	2138	1061	0.34	7.10	2.66	7.24
R2A31	2371.00	Maui Sand	Sandstone	2.28	1609	823	0.32	4.09	1.55	3.85
R2A35	2354.00	Turi Shale	Siltstone	2.63	2890	1320	0.37	12.55	4.59	15.87
R2A36	2344.00	Turi Shale	Sandstone	2.63	1240	657	0.30	2.97	1.14	2.53
R2A38	2337.50	Upper Turi	Sandstone	2.57						
R2A43	1533.00	Moki 1.1	Sandstone	2.31						
R2A47	1450.00	Whio A to M2A	Siltstone	2.50						


#1
1460m

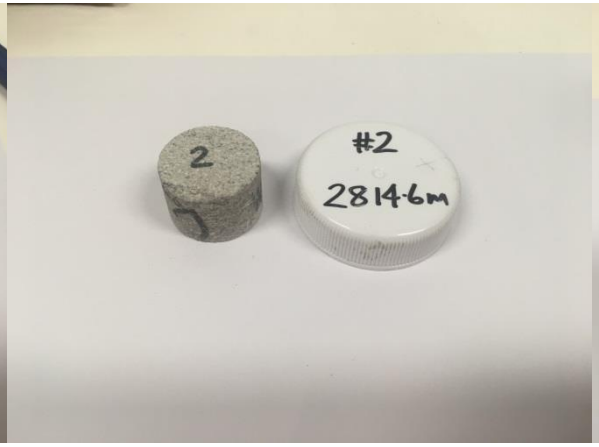
2
#2
2814.6m

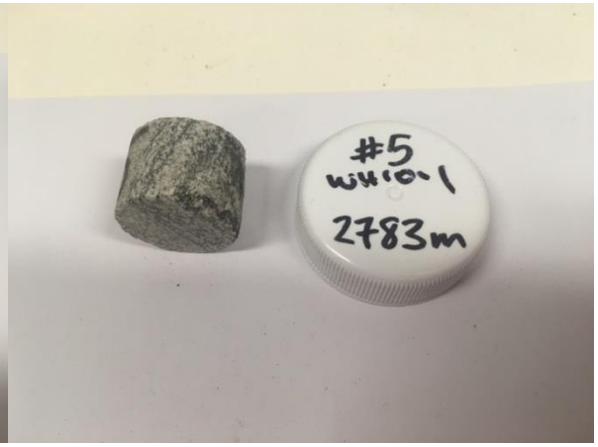
#5
2783m

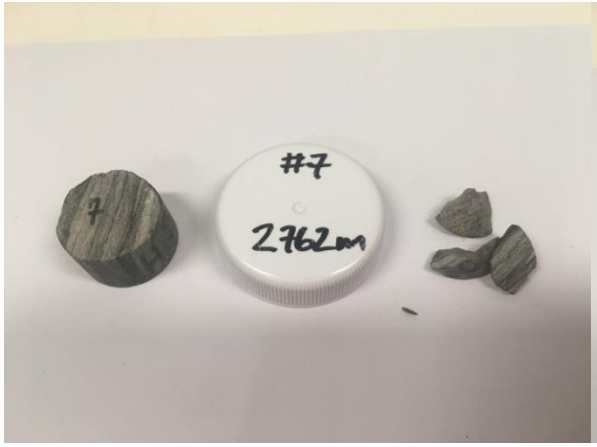
7
#7
2762m


#8
2758m


6
#9
2751m


#12
2728m


13
#13
2725m


#14
2687.5m


#15
2682.5m


#17
2670m


#22
2601m


#23
23
2592m
25
#25
2507m
#27
2404-5m


#29
2389m
#31
2371m
#33
WH10-1
33
2364m


#36
2344m
#38
2337.5m
#42
2322m


#43
WH101
1533m
#44
1525m


#47
1950m
#48
1994m